

PALEOCLIMATE TESTS OF A MODEL OF THE ATMOSPHERIC  
GENERAL CIRCULATION

*by*

***Guido Vettoretti***

A thesis submitted in conformity with the requirements  
for the degree of Doctor of Philosophy  
Graduate Department of Physics  
University of Toronto

Copyright ©2001 by Guido Vettoretti



**National Library  
of Canada**

**Acquisitions and  
Bibliographic Services**

395 Wellington Street  
Ottawa ON K1A 0N4  
Canada

**Bibliothèque nationale  
du Canada**

**Acquisitions et  
services bibliographiques**

395, rue Wellington  
Ottawa ON K1A 0N4  
Canada

*Your file Votre référence*

*Our file Notre référence*

**The author has granted a non-exclusive licence allowing the National Library of Canada to reproduce, loan, distribute or sell copies of this thesis in microform, paper or electronic formats.**

**The author retains ownership of the copyright in this thesis. Neither the thesis nor substantial extracts from it may be printed or otherwise reproduced without the author's permission.**

**L'auteur a accordé une licence non exclusive permettant à la Bibliothèque nationale du Canada de reproduire, prêter, distribuer ou vendre des copies de cette thèse sous la forme de microfiche/film, de reproduction sur papier ou sur format électronique.**

**L'auteur conserve la propriété du droit d'auteur qui protège cette thèse. Ni la thèse ni des extraits substantiels de celle-ci ne doivent être imprimés ou autrement reproduits sans son autorisation.**

0-612-63759-X

**Canada**

---

## FRONTISPIECE

### Arctic Bathymetry:

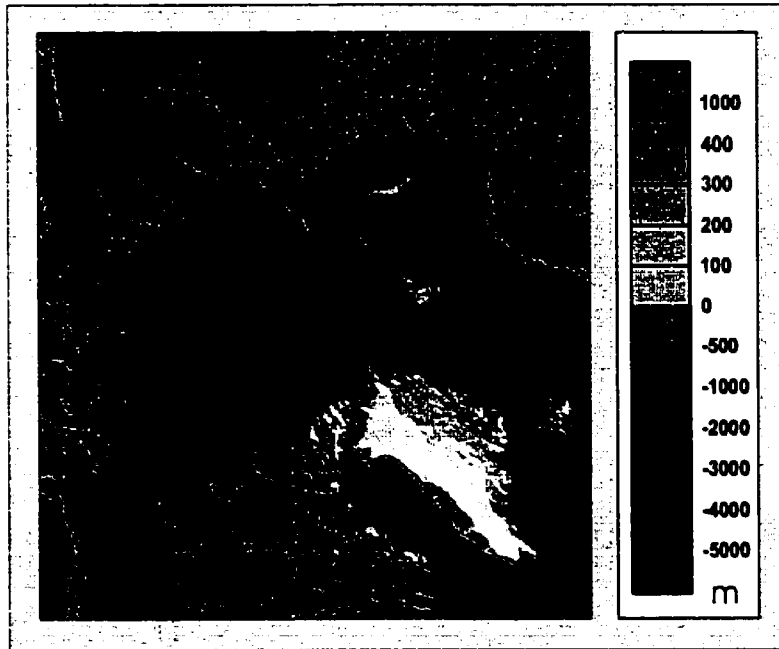
Continent-Ocean distribution in the Arctic centred on the North Pole. The elevation of the continents with respect to sea level and the bathymetry of the oceans are shown on the colour bar. The ocean depth and continental elevation information have been derived from two sources: the GEBCO Digital Atlas (Jones et al, 1994)[104]; and the ETOPO5 digital grid which describes global depths and elevations at intervals of 5 minutes of latitude and longitude (Loughridge, 1986)[133]. This image is reproduced from the web site of the Geological Survey of Canada at <http://agcwww.bio.ns.ca/pubprod/of2900/of2900.html>

### LGM Continental Topography:

A relief map of Last Glacial Maximum (LGM) topography over North America. The LGM reconstruction is based upon the ICE-4G data sets of Peltier (1994).

---

**Modern Arctic Bathymetry**



**The Laurentide Ice Sheet at Last Glacial Maximum**



---

Paleoclimate Tests of a Model of the Atmospheric General Circulation  
Guido Vettoretti, Department of Physics, University of Toronto, Ph.D. Thesis (2001)

ABSTRACT

Late-Pleistocene and mid-Holocene climate states at three selected 'time-slices' within the last ice age cycle have been simulated with the Canadian Climate Centre for modelling and analysis Atmospheric General Circulation Model (CCCma AGCM).

Simulations of the mid-Holocene optimum climate at 6000 years before present (6 ka BP) are performed to test the sensitivity of the model to modifications of the land surface parameterizations. The primary mechanisms responsible for an anomalous model response as compared with other models from the international Paleoclimate Model Intercomparison Project (PMIP) are thereby identified.

An AGCM reconstruction of Last Glacial Maximum (LGM) climate at 21 ka BP was also conducted to test predictions of LGM tropical SSTs and to investigate the mechanisms responsible for the maintenance of the southeasterly lobes of the Laurentide ice sheet. The model simulation of LGM climate is also compared with results from other models in the PMIP set and to the predictions of an intermediate complexity model that has been developed to simulate glacial-interglacial cycles. Model predictions of LGM tropical SSTs are found to be in good agreement with sea surface temperatures (SSTs) inferred from proxy reconstructions of LGM climate.

The onset of continental glaciation that occurred in the Post Eemian Glacial period (116 ka BP) provides a further means of testing the ability of the CCCma GCM under conditions that differ radically from the modern conditions to which the parameterization schemes in the model are tuned. The analyses described herein demonstrate that entry into glacial conditions at 116 ka BP is successfully predicted when the mixed layer slab ocean component of the CCCma AGCM is constrained to accurately reproduce AMIP2 observed modern SSTs under conditions of modern radiative forcing. A set of sensitivity experiments in which the solar radiation parameterization and the implied oceanic heat transport are modified, reveal a number of novel feedback mechanisms that are key to understanding the initiation of large-scale continental glaciation.

---

## ACKNOWLEDGMENTS

I would like to thank Professor Richard Peltier for the enthusiasm, knowledge, guidance, and encouragement that he has offered over the years. I am also very grateful to him for introducing me to the field of atmospheric physics and large scale computing. I would like to thank Dr. Norman McFarlane for his enthusiasm and knowledge of the physics of climate and global climate modelling and also the Canadian Climate Centre for modelling and analysis and the Meteorological Service of Canada for providing me with some of the software resources that have been required to carry out the research reported in this thesis. Financial support for this work has been provided by the Climate System History and Dynamics Research Network that is funded by the Natural Sciences and Engineering Research Council of Canada and by the Meteorological Service of Canada. I am also grateful to Dr. Rosemarie Drummond and Ms. Ana Sousa for their assistance with computational and administrative issues, respectively, and Mr. Khadar Khan and Mr. Raul Cunha for help in the area of computer graphics. I would also like to acknowledge thanks to the NRC research press for the authorization to include previously published material into this thesis. In particular, chapters 2 and 3 appear in the Canadian Journal of Earth Sciences. Finally and most importantly, I would like to thank my family and friends for their continuous support.

# CONTENTS

## CONTENTS

<b>1</b>	<b>Introduction</b>	<b>1</b>
1.1	Late Quaternary Climate and the Astronomical Theory of the Ice Ages . . . . .	1
1.2	Paleoclimate Modelling and Paleoclimate Reconstruction . . . . .	12
1.2.1	Description of the CCCma Global Climate Model . . . . .	18
1.3	Thesis Organization and Research Strategy . . . . .	22
<b>2</b>	<b>Climate Simulation of the Holocene Optimum: The Climate System Response to Changes in Soil Moisture Parameterization</b>	<b>23</b>
2.1	Introduction . . . . .	23
2.2	Land Surface Processes and Experimental Design . . . . .	26
2.2.1	Land Surface Processes . . . . .	26
2.2.2	Experimental Design . . . . .	29
2.3	Results: The Modern and 6 ka BP climate simulations . . . . .	31
2.3.1	Zonally Averaged Soil Moisture and PMIP Land Surface Schemes . . . . .	34
2.3.2	Zonally Averaged Surface Air Temperature at Screen Height (2m) . . . . .	37
2.3.3	Land surface response in the control simulations. . . . .	41
2.3.4	Land surface response in the 6 ka BP simulations . . . . .	44
2.3.5	The PMIP mid-latitude land surface response . . . . .	48
2.3.6	Intercomparisons with North American climate reconstructions . . . . .	54
2.4	Discussion and Conclusions . . . . .	58
<b>3</b>	<b>Climate Simulation of the Last Glacial Maximum: Global Water Balance and Atmospheric Water Vapour Transport</b>	<b>62</b>
3.1	Introduction . . . . .	62
3.2	Model Descriptions . . . . .	65
3.2.1	Energy Balance-ice-sheet model . . . . .	65
3.3	Experimental Design . . . . .	67
3.4	Results . . . . .	70
3.4.1	Model-Model Model-Data comparison at LGM . . . . .	70
3.4.2	Simulated AGCM and ISM/EBM climatology at LGM . . . . .	73

## CONTENTS

---

3.4.3	Mass Balance and the AGCM hydrological cycle at LGM . . . . .	78
3.4.4	The General Circulation and Eddy Moisture Transport at LGM . . . . .	83
3.5	Summary and Conclusions . . . . .	98
<b>4</b>	<b>Climate Simulation of Post Eemian Glacial Inception</b>	<b>102</b>
4.1	Introduction . . . . .	102
4.2	Model Constraints and Experimental Design . . . . .	106
4.2.1	Experimental Design . . . . .	107
4.3	Results . . . . .	110
4.3.1	Post Eemian Glacial Inception Climate . . . . .	111
4.4	Summary and Conclusions . . . . .	137
<b>5</b>	<b>Conclusion</b>	<b>142</b>
5.1	Model Development and Climate Prediction . . . . .	142
5.2	General Conclusions . . . . .	150
<b>A</b>	<b>The Earth's Insolation Distribution Over Time</b>	<b>152</b>
A.1	Daily Insolation . . . . .	152
A.2	Radiative Forcing at the Top of the Model . . . . .	154
A.3	Defining the Seasons . . . . .	155
<b>B</b>	<b>The Dynamical Core of an AGCM</b>	<b>156</b>
<b>C</b>	<b>Model Documentation: CCCma Version 2 (T32 L10) 1992</b>	<b>160</b>
<b>D</b>	<b>Constraining the Model so as to Reproduce Modern Climate</b>	<b>167</b>
D.1	Oceanic Heat Flux Correction . . . . .	167
D.2	Solar Radiation Parameterizations . . . . .	169
<b>E</b>	<b>Glacial Inception Modelling Issues within Spectral AGCMs.</b>	<b>174</b>
<b>F</b>	<b>The Modern Simulated Polar Climate</b>	<b>178</b>

## LIST OF TABLES

### LIST OF TABLES

2.1	PMIP model land surface processes. Listed are the number of soil layers for prognostic soil temperature (T) and moisture (Q) (0 layers denotes no heat storage or prescribed moisture). . . . .	32
3.1	The global hydrological cycle. Area averaged quantities for modern observed (from Baumgartner and Reichel 1975 ) [12], modern AGCM simulated and 21 kyr BP AGCM simulated hydrological components over land and ocean . . . . .	80

# LIST OF FIGURES

## LIST OF FIGURES

1.1	The Earth's orbital variations. (a) The eccentricity cycle: The deviation of the Earth's orbit from circular over time fluctuates with periods of 413 and 100 ka. Large eccentricity accentuates precessional forcing. (b) The obliquity cycle: The tilt of the Earth's rotational axis with respect to the perpendicular to the ecliptic varies with a period of approximately 41 ka. Large obliquity affects the amount of sunlight received at high latitudes. (c) The eccentricity-precessional cycle: The precession of the rotational axis of the Earth, whose amplitude is modulated by the orbital eccentricity determines the position of the solstices and equinoxes with respect to perihelion. The eccentricity-precessional parameter determines the magnitude of the seasonal contrast during an annual cycle. The orbital data plotted for the past 150 ka is from Quinn et al. (1991)[184]. . . . .	5
1.2	(a) The time series and (b) spectrum of the $\delta^{18}\text{O}$ record from ODP-677 and (c) the time series and (d) spectrum of the summer insolation signal at 65 °N for the first and second million years of Earth history. The 90%, 95% and 99% curves in (b) represent the confidence level of the peaks above the background noise. The $\epsilon$ -band, $\epsilon$ -band, $\omega$ -band represent the band width covered by the main eccentricity, obliquity and precessional modes. . . . .	9
1.3	Various proxy data from geological inferences of past climate. (a) The summer insolation signal at 65 °N and $\delta^{18}\text{O}$ record from ODP-677 for the last 350 000 years. (b) African lake level data for 6 ka BP. (c) Annual mean reconstructions of CLIMAP sea surface temperatures. . . . .	14
1.4	The isolation at the top of the atmosphere as a function of latitude and time of year for (a) present day, (b) the difference between 6 ka BP and modern, (c) the difference between 21 ka BP and modern and (d) the difference between 116 ka BP and modern. The reference time for the vernal equinox in (b), (c) conform with the PMIP specification, while that in (d) minimizes the annual root mean square insolation (see Appendix A). Units are in $\text{W m}^{-2}$ . Contour intervals are 50 $\text{W m}^{-2}$ in (a) and 4 $\text{W m}^{-2}$ in (b), (c) and (d). . . . .	18

## LIST OF FIGURES

---

1.5	The major components and processes that determine the state of the global climate system. . . . .	20
2.1	(a) North American and (b) Asian water holding field capacity ( $\text{kg m}^{-2}$ ) prescribed within the CCCma GCMII variable bucket scheme. The contour interval is $150 \text{ kg m}^{-2}$ ( $\text{kg m}^{-2} = 0.1 \text{ cm}$ ). (c) Zonally averaged water holding field capacity ( $\text{kg m}^{-2}$ ) prescribed within the CCCma GCMII variable bucket scheme. (d) Zonally averaged evapotranspiration slope factor. . . . .	27
2.2	Liquid and frozen soil moisture spin up within the CCCma AGCM ( $\text{Kg m}^{-2}$ ). . . . .	30
2.3	Annually and zonally averaged PMIP (a) modern soil moisture and the (b) 6 ka BP - modern anomaly. Units are in $\text{Kg m}^{-2}$ ( $\text{Kg m}^{-2} = 0.1 \text{ cm}$ ). c) Percent change in 6 ka BP anomaly $100 * (6\text{ka}-0\text{ka})/6\text{ka}$ . The solid and dashed black lines represent the CCCma model with the variable bucket scheme/variable slope factor (VB $V\beta$ ) and the CCCma model with the 20 cm constant bucket scheme/constant slope factor (FB $F\beta$ ), respectively . . . . .	35
2.4	Seasonally and zonally averaged northern hemisphere PMIP 2m surface air temperatures ( $^{\circ}\text{C}$ ) over land for (a) modern DJF, (b) 6 ka BP - modern DJF, (c) modern JJA, and (d) 6 ka BP - modern JJA. The thick grey lines are the modern observed in (a) and (c) (Legates and Willmott 1990)[126] and the model mean in (b) and (d). . . . .	38
2.5	Seasonally and zonally averaged northern hemisphere 2m surface air temperatures ( $^{\circ}\text{C}$ ) over land for (a) modern (b) 6 ka BP - modern JJA. The thick grey lines are the modern observed in (a) (Legates and Willmott 1990)[126] and the PMIP model mean in (b). In the legend, V=variable, F=fixed, B=bucket, and $\beta$ =evapotranspiration slope factor. . . . .	40

## LIST OF FIGURES

---

- 2.6 Modern zonally averaged JJA surface energy budget anomalies between the CCCma simulation with constant 20 cm bucket (FB  $F\beta$ ) and the simulation with a variable bucket scheme (VB  $V\beta$ ). a) The shortwave absorption (dashed line) is plotted with the net longwave radiation (solid line). b) The surface albedo (dashed line) and total cloudiness (solid line) for the control anomaly are denoted in percentage terms. c) The latent (solid line) and sensible heat (dashed line) flux anomalies between the two control simulations are plotted. Negative values denote upward fluxes of radiation and heat fluxes in  $W m^{-2}$ . d) The control anomalies for ground temperature ( $^{\circ}C$ ) and the sum of the components in (a) and (c) which make up the surface energy balance ( $W m^{-2}$ ) are plotted in solid and dashed lines, respectively. . . . . 43
- 2.7 6 ka BP - modern JJA northern hemisphere zonally averaged surface anomalies in the 4 simulations are displayed for (a) shortwave absorption in  $W m^{-2}$ , (b) net longwave in  $W m^{-2}$ , (c) sensible heat flux in  $W m^{-2}$ , (d) latent heat flux in  $W m^{-2}$ , (e) total cloudiness (%), (f) surface albedo (%), (g) snow mass ( $Kg m^{-2}$ ) and (h) ( $SW+LW+SHF+LHF$ ) in  $W m^{-2}$ . In the legend, V=variable, F=fixed, B=bucket, and  $\beta$ =evapotranspiration slope factor. . . . . 46
- 2.8 Global distributions of JJA 2m surface air temperature anomalies (6 ka BP - modern ) ( $^{\circ}C$ ) for the CCCma simulation with the (a) variable bucket scheme (VB  $V\beta$ ) and the (b) constant 20 cm bucket scheme (FB  $F\beta$ ). The contour interval is at  $1^{\circ}C$  with shaded regions designating changes above  $1^{\circ}C$  for JJA. The boxed regions highlight regions which are responsible for the zonally averaged response seen in Fig. 2.1d. . . 49
- 2.9 Scatter plot of the JJA ground temperature versus 6 ka BP JJA ground temperature anomaly for the PMIP simulations. b) Scatter plot of the JJA precipitation vs. 6 ka BP JJA precipitation anomaly for the PMIP simulations. Precipitation is plotted in  $mm day^{-1}$  while temperature is in  $^{\circ}C$ . The intersection of the horizontal and vertical solid lines represent the model mean, while the box represents one standard deviation in the abscissa and ordinate directions. The dashed line is the linear regression. . . . 51
- 2.10 Scatter plots of net longwave vs. shortwave absorption for the PMIP (a) JJA control, and (b) JJA 6 ka BP - modern anomaly. Scatter plots of sensible heat flux vs. latent heat flux for the PMIP (c) JJA control, and (d) JJA 6 ka BP - modern anomaly. Units are in  $W m^{-2}$ . . . . . 53

## LIST OF FIGURES

---

2.11	Lake level status and Precipitation minus Evaporation (P-E) anomalies at 6 KBP for the (a) variable bucket simulation (VB $V\beta$ ) and (b) fixed bucket simulation (FB $F\beta$ ). P-E is in $\text{mm yr}^{-1}$ in contour intervals of $20 \text{ mm yr}^{-1}$ . . . . .	57
2.12	Changes in JJA surface temperature between 6 KBP and modern for (a) the variable bucket simulation (VB $V\beta$ ) and (b) the fixed bucket simulation (FB $F\beta$ ). . . . .	58
3.1	(a) Globally and annually averaged LGM ground temperature ( $^{\circ}\text{C}$ ) vs. model time (years) for the CLIMAP prescribed SST and computed SST simulations. (b) northern and southern hemisphere annually averaged ground temperature for the LGM computed SST simulation. An exponential fit to the decay curves for global and northern hemisphere temperatures are displayed for the computed SST experiments. . . . .	69
3.2	PMIP differences in tropical ground temperature vs. tropical ocean SSTs between $30^{\circ}\text{S}$ and $30^{\circ}\text{N}$ . (a) LGM - Modern tropical land and ocean differences in the computed SST PMIP experiments. (b) Present and LGM tropical temperatures for the computed SST experiments. (c) LGM - Modern tropical land and ocean differences in the CLIMAP fixed SST PMIP experiments. (d) Present and LGM tropical temperatures for the fixed SST experiments. . . . .	72
3.3	Last Glacial Maximum topography. (a) ICE-4G hi-resolution data set. (b) AGCM T32 spectrally smoothed ICE-4G LGM topography. (c) ISM topography at maximum ice volume. (d) AGCM minus ISM LGM topographic anomaly. The ice-sheet margin in Figs. (a),(b) and (c) is displayed by a white line along with the southern ice margin extent of Figs. (b) and (c) in (d). . . . .	75
3.4	Annual mean ground temperature reconstructions ( $^{\circ}\text{C}$ ). Contour and shading intervals are 5 and $10^{\circ}\text{C}$ , respectively. (a) Modern AGCM simulated climate with computed SSTs. (b) LGM AGCM simulated climate with computed SSTs. (c) ISM ground temperature at maximum ice extent. (d) AGCM minus ISM LGM ground temperature anomaly. . . . .	76
3.5	Annual mean precipitation distributions ( $\text{m a}^{-1}$ ). (a) Modern AGCM simulated climate with computed SSTs. (b) LGM AGCM simulated climate with computed SSTs. (c) ISM precipitation at maximum ice extent. (d) AGCM minus ISM LGM precipitation anomaly. . . . .	78

3.6	AGCM simulated zonally averaged P-E anomaly over the Laurentide ice-sheet ( $\text{cm a}^{-1}$ ). (a) The region of interest: $35^{\circ}\text{N}$ to $75^{\circ}\text{N}$ and $138^{\circ}\text{W}$ to $56^{\circ}\text{W}$ . (b) Changes in P-E between LGM and present zonally averaged over the region of interest. . . . .	81
3.7	LGM ice-sheet mass balance simulated in the AGCM computed SST experiment over the region of interest (Fig. 5a). (a) Annual mean P-E anomaly between LGM and present ( $\text{Kg m}^{-2} \text{ a}^{-1}$ ). (b) Snow mass accumulation rate at LGM ( $\text{Kg m}^{-2} \text{ a}^{-1}$ ). (c) Snow mass ablation rate at LGM ( $\text{Kg m}^{-2} \text{ a}^{-1}$ ) (d) Positive mass balance at LGM ( $\text{Kg m}^{-2} \text{ a}^{-1}$ ). . . . .	82
3.8	Laurentide ice-sheet ablation zones for the (a) ISM and (b) AGCM. Units are in $\text{Kg m}^{-2} \text{ a}^{-1}$ . . . . .	84
3.9	Northern hemisphere mean sea level pressure (hPa) and surface winds (meters/second) for (a) modern DJF, (b) computed SST LGM DJF, (c) fixed SST LGM DJF, (d) modern JJA, (e) computed SST LGM JJA, and (f) fixed SST LGM JJA. Contour interval is 10 hPa. . . . .	85
3.10	Northern hemisphere mean sea level pressure (hPa) and surface winds (meters/second) anomalies (LGM -Present) for (a) computed SST DJF, (b) computed SST JJA, (c) fixed SST DJF, and (d) fixed SST JJA. Contour interval is 5 hPa. . . . .	87
3.11	Northern hemisphere winter 500 hPa geopotential height (decameters) and wind vectors (meters/second) for (a) modern, (b) LGM, (c) computed SST LGM - modern, and (d) fixed SST LGM - modern. In (a) and (b) contours are at 10 decameter intervals with wind vectors greater than $10 \text{ m s}^{-1}$ shown. In (c) and (d) contours are at 2 decameters with shaded regions greater than -10 and 0 decameters, respectively. . . . .	89
3.12	Annual mean sea ice mass distributions ( $\text{Kg m}^{-2}$ ). (a) Computed SSTs and sea ice distribution. (b) CLIMAP SSTs and sea ice distribution. . . . .	91
3.13	DJF ground temperatures and sea surface temperatures. (a) CLIMAP fixed SSTs - Modern (b) Computed SSTs - CLIMAP SSTs. Contour interval is $5^{\circ}\text{C}$ . . . . .	93
3.14	Annual mean total water vapour transport ( $\text{Kg m}^{-1} \text{ s}^{-1}$ ). (a) Modern observed. (b) Modern computed SST simulation. (c) LGM computed SST simulation. (d) LGM - modern anomaly. Contour interval is $100 \text{ Kg m}^{-1} \text{ s}^{-1}$ in (a), (b), and (c) and $50 \text{ Kg m}^{-1} \text{ s}^{-1}$ in (d). . . . .	94
3.15	Annual mean northward meridional transient eddy moisture transport ( $\text{Kg m}^{-1} \text{ s}^{-1}$ ). (a) Modern observed. (b) Modern computed SST simulation. Contour interval is $10 \text{ Kg m}^{-1} \text{ s}^{-1}$ . . . . .	96

## LIST OF FIGURES

---

3.16	Annually and zonally averaged northward meridional transient eddy moisture transport ( $\text{Kg m}^{-1} \text{s}^{-1}$ ). (a) Modern with a contour interval of $10 \text{ Kg m}^{-1} \text{s}^{-1}$ (b) LGM - modern anomaly with a contour interval of $2 \text{ Kg m}^{-1} \text{s}^{-1}$ . . . . .	97
3.17	North American and (b) European annual mean northward meridional transient eddy moisture transport anomalies between LGM and modern ( $\text{Kg m}^{-1} \text{s}^{-1}$ ). The contour interval is $4 \text{ Kg m}^{-1} \text{s}^{-1}$ . . . . .	98
4.1	A timeseries of eccentricity, obliquity, precession and top of the atmosphere insolation anomaly from the penultimate deglaciation to post Eemian glacial inception spanning 35 ka. The point at which conditions would be most favourable for glacial inception is signified by the line labeled "GI". The insolation curve (left vertical axis) measures the total energy anomaly with respect to modern (in units of $10^{23}$ Joules) received in the Arctic polar cap during summer. The orbital parameters for each of the three orbital elements are indicated on the right vertical axis. . . . .	108
4.2	Northern hemisphere polar contour plots of August 10 year perennial snow accumulation for the (a) warm, (b) unbiased and (c) cold biased 116 ka BP experiments. Values above $10 \text{ kg m}^{-2}$ are shaded. The contour interval is $500 \text{ kg m}^{-2}$ . The difference between (c) and (b) is displayed in (d). . . . .	112
4.3	Time series of northern hemisphere (a) snow cover and (b) sea ice cover anomalies in millions of $\text{km}^2$ for the warm, cold and unbiased 116 ka BP experiments. . . . .	116
4.4	Arctic time series of (a) surface temperature and (b) surface albedo anomalies over land in the warm biased, unbiased, and cold biased experiments. The contour interval for the temperature is $2 \text{ }^\circ\text{C}$ while that for the albedo is 0.1. Negative values are dashed. . . . .	118
4.5	Arctic time series of (a) shortwave absorbed radiation and (b) surface net longwave radiation anomalies over land in the warm biased, unbiased, and cold biased experiments. The contour interval for the shortwave radiation is $10 \text{ W m}^{-2}$ while that for the longwave radiation is $5 \text{ W m}^{-2}$ . Negative values are dashed. . . . .	121
4.6	Arctic time series of (a) latent and (b) sensible heat flux anomalies over land in the warm biased, unbiased, and cold biased experiments. The contour interval is $10 \text{ W m}^{-2}$ . Negative values are dashed. . . . .	123
4.7	Arctic time series of (a) precipitation and (b) evaporation anomalies over land in the warm biased, unbiased, and cold biased experiments. The contour interval is $0.2 \text{ mm/day}$ . Negative values are dashed. . . . .	125

4.8 Time series of (a) the rate of change in total Arctic precipitable water, (b) Arctic E-P and (c) northward transport of water vapour into the Arctic circle for the three modern control and three 116 ka BP experiments. Observed values are indicated in black. Arrows indicate the direction of increasing divergence and convergence. Units are in  $\text{kg m}^{-2} \text{yr}^{-1}$ . . . . . 127

4.9 Time series of the 116 ka BP anomalies for (a) the rate of change in total Arctic precipitable water, (b) Arctic E-P and (c) northward transport of water vapour into the Arctic circle. Arrows indicate the direction of increasing divergence and convergence anomalies. Units are in  $\text{kg m}^{-2} \text{yr}^{-1}$ . . . . . 130

4.10 Contour plot of the modern simulated annual average total water vapour transport for the unbiased experiment. The 116 ka BP anomalies in total water vapour transport for the (b) warm biased, (c) unbiased, and (d) cold biased experiments. The contour interval is  $10 \text{ kg m}^{-1} \text{ s}^{-1}$  in (a) and  $5 \text{ kg m}^{-1} \text{ s}^{-1}$  in (b), (c), and (d). . . . . 132

4.11 Contour plot of the annual mean northward transport of latent heat by transient eddies for the unbiased experiment. The 116 ka BP anomalies in northward transient eddy latent heat transport for the (b) warm biased, (c) unbiased, and (d) cold biased experiments. The contour interval is  $2 \times 10^7 \text{ W m}^{-1}$  in (a) and  $1 \times 10^7 \text{ W m}^{-1}$  in (b), (c), and (d). To convert to latent heat transport ( $\text{W m}^{-1}$ ), the moisture transport ( $\text{kg m}^{-1} \text{ s}^{-1}$ ) is multiplied by the latent heat of vaporization:  $L_e = 2.5 \times 10^6 \text{ J kg}^{-1}$ . 134

4.12 Contour plot of the annual mean northward transport of sensible heat by transient eddies for the unbiased experiment. The 116 ka BP anomalies in northward transient eddy sensible heat transport for the (b) warm biased, (c) unbiased, and (d) cold biased experiments. The contour interval is  $5 \times 10^7 \text{ W m}^{-1}$  in (a) and  $2 \times 10^7 \text{ W m}^{-1}$  in (b), (c), and (d). To convert to sensible heat transport ( $\text{W m}^{-1}$ ), the temperature flux ( $^\circ\text{C m s}^{-1}$ ) is multiplied by the specific heat capacity of air at constant pressure, the surface pressure and the inverse of gravity:  $c_p p_0 \text{ g}^{-1} \simeq 1 \times 10^7 \text{ J m}^{-2} \text{ }^\circ\text{C}^{-1}$ . . . 136

5.1 The same plot as in Fig. 2.5 but for the GCM2 version with the land surface which employs the variable buck and variable evapotranspiration slope factor and two GCM3 simulations of 6 ka BP climate which use modern (GCM3-i) and pre-industrial (GCM3-ii)  $\text{CO}_2$  levels. . . . . 144

## LIST OF FIGURES

---

5.2	Differences in August solid precipitation between modern and 116 ka BP for the standard model resolution (a) and (b). Differences in August solid precipitation between modern and 116 ka BP for the lapse rate adjusted downscaling parameterization at double the model resolution (c) and (d). . . . .	145
5.3	Annual mean surface temperature over North America in CO <sub>2</sub> doubling experiments with the original 1992 CCC version of GCM2 (a) and the current U of T 2000 version of the model (b). Contour interval is 1 °C. . . . .	146
5.4	Annual Arctic insolation above 60 °N latitude from 600 000 years before present to 200 000 years after present (dashed line) and the δ <sup>18</sup> O record from ODP-677 for the last 600 000 years (solid line). The measures at the top of the plot indicate the length of the dominant modes of the glacial-interglacial cycles. Three future climate scenarios are also presented. (A) A short 82 ka cycle. (B) A longer 123 ka cycle. (C) The collapse of the glacial-interglacial cycles due to the influence of future anthropogenic CO <sub>2</sub> levels in the atmosphere. . . . .	147
5.5	The difference from modern in isolation at the top of the atmosphere as a function of latitude and time of year for the next 8 000 years at 1000 year intervals are displayed in (a) to (h). Contour intervals 4 W m <sup>-2</sup> . . . . .	149
A.1	(a) The definition of the Zenith angle Z, using the (zenith-pole-sun) spherical triangle. The vector <b>p</b> denotes the vector from the center of the Earth to the point on the surface. The vector <b>s</b> , is the vector from the centre of the Earth to the Sun; φ is the latitude; δ is the declination of the sun and <i>h</i> is the hour angle of the sun. (b) The elements of the elliptical geometry: ω is the longitude of the perihelion with respect to the autumnal equinox; <i>a</i> and <i>b</i> are the lengths of the semi-major and semi-minor axes; <i>e</i> is the eccentricity; β is the true longitude of the Earth with respect to the perihelion; λ is the true longitude of the Earth measured from the vernal equinox. . . . .	152
A.2	The vernal equinox drift in days from January 1 <sup>st</sup> . This drift is used to facilitate comparison of seasons with the same duration but in different paleoclimate epochs. The drift which varies with precession is modulated by the 413 ka and 100 ka components of the eccentricity. . . . .	155

## LIST OF FIGURES

---

- D.1 The zonally and annually averaged all basin northward oceanic heat transport for the observed and the modern AGCM climate with computed SSTs. The observed values (Trenberth and Solomon 1994)[225] are derived indirectly by analyzing atmospheric measurements and heat fluxes from satellite data. The scale is in units of  $10^{15}$  Watts = 1 PetaWatt. . . . . 170
- D.2 A Hovmuller diagram of the northern hemisphere zonally averaged solar radiation anomaly absorbed at the surface in  $W m^{-2}$  between two AGCM simulations of modern climate. Each simulation employs ocean heat transports derived with full solar radiation calculations every 9 model timesteps but with one simulation subsequently run with full solar radiation calculations at every model timestep. High latitude negative anomalies reflect the deficit in solar radiation received at the surface when the model does not compute full solar radiation calculations at every timestep. . . . . 172
- E.1 Topographic anomalies over Canada (in meters) between T32 spectral and  $1 \times 1^\circ$  grid point representation of the land-ocean surface in the model. (b) A cross-section at  $78^\circ N$  latitude demonstrating the elevation difference and spatial misrepresentation between spectral and grid point inferences of major continental features in the northern polar hemisphere. . . . . 177
- F.1 A global plot of the annually averaged differences between two modern observed SST data sets (AMIP2 (Fiorino 1996) and Alexander and Mobley (1976))[61][3]. (b) A global plot of the annually averaged differences between two sets of simulated modern SSTs (the unbiased (AMIPS1) and cold biased (AMS9) experiments). (c) The differences between observed AMIP2 SSTs and the corresponding simulated SSTs (AMIPS1) and (d) the differences between observed Alexander and Mobley SSTs and the corresponding simulated SSTs (AMS9). Contours above  $0^\circ C$  are shaded and the contour interval is  $0.5^\circ C$ . . . . . 179
- F.2 A scatter plot of modern northern hemisphere land vs. ocean surface temperatures in the warm (AMS1), cold (AMS9) and unbiased (AMIPS1) experiments for (a) summer and (b) winter. Each point in the cluster of ten points in each simulation represents the average from each of the ten equilibrium years obtained for each simulation. The vertical and horizontal lines represent land and ocean temperature from observed data sets. The grey areas of intersection represent the best observed estimates. . . . . 181

## LIST OF FIGURES

---

- F.3 (a) Northern hemisphere polar contour plots of summer surface temperature for modern observed values in °C. The contour interval is 4 °C. The modern control temperature anomalies with respect to observed are displayed for the (b) warm, (c) unbiased and (d) cold biased simulations. The anomaly contour interval is 2 °C. Positive values are shaded in the observed data, while negative anomalies in the modern simulated are shaded (i.e. simulated - observed). . . . . 183
- F.4 Northern hemisphere polar contour plots of winter surface temperature for modern observed values in °C. The contour interval is 10 °C. The modern control temperature anomalies with respect to observed are displayed for the (b) warm, (c) unbiased and (d) cold biased simulations. The anomaly contour interval is 4 °C. Negative values and negative anomalies are shaded. . . . . 185
- F.5 Northern hemisphere polar contour plots of summer precipitation for the modern observed climate. The modern control precipitation anomaly (simulated - observed) for the (b) warm, (c) unbiased and (d) cold biased simulations. Positive values are shaded. The contour interval is 1 mm/day. . . . . 186
- F.6 Northern hemisphere polar contour plots of summer snow depth for the modern observed climate. The modern control snow depth for the (b) warm, (c) unbiased and (d) cold biased simulations. Values above 1 cm depth are shaded. The contour interval is 2 cm. . . . . 188



---

*The calculation gives for the planet Mercury a rotation of the orbit of 43" per century, corresponding exactly to the astronomical observation (Leverrier); for the astronomers have discovered in the motion of the perihelion of this planet, after allowing for disturbances by the other planets, an inexplicable remainder of this magnitude.*

*-Albert Einstein in concluding his presentation of the vacuum field equations in his 1916 paper on general relativity pointed out that they explained the anomalous precession of Mercury.*

---

# CHAPTER 1

---

## Introduction

This thesis is devoted to an investigation of Earth's climate during selected epochs of the late-Pleistocene (Pleistocene: 1.6 million to 10 000 years before present) and mid-Holocene (Holocene: 10 000 years ago to present) periods of Earth history. Three specific epochs within the last 125 000 years will be addressed through a series of numerical simulations of the global climate system under the radically different boundary conditions and/or radiative forcing regimes characteristic of conditions at these times. In the introduction to this thesis I will address a number of outstanding issues in the current literature in the area of Late Quaternary paleoclimate research, from both a numerical modelling and geological proxy climate data perspective. The application of modern coupled atmosphere-ocean models of the climate system to the reconstruction of climate states in the distant past for times at which sufficient geological data exist to constrain the climate regime has become an important means of testing the robustness of the parameterization schemes employed to represent sub-grid scale processes in such models. The first subsection of this introduction will review the astronomical theory of the ice-ages and the nature of the dominant modes of climate variability in the Earth system that have determined the climate state of the Late Quaternary of Earth history (Quaternary: Subdivided into the Pleistocene and Holocene epochs defined above). The second subsection will describe the numerical model that has been employed in this study along with the major changes to this structure that have been required for the successful completion of the research. The third and final subsection will briefly describe the organization of the main body of the thesis to follow.

### **1.1. Late Quaternary Climate and the Astronomical Theory of the Ice Ages**

In a summary for policymakers in the latest assessment report from the Intergovernmental Panel on Climate Change (IPCC 2001)[101] it is stated that:

An increasing body of observations gives a collective picture of a warming world and other changes in the climate system.

In particular the delegation of representatives attending the final meeting of this group agreed that it is very likely<sup>1</sup> that the decade of the 1990s was the warmest of the last century and that 1998 was the warmest year in the instrumental record since 1861. In addition to this it was agreed that it is likely<sup>2</sup> that the 1990s and 1998 were the warmest decade and warmest year, respectively, within the last millennium. The general consensus expressed in IPCC 2001 is that the body of scientific research that has been conducted to date indicates that global warming through the so called "greenhouse effect" (Houghton 1997)[91] is indeed occurring and is very likely<sup>1</sup> the result of anthropogenic effects. The modern atmospheric concentration of carbon dioxide (CO<sub>2</sub>) and other greenhouse gases such as methane (CH<sub>4</sub>) have not existed, according to inferences from the geological record, for at least the past 420 000 years (Petit et al. 1999; Falkowski et al. 2000)[176][59]. The atmospheric CO<sub>2</sub> concentration is now at the level of 365 parts per million by volume (ppmv), a very substantial increase above the pre-industrial level of 280 ppmv. It is still uncertain as to what the eventual effect of humankind will be upon the planetary environment but at present rates of increase it is expected that the CO<sub>2</sub> concentration in the atmosphere will have doubled by approximately 2065 by which time the impact upon global climate is expected to be highly significant. By comparing the state of the modern climate system, which is accurately known on the basis of the instrumental record, with climate states that existed in the past, which are constrained by geological proxy data, and by comparing simulations of these different climate states produced by modern numerical models of the climate system, we may reasonably hope to achieve a greater understanding of the complex feedback mechanisms which operate within the highly non-linear Earth system. In fact, it is likely that to understand the significant changes that may occur within the climate system, even within the next 100 years, a detailed knowledge of the extreme climate system variability inferred on the basis of the geological record to have occurred over the past 125 000 years will be a prerequisite to understanding the extreme impacts that could arise in the greenhouse warmed world into which we are evolving.

There is a large volume of evidence which supports the notion that since the formation of the Earth and the development of its solid and fluid components, the planet has experienced several periods of wide-spread continental glaciation (Crowley 1983)[42]. It is even suggested, according to geological and paleomagnetic studies, that during the late Proterozoic epoch, 600-800 million years before present (600-800 Ma BP), ice sheets may have reached equatorial latitudes and that the Earth may then have been in a completely ice covered or "snowball" state (see Hyde et al. 2000 and

---

<sup>1</sup>very likely: 90-99% confidence level

<sup>2</sup>likely: 66-90% confidence level

references therein)[96]. From the viewpoint of climate dynamics, the so-called astronomical theory of glaciation is the oldest explanation for the existence of the occurrence of continental glaciation cycles in the Quaternary geological record (1.6 - 0 Ma BP). Within the hundred years following Agassiz (1838)[2] proposal of a connection between glaciations and the Earth's precession, theories evolved and a mathematical formulation of the astronomical theory was developed (see Imbrie and Imbrie 1979 for a review)[98]. In 1920, the astronomer Milutin Milankovitch analytically produced detailed tables of the solar irradiance at 65 °N and other latitudes and as a function of season for the past 600 000 years (Milankovitch 1941)[148]. By correlating the inferred times of occurrence of four European Ice ages reconstructed 11 years earlier by Penck and Bruckner (1909)[174] with times of low incoming solar radiation at high latitudes he was led to introduce an hypothesis as to the reason for the occurrence of glacial epochs. Based upon his detailed calculation of the variations in the geometry of the Earth's orbit around the Sun and thus the impact upon received solar radiation, Milankovitch was the first to argue that:

Under those astronomical conditions in which the heat budget around the summer solstice falls below average, so will summer melt, with uncompensated glacial advance being the result.

Until roughly 1970, this Milankovitch theory was largely disputed due to the fragmented evidence available from the sedimentary record up to that point and the general assumption that the climate system was considered too resilient to small changes in summer insolation for this hypothesis to be sensible (see Berger 1988 for a history of the astronomical theory)[15]. With improvements in radioactive dating and the development of other techniques to constrain the details of the timescale of the geological records, and with better instrumental methods for measuring the continental ice-volume proxy consisting of the ratio of the concentrations of the stable isotopes of oxygen,  $^{18}\text{O}$  to  $^{16}\text{O}$ , in deep sea sedimentary cores (Shackleton and Opdyke 1973)[202], it was eventually established that the "Milankovitch forcing" of the climate system due to variations in the geometry of Earth's orbit around the Sun was playing a central role in the glaciation process (Hays et al. 1976)[82]. To obtain a more fully satisfactory demonstration of the validity of the Milankovitch theory, however, will require three main ingredients: 1) highly accurate computations of the Earth's orbital parameters and incoming solar radiation at the top of the atmosphere due to their variation, 2) accurate analyses of the proxy data employed to constrain past climates in both the time and frequency domains, and 3) the development and use of both intermediate and fully complex climate models to verify that the glaciation process that is known to have occurred, is expected on the basis of rational physical theory.

With respect to the first point above, the earliest approach to the computation of the evolution of planetary orbits over long timescales was to apply secular perturbation methods in an attempt to solve the equations of motion for the solar system many body problem (Lagrange 1781)[119]. Of particular interest here is the highly accurate recent numerical integration of the n-body solar system problem by Quinn et al. (1991)[184]. Such calculations are now available at very high accuracy and deliver accurate computations of the Earth's orbital parameters that extend several million years into the past. In fact, solutions of the gravitational n-body problem are known to be stable to small perturbations in initial condition for times as long as  $\pm 5$  Ma (Laskar 1990)[123]. Such highly accurate calculations of the Earth's orbital elements are employed to obtain the top of the atmosphere (TOA) solar irradiance distributions at selected time periods which are of interest in paleoclimate studies. The energy that is available at the top of the atmosphere at any given latitude  $\phi$ , under the assumption of constant solar output, depends on the solar constant  $S$ , and the Earth's orbital and rotational parameters (Appendix A). Of interest in paleoclimate studies are the three parameters that determine the long term evolution of the insolation. These are the eccentricity of the Earth's orbit around the sun, the obliquity or the tilt of the Earth's rotational axis with respect to the normal to the ecliptic plane and the longitude of the solstice and equinoctial axes with respect to perihelion which change due to precession (Fig. 1.1). The rotational angular velocity of the Earth is also relevant to paleoclimate studies extending into the very distant past of Earth history, but is not of interest in this thesis and is therefore assumed constant. Of special interest to this thesis, however, will be the precise computation of these orbital parameters and insolation within the last 150 000 years (150 ka BP) of Earth history (Fig. 1.1).

The eccentricity,  $e$ , defines the deviation of the shape of the orbit from circular (presently 1.6%), which determines the Earth-Sun distance at perihelion and aphelion. The eccentricity has fundamental modes of temporal variability with periods of 413 ka, 100 ka and 95 ka that arise due to resonant interactions within the solar system. The eccentricity can vary by as much as 5% even over a period as short as 100 000 years (Fig 1.1a). At present the Earth's eccentricity is quite low as compared with other times in the geological past. The eccentricity serves as a primary control on the amplitude of the precessional forcing as discussed below. The changes in received insolation caused by the variations in orbital eccentricity under present conditions arise from changes in the distance between aphelion and perihelion which reach 3.3% of the mean Earth-Sun distance over an annual cycle. The major effect of the variation in the eccentricity manifests itself in seasonal differences which arise as a result of the obliquity or tilt in the Earth's rotation axis with respect to the normal to the plane of the ecliptic. The obliquity varies with dominant modes of variability at the periods

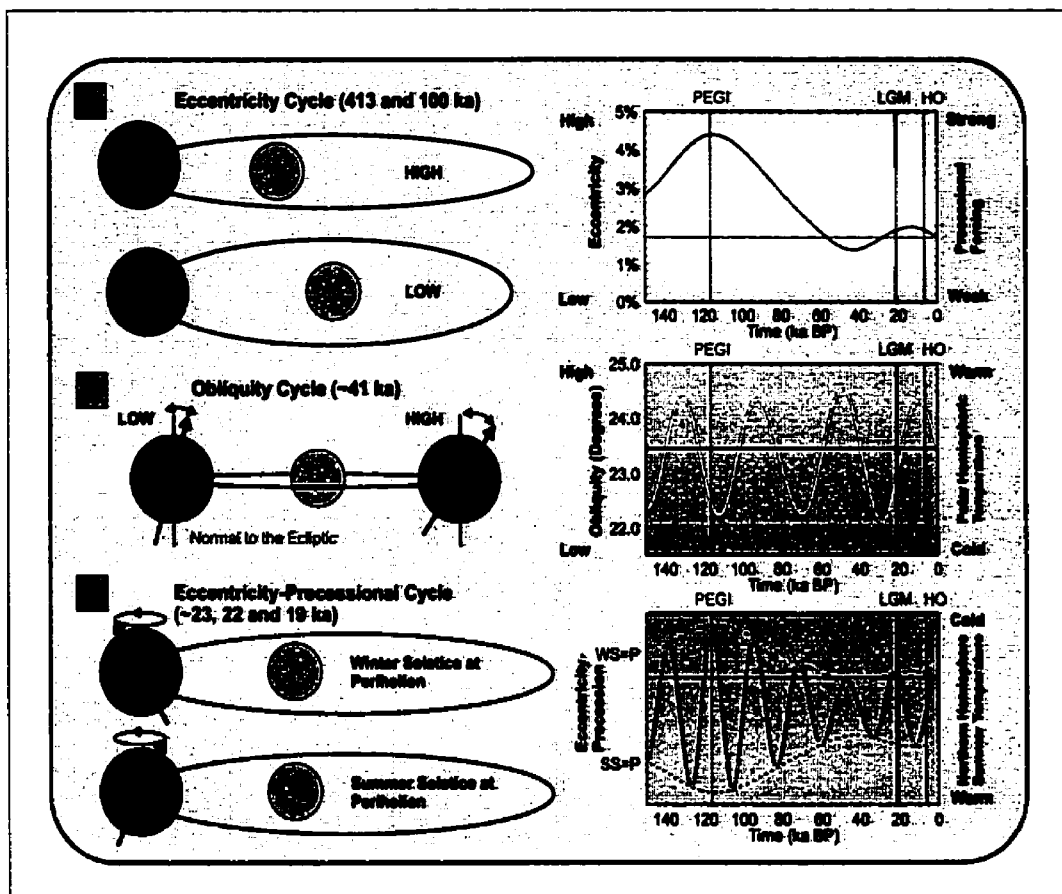


Figure 1.1: The Earth's orbital variations. (a) The eccentricity cycle: The deviation of the Earth's orbit from circular over time fluctuates with periods of 413 and 100 ka. Large eccentricity accentuates precessional forcing. (b) The obliquity cycle: The tilt of the Earth's rotational axis with respect to the perpendicular to the ecliptic varies with a period of approximately 41 ka. Large obliquity affects the amount of sunlight received at high latitudes. (c) The eccentricity-precessional cycle: The precession of the rotational axis of the Earth, whose amplitude is modulated by the orbital eccentricity determines the position of the solstices and equinoxes with respect to perihelion. The eccentricity-precessional parameter determines the magnitude of the seasonal contrast during an annual cycle. The orbital data plotted for the past 150 ka is from Quinn et al. (1991)[184].

of 41 ka and 53 ka. This causes the Earth's rotation axis to vary between approximately  $22.5^\circ$  and  $24.5^\circ$  from the perpendicular to the ecliptic over a 41 000 year period (Fig. 1.1b). At present the magnitude of the obliquity ( $23.44^\circ$ ) is near its mean value. The main effect of changes in obliquity is to determine the high latitude variation in insolation between winter and summer and the equator to pole latitudinal gradient of insolation. At times of high obliquity the polar hemispheres are warmer in summer and colder in winter and vice versa. The summer and winter seasons of course arise as a result of the obliquity and the annual rotation of the Earth around the Sun, but it is the long term eccentricity modulated precession of the Earth's rotational axis about the normal to the plane of the ecliptic that effects the contrast between summer and winter seasons (Fig. 1.1c). The fundamental mode of precession, with a period of 23.7 ka, exists because of the interaction of the general precession of the Earth's rotational axis (25.7 ka), which in turn arises because of the torque exerted by the Sun on the oblate figure of the Earth, and the variation in the precession of the perihelion of Jupiter with respect to the fixed stars (308 ka)(Berger 1988)[15]. This 23.7 ka precessional mode is in turn modulated by the main modes of the Earth's eccentricity at 413 ka, 100 ka and 95 ka periods to "split" the precessional singlet so as to induce radiation forcing at the multiplet periods 22.4 ka, 19.2 ka and 19.0 ka. As the Earth's rotational axis precesses, the summer solstice precesses between perihelion and aphelion. When the summer solstice coincides with perihelion, northern hemisphere summer latitudes experience a maximum in the insolation received at the top of the atmosphere. At present the summer solstice is near aphelion (Fig 1.1c). The eccentricity has the effect of increasing the contrast between summer and winter at points of high eccentricity and thus the eccentricity and precession are combined into the eccentricity-precessional parameter  $e \cdot \sin\omega$  (Fig 1.1c; See also Appendix A).

The three temporal epochs denoted on Fig 1.1 by colored vertical lines are to be the foci of the analyses performed in this thesis and will be described in great detail in the following chapters. Post Eemian Glacial Inception (PEGI) at 116 ka BP is a period with an optimal orbital configuration for producing cold high latitude northern hemisphere summer temperatures. Eccentricity is at the maximum in the most recent 100 ka period, obliquity is near its minimum and the summer solstice occurs precisely at aphelion. This period is known to coincide with the most recent time of initiation of continental glaciation. The next period that will be the focus of attention in this thesis, namely Last Glacial Maximum (LGM), occurred at 21 ka BP and has insolation characteristics which are similar to modern. During this period, large continental ice sheets covered much of the continental land mass in the northern hemisphere from mid to high latitudes. The final period to be considered in this thesis, which is usually referred to as the Holocene Optimum (HO) at 6 ka BP, is a period

which has an orbital configuration which produces northern hemisphere summer conditions that are warmer than present. Although the orbital configuration at the somewhat earlier time of 11 ka BP led to a more significant enhancement of summer insolation during the last 20 ka, there were still large amounts of land ice present in the Northern Hemisphere at this time. The period centred on 6 ka therefore provides a preferred epoch for analysis because the sole significant modification to the climate regime is due to the difference in radiative forcing. When coupled with the abundant proxy data available for a priori climate reconstruction during the ice-free mid-Holocene it is easy to understand why this epoch was selected as a preferred time for analyses in the context of the international Paleoclimate Model Intercomparison Project (PMIP).

One of the reasons why these three periods are of such great interest to the paleoclimate modelling and proxy data community is that they represent unique periods in the history of Late Quaternary climate change. By studying them, as will be demonstrated in this thesis, we may attempt to better understand the factors responsible for the large changes in climate system variability that have occurred in the past. As mentioned under point 2) above, more refined analyses of the astronomical theory than those published to date will require more accurate analysis of proxy data in both the time and frequency domains. One of the most important indications of Pleistocene climate variability has been obtained through the inferences of continental ice mass and surface temperature that may be acquired by mass spectrometric analyses of isotopic concentrations in the tests of foraminifera in deep-sea sedimentary cores and on samples of ice and air bubbles trapped in the ice in high resolution ice cores from Greenland and Antarctica. Initial investigations by Emiliani and others (Emiliani 1955; Broecker and Van Donk 1970; Hays et al. 1976)[56][29][82] provided the first indications of Pleistocene temperatures based upon mass spectrometric measurements of the relative concentrations of  $^{18}\text{O}$  and  $^{16}\text{O}$  in the shells of various ocean dwelling foraminifera in deep-sea sedimentary cores. Subsequently, retrieval and analysis of the same oxygen isotopic data from ice cores in modern continental ice sheets revealed the same late Pleistocene patterns of temporal climate variability (Lorius et al. 1985; GRIP project members 1993)[132][75].

The main proxy indicator of climate variability that is used in the analysis of both deep-sea sedimentary cores and deep ice cores from the existing continental ice-sheets on Greenland and Antarctica has been  $\delta^{18}\text{O}$ . This isotopic ratio is a measure of the normalized deviation of the ratio of the concentration of the rare heavy oxygen isotope  $^{18}\text{O}$  to that of the more common lighter isotope  $^{16}\text{O}$  from that of standard mean ocean water (SMOW). During glacial times the isotopically lighter  $^{16}\text{O}$  molecule is preferentially removed from the ocean during the evaporation of  $\text{H}_2\text{O}$  and trapped in glacial land ice, thereby enriching the  $^{18}\text{O}$  concentration in the ocean at times in the past

when large ice-sheets existed on the continents. By examining the isotopic composition of benthic (bottom dwelling) forams, the effects of changing temperature and the changing isotopic composition of the seawater can be separated. Benthic forams are employed in this manner because deep ocean temperature decreases during glacial times but is constrained in doing so by the freezing point of seawater. There is an approximately 1.9 ‰ difference in the  $\delta^{18}\text{O}$  oxygen isotopic ratio between glacial and interglacial times with the glacial value being higher (e.g. Shackleton 1973)[202]. The maximum long term temperature shift in the deep ocean is of the order of the difference between the present day temperature of the abyssal ocean, which is near 1°C, and the freezing point of sea water (-1.8 °C). This 2.8 °C temperature shift can lead to an isotopic shift of no more than  $2.8\text{ °C} \times 0.22\text{ ‰ °C}^{-1}$  or 0.6 ‰ in the isotopic ratio (Shackleton 1973)[202]. A shift of at least 1.3 ‰ remains to be explained by the change in the isotopic composition of the water, and a still greater shift if the temperature difference in deep water is less than 2.8 °C. The variation of  $\delta^{18}\text{O}$  in benthic forams is therefore believed to primarily reflect the growth and decay of continental ice sheets (which is taken to explain 70 % of the variance) rather than the temperature change of the deep water (which is taken to explain 30 % of the variance). On the contrary, the  $\delta^{18}\text{O}$  measured in a continental ice sheet primarily records the variation in atmospheric temperature in the air from which the precipitation was derived that feeds the ice sheet. During condensation and precipitation,  $^{18}\text{O}$  molecules are preferentially removed as water vapour is transported from the source (i.e. the oceans) to the ice sheets. The atmospheric temperature difference between the source region and the region where the glacial ice is accumulating is reflected in a decrease in the  $\delta^{18}\text{O}$  of the ice as there is an increase in the depletion of  $^{18}\text{O}$  with the decrease in temperature over the ice sheet region (e.g. see Hendricks et al. 2000)[84].

The volume of continental ice that is inferred to have been present on land and the temperature of the air over the glaciated regions that is inferred to have existed based upon each of these proxy indicators of Pleistocene climate variability, independently demonstrate that the Earth has undergone a recurrent series of glaciation and deglaciation events with a characteristic period of approximately 100 ka since approximately 900 ka BP. The  $\delta^{18}\text{O}$  signature from deep sea sedimentary core ODP-677 that was retrieved in the Panama Basin in the Eastern Pacific off the coast of Peru at 4 °N latitude is displayed in Fig. 1.2a. This core has been instrumental in redefining much of the basic chronology of Quaternary climate change (Shackleton et al. 1990)[204]. The  $\delta^{18}\text{O}$  data in Fig. 1.2a is displayed in two sections, one from 2 Ma BP to 1 Ma BP and one from 1 Ma BP to present. If one considers the data in Fig. 1.2a to primarily reflect continental ice volume, the nature of the 100 ka quasi-periodic series of glaciation and deglaciation events is clearly evident in the

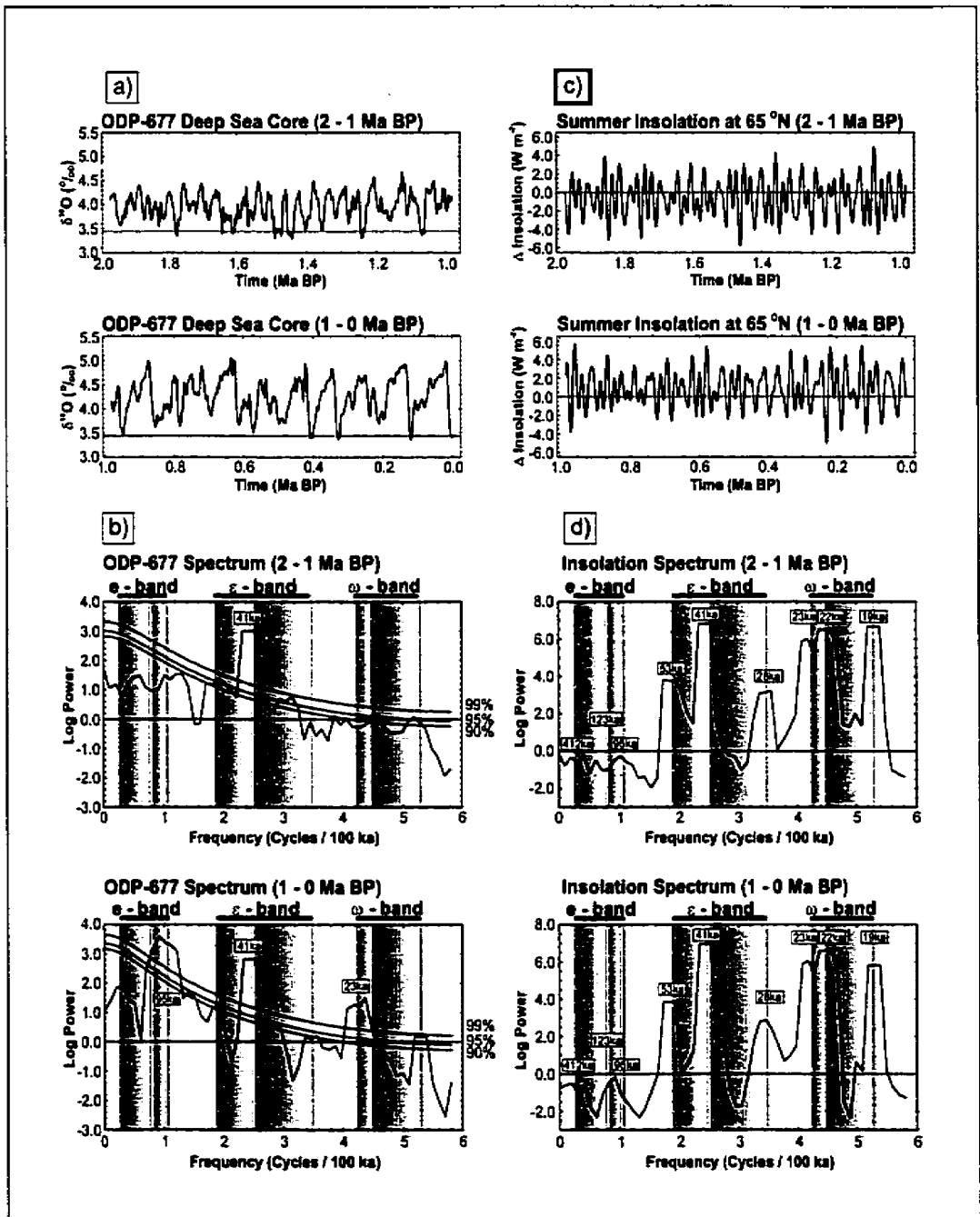


Figure 1.2: (a) The time series and (b) spectrum of the  $\delta^{18}\text{O}$  record from ODP-677 and (c) the time series and (d) spectrum of the summer insolation signal at 65°N for the first and second million years of Earth history. The 90%, 95% and 99% curves in (b) represent the confidence level of the peaks above the background noise. The e-band,  $\epsilon$ -band,  $\omega$ -band represent the band width covered by the main eccentricity, obliquity and precessional modes.

latter half of the Pleistocene epoch. A detailed spectral analysis of the same time series data using the MultiTaper Method (MTM: Thomson 1982; Percival and Walden 1993)[224][175] is displayed in Fig. 1.2b for the time series from 2 Ma BP to 1 Ma BP and for the time series from 1 Ma BP to present. The MTM method provides a novel means for analyzing a wide range of geophysical data sets. MTMs reduce the variance of spectral methods by applying a small set of tapers rather than a unique spectral window such as those used in Blackman-Tukey methods (Blackman and Tukey 1959)[19]. The MTM spectra are tested for significance relative to the null hypothesis of a colored noise background estimated empirically from the data. This is particularly important in geophysical applications where the intrinsic inertia of the system leads to greater power at lower frequencies, even in the absence of any signals (Hasselmann 1976)[81]. To accommodate the colored noise background assumption, an autoregressive AR(1) noise process is assumed. The spectral analysis of Fig. 1.2b also displays the 90 %, 95 % and 99 % confidence levels of the spectral peaks above the colored noise spectrum that is characteristic in many geophysical data sets. What is visually apparent from Fig. 1.2a and quantitatively established in Fig. 1.2b is that the dominant mode of Earth system variability prior to the mid-Pleistocene has a characteristic period of 41 ka. Following the so-called "mid-Pleistocene transition" (Deblonde and Peltier 1991)[47], the proxy record of continental ice volume variability contains significant power at the periods of 100 ka, 41 ka and 23 ka. The late-Pleistocene ice age cycle of glacial-interglacial transitions has a dominant mode with a period of 100 ka, with smaller variations at 41 ka and 23 ka periods superimposed upon this main mode of variability. Prior to the "mid-Pleistocene transition" at approximately 900 ka BP, the 100 ka eccentricity and 23 ka eccentricity-precessional cycle are virtually absent from the spectrum of the ice volume proxy. Based upon the astronomical theory of the ice ages, the main northern hemisphere continental ice sheets are expected to respond to variations in high-latitude summer insolation. An investigation of the summer insolation at 65 °N as calculated (see Appendix A) from the orbital parameter reconstruction of Quinn et al. (1991)[184] for the past two million years (Fig. 1.2c) and the corresponding spectral analysis (Fig. 1.2d) reveals that there is no such transition in the high latitude insolation forcing that is due to the Earth's orbital variations between the 2 to 1 Ma BP and the 1 to 0 Ma BP portions of the Pleistocene epoch of Earth history. What is even more striking is that the insolation spectrum reveals an insignificant amount of insolation forcing in the eccentricity band. Although the Earth's orbital eccentricity, and hence the average distance from the sun, varies with a period of 100 ka, the changes in solar heating associated with this variation are believed to be too small to be climatically significant. Milankovitch forcing at the 41 ka and 23 ka periods does, however, appear to play a direct role in the past million years of continental ice volume variations.

The main questions raised by results such as those shown on Figure 1.2 clearly include the issue as to how such a strong climate response could arise at the period of 100 ka when the forcing at this period is so insignificant. Furthermore, why does the 100 ka ice age cycle in continental ice volume only appear in the latter half of the Pleistocene epoch? A great deal of progress in seeking the answers to these questions has been made, especially in the last decade of the 20th century. However, there is still a good deal of disagreement among different groups of researchers, which it will be useful to summarize. One view is that Earth's atmosphere-ocean-cryosphere climate system supports a free oscillation with a fundamental 100 ka period that may become phase locked to the external orbital forcing. Advocates of a theory of this kind invoke low-order dynamical systems models tuned to support a free oscillation of the required period (e.g. Maasch and Saltzman 1990)[135]. The primary competing view is that the strong nonlinearity of the climate system enables it to "see" the 100 ka eccentricity modulation of the precessional forcing. The analyses of this mechanism have involved the use of energy balance models of the atmosphere coupled with explicit models of ice-sheet accumulation and flow (Hyde and Peltier 1985; Deblonde and Peltier 1991; Tarasov and Peltier 1999)[95][47][218]. A third class of theory of the 100 ka cycle is that that invokes temporal variations in the Earth's orbital inclination with respect to the plane of the original accretion disk that occur with an almost precisely 100 ka periodicity (Muller and McDonald 1997)[159]. A fourth category of theory is that which imagines the ice-ocean-atmosphere to consist of multiple equilibria which are visited by the climate system according to a predefined set of rules for moving from interglacial to mild glacial to full glacial regimes whenever a specific insolation threshold is passed (Paillard 1998)[167]. Carefully modelling studies have enabled certain of these theories to be rejected relative to others. For example, modelling studies (e.g. Paillard 1998)[167] and proxy data analysis (e.g. Rial 1999)[188] have been invoked to argue that certain orbital forcings can be ruled out, such as that hypothesized to result from the 100 ka periodic movement of the inclination of the Earth's ecliptic plane through a solar system dust sheet as suggested by Muller and McDonald (1997)[159].

In my opinion, to fully understand the Earth's late-Pleistocene climate behaviour will require detailed modelling that includes all 5 major components of the Earth system. These include the interactions between the atmosphere, the oceans, the biosphere, the cryosphere and lithosphere. To attempt to accurately model even two of these components (e.g. coupled Atmosphere-Ocean models) represents a formidable task. All of the existing theories mentioned above have merit in explaining certain aspects of the 100 ka cycle but fail in other respects. Investigations using simple models such as Paillard's (1998)[167] reproduce the oxygen-isotope time series to some degree based upon orbital considerations alone, but fail to replicate certain stages of glacial-interglacial transition. It

is likely that full 3-D models of the 5 component system must be employed to accurately resolve the interactions that occur in the climate system over these long timescales. The dominance of the 100 ka period may arise as a "demodulation" (through non-linear climate system feedbacks) of the beat in the eccentricity-precessional envelope that varies at this 100 ka period due to the linear superposition of the 23 ka and 19 ka periods, as first suggested by Wigley (1976)[241]. Recently, Shackleton (2000)[205] has investigated the correlation between oxygen isotope records in Vostok ice cores from Antarctica and from deep sea sedimentary cores. This study, which appears to have been more successful than previous attempts by Shackleton (1987)[203] in separating ocean temperature variations from ice-volume changes in deep sea core  $\delta^{18}\text{O}$  measurements, concludes that orbital eccentricity, deep-sea temperature and atmospheric  $\text{CO}_2$  all vary in step with the same 100 ka cycle while the ice volume signal lags behind. Modelling studies also suggest that the gradual decrease in  $\text{CO}_2$  over the past 3 million years may explain the mid-Pleistocene climate transition that is known to have occurred at approximately 900 ka BP. It is suggested that the gradual decrease in atmospheric  $\text{CO}_2$  resulted in the transition from weak 41 ka ice volume cycles to 100 ka ice volume cycles due to reductions in "greenhouse" forcing (Berner 1994; Saltzman and Verbitsky 1994)[16][200]. These recent advances suggest that atmospheric  $\text{CO}_2$ , and therefore the carbon cycle, is a primary driver in the climate system and not simply a weak feedback, a result which is entirely consistent with the result obtained from an explicit theoretical model of the 100 ka ice-age cycle by Tarasov and Peltier (1997a)[216]. In the model of Tarasov and Peltier, the 100 ka cycle exists only because of the direct 100 ka cyclic forcing due to variations in the atmospheric concentration of  $\text{CO}_2$ . These results have strong implications for our understanding of future climate change.

In seeking to further advance our understanding of the astronomical theory of climate change as described above, this thesis will be based upon the premise that a full appreciation of the complexity of the real climate system will be required to fully reveal the mechanisms contributing to late-Pleistocene climate variability. By using complete models to replicate past climate conditions such as will be described in the next subsection of this introduction, we can hope to more fully appreciate the internal mechanisms which are responsible for climate change.

## **1.2. Paleoclimate Modelling and Paleoclimate Reconstruction**

Atmospheric models are in a state of continual development so as to improve their ability to simulate the major features of the modern climate system. Through intercomparisons of these models, it is being demonstrated that there is a substantial amount of agreement in the simulations they

deliver of the observed climate system, but there are also many differences in the details of the predictions they make under identical forcing conditions. There currently exist major international initiatives that have been undertaken to intercompare them, for example the Atmospheric Model Intercomparison Project (AMIP: Gates et al. 1998)[71] and the Coupled Model Intercomparison Project (CMIP: Lambert and Boer 2001)[120]. The application of global climate model or general circulation model (GCM) capability to the understanding of past climate or "paleoclimate" regimes has often been motivated by the availability of specific proxy data based inferences of climate state for well constrained epochs. If we can fully understand the evolution of the climate system in the distant past we will clearly be in a better position to realistically assess our ability to predict the future. Such modelling studies can be used not only to investigate past climate mechanisms, but to intercompare the response of different models under identical regimes of forcing as well as to compare model "predictions" with available proxy reconstructions. In an attempt to coordinate this effort, the Paleoclimate Modelling Intercomparison Project was initiated (PMIP: Jousaume and Taylor 1995)[107]. This project was developed not only to increase the intensity of collaboration among the main international groups involved in paleoclimate modelling but also to stimulate the refinement of global reconstructions of paleoclimate state at specific epochs in the past that could be employed for model validation.

The PMIP collaboration, to which the work described in this thesis belongs, initially agreed to focus upon only two specific "time-slices", respectively at 6000 years and 21 000 years before present (6 ka and 21 ka BP). These periods were selected from the relatively recent geological past (Fig. 1.3a). The last three glacial-interglacial cycles are displayed in Fig. 1.3a along with the summer insolation at 65 °N latitude. As previously discussed, the 6 ka period, which is referred to as the "Holocene Optimum" (HO), is a period when almost all of the remnants of the massive continental ice sheets that had existed at Last Glacial Maximum had been reduced to their modern forms. The marked difference in the insolation regime that existed at this time, however, resulted in northern hemisphere summers which were much warmer than today. The major effect of the difference in insolation forcing during the mid-Holocene was to significantly strengthen the monsoon circulations over Asia and Africa (see e.g. Vettoretti et al. 1998; Jousaume et al. 1999)[229][108]. The 21 ka period, on the other hand, which is referred to as "Last Glacial Maximum" (LGM), is a period during which much of the high latitude northern hemisphere continents were covered by large continental ice sheets (see Frontispiece). The insolation forcing at the top of the atmosphere was similar to modern but CO<sub>2</sub> concentrations were lower than today and the ice sheets had a profound influence on climate due to the enhanced topographic forcing, and the influence of their high albedo on the

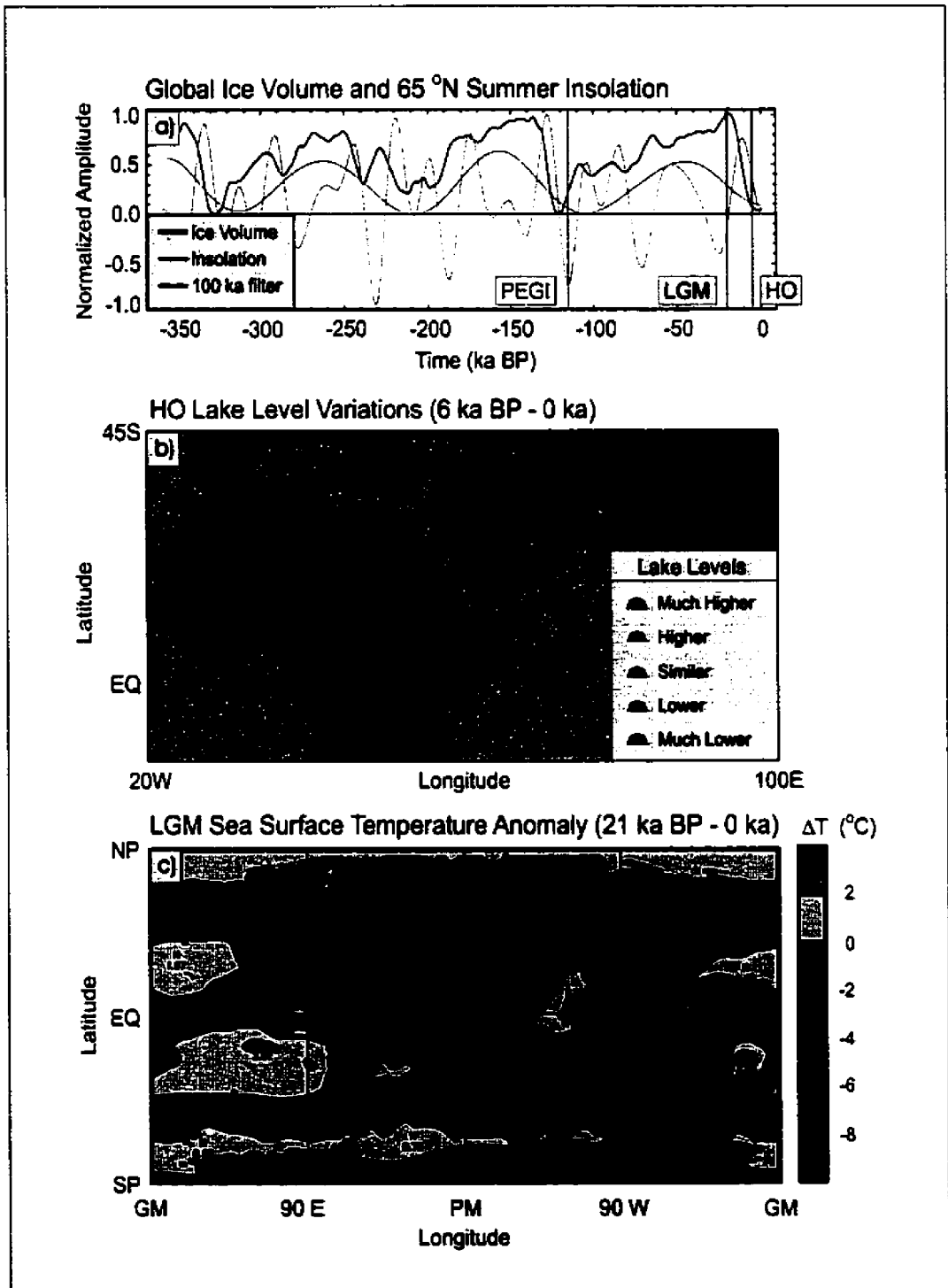


Figure 1.3: Various proxy data from geological inferences of past climate. (a) The summer insolation signal at 65 °N and  $\delta^{18}\text{O}$  record from ODP-677 for the last 350 000 years. (b) African lake level data for 6 ka BP. (c) Annual mean reconstructions of CLIMAP sea surface temperatures.

Earth's radiation balance (Taylor et al. 2000)[219]. The other "time-slice" that is of great interest in the last glacial cycle corresponds to the time of inception of the cycle itself. As previously discussed, this period, centred upon 116 ka BP, which is referred to as the time of "Post Eemian Glacial Inception" (PEGI), is a period during which the Earth's surface was likely very similar to that of the Earth in the modern pre-industrial era. However, it was subject at that time to a large reduction in high latitude summer insolation as compared with modern as will be demonstrated in this thesis. This was a period during which a large amount of high northern latitude continental land ice began to accumulate. This period is not one that was mandated by the PMIP collaboration as the issue of glacial inception was considered to be overly complex to serve as a focus for intercomparison and because there is relatively little global proxy climate data that may be invoked for the purpose of model validation. Nevertheless, this period serves as a unique test for modern atmospheric general circulation models because of the fact that many such models have failed entirely to predict the high latitude perennial snow fields that are the required precursors to continental glaciation. Along with the LGM and HO epochs, a primary focus of investigation in this thesis will be the epoch of PEGI.

The relatively abundant amounts of proxy data that have been obtained for the 6 ka period has made the mid-Holocene period the subject of extensive investigation. It has in fact been modelled with GCMs of ever increasing complexity for more than 20 years (e.g. Kutzbach 1981)[116] in an attempt to establish contact with the first available proxy reconstructions from North Africa and Asia which strongly suggested that the regions were both warmer and wetter in this recent geologic period (Street and Groove 1979)[212]. Presently, the two types of data available for model validation at 6 ka BP consist of the Global Lake Status Data Base (GLSDB) and the BIOME 6000 datasets (Harrison 2000)[80]. Lakes respond in a relatively simple and well-understood manner to changes in the balance between precipitation and evaporation by changing their volume (Cheddadi et al. 1997)[34]. A sub-area of the GLSDB data is displayed in Fig. 1.3b over Africa and parts of Asia and indicates that conditions were indeed generally much wetter across Northern Africa and the Arabian Peninsula. Similar conditions are found over Northern India and Southern China at 6 ka BP. These conditions indicate an intensification of the African-Asian monsoon during the mid-Holocene period. Through the generation of the BIOME 6000 datasets, broadscale vegetation types have been reconstructed from pollen and related plant-macrofossil data (Prentice et al. 1996)[183]. These vegetation reconstructions show that the northern temperate forests as well as the Arctic forest limit extended northwards at 6 ka BP (e.g. Texier et al. 1997)[220]. The PMIP suite of simulations and the model-data comparisons based upon them show that all of the models simulate an increase in the summer monsoon over Africa and that there is qualitative agreement with lake level proxy

data. However, the models tend to underestimate changes based upon pollen estimates in this region (Jolly et al. 1998)[103]. Most of the changes over Northern Africa in the PMIP set of simulations indicate that the response of the individual models is strongly controlled by the nature of the fit to modern climate delivered by the models. In the case of North Africa, the northward expansion of the tropical region is found to be dependant upon the simulated modern position of the intertropical convergence zone (ITCZ) (Joussaume et al. 1999)[108]. Further simulations have been designed to investigate the effects of modifications to the land surface scheme and vegetation patterns upon the magnitude of the change in monsoon intensity and on summer warming at high northern latitudes (Ganapoloski et al. 1998; Vettoretti et al. 2000a)[70][230]. The impact of ocean feedbacks on the monsoon response is evident in simulations which couple the atmospheric models to a mixed-layer ocean (Vettoretti et al. 1998)[229] and full 3-D ocean models (Hewitt and Mitchell 1998)[86]. Land surface and ocean feedbacks alone still fail to explain the observed biome shifts over the Sahara. More recently, experiments with coupled ocean-atmosphere-vegetation simulations have been shown to produce an additional enhancement of the northward migration of the monsoon precipitation region over Africa (Braconnot et al. 1999)[27] indicating the importance of this additional feedback to the successful reproduction of mid-Holocene climate conditions.

The Last Glacial Maximum epoch has also been investigated extensively through modelling studies and through the reconstruction of Earth's land surface at 21 ka BP from geological proxy indicators. One of the first analyses of surface conditions for LGM was that which lead to the reconstruction of LGM surface conditions by the Climate/Long-Range Investigation, Mapping and Prediction (CLIMAP 1981)[38] group. CLIMAP ice sheet reconstructions indicated that the ice trapped on land resulted in a drop of mean (eustatic) sea level of as much as 150 meters. On the basis of later theoretical and observational analyses, such as through the deconvolution of  $^{14}\text{C}$  dated post-glacial relative sea level histories, the amount of continental ice volume was found to correspond to a revised sea level drop nearer to 120 meters (Peltier 1994, 1996, 1998a, 1998b)[170][171][172][173]. Reconstructions of this type, combined with terminal moraine reconstructions of the ice sheet margins for North America (Dyke and Prest 1987)[55] and for North Western Europe demonstrate that vast continental ice sheets existed at LGM and very well constrain their locations. The issue with respect to the amount of cooling that occurred at this time as a result of changes in the general circulation of the atmosphere is still a matter of great debate, especially at equatorial latitudes. The first global sea surface temperature (SST) reconstructions for LGM provided by CLIMAP were based upon the statistical evaluation of changes in microplankton assemblages based upon the use of the transfer function method described by Imbrie and Kipp (1971)[97]. These reconstructions,

based primarily upon data from deep-sea sedimentary cores, suggested that tropical SSTs were approximately  $-1^{\circ}\text{C} \pm 2^{\circ}\text{C}$  lower than modern (Fig. 1.3c). Datasets such as that shown in Fig. 1.3c serve as foundations for paleoclimate research, but the results remain controversial. In some regions, CLIMAP inferred changes in equatorial Pacific SSTs suggest them to have been  $2^{\circ}\text{C}$  warmer than present at LGM. In fact, significant errors in the CLIMAP SST reconstruction have been identified in several recent publications (e.g. see Hostetler and Mix 1999)[90]. There is also a high degree of controversy as to the spatial extent of the sea ice in high latitudes, a variable that was also inferred in the context of the CLIMAP project (de Vernal 2000)[51].

Since the reconstructions produced by the CLIMAP group, several new approaches to SST reconstruction have been developed. Revised studies based upon faunal analyses, in particular, support up to  $2^{\circ}\text{C}$  greater cooling than originally suggested by CLIMAP (Crowley 2000)[43]. Results from alkenone (a group of temperature sensitive lipids) unsaturated ratio data suggest a tropical SST cooling of  $2^{\circ}$  to  $3^{\circ}\text{C}$  (Lyle et al. 1992; Pelejero et al. 1999)[134][169]. In contrast to these studies, inferences based upon coral Strontium/Calcium (Sr/Ca) measurements suggest equatorial cooling of as much as  $6^{\circ}\text{C}$  (Guilderson et al. 1994; Beck et al. 1997)[76][13]. Furthermore, ice core records from mountains in equatorial latitudes that record glacial snow line depression suggest that terrestrial temperatures during LGM were cooler than Holocene temperatures by as much as  $5^{\circ}\text{C}$  (Rind and Peteet 1985; Thompson et al. 1995)[189][221]. Noble gas measurements in gas from ground water also initially indicated drops of  $5^{\circ}\text{C}$  but were later revised to suggest changes of  $1.9^{\circ}$  to  $2.5^{\circ}\text{C}$  (Stute et al. 1995)[213]. Estimates from Magnesium/Calcium (Mg/Ca) data in planktonic foraminifera in equatorial Pacific sedimentary cores have very recently been suggested to require that equatorial Pacific SSTs be  $2.8^{\circ} \pm 0.7^{\circ}\text{C}$  colder than modern at LGM (Lea et al. 2000)[125]. The inconsistencies in temperature reconstructions arise mainly from the differences in the geochemical and micropaleontological methods which rely on different assumptions and are applied to different samples (Nurnberg 2000)[162]. These methods also have other limitations just as do those employed in the context of previously discussed  $\delta^{18}\text{O}$  inferences of ice volume.

The Pacific ocean dominates the tropical oceans and encompasses the warmest region, namely, the west Pacific warm pool. It is therefore the principal source of water vapour that is added by evaporation to the atmosphere and it strongly influences interannual climate variability through the ENSO phenomenon. Synchronous atmospheric teleconnections between tropical Pacific SSTs and temperature changes in the Antarctic atmosphere have revealed that ice sheet melting lags SST warming by 3000 to 5000 years (Lea et al. 2000)[125]. These and other studies reveal the significant impact that the tropical Pacific has upon the mechanisms of high latitude climate change.

By employing the changes in boundary condition which are known to have existed at LGM, such as the spatial distributions and topography of the continental ice sheets, the annual cycle of global insolation (Fig. 1.4) and changes in SSTs, GCMs may be tested for their ability to reproduce observed features in the paleoclimate record. The model that is employed in this thesis to simulate the conditions at 6, 21, and 116 ka BP is described in the following subsection.

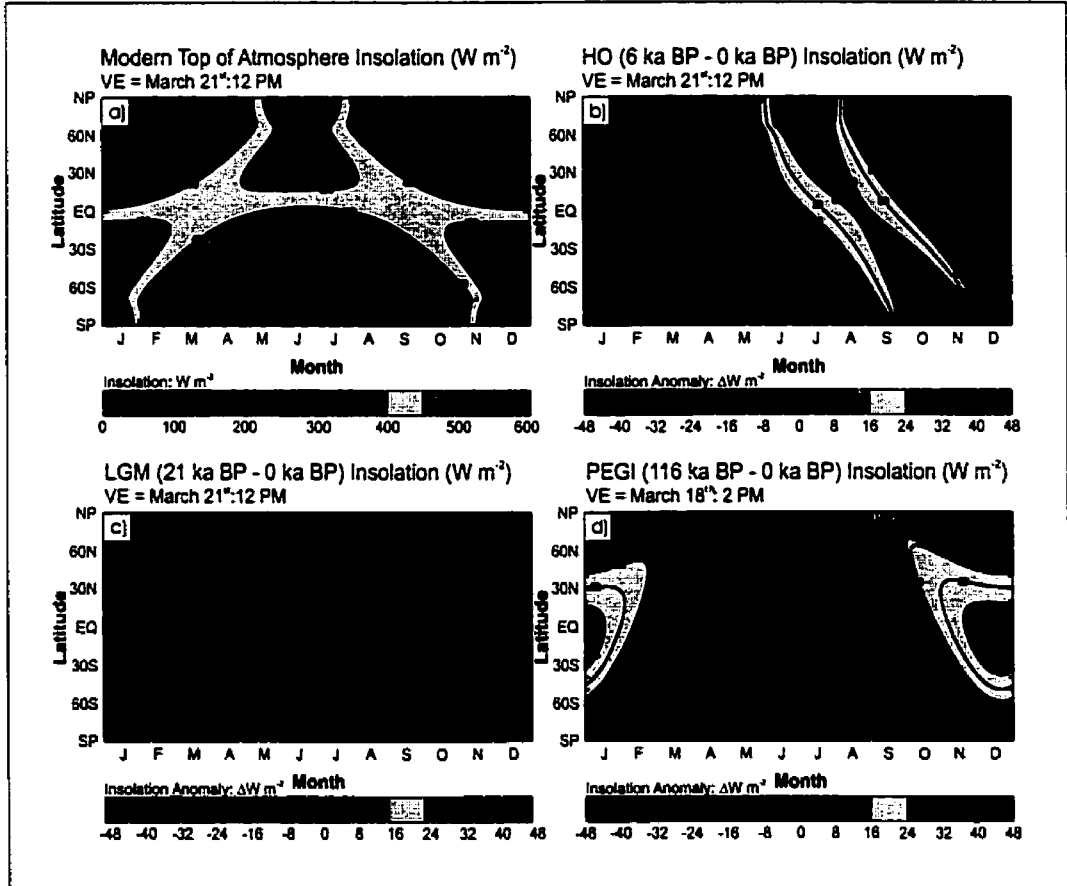


Figure 1.4: The insolation at the top of the atmosphere as a function of latitude and time of year for (a) present day, (b) the difference between 6 ka BP and modern, (c) the difference between 21 ka BP and modern, and (d) the difference between 116 ka BP and modern. The reference time for the vernal equinox in (b), (c) conform with the PMIP specification, while that in (d) minimizes the annual root mean square insolation (see Appendix A). Units are in  $W m^{-2}$ . Contour intervals are  $50 W m^{-2}$  in (a) and  $4 W m^{-2}$  in (b), (c) and (d).

### 1.2.1. Description of the CCCma Global Climate Model

General Circulation Models or Global Climate Models (GCMs), attempt to simulate the observed state of the atmosphere and oceans by implementing the current state of understanding of the

transports of heat, momentum, and water substance in this physical system. Fig. 1.5 displays a schematic of the primary elements of the global climate system. Climate system variability is governed by the interactions between the atmosphere, oceans, biosphere, cryosphere and lithosphere. These interactions, which are ultimately driven by solar radiative forcing, involve a distinct set of reservoirs of energy which are not independent of one another but which are interconnected through flows of energy of various forms. This coupled network of interactions comprises the climate system heat engine. Examples of climate system components include the radiative transfer in the atmosphere which determines the balance of energy that exists on Earth as a result of the fluxes of solar and terrestrial radiation. The thermohaline and wind driven circulations of the ocean and the atmospheric general circulation that together determine the transfer of energy from equator to poles are also crucial ingredients of the coupled system. Hydrological interactions between land, ocean and atmosphere which involve the exchange of sensible and latent heat energy between the climate system components are also vitally important. In a typical global climate model, many of these processes are based upon physical "parameterizations" of sub-grid scale processes in terms of the resolved large-scale fields of the model while others are explicitly resolved. A brief description of the model components is given in what follows.

The model that has been employed in this thesis is the second generation AGCM of the Canadian Centre for Climate Modelling and Analysis (CCCma). The dynamical core (Appendix B) is implemented in terms of a spectral decomposition of the horizontal variations of the prognostic variables on a basis of spherical harmonics truncated to degree and order 32 (T32). The governing equations are written in terms of generalized terrain following coordinates that employ a vertical discretization based upon the use of rectangular finite elements following Laprise and Girard (1990)[121]. Vertical structure is defined on 10 unevenly spaced levels in this coordinate system.

The land surface in the model is represented by a single soil layer which has water-holding field capacity and surface properties that vary with location. The model accounts for the effects of vegetation on surface evaporation and evapotranspiration through the variation of vegetation and bare soil characteristics of the surface. When the local water content of the soil exceeds the locally varying field capacity, the excess water is assumed to be runoff. Ice-sheets are included in the land surface model with ice albedos for both infrared and visible radiation prescribed. When snow melts over an ice-sheet, it is assumed that none of the meltwater refreezes, but is instead shed as runoff. Heat, momentum, and moisture fluxes arise as a result of the small-scale turbulence, and these fluxes are formulated in terms of eddy diffusivities within the free atmosphere and bulk exchange coefficients at the surface.



The model contains a complete representation of the hydrological cycle. The distribution of water vapour is determined from the prognostic equation for specific humidity. Precipitation is assumed to occur when the local relative humidity exceeds a specified threshold such that supersaturation develops within a given atmospheric column. If precipitation occurs when the surface air temperature is below freezing, then it is assumed to take the form of snow, otherwise precipitation is assumed to fall as rain. Both condensation and moist convection are treated by employing a convective adjustment scheme.

Carbon dioxide is assumed to have a constant mixing ratio throughout the atmosphere, while ozone is prescribed as a function of latitude, height, and season. Cloud albedo is computed as a function of liquid water content for low, medium, and high level clouds. Cloud water content is derived diagnostically as a function of relative humidity and temperature as described in McFarlane et al. (1992)[146]. Cloud amount and cloud optical properties evolve interactively within the system.

Terrestrial radiation in the model is treated using the methodology developed by Morcrette (1991)[157] which allows for an adequate accounting of the pressure and temperature dependence of longwave line absorption. The solar radiation is treated using a modified version of the approach employed in the first version of the model (Fouquart and Bonnel 1980)[67], in which the upward and downward irradiance profiles are evaluated.

The ocean surface characteristics and sea ice may be prescribed, or the model may be coupled to mixed-layer ocean and thermodynamic sea ice modules. The ocean mixed-layer is assumed to have a fixed depth of 50m within which the temperature of the layer is determined by the vertical heat flux at the surface, along with a specified internal heat transport term that is a function of location and time of year. The specified internal heat transport is chosen under the constraint of a specified set of boundary conditions to ensure that the model produces a realistic distribution of modern sea ice boundaries and the correct SST annual cycle. The sea ice model does not allow for fractional sea ice within a grid box, nor does it account for internal ice dynamics and dynamical transport, the lack of which results in sea ice thickness being under represented in certain high latitude regions (see McFarlane et al. 1992)[146].

For a more complete description of the physical parameterizations and other model aspects of this AGCM consult Appendix C.

### 1.3. Thesis Organization and Research Strategy

As described in the introduction to this thesis, an investigation of three time periods that are vital to understanding changes that have occurred in the recent geological past and which may be required to understand future climate change are presented in what follows. This thesis will begin in Chapter 2 by investigating the climate sensitivity of the model used in this study for the most recent period of interest described above, namely the Holocene Optimum at 6 ka BP. This chapter focuses on an investigation of the Canadian model simulation of 6 ka BP climate and its anomalous response as compared with other GCMs. Next, in Chapter 3, a study of some of the mechanisms that may have determined the nature of the LGM climate state are revealed. In particular, an investigation of the southern extent of the south eastern lobes of the Laurentide ice sheet demonstrates some of the atmospheric phenomena that determine the LGM ice configuration, specifically those connected with the climate impact of the stationary planetary Rossby waves launched by flow over the enhancement of the topography due to the presence of the ice sheet itself. Both Chapter 2 and Chapter 3 involve investigations conducted in the context of PMIP in which both model-model and model-data comparisons are discussed. In the penultimate Chapter 4 of the thesis, I will demonstrate how glacial inception was successfully achieved in the CCCma model and illustrate a number of novel mechanisms and feedback processes which influence Post Eemian glacial inception at 116 ka BP. In the concluding Chapter 5 of the thesis I will briefly provide suggestions for future lines of research and commentary concerning future climate states expected based upon the results obtained in this thesis and upon projected insolation distributions. I will also briefly discuss the nature of the global warming to be expected based upon the modifications to the original CCCma model that were made in order to correct the defects detected by performing the paleoclimate tests which form the central body of work performed in the context of the thesis. The following Chapter 2 of the thesis, which builds upon the work previously established in Vettoretti et al. (1998)[229], has already been published in the refereed literature in Vettoretti et al. (2000a)[230]. Chapter 3 has also appeared as Vettoretti et al. (2000b)[231] whereas Chapter 4 is currently under consideration by the Journal of Climate.

---

## CHAPTER 2

---

# Climate Simulation of the Holocene Optimum: The Climate System Response to Changes in Soil Moisture Parameterization

### 2.1. Introduction

One of the main goals in climate research is to understand the way the various mechanisms involved in climate change combine to elicit a particular response to an imposed forcing. Most quantitative experiments designed to assess the dynamical mechanisms involved in climate change must of necessity incorporate all or most of the processes that are supported by the actual system. Most investigations of climate sensitivity therefore employ such General Circulation or Global Climate Models (GCM's) as the primary vehicle with which to develop such understanding. Such models have an extraordinarily high degree of complexity, such that it is often as difficult to separate cause from effect in the model as it is in the physical system that the model is intended to represent. Over the course of the past few decades it has become increasingly apparent that the robustness of these models, which are employed to make predictions of the future climate under conditions of increased greenhouse gas forcing, may be usefully tested by using them to predict the climate state at times in the past. Verification of such "predictions" of past climate state, in turn, relies on the availability of sufficiently abundant geological data that may be employed to adequately reconstruct this state.

One of the target epochs that has been chosen for such analyses in the context of the ongoing Paleoclimate Model Intercomparison Project (PMIP) is the mid-Holocene warm period that occurred subsequent to the end of the last deglaciation event of the most recent ice age (approximately 6 000 calendar years before present; 6 ka BP). Since modern GCMs are "tuned" to modern climate by adjusting the parameterization schemes that are employed to represent sub-grid-scale processes that cannot be explicitly resolved, there is no guarantee that such a model will respond correctly to a change in climate forcing. It is crucial, for a better understanding of the models and of the climate system, and for a better prediction of future climate, that we understand how different parameterizations can impact upon climate sensitivity. In a recent PMIP summary paper (Joussaume et al. 1999)[108], for example, it was demonstrated that paleodata based reconstructions of

biome shifts at 6 ka BP over northern Africa were not consistent with the changes in the African monsoon circulation simulated by the models for this target epoch. In particular, it was found that the individual model Holocene monsoon response was strongly influenced by the position and strength of the simulated modern day intertropical convergence zone (ITCZ). The utility of such model-model intercomparisons will become further apparent on the basis of the present study which will focus upon a comparison of the Atmospheric General Circulation Model (AGCM) predictions for 19 of the models involved in the PMIP project, for both modern and orbitally perturbed 6 ka BP boundary conditions. Of particular interest, these analyses will clearly reveal the fact that although the CCCma model is one of the better models at simulating modern surface air temperatures over land as compared with observations, it is clearly an outlier in the mid to high latitude surface air temperature response under the significantly different radiation regime that characterized Holocene Optimum conditions. Detailed further discussions of the CCCma 6 ka BP investigation, focusing on the impact of the changes of orbital forcing upon the monsoon circulations, will be found in Vettoretti et al. (1998; hereinafter V98)[229]. An important issue that immediately arises as a consequence of these intercomparisons concerns the reason why the Canadian model exhibits a mid to high latitude response which is so different from the other models in this first of the PMIP "paleo-tests."

The surface response of a suite of AGCMs subject to a modification of external boundary conditions provides a framework within which to begin an investigation of this issue. The hydrological cycle is, of course, an integral part of the surface energy balance and is a prime factor in the determination of climate state, both present and past. Interactive elements within the hydrological cycle such as soil characteristics, soil moisture "field capacities", vegetation, and clouds all contribute to the state of the atmospheric general circulation. The purpose of the present chapter is to examine the issues surrounding the influence of a modification of the representation of land surface processes on both the modern climate state itself as well as on the response to the orbital insolation perturbation that was characteristic of 6 ka BP. Since simple sensitivity experiments often provide the most useful information concerning the impact of such modified conditions, I will focus herein on determining the extent to which soil moisture field capacities and evapotranspiration from the surface determine the changes to the climate state over land that are caused by the 6 ka BP orbital insolation regime. A hypothesis that might explain the somewhat aberrant behaviour connected with the low surface air temperature response as simulated by the Canadian GCM for 6 ka BP is that the large soil moisture amounts present in the variable bucket model may lead to excessive evaporative cooling as compared with standard fixed bucket models. It is also possible that part of the anomalous response is associated with negative cloud feedbacks (Cess et al. 1990)[32]. This intercomparison among 19

atmospheric GCMs demonstrates that there is a wide range of sensitivities that characterize this set of AGCMs in so far as cloud-feedback is concerned. Boer (1993)[21] has furthermore argued that cloud feedback is a factor in the over all response of the CCCma model to a doubling of CO<sub>2</sub>. It is noteworthy that the largest surface warmings in the PMIP sequence of models are associated with positive cloud feedback, while the model with negative cloud feedback (the CCCma model) displays the smallest warming (Joussaume et al. 1999)[108]. Detailed examination of the role of cloud-feedback in paleotests of the CCCma model will be left for future analysis.

The sensitivity of the global energy and water cycles to changes in the physical properties of the land surface is currently under active investigation internationally. Recently, the Project for Intercomparison of Land Surface Parametrization Schemes (PILPS) employed the most advanced land surface schemes in stand-alone mode, i.e., without GCM atmospheric feedbacks, to investigate the seasonal cycle of surface fluxes (e.g., Chen et al. 1997)[35]. This investigation demonstrated that the differences between such schemes are still large. This study also suffered from spinup problems which make interpretation of the results rather difficult (Robock et al. 1995)[192]. Another recent study by Robock et al. (1998)[194] described a sub-project analysis of soil moisture parameterizations in the Atmospheric Model Intercomparison Project (AMIP) which is an intercomparison among 30 different AGCMs forced by modern observed SSTs (Sea Surface Temperatures). This study compared the simulation of soil moisture in the models with actual observations of soil moisture and concluded that model generated data sets are quite different from the observed data. In particular, models with 15-cm field capacities did not replicate observed high latitude values of soil moisture. AGCM sensitivity studies of the atmospheric response to varying soil conditions have shed some light on the basic mechanisms that are involved in the response of the land surface to changes in surface characteristics, such as tropical deforestation studies (e.g., Dickenson and Henderson-Sellers 1988; Shukla et al. 1990)[52][209]. Through changes in vegetation, which in turn affect soil moisture, these studies have also incorporated changes in albedo and surface roughness. Shukla and Mintz (1982)[208], for example, employed simple wet and dry soil condition example cases to show that there was increased rising motion, due to increased surface temperatures over land, in the dry soil case but no associated increase in precipitation due to the reduced strength of the surface moisture source. This work demonstrated that global climate is in fact strongly affected by evaporation from the land surface, which in turn affects surface temperature (through evaporative cooling) and precipitation. In a more recent but similar study, Milly and Dunne (1994)[149] investigated the impact on equilibrium AGCM climate for 9 values of globally constant soil water holding capacities. One of the main results of their analyses was the demonstration that the globally averaged land

surface temperature was 2 K lower with a field capacity of 60 cm as compared with that obtained when a capacity of 4 cm was assumed. In a later study Milly (1997)[150] investigated the change in mid-latitude summer dryness and soil moisture field capacity for future climate simulation, and demonstrated that changes in bucket depth can enhance or diminish the changes in summer dryness associated with CO<sub>2</sub> doubling experiments.

The present study provides further information to that in the above-cited analyses by addressing the issue of how surface characteristics affect the climate response to changes in orbital insolation representative of Holocene optimum conditions. Section 2.2 provides an overview of the relevant model characteristics and a discussion of the design of the experiment to be performed in which the land surface scheme is modified to clarify its role in determining the simulated climate for both present day and paleoclimate boundary conditions. Section 2.3 describes the results obtained for changes in both the simulated modern climate and the simulated Holocene Optimum climate. I will specifically focus on the role of soil moisture in determining the anomalous behaviour of the model. Section 2.4 provides a summary of the results and conclusions.

## **2.2. Land Surface Processes and Experimental Design**

In the first subsection I describe the representation of AGCM land surface processes. In the second subsection I describe the design of the experiments performed in order to investigate the role played by the land surface scheme in determining mid-Holocene climate state.

### **2.2.1. Land Surface Processes**

The land surface hydrology in the model is represented in terms of a single soil layer which has a soil moisture field capacity and soil properties that vary with location (Fig. 2.1a-2.1c). In contrast to most other GCMs that employ the simple "bucket" representation, the soil water-holding capacity, whether the water is in liquid or solid form, is not assumed to be constant in GCMII but rather depends on vegetation and soil type which varies with location in accordance with the specifications of Wilson and Henderson-Sellers (1985)[243]. This variable water holding capacity of the buckets in GCMII, which constitutes an attempt to mimic deep rooted vegetation regions such as those within the tropical and boreal forests, is implemented such that field capacities and evapotranspiration slope factors (Fig. 2.1d) are taken to vary as a function of latitude and longitude through the vegetation dependence. Consistent with this, Robock et al. (1997)[193] have demonstrated that by incorporating actual field capacities instead of the standard 15-cm bucket used in many GCMs,

that a dramatic improvement in soil moisture simulation is obtained. Along with the variable

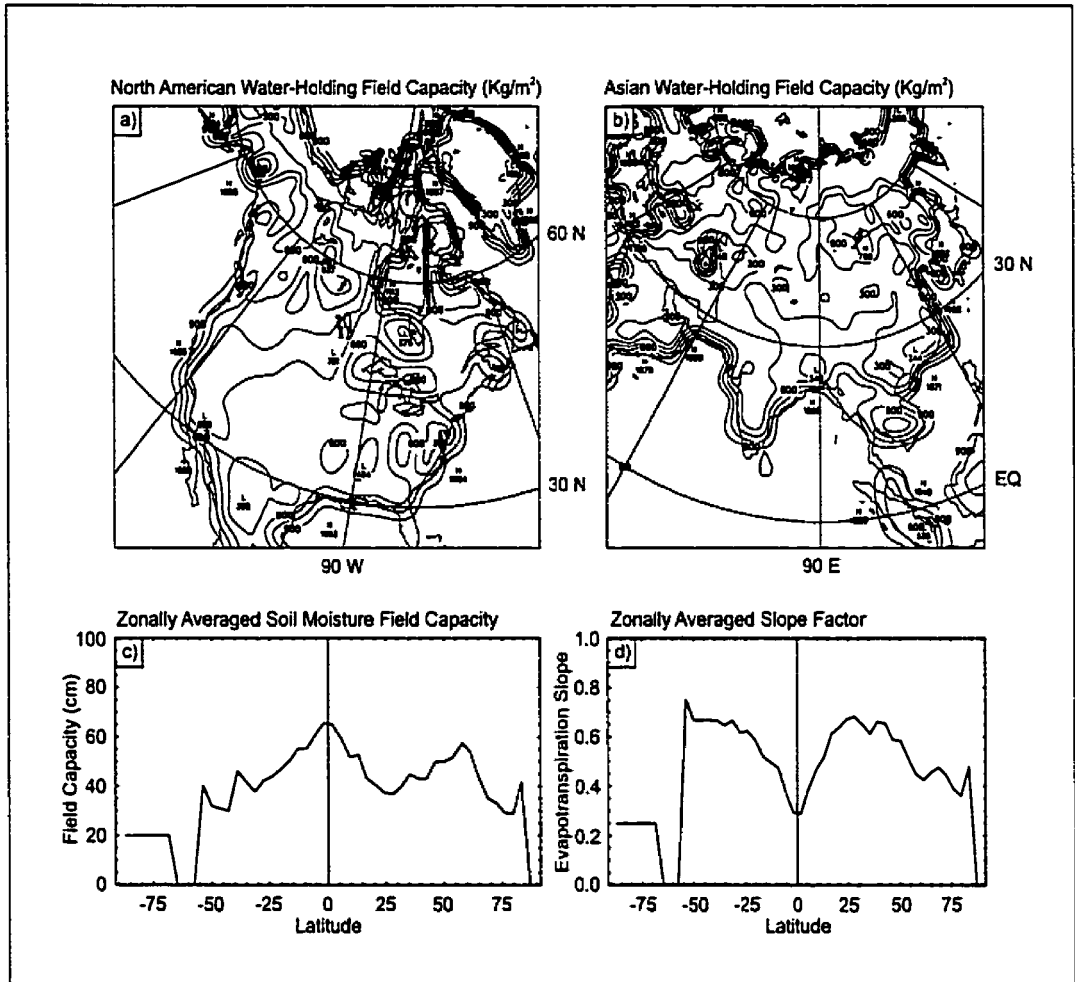


Figure 2.1: (a) North American and (b) Asian water holding field capacity ( $\text{kg m}^{-2}$ ) prescribed within the CCCma GCMII variable bucket scheme. The contour interval is  $150 \text{ kg m}^{-2}$  ( $\text{kg m}^{-2} = 0.1 \text{ cm}$ ). (c) Zonally averaged water holding field capacity ( $\text{kg m}^{-2}$ ) prescribed within the CCCma GCMII variable bucket scheme. (d) Zonally averaged evapotranspiration slope factor.

hydrologic capacity, the model uses a force-restore method rather than the thermal inertia method to calculate sub-surface heat fluxes (Deardorff 1978)[46]. The model accounts for the effects of vegetation on surface evaporation and evapotranspiration through the variation of vegetation and bare soil characteristics of the surface. When the local water content of the soil exceeds the locally varying field capacity, the excess water is assumed to be runoff.

Of particular interest here is the evolution of the temperature at the ground which must be such as to ensure a balance of surface energy fluxes to and from the atmosphere and the conduction of heat within the soil layer. This surface energy balance is represented, in GCMII, by the following

balance equation:

$$H_G = (1 - \alpha)S - F_L - (H_{VT})_S - L_e(E_{VT})_S - L_f(M_F - M_L + M_S), \quad (2.1)$$

in which  $H_G$  accounts for the variation of heat storage and the heat flux within the soil layer expressed in the force-restore formalism as

$$H_G = C_*[\partial T_g/\partial t + \omega(T_g - T_0)]/2 \quad (2.2)$$

In the balance equation (2.1) the net radiative flux is comprised of the difference between the net solar radiation absorbed by the surface  $(1 - \alpha)S$ , which depends on the surface albedo  $\alpha$ , and the net upward positive flux of terrestrial radiation from the surface,  $F_L$ . The upward fluxes of sensible and latent heat from the surface to the atmosphere are respectively  $(H_{VT})_S$  and  $L_e(E_{VT})_S$ , where  $L_e$  is the latent heat of evaporation. The last term in (2.1) describes the flux of energy associated with the melting of frozen soil moisture  $M_F$ , and snow  $M_S$ , and the freezing of liquid soil moisture  $M_L$ , where  $L_f$  is the latent heat of fusion.

The heat storage term  $H_G$ , is composed of the product of the diurnal frequency  $\omega$ , and the difference between the ground temperature  $T_g$ , and the mean temperature in the previous 24-hour period,  $T_0$ . The effective heat capacity of the layer  $C_*$ , is in part the product of the soil heat capacity and the thermal conductivity of the soil. These quantities are functions of soil type, soil moisture content, and snow cover.

The evaporation rate is given by

$$(E_{VT})_S = [\min[1/\beta * W/W_c, 1] * (1 - \delta_s) + \delta_s] * E_{pot} \quad (2.3)$$

The potential evapotranspiration  $E_{pot}$ , is positive definite in the above equation. The evapotranspiration (the R.H.S. quantity in the outer square brackets) is the minimum of the product of the inverse of the evapotranspiration slope factor  $\beta$ , and the moisture availability  $(W/W_c)$  times a quantity which involves the fractional snow cover,  $\delta_s$ . At low latitudes the evaporation is governed by the evapotranspiration slope factor and the moisture availability, while at snow covered high latitudes it is governed by the potential evapotranspiration.  $W$  is the soil moisture amount and  $W_c$  is the soil moisture field capacity which depends on vegetation and soil type.

For a more detailed description of the representation of these individual flux components, see McFarlane et al. (1992)[146] and Boer et al. (1984)[20].

### 2.2.2. Experimental Design

The design of the numerical experiments that I have performed conforms with that of the 6 ka BP simulation specified in PMIP collaboration documentation (Joussaume and Taylor 1995)[107]. Detailed documentation for these models will be found in Bonfils (1999)[23]. In total, four control simulations and four 6 ka BP paleoclimate simulations were performed. The four experiments, each with modern fixed SST's, involved replacing the variable bucket depth representation  $W_c$  (Fig. 2.1c), by one that has a globally constant bucket depth over land of 20 cm and replacing the variable evapotranspiration slope factor  $\beta$  (Fig. 2.1d), with a constant factor of 0.5. The experiments based upon the assumption of variable bucket/variable slope factor (VB  $V\beta$ ) and constant bucket/constant slope factor (FB  $F\beta$ ) comprised two distinct modern control simulations and two 6 ka BP paleoclimate simulations each of which was run for 12 years (2 spinup years). To resolve the influence of the evapotranspiration slope factor, a variable bucket/constant slope factor (VB  $F\beta$ ) and a constant 20 cm bucket/variable slope factor (FB  $V\beta$ ) experiment were each run for 6 years (2 spinup years). Each simulation was initialized with a modern climatology. There has been a considerable amount of interest in the spinup time that these land surface schemes require to reach equilibrium and also on how the initialization and forcing imposed in these models affect the spinup process (Robock et al. 1998)[194]. Milly and Dunne (1994)[149] have found that the time to reach equilibrium requires between 2 and 32 years of integration depending on soil moisture field capacities in the range from 1 to 240 cm. The scheme which employed the typical 15 cm bucket depth was found to require only 2 years to reach equilibrium. One might suspect that the CCCma model simulation which employs the variable bucket scheme might require a much longer spinup period. Fig. 2.2 displays the spinup behavior for the model which employs the variable bucket scheme for each hemisphere (Figs. 2.2a-2.2d), and for mid-latitude regions from the western and eastern parts of the northern hemisphere (Figs. 2.2e and 2.2f). Upon inspection of Fig. 2.2 it is apparent that the model reaches equilibrium conditions within approximately 2 years with respect to both the liquid and frozen ground water, over much of the globe. The exception to this concerns southern hemisphere frozen soil moisture which occurs along the coastal regions of Antarctica, and apparently requires more than 15 years to reach equilibrium.

The eight simulations thus comprise 4 experiments designed to investigate the changes in the response of the climate system to changes in boundary conditions between 6 ka BP and present (for more detailed descriptions of the design of the 6 ka BP experiment see V98 and Chapter 1)[229]. The value of 20 cm chosen for the constant bucket depth is typical of simplified land surface schemes of

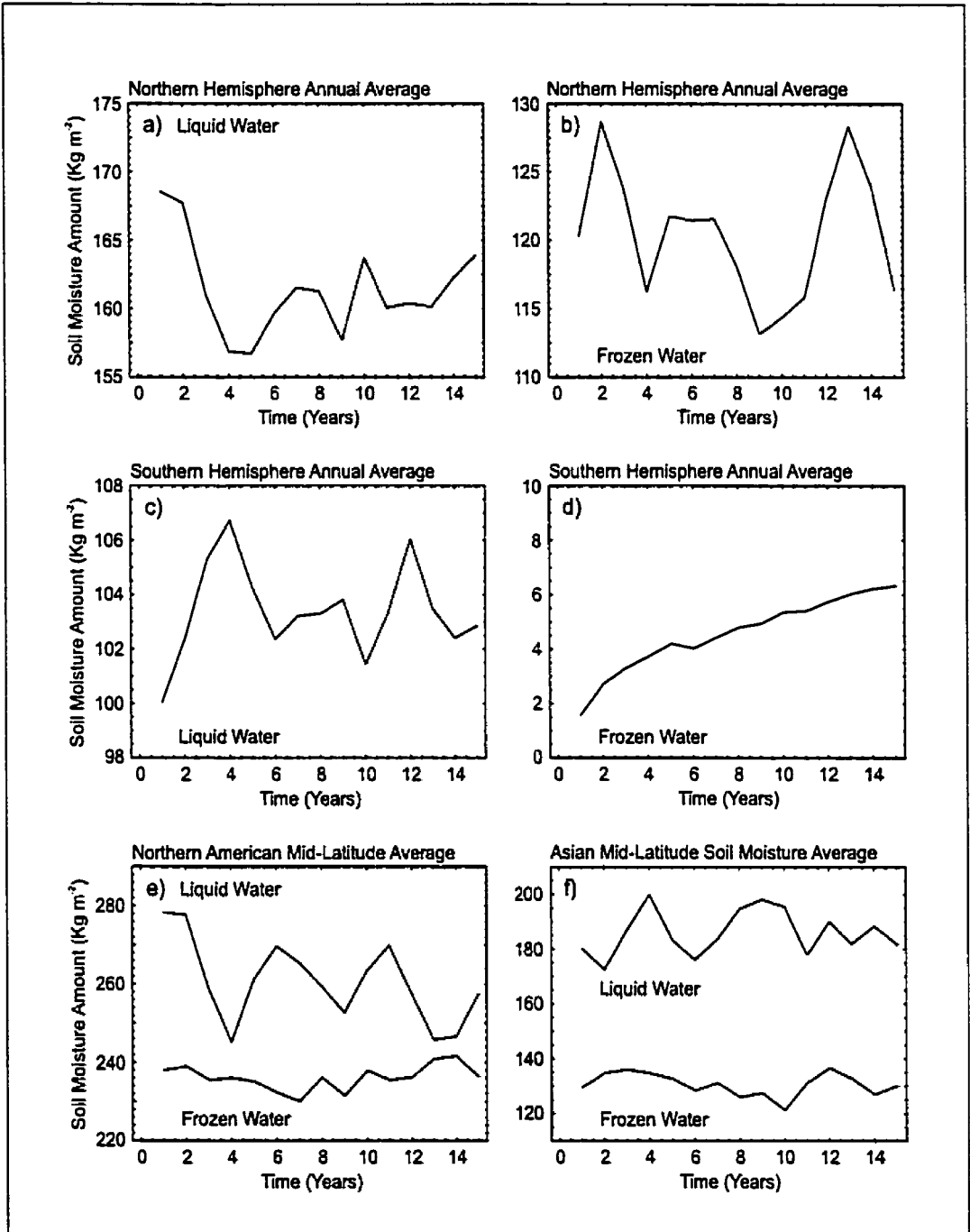


Figure 2.2: Liquid and frozen soil moisture spin up within the CCCma AGCM (Kg m<sup>-2</sup>).

this type (Manabe 1969; Boer et al. 1984)[138][20]. The evapotranspiration slope factor over land is also set to a constant value of 0.5 globally (see McFarlane et al. 1992)[146], and is consistent with its globally averaged value. In contrast to the fixed bucket model, the variable bucket model employed in GCMII has a much larger (global) average soil moisture water holding capacity of 43.3 cm. One might argue that the more than 40 cm global average bucket depth is probably excessive since a 15 cm average is more hydrologically representative of the Earth (Milly and Dunne, 1994)[149]. Much of the contribution to this large average value comes from the deep buckets of GCMII located in the tropics and in the northern mid-latitudes between 50°N and 70°N (Fig. 2.1). In particular, spatial distributions of the bucket capacity around the Arctic Circle in Canada and Asia are characterized by rather deep buckets from 60 to 90 cm in depth. The evapotranspiration parameterization also has important implications for climate sensitivity. Koster and Milly (1997)[115] investigated a set of land surface models (LSMs) in the PILPS project and demonstrated that the variability of these models can be reproduced by simulating the annual and seasonal water-balance by prescribing the LSM prognostic fields in a monthly water balance model (MWBM). The chapter demonstrates that an understanding of how the evapotranspiration and runoff affect soil moisture in the LSMs is crucial to understanding their behaviour. This intercomparison furthermore demonstrated that the bucket model delivered the largest value for the inferred evapotranspiration efficiency and thus had the greatest sensitivity of evaporation rate to soil moisture. The impact on simulated climate of a significant reduction of the depth of the buckets and of changes in evapotranspiration slope factor at high latitudes will be central to the discussion that follows.

### **2.3. Results: The Modern and 6 ka BP climate simulations**

In the following subsections I investigate the impact on simulated climate of the modified bucket schemes along with 6 ka BP insolation forcing on the fluxes across the atmosphere-land surface interface, which together result in the simulated equilibrium surface temperature in the model. In these analyses a selected set of properties of the climate response revealed by the series of simulations that I have performed are discussed. The discussion of these results will culminate with conclusions concerning the sensitivity of the atmospheric circulation to the incorporation of the modified land surface scheme and of the possible need for corrections to other model parameterizations.

Table 2.1: PMIP model land surface processes. Listed are the number of soil layers for prognostic soil temperature (T) and moisture (Q) (0 layers denotes no heat storage or prescribed moisture).

<i>Model Version</i>	<i>T</i>	<i>Q</i>	<i>Land Surface Processes</i>
BMRC V3.2 (R21 L9) 1993	2	1	Prescribed deep soil layer temperature with surface energy balance; spatially uniform 15 cm bucket (Manabe and Holloway 1975)[139]; evapotranspiration efficiency proportional to the ratio of soil moisture to field capacity over land.
CCCma GCMII (T32 L10) 1992	1	1	Deardorff (1978)[46] force-restore surface energy balance; variable bucket dependant on soil/vegetation type; evapotranspiration efficiency proportional to the ratio of soil moisture to the local field capacity over land.
CCSR/NIES V5.4.02 (T21 L20) 1995	3	1	Heat diffusion surface energy balance; spatially uniform 15 cm bucket (Manabe et al. 1985)[137]; evapotranspiration efficiency proportional to the ratio of soil moisture to field capacity over land limited by stomatal resistance of vegetation type.
CNRM-2 ARPEGE Cy14c (T31 L19) 1996	4	0	Deardorff (1978)[46] force restore surface energy balance; Five prognostic soil moisture variables contained within Interactions between Soil-Biosphere-Atmosphere (ISBA) scheme of Noilhan and Planton (1989).
CSIRO v4-7 (R21 L9) 1992	3	2	heat diffusion surface energy balance; Deardorff (1977)[45] force-restore prognostic soil moisture; spatially uniform upper 0.18 cm and lower 16 cm bucket; evapotranspiration efficiency proportional to the ratio of upper layer soil moisture to upper layer field capacity over land.
GFDL CDG (R30 L20) 1997	0	1	no heat storage surface energy balance; spatially uniform 15 cm bucket (Manabe 1969)[138]; evapotranspiration efficiency equal to 3/4 of the ratio of soil moisture to field capacity over land.
GISS Model II Prime (4x5 L9) 1997	6	6	heat diffusion surface energy balance; land surface hydrology based on model of Abramopoulos et al. (1988)[1]; evaporation and evapotranspiration are modelled.
LMCE LMD4.3 (sin(lat)x7.5 L11) 1991	1	1	Corby et al. (1976)[40] surface energy balance; spatially uniform 15 cm bucket (Manabe 1969)[138]; evapotranspiration efficiency equal to 2 times the ratio of soil moisture to field capacity over land.
LMCE LMD5.3 (sin(lat)x5.6 L11) 1994	7	1	Corby et al. (1976)[40] plus surface latent and sensible heat flux forcing from SECHIBA (Ducoudre et al. 1993)[53]; spatially uniform 15 cm bucket (Manabe 1969)[138].

Table 2.1 (continued): PMIP model land surface processes. Listed are the number of soil layers for prognostic soil temperature (T) and moisture (Q) (0 layers denotes no heat storage or prescribed moisture).

<i>Model Version</i>	<i>T</i>	<i>Q</i>	<i>Land Surface Processes</i>
MPI ECHAM3 (T42 L19) 1994	5	1	Warrilow et al. (1986)[235] heat diffusion surface energy balance: 20 cm bucket (Manabe 1969)[139] modified by vegetation and orographic effects; evaporation and evapotranspiration are modelled.
MRI GCM-IIb (4x5 L15) 1995	4	4	Katayama (1978)[112] heat diffusion surface energy balance; Kitoh (1988)[114] soil moisture treatment; Soil layer bottom boundaries at 0.1, 0.5, 1.5 and 10 m; evapotranspiration efficiency equal to 2 times the ratio of soil moisture to field capacity over land if moisture availability is less than 0.5, otherwise efficiency is 1.
MSU (10x15 L3) 1989	1	0	Soil heat storage is determined as a residual of the surface heat fluxes (Kislov 1991)[113]. Soil moisture is prescribed.
NCAR CCM3 (T42 L18) 1992	6	0	LSM land surface model (cf. Bonan 1996)[24].
GENESIS2 (T31 L18 atmosphere/2x2 surface) 1995	6	6	LSX model (cf. Follard and Thompson 1994, Thompson and Pollard 1995)[181][223].
UGAMP UGCM2 (T42 L19) 1994	3	3	Diffusion of heat/moisture with prescribed values of heat and moisture in a third deep layer (Mintz and Serafini 1981)[151]; spatially uniform upper layer 15 cm thick; evapotranspiration efficiency equal to 3/4 of the ratio of soil moisture to field capacity over land.
UIUC MLAM-PMIP (4x5 L11) 1996	1	1	Bhumralkar (1975)[18] force-restore; variable-capacity bucket after Vinnikov and Yeserkepova (1991)[234]; evapotranspiration efficiency equals the lesser of 1.33 times the ratio of soil moisture to field capacity over land or 1.
UKMO HADAM2 (2.5x3.75 L19) 1997	4	1	heat diffusion after Warrilow et al. (1986)[235]; single moisture reservoir with variable hydraulic capacity/conductivity; evaporation and evapotranspiration are modelled.
YONU Tr7.1.1 (4x5 L8) 1997	1	1	Bhumralkar (1975)[18] force-restore; spatially uniform 15 cm bucket; evapotranspiration efficiency equals the lesser of 2 times the ratio of soil moisture to field capacity over land or 1.

### 2.3.1. Zonally Averaged Soil Moisture and PMIP Land Surface Schemes

The models being exercised within the PMIP collaboration are of varying degrees of sophistication and resolution. While separating cause from effect in each individual model is a difficult task, a comparison of the soil moisture amount and land surface parameterizations reveal some of the differences between the model employed in this study and some of the other models which comprise the PMIP set. Although the land surface parameterizations employed in the PMIP generation of models do vary somewhat in sophistication they are nevertheless very similar in their basic features. A list of the land surface components that are directly relevant to the present study is provided in Table 2.1. Soil moisture is either prescribed or computed prognostically, with the latter methodology being most common. The temperatures in the soil layers are usually obtained through a calculation of the heat storage in the layer obtained using either a "force-restore" method (e.g., Bhumralkar 1975; Deardorff 1978)[18][46] or in multiple soil layer models by solving the heat conduction equation directly (e.g., Katayama 1978; Warrilow 1986)[112]. The moisture storage capacity in the soil layers is usually determined by prescribing a uniform bucket depth, typically 15 cm (e.g., see Manabe 1969)[138] or by employing a model that adjusts to different vegetation and/or soil type. More advanced land surface schemes employ a hydrological model with multiple soil layers and a vegetative canopy (e.g., Abrampoulos 1988; Shuttleworth 1988)[1][210]. The level of sophistication of the surface parameterization then regulates the interaction between the surface and atmosphere through the potential evapotranspiration and evapotranspiration efficiency which are either modelled or prescribed based on moisture availability. Further interaction across the atmosphere-land surface boundary in AGCMs occurs through parameterizations that model the surface characteristics and surface fluxes. Some of these include snow, surface roughness, surface albedo, and the turbulent vertical eddy fluxes of momentum, heat, and moisture that will not be described here (see Bonfils et al. 1999 for references)[23]. To compare the results delivered by these models, their soil moisture schemes have been classified in previous studies to illustrate the major differences between them. Robock et al. (1998)[194] have previously categorized soil moisture schemes as an AMIP sub-project according to seven different criteria, all of which are vital aspects of any land surface scheme. This study only looks at two of these criteria, 1) the field capacity and 2) the influence of evapotranspiration on climate sensitivity which is dictated by the implicit vegetation and soil type in the CCCma GCM.

The zonally and annually averaged modern simulated soil moisture amounts are displayed in Fig. 2.3a for the seven PMIP models which archived soil moisture data. The majority of the models have

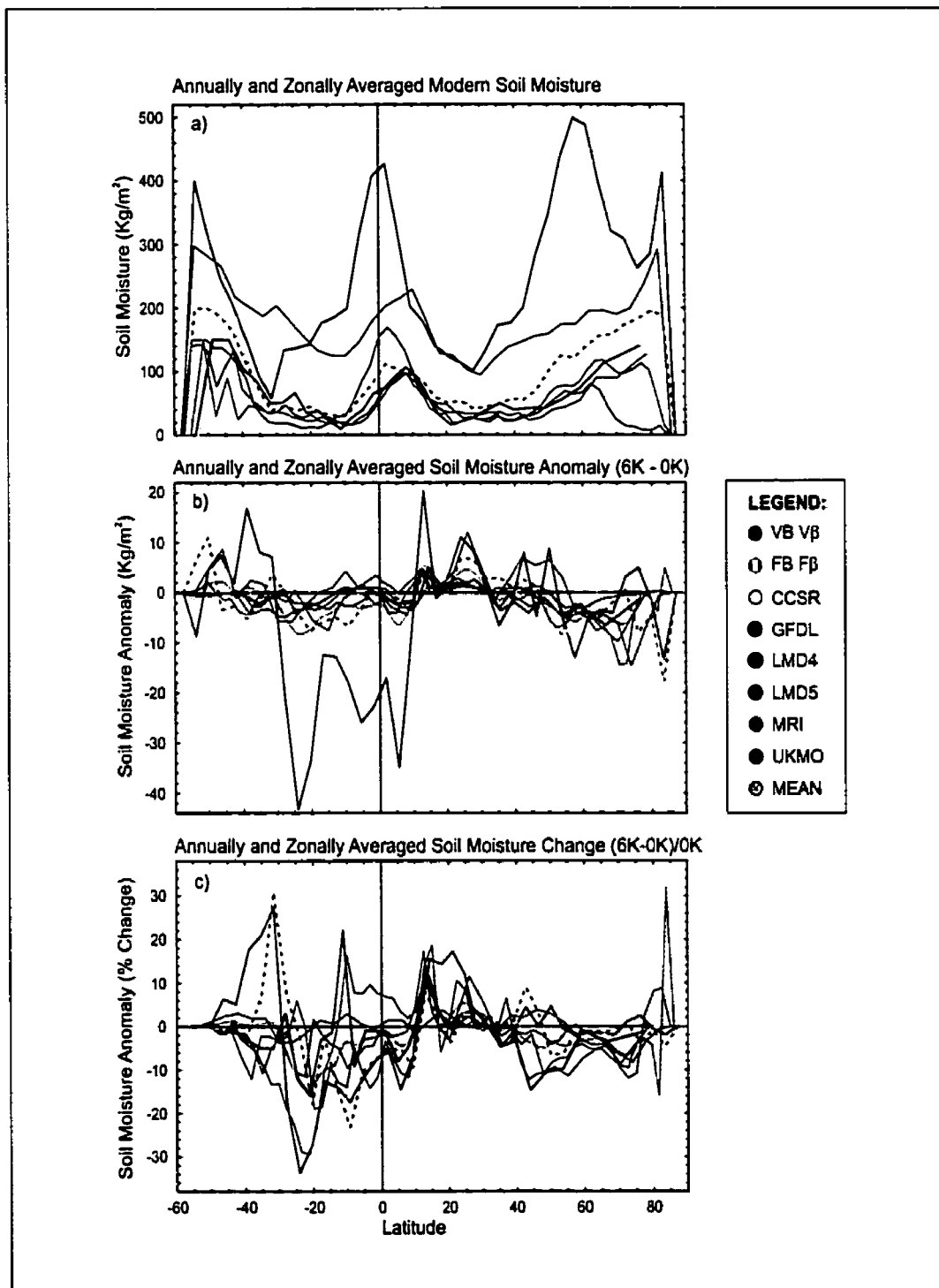


Figure 2.3: Annually and zonally averaged PMIP (a) modern soil moisture and the (b) 6 ka BP - modern anomaly. Units are in  $\text{Kg m}^{-2}$  ( $\text{Kg m}^{-2} = 0.1 \text{ cm}$ ). c) Percent change in 6 ka BP anomaly  $100 \cdot (6\text{ka} - 0\text{ka}) / 6\text{ka}$ . The solid and dashed black lines represent the CCCma model with the variable bucket scheme/variable slope factor (VB V $\beta$ ) and the CCCma model with the 20 cm constant bucket scheme/constant slope factor (FB F $\beta$ ), respectively

one soil layer for prognostic moisture except for the MRI model which has 4 soil layers. The zonally averaged soil moisture is characterized by high values in the tropics and high latitudes which are associated with high precipitation in the ITCZ and along the polar frontal zones, respectively. It is apparent that the CCCma model contains excessive amounts of soil moisture compared to most of the other models. In fact there is up to 50 cm of soil moisture from 50°N to 65°N latitude where most of the models contain between 6 and 20 cm of soil moisture. Again there are similar discrepancies but of smaller magnitude in the tropics and southern mid-latitudes. The modification of the land surface parameterization to that which has a 20 cm bucket everywhere clearly reduces these anomalous amounts of soil moisture to levels that are more consistent with the other models. This is an expected consequence of the fact that the shallower bucket can no longer hold as much moisture. As expected, the models with similar bucket depth have similarly limited soil moisture amounts, for example, GFDL, LMD4, and LMD5 have a 15 cm bucket while CCCma model with fixed bucket depths (FB  $F\beta$ ) and CCSR have 20 cm buckets. The MRI model, which has 4 soil layers, appears to have a limiting soil moisture value of 30 cm. The other CCCma simulation (VB  $V\beta$ ) and the UKMO model have variable bucket schemes. As a comparison with observed available soil moisture over Russia (Robock et al. 1998)[194], half of the models in Fig. 2.3a are probably underestimating the amount of simulated soil moisture in northern mid-latitudes, while the 20 cm bucket schemes are more consistent with the observations. The original CCCma variable bucket scheme (VB  $V\beta$ ) which has soil moisture amounts in the 50 cm range is probably 2 to 3 times in excess of the observations.

The zonally and annually averaged 6 ka BP soil moisture anomalies are shown in Figs. 2.3b and 2.3c. The actual changes in soil moisture amount are displayed in Fig. 2.3b while the percent change in anomaly is shown in Fig 2.3c. The CCCma variable bucket model simulation (VB  $V\beta$ ) delivers anomalous behaviour with respect to the other models and reveals much larger variations in soil moisture than the other models, especially in the tropical regions of the globe. This version of the model delivers changes of up to 4 cm of soil moisture between 6 ka BP and present whereas the other models have more zonally consistent changes of around 0.5 to 1 cm. The CCCma 20 cm bucket model (FB  $F\beta$ ) delivers a response that is much more consistent with the other models in terms of the 6 ka BP anomaly. The general pattern of the zonally averaged soil moisture among the models is characterized by a decrease in the tropical regions and increases in the northern hemisphere extra-tropics (Fig 2.3b). This can be attributed to shifts in the ITCZ along with shifts of precipitation to more northerly latitudes. It is interesting to note that the differences in the 6 ka BP response in soil moisture between the 2 CCCma simulations, VB  $V\beta$  and FB  $F\beta$ , is consistent in their anomalous

percent change. The two curves track one another closely especially in the northern hemisphere tropics and the linear nature of this response gives an indication that there is little or no feedback occurring with the soil moisture in the CCCma AGCM under the 6 ka BP perturbed climate. It is also interesting to note that the variability of the response among the PMIP collection of models in the southern hemisphere is much stronger than that in the northern hemisphere and reaches  $\pm 30\%$  at certain latitudes. The region in the northern hemisphere which displays the most variability among the PMIP collection of models is in the mid-latitudes between  $40^\circ\text{N}$  and  $60^\circ\text{N}$  and this is the region upon which I will focus primarily in what follows.

### 2.3.2. Zonally Averaged Surface Air Temperature at Screen Height (2m)

One of the main features of the climate response forced by the 6 ka BP insolation anomaly is the change in surface temperature resulting from the difference in net absorbed radiation as compared to present. There is an increased heating over land from June to October and cooling during the rest of the annual cycle evident in 6 ka BP AGCM experiments which is consistent with the insolation change observed for this time period (see, for example, V98)[229]. The detailed energy balance that obtains at the surface of the model in response to the orbital perturbation is of course dependant upon the specific parameterizations employed in the land surface scheme. The objective here is to assess the result of the perturbation to the land surface scheme in the control climate and the further changes that then result in the 6 ka BP orbitally perturbed climate. The control temperature response is evident in Figs. 2.4a and 2.4c, which compare the magnitude of the northern hemisphere zonally averaged surface air temperature at screen height (2m) for both DJF and JJA, respectively. Also shown by the grey line in these figures is the zonally averaged response over land obtained from observations (Legates and Willmot 1990)[126]. The variable bucket (VB  $V\beta$ ) CCCma control simulation is denoted by the black solid line in Fig. 2.4. In winter (Fig. 2.4a) the control simulation is rather cold, by a few degrees, as compared with the observed temperature. In summer (Fig. 2.4c) the CCCma simulation is close to the observed temperature, especially in mid to high northern latitudes, whereas in the PMIP collection of models there is a general spread of the models about the observed temperature with a slight collective model tendency to be warmer than observed in the summer season.

A comparison of the 6 ka BP JJA response of the CCCma model with respect to the same set of PMIP models (Fig. 2.4d) delivers results that are somewhat counter intuitive. Although the Canadian model is one of the models that best represents the modern summer response, the 6 ka

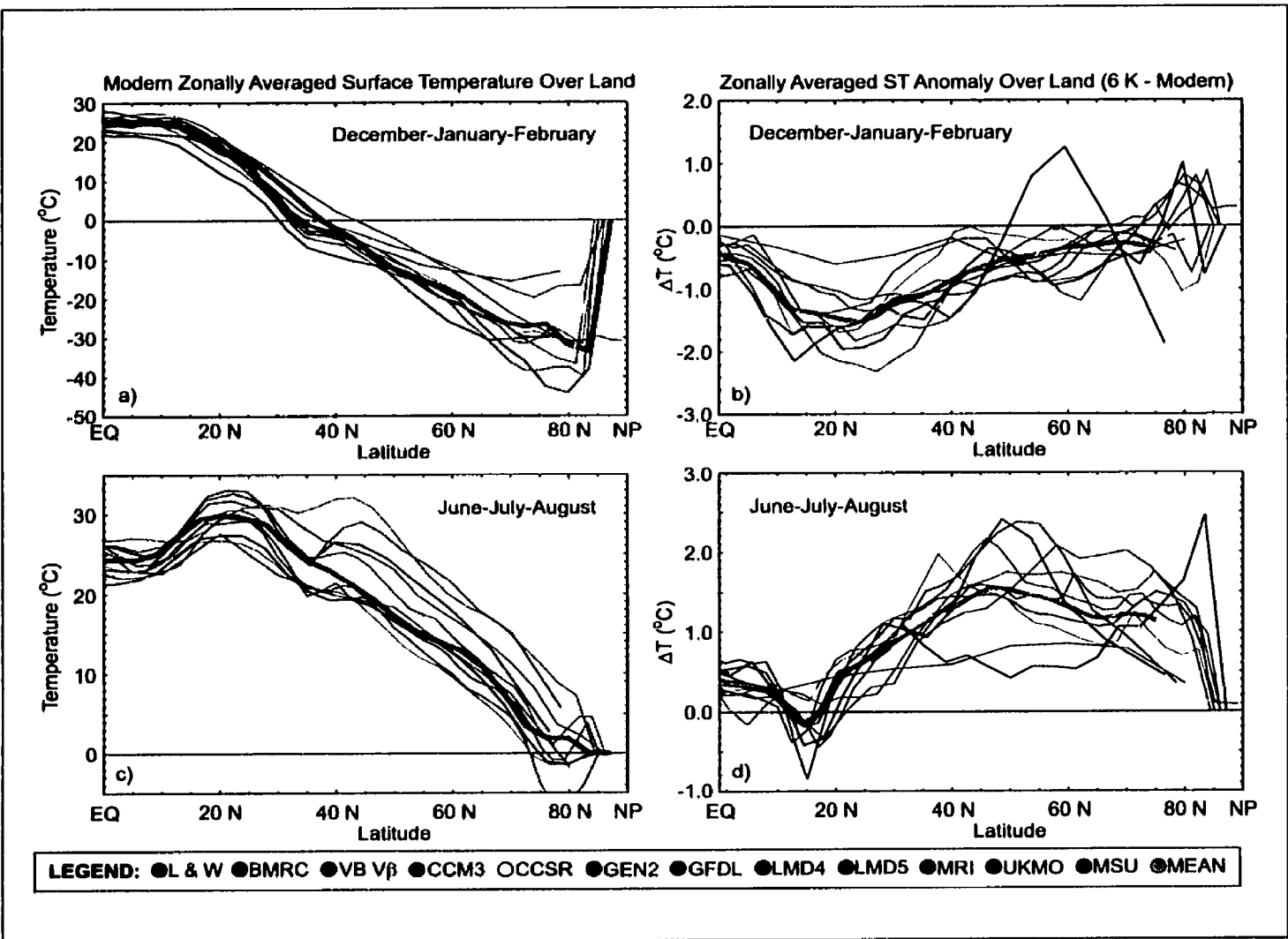


Figure 2.4: Seasonally and zonally averaged northern hemisphere PMIP 2m surface air temperatures (°C) over land for (a) modern DJF, (b) 6 ka BP - modern DJF, (c) modern JJA, and (d) 6 ka BP - modern JJA. The thick grey lines are the modern observed in (a) and (c) (Legates and Willmott 1990) and the model mean in (b) and (d).

BP JJA surface air temperature anomaly (Fig. 2.4d) clearly demonstrates that the model is an outlier in mid and high latitudes over land. The mid-latitude region (30°N to 70°N), is an area comprising approximately 35% of the northern hemisphere land surface, in which most of the PMIP model differences arise. The model's response is relatively large in Arctic latitudes unlike the other models and is also an outlier in this region. The PMIP mean model response, which is represented by the grey line in Figs. 2.4b and 2.4d, demonstrates that the CCCma model responds in a typical manner to the 6 ka BP insolation perturbation between the equator and the sub-tropics (0 °N to 30°N) in JJA. This is a region in which there is less variability between models and which is characterized by cooling in the tropics in the vicinity of 15°N latitude which is primarily explained by increased evaporative cooling and changes in cloud cover. The 6 ka BP DJF anomaly (Fig. 2.4b) is characterized by extreme variability between the models in both the sub-tropics and polar latitudes. Greater consistency between the models (excepting the LMD4 model) is evident between 50°N and 70°N. It is interesting to note that the LMD5 model does not suffer from the warming anomaly evident in the output from the LMD4 model (see Mason et al. 1998, for an explanation). The CCCma model behaves similarly to the other models except in high polar latitudes, where there is large variability between the models. This is expected since there is large variability in the control simulations also. The cooling anomalies in winter and the warming anomalies in summer are generally consistent among all of the models in PMIP, and are consistent with changes expected on the basis of the orbital configurations characteristic of 6 ka BP.

The JJA surface air temperature response over land in the 4 sets of experiments which I have performed reveal significant differences in both the modern control and 6 ka BP climate characteristics (Fig. 2.5). When the bucket scheme and the evapotranspiration slope factor are altered, both together and separately, an interesting behaviour is revealed in the modern control simulations. In summer, the 20 cm fixed bucket simulations (FB  $F\beta$  and FB  $V\beta$ ) are approximately two degrees warmer than both the variable bucket simulations (VB  $V\beta$  and VB  $F\beta$ ) and observed temperature in northern mid-latitudes (40°N to 60°N) (Fig. 2.5a). What is interesting is that by changing the evapotranspiration slope factor, from one that is spatially varying to one which is constant, the result is no significant change in the modern climate prediction. However, by inspection of Fig. 2.5b, which depicts the 6 ka BP anomalies in the 4 sets of simulations, it will be clear that the range of response is much more highly variable (and likely not statistically significant) at mid to high latitudes in some of the experiments. Furthermore, all 4 experiments remain below the PMIP model mean temperature predictions at mid to high latitudes and produce unique reactions to modifications of the land surface scheme. The only consistency between the 4 simulations occurs in the

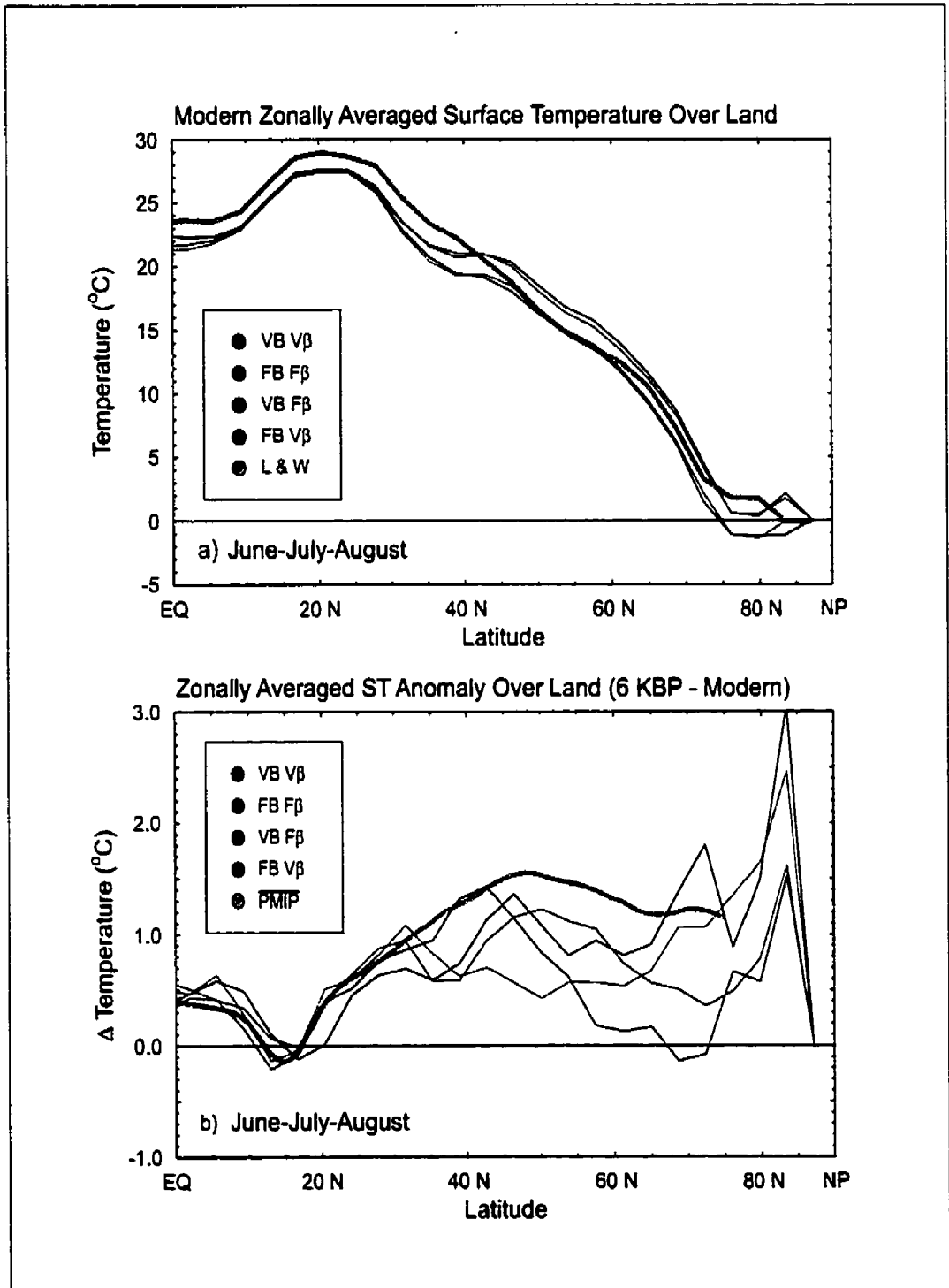


Figure 2.5: Seasonally and zonally averaged northern hemisphere 2m surface air temperatures (°C) over land for (a) modern (b) 6 ka BP - modern JJA. The thick grey lines are the modern observed in (a) (Legates and Willmott 1990)[126] and the PMIP model mean in (b). In the legend, V=variable, F=fixed, B=bucket, and  $\beta$ =evapotranspiration slope factor.

tropics and in sub-tropical latitudes. In the high latitude region similarities in response exist only between particular model pairs. The mid-Holocene surface air temperature response in the tropics therefore appears to be rather insensitive to changes in the land surface parameterization, which is also consistent with the full range of behaviours revealed by the PMIP collection of models in this region. The pairing of the 4 experiments at high latitudes, VB  $V\beta$ /VB  $F\beta$  and FB  $F\beta$ /FB  $V\beta$ , may be understood in terms of the influence of the evapotranspiration at high latitudes. The evapotranspiration is controlled by the fractional snow cover at high latitude as described in the above-section on land surface processes. In fully snow covered regions the evapotranspiration is controlled by the potential evapotranspiration and thus the influence of the slope factor,  $\beta$ , becomes negligible. What is most interesting is the fact that the response of the simulation at 70 °N is highly variable, ranging from no change at 6 ka BP to a response which exceeds the PMIP mean model response. This sensitivity is likely a result of the fact that rapid changes in fractional snow cover as a function of latitude occur in the summer season, a characteristic of the simulations which will be investigated further in what follows. The model sensitivity in mid-latitudes, where there is no fractional snow cover in summer, was such as to produce counter-intuitive behaviour. It was hypothesized initially that the reduction in bucket depth in this region would lead to the removal of excessive amounts of moisture from the land and thus reduce changes in evaporative cooling in this region at 6 ka BP. This can only be argued in explanation of the differences between two of the sensitivity experiments, namely VB  $V\beta$  and FB  $F\beta$ . The other set, VB  $F\beta$  and FB  $V\beta$ , are characterized by much different zonally averaged responses at mid-latitudes. The experiment with constant 20 cm bucket and variable evapotranspiration slope factor (FB  $V\beta$ ), delivered a rapid decrease in temperature from 40 °N to 70 °N, something which is also seen, but not to the same extent, in the other fixed bucket simulation (FB  $F\beta$ ). An attempt to explain this behavior will be described in what follows. To begin, however, I will investigate the sensitivity of the statistically significant response of the modern model control simulation to changes in bucket depth.

### **2.3.3. Land surface response in the control simulations.**

The generation of models involved in the PMIP collaboration tend to have relatively simple water budgeting and individual models often employ simple bucket representations (Table 2.1) to govern the physically complicated processes of moisture storage and runoff. The energy partitioning is more sophisticated, with all the models employing a general surface energy budget equation similar to that described in section 2.2. In this subsection the focus is upon energy partitioning within the

CCCma model under the variable and fixed bucket schemes in both the control and 6 ka BP orbital perturbation experiments.

The evolution of the seasonal cycle over land is determined by the net seasonal balance between absorbed solar radiation at the surface, the subsequent emission of thermal radiation, and the exchange of both sensible heat and moisture with the atmosphere. The dynamics of this process are for the most part governed by the balance within the surface energy budget and also include changes in the various phases of water within the surface sub-system. An excess or deficit in the balance is reflected in the time evolution of the ground temperature. The differences in the net radiation balance and the partitioning of sensible and latent heat at the surface between the 20 cm bucket (FB  $F\beta$ ) and variable bucket (VB  $V\beta$ ) control simulations are displayed in the zonally averaged fields over land in Fig. 2.6. Negative values denote upward fluxes of longwave radiation, sensible and latent heat. These two simulations are chosen for this investigation because they were averaged over the same period (10 years) and because the sensitivity of the evapotranspiration slope factor on modern climate was shown to be negligible as compared with the reduction in bucket depth in the previous section. The differences in the JJA energy balance components clearly demonstrate a significant energy budget adjustment in response to the reduction in the bucket depth in summer. The shortwave absorbed radiation (Fig. 2.6a) is increased in the tropics and at middle to high northern latitudes over land. The net longwave radiation (Fig. 2.6a) at the surface mirrors the response of the shortwave absorption. The incoming solar radiation not absorbed or scattered within the atmosphere is absorbed by the surface in an amount dictated by the surface albedo. Inspection of the zonal change in total cloudiness and surface albedo over land (Fig. 2.6b) explains most of the changes observed in the control simulation due to the reduction in bucket depth. Decreases in total cloudiness in the tropics and middle latitudes in the fixed bucket simulation constitute the dominant forcing for the changes in the solar absorption at the surface (and also for the change in net longwave radiation) since the reduction of bucket depth has little impact on the surface albedo in these regions. This change is primarily explained by the impact on cloudiness: decreases in cloud cover increase the absorbed shortwave radiation and also increase the net longwave radiation at the ground through the decrease in longwave radiation received at the surface from the reduced cloud cover. At high northern latitudes changes in the surface albedo become significant and are responsible for the majority of the increases in the solar absorption in the fixed bucket simulation. Decreases in total cloudiness are a result of a drier surface and thus less evaporation (Fig. 2.6c) to form clouds while decreases in surface albedo arise from a decrease in the snow mass at high latitudes (not shown).

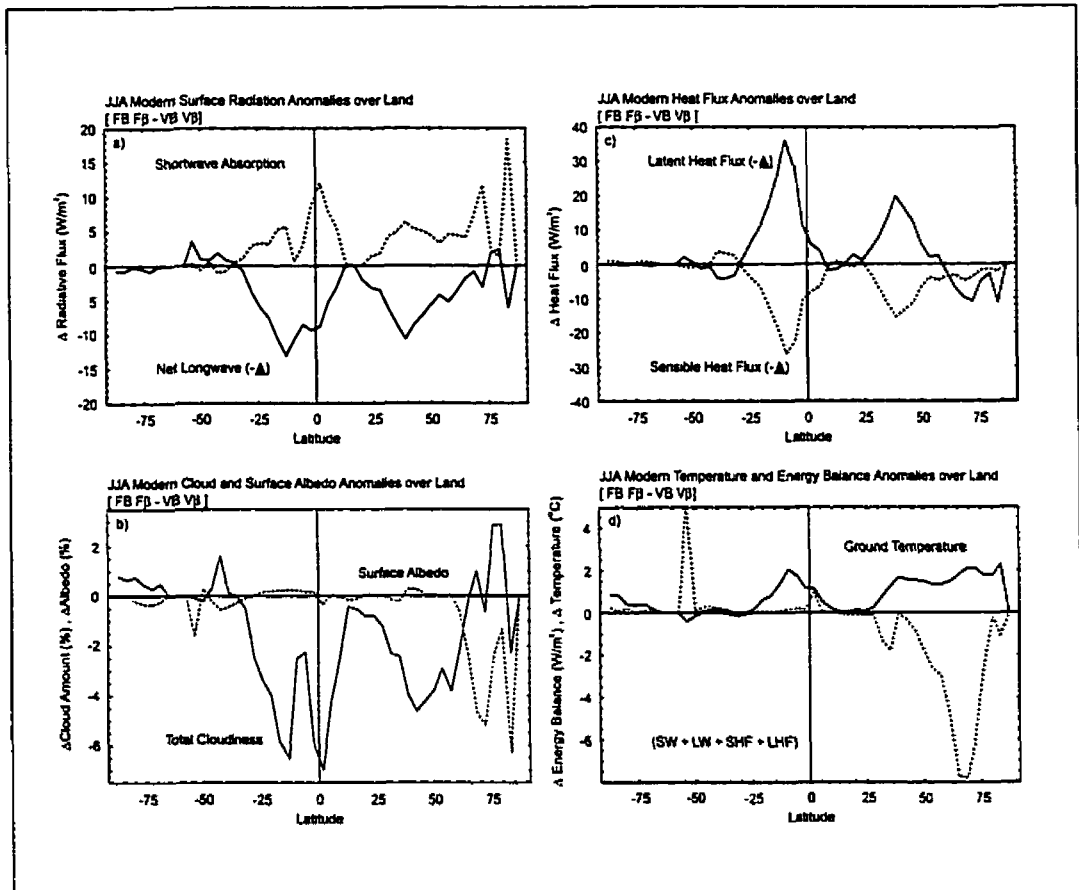


Figure 2.6: Modern zonally averaged JJA surface energy budget anomalies between the CCCma simulation with constant 20 cm bucket (FB F $\beta$ ) and the simulation with a variable bucket scheme (VB V $\beta$ ). a) The shortwave absorption (dashed line) is plotted with the net longwave radiation (solid line). b) The surface albedo (dashed line) and total cloudiness (solid line) for the control anomaly are denoted in percentage terms. c) The latent (solid line) and sensible heat (dashed line) flux anomalies between the two control simulations are plotted. Negative values denote upward fluxes of radiation and heat fluxes in W m $^{-2}$ . d) The control anomalies for ground temperature (°C) and the sum of the components in (a) and (c) which make up the surface energy balance (W m $^{-2}$ ) are plotted in solid and dashed lines, respectively.

The changes in partitioning of latent and sensible heat flux from the surface due to the reduction in bucket depth are revealed in the zonal temperature averages over land for JJA (Fig. 2.6d). The reduction of available surface moisture, a consequence of the reduced water holding field capacity, significantly reduces the upward latent heat flux in the tropics and mid-latitudes. The available soil moisture in the two simulations can be inferred from Figs. 2.3a and 2.1c. By taking the ratio of soil moisture to bucket depth, the two peaks in Fig. 2.4b are associated with a 15 % drop in moisture availability in the tropics and northern mid-latitudes. The decrease in upward latent heat flux is accompanied by a corresponding increase in the upward sensible heat flux, a clear demonstration of the energy partitioning between these two components in the surface energy budget. This mirror like behaviour ceases to obtain at high northern latitudes where the impact of the phase change of water from its solid to liquid form is significant. The radiative and heat flux components in the surface energy balance compensate one another to bring about a near equilibrium over land. A modification to the bucket scheme has changed the modern behaviour of these components over land to a significant extent. Fig. 2.6d demonstrates that the changes in Figs. 2.6a and 2.6c result in a reduction in the sum of these components at middle to high northern latitudes. This reduction is in part due to the changes in snowmelt which occurred over the course of this season. The negative value of the sum of the 2 radiative and 2 heat flux components should balance with the energy imparted to or removed from the ground due to phase changes in water in the surface layer. The energy balance equation also involves a force-restore component which attempts to mimic sub-surface energy storage, however one would expect the daily average of this quantity to be quite small, but nevertheless sign definite for long periods of time. On a seasonal average, one might argue that this residual quantity should be quite small for summer and winter months but not for the equinoctial seasons which are periods of transition. This suggests that there is less snowmelt in the fixed bucket simulations in summer. The new balance appears to play a role in the new equilibrium northern hemisphere summer air temperature which is attained in the 20 cm bucket simulations. The other curve in Fig. 2.6d demonstrates that the fixed bucket control simulations are almost 2°C warmer than the original control in northern mid-latitudes and this appears to be connected to the phase changes of water in the surface energy balance.

#### **2.3.4. Land surface response in the 6 ka BP simulations**

The nature of the paleoclimate experiments performed in the context of this study provides a unique opportunity to assess how the changes observed in the modern control simulations will influence the

changes in the surface characteristics under the modified insolation "regime" characteristic of 6 ka BP. This climate regime is one in which insolation forcing is greater by approximately 5% in northern hemisphere summer. The northern hemisphere response over land at 6 ka BP is displayed in Fig. 2.7 for the anomalies in the four variations of the simulations described in Fig. 2.5b. The changes in the surface radiation balance (Figs. 2.7a and 2.7b) and the changes in the surface heat fluxes (Figs. 2.7c and 2.7d) are much the same in all 4 paleoclimate simulations of mid-Holocene climate. On the basis of Fig. 2.5b, I previously noted that the major changes which appear in the 6 ka BP anomaly are from north of 40°N latitude to high polar latitudes. In particular there are three regions which display a large degree of sensitivity, namely the regions centred on 50°N, 70°N, and 83°N. These sensitive latitude bands seem to correlate well with regions in which changes were observed in the control simulations.

The surface shortwave absorption anomaly (Fig. 2.7a) and net longwave anomaly (Fig. 2.7b) have about  $6 \text{ W/m}^2$  of variability at 50°N. The changes in the shortwave absorption and net longwave in this region appear as a result of a decrease in the total cloud cover (Fig. 2.7e). Again, the radiative components result from the cloud effect in this mid-latitude region. Upon inspection of Figs. 2.7a, 2.7b and 2.7e, it becomes apparent that the 4 experiments have 6 ka BP changes which are ordered in a manner that is either correlated or anti-correlated with the changes in total cloud cover in this mid-latitude region. The shortwave radiation is anti-correlated with total cloud amount, while the net longwave radiation is correlated. The shortwave absorption varies from largest to smallest in the simulations which range from a decrease to an increase in total cloud cover at 6 ka BP, with the fixed bucket simulations being characterized by the greatest absorbed shortwave radiation and decrease in cloud cover. Likewise, the two simulations characterized by upward anomalies in net longwave radiation (FB  $V\beta$  and FB  $F\beta$ ) are also characterized by the largest decreases in total cloud cover, whereas the two simulations that deliver downward anomalies in net longwave radiation (VB  $V\beta$  and VB  $F\beta$ ) also have the largest increases in total cloud cover. The net longwave radiation (Fig. 2.7b) also appears to have a zonal average structure which is very similar to that of the total cloud amount (Fig. 2.7e) in all 4 simulations over much of the northern hemisphere with the exception of the polar region. The shortwave absorbed radiation, however, appears to be less strongly correlated with the changes in cloud cover.

At high latitudes, there is a large difference in the response characteristics of the four experiments. The fixed bucket schemes (FB  $V\beta$  and FB  $F\beta$ ) have less shortwave absorbed radiation than the variable bucket schemes (VB  $V\beta$  and VB  $F\beta$ ) at 70°N. There also appears to be little explanation for this in terms of the total cloud cover at this latitude (Fig. 2.7e). However, inspection of the

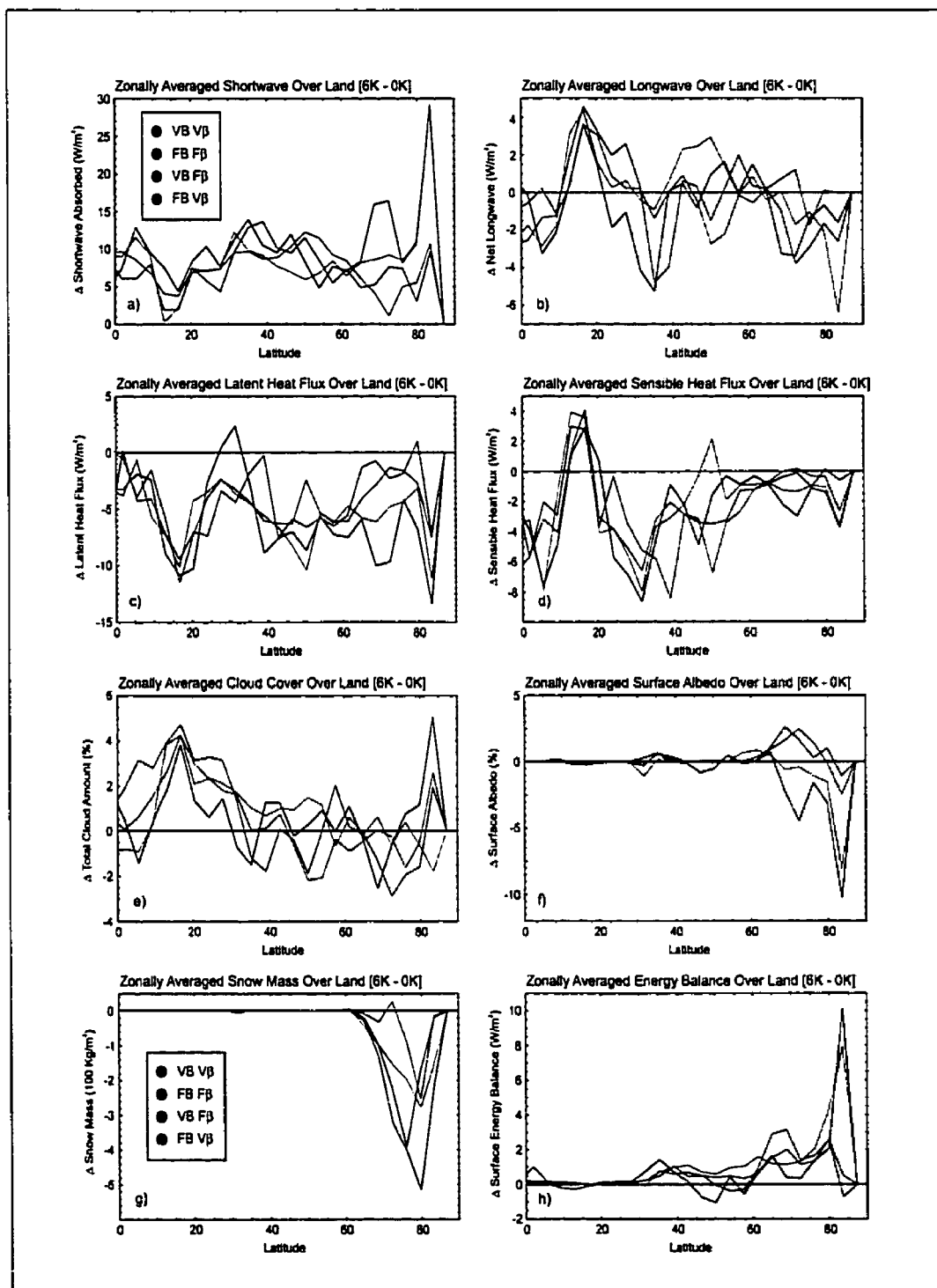


Figure 2.7: 6 ka BP - modern JJA northern hemisphere zonally averaged surface anomalies in the 4 simulations are displayed for (a) shortwave absorption in  $W m^{-2}$ , (b) net longwave in  $W m^{-2}$ , (c) sensible heat flux in  $W m^{-2}$ , (d) latent heat flux in  $W m^{-2}$ , (e) total cloudiness (%), (f) surface albedo (%), (g) snow mass ( $Kg m^{-2}$ ) and (h)  $(SW+LW+SHF+LHF)$  in  $W m^{-2}$ . In the legend, V=variable, F=fixed, B=bucket, and  $\beta$ =evapotranspiration slope factor.

zonally averaged surface albedo at 70°N (Fig. 2.7f) demonstrates that the shortwave response is controlled by the increased anomaly in surface albedo at 6 ka BP. Further inspection of the changes in snow cover at this latitude (Fig. 2.7g) indicate that these albedo changes may not be a result of the decreases in snow amount observed at 6 ka BP, but rather might arise from the decrease in soil moisture in the two fixed bucket simulations.

In polar latitudes, the strange spiked behavior which was observed in the 6 ka BP temperature response (Fig. 2.5b), is consistent with the 6 ka anomalies in absorbed shortwave radiation (Fig. 2.7a). This large radiative anomaly is mostly compensated by the exchange of latent heat with the atmosphere (Fig. 2.7c). At this polar latitude, it becomes apparent that the potential evapotranspiration dictates the latent heat flux while the evapotranspiration slope factor has no influence, an effect which was also observed in the surface temperature response (Fig. 2.5b). An explanation for this polar latitude 6 ka BP response is revealed by investigation of the surface albedo (Fig. 2.7f) and snow cover (Fig. 2.7g) anomalies at 6 ka BP. There is a consistent correlation between decreases in albedo and decreases in snow cover in the variable bucket schemes (VB  $V\beta$  and VB  $F\beta$ ) which result in both the large shortwave absorption anomaly and the large surface temperature response. The two fixed bucket schemes (FB  $V\beta$  and FB  $F\beta$ ) do not deliver the same degree of warming at this polar latitude as a result of the smaller decrease in both albedo and snow cover.

The partitioning of sensible and latent heat flux in the mid-latitude region (Figs. 2.7c and 2.7d) displays the same behavior as in the shortwave and longwave radiation. The 4 experiments have variability which ranges over about 8 W/m<sup>2</sup> for these surface heat fluxes centred at approximately 50°N. The experiments which have decreased upward latent heat fluxes (FB  $V\beta$  and FB  $F\beta$ ) have increased upward sensible heat fluxes, which is consistent with the reduction in bucket depth among the 4 experiments. At the higher polar latitudes where much of the variability in the response was observed (70°N and 83°N), the latent heat flux appears to compensate for the large increase in solar absorption, to a larger degree than the increased upward sensible heat flux anomaly or the longwave radiation anomaly. The larger increases in upward latent heat flux anomalies in the variable bucket simulations rather than in the fixed bucket simulations is again simply a consequence of increased soil moisture.

Inspection of the sum of the 4 flux components in Figs. 2.7a-2.7d, which make up a majority of the surface energy balance (Fig. 2.7h) in equation (2.1), indicates a connection between the temperature response and the energy balance at high latitudes. Interestingly, there is a large correlation between the changes at 70°N and 83°N in this balance and the 6 ka BP temperature response in Fig. 2.5b. The sum of the flux anomalies is anti-correlated with the surface temperature anomaly at 70°N,

then switches over and becomes correlated at 83°N. The large deviation of the energy balance from zero at high latitudes indicates that the influence of the conversion of liquid and solid forms of soil moisture and changes in snow cover melt are influencing the temperature response at this latitude. In particular, at 70°N north, the largest temperature anomalies are associated with the energy balance which is nearest zero. The fixed bucket simulations show little or no change in the 6 ka BP surface temperature response, but have rather large anomalies in the sum of the four flux components. This suggests that there are large changes from frozen to liquid soil moisture in the fixed bucket simulations, which acts to draw energy away from the surface. Decreases in the heat capacity of the soil in these simulations due to the reduced bucket depth would only act to strengthen the temperature response and there appears to be no consistent changes of snow melt at this latitude. The surface energy balance at 83°N, confirms the previous hypothesis that the large decreases in snow cover seen in the variable bucket schemes at 6 ka BP (Fig. 2.7g) result in some compensation for the large surface energy balance seen in these simulations at this high latitude.

### **2.3.5. The PMIP mid-latitude land surface response**

In this sub-section I will proceed to investigate the differences observed in selected CCCma zonally averaged surface variables over land as compared with other PMIP models by performing comparisons restricted to the northern mid-latitude sector of the globe. The global distribution of the 6 ka BP surface temperature anomaly from the simulation with variable bucket depth and variable evapotranspiration slope factor (VB  $V\beta$ ) is displayed in Fig. 2.8a. The 6 ka BP surface temperature anomaly from the simulation with fixed bucket depth and fixed evapotranspiration slope factor (FB  $F\beta$ ) is displayed in Fig. 2.8b. The mid-latitude region between 45°N and 65°N over North America and Asia is highlighted to show the spatial distribution of the increase in the surface temperature response at 6 ka BP over North America and Asia. As was demonstrated in the previous subsection, the 6 ka BP response is very sensitive to the prescription of the land surface parameterization, making inferences concerning the physical significance of the changes in the 6 ka BP anomaly from this sensitivity study debatable. Nevertheless, the enhanced response over Asia and North America in Fig. 2.8b, which is now statistically significant over the highlighted region, provides a framework in which to gauge the magnitude of this sensitivity with respect to the PMIP collection of models. The differences between the two simulations also provides a measure of the variability which is present in the 6 ka BP simulations averaged over a 10 year period. Changes over 1°C are shaded, illustrating the fact that the weak response (approximately 0.5 °C) originally documented in the first

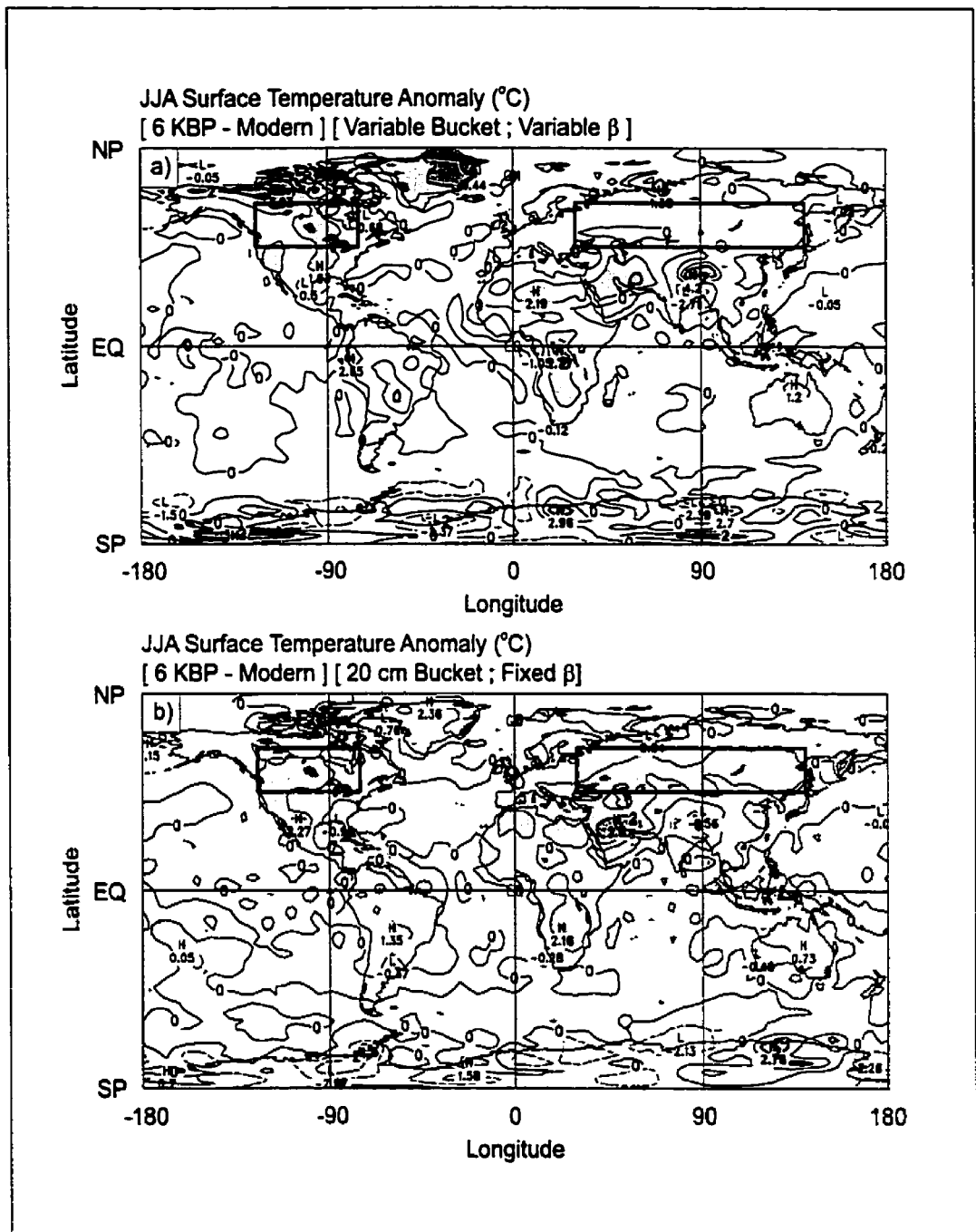


Figure 2.8: Global distributions of JJA 2m surface air temperature anomalies (6 ka BP - modern ) ( $^{\circ}\text{C}$ ) for the CCCma simulation with the (a) variable bucket scheme (VB  $V\beta$ ) and the (b) constant 20 cm bucket scheme (FB  $F\beta$ ). The contour interval is at 1  $^{\circ}\text{C}$  with shaded regions designating changes above 1  $^{\circ}\text{C}$  for JJA. The boxed regions highlight regions which are responsible for the zonally averaged response seen in Fig. 2.1d.

simulation (VB  $V\beta$ ) has now almost doubled in this mid-latitude region. Central Asia and Western North America now display an enhanced response to the 6 ka BP insolation in JJA. This is a simple demonstration of the sensitivity of the climate to the land surface parameterizations under changes in paleoclimatic boundary conditions.

The next set of figures (Figs. 2.9 and 2.10) have been constructed to further investigate the average behaviour of selected surface variables in the mid-latitude region highlighted in Fig. 2.8. This mid-latitude band over land is locally averaged to intercompare models in the PMIP project and thereby possibly illustrate the mechanisms for some of the anomalous behaviour of the CCCma model. A scatter plot of the 6 ka BP ground temperature anomaly versus modern ground temperature for JJA over the subarea in Fig. 2.8 is displayed in Fig. 2.9a. In this plot the linear regression between the models is displayed as a dashed line, while a box centred on the model mean represents one standard deviation from the mean in both the abscissa and ordinate directions. There appears to be a trend among the models, showing a bi-modal separation of the models into two groups, one which is warm biased and one which is cold biased. The modern summer ground temperatures range from 13 °C to 25° C among the models, demonstrating about 10°C of variability in the JJA season. This large variability among the modern control simulations is also true of the winter season (not shown). The 6 ka BP response of the models vary from a warming of approximately 0.5° C to 2.5° C with an average of 1.5 °C in summer. The majority of the models which have a warm control climate have a 6 ka BP temperature response which is rather large, while the models which have a cold control climate have a smaller response at 6 ka BP. This revisits a common problem which has been illustrated in other PMIP studies (e.g. Joussaume et al. 1999, Chapter 3)[108]; namely that the paleoclimate response in these models is often dictated by the properties of the modern control simulation. In JJA, the original variable bucket CCCma calculation (VB  $V\beta$ ) is cold-biased and the major outlier. The simulation with the 20 cm bucket calculation (FB  $F\beta$ ) is no longer an outlier, but rather is closer to the model mean temperature in the control simulation and 6 ka BP response. The winter ground temperature response among the models does not reveal the same bias in the modern climate simulation (not shown).

A scatter plot of the change in precipitation at 6 ka BP versus modern precipitation for JJA over the subarea in Fig. 2.8 is displayed in Fig. 2.9b. The models display a rather uncorrelated behavior in modern precipitation versus the 6 ka BP precipitation anomaly. There is still a large variation among the models in their depiction of the modern mid-latitude precipitation averaged over the subarea shown in Fig. 2.8. The precipitation varies from approximately 0.75 mm/day to 3.2 mm/day, or 70 mm to 300 mm during the summer season. The 6 ka BP precipitation anomaly

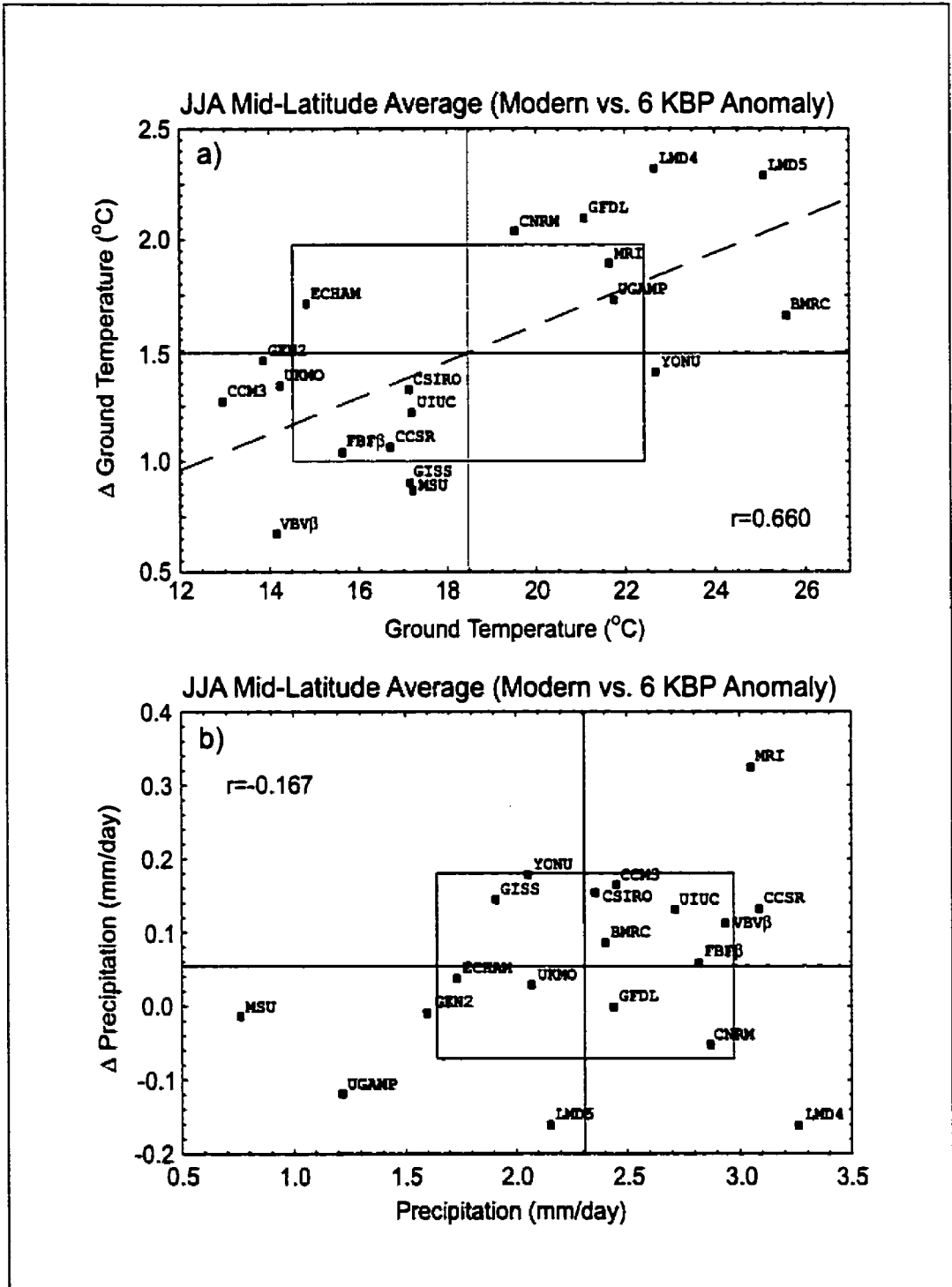


Figure 2.9: Scatter plot of the JJA ground temperature versus 6 ka BP JJA ground temperature anomaly for the PMIP simulations. b) Scatter plot of the JJA precipitation vs. 6 ka BP JJA precipitation anomaly for the PMIP simulations. Precipitation is plotted in  $\text{mm day}^{-1}$  while temperature is in  $^{\circ}\text{C}$ . The intersection of the horizontal and vertical solid lines represent the model mean, while the box represents one standard deviation in the abscissa and ordinate directions. The dashed line is the linear regression.

ranges from approximately -0.15 mm/day to 0.35 mm/day, or -15 mm to 30 mm during the summer season. The mean 6 ka BP precipitation anomaly among the models is near zero which implies that the mid-Holocene modeled precipitation change will be difficult to reconcile with proxy climate data in the northern mid-latitude regions. It is difficult to argue for the existence of any correlation between modern control simulations of precipitation and the 6 ka BP response among the models since the correlation coefficient is rather low, and therefore the linear regression is not shown. The variation of the PMIP winter precipitation response at 6 ka BP (not shown) is about 20% of that in summer and also centred around zero, which implies that the mid-Holocene winter response is even less significant than in summer. The original variable bucket CCCma calculation (VB  $V\beta$ ) and 20 cm bucket calculation (FB  $F\beta$ ) deliver little response in precipitation in both the modern control and the 6 ka BP anomaly.

The surface energy balance changes described in the previous section can be extended to an intercomparison with the other PMIP models where the changes in the surface hydrology appeared most sensitive. Fig. 2.10 displays the average over the same region as in Fig. 2.9 but for JJA net longwave versus shortwave absorbed radiation (Figs. 2.10a and 2.10b) and for JJA sensible versus latent heating (Figs. 2.10c and 2.10d). The modern behavior of the PMIP models is generally consistent with the changes observed in the differences between the variable bucket (VB  $V\beta$ ) and fixed bucket (FB  $F\beta$ ) CCCma simulations in Fig. 2.6. The models which have the most surface shortwave absorbed radiation also emit the most upward longwave radiation. The same is true for the 6 ka BP anomaly (Fig. 2.10b), where the models with the greatest change in absorbed shortwave radiation at 6 ka BP also have the most upward longwave emission. Once again the variable bucket depth CCCma model (VB  $V\beta$ ) performs consistently with the other models in the control simulation but anomalously at 6 ka BP. The fixed 20cm bucket simulation (FB  $F\beta$ ) brings the 6 ka BP anomaly into better agreement with the other models, demonstrating the large variability that can be induced in a paleo-simulation by a change in the land surface parameterization. Based on the fact that the changes in surface albedo (not shown) are negligible in this region, the discrepancies in absorbed shortwave radiation are likely attributable to the cloud parameterizations employed in the model. Indeed, if one examines the range of cloud cover that the PMIP collection displays in the modern control (not shown) one finds that differences range from 30% to more than 80% in simulated modern cloud cover. There is also a strong anti-correlation between the linear regression (shortwave vs. longwave) in Figs. 2.10a and 2.10b, and the modern cloud cover and 6 ka BP cloud cover anomaly, respectively. Again, as in Fig. 2.6a, this is explained by the influence of cloudiness: increases in cloud cover decrease the absorbed shortwave radiation and also decrease the net longwave radiation

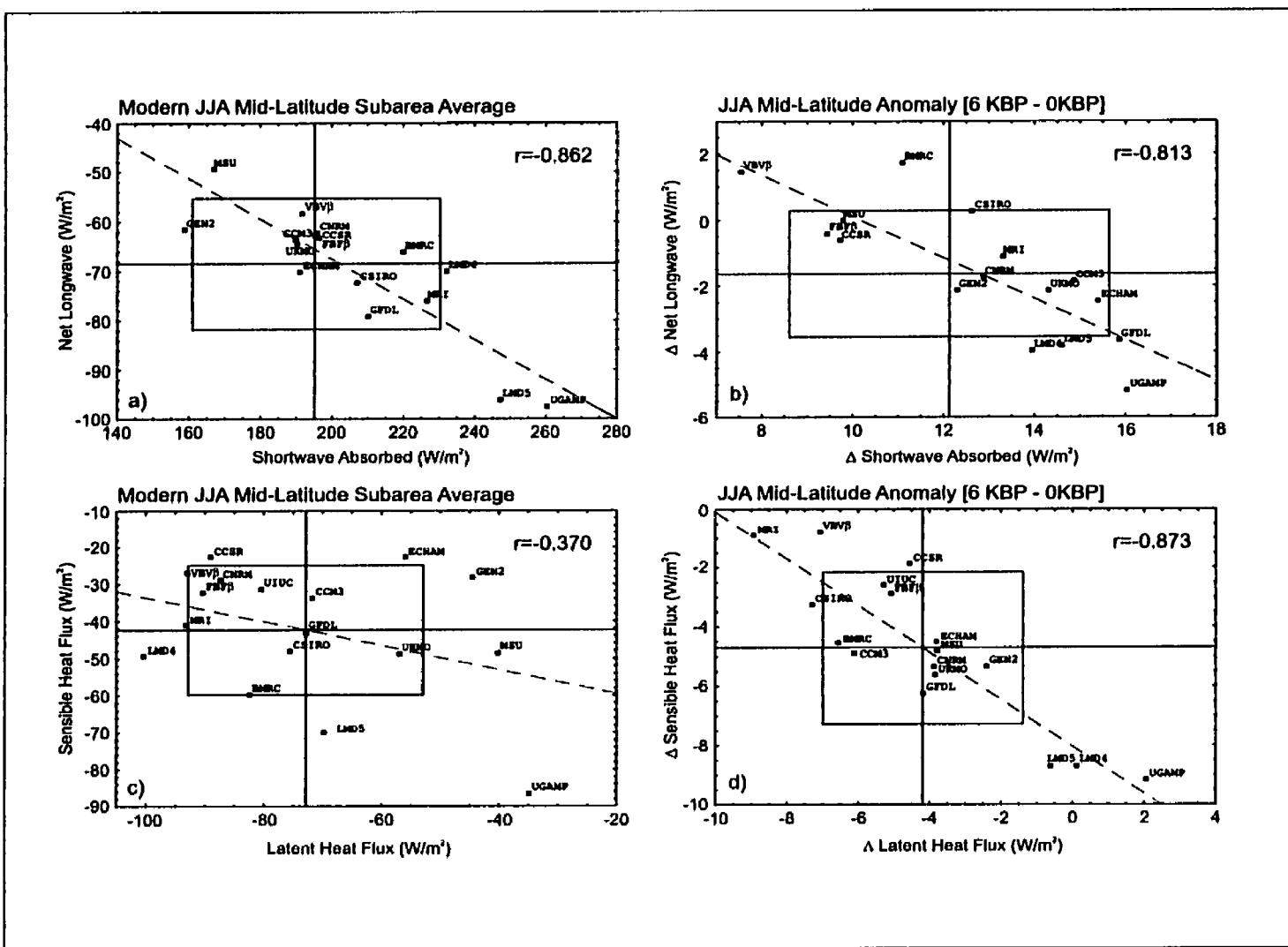


Figure 2.10: Scatter plots of net longwave vs. shortwave absorption for the PMIP (a) JJA control, and (b) JJA 6 ka BP - modern anomaly. Scatter plots of sensible heat flux vs. latent heat flux for the PMIP (c) JJA control, and (d) JJA 6 ka BP - modern anomaly. Units are in  $W m^{-2}$ .

at the ground through the increase in longwave radiation received at the surface from the increased cloud cover.

The partitioning of latent and sensible heat flux in the modern PMIP control simulations is less evident in that there is a general spread of the models about the model mean (Fig. 2.10c) with little correlation among the models. The 6 ka BP PMIP anomalies (Fig. 2.10d), however, demonstrate a clear partitioning of the sensible and latent heat fluxes. The models that exhibit the largest upward sensible heat flux anomalies exhibit a decrease in the upward latent heat flux at 6 ka BP as compared with modern. Again, the variable bucket model (VB  $V\beta$ ) is an outlier in the 6 ka BP anomaly, having little change in the upward sensible heat flux with a large change in the upward latent heat flux. The reduced moisture constant bucket model (FB  $F\beta$ ) delivers a behaviour that is more consistent with that of the other models having both an increased upward sensible heat flux and a decreased upward latent heat flux.

Of all the diagnostics examined, the shortwave radiation absorbed at the surface has always proven to be closely connected with the total cloud cover, as one might reasonably expect. The total cloud cover as well as its influence on radiative transfer, is influenced by a number of feedbacks and is strongly controlled by the radiation parameterizations within the model. As we have seen, the cloud cover is also influenced by the decrease in soil moisture employed in the 20 cm bucket version of the CCCma model (FB  $F\beta$ ), which in turn influences the amount of shortwave radiation absorbed at the surface. The work reported here therefore reveals the need for deeper investigation into the role of cloud parameterizations and cloud feedback, not only in modelling control climates but also in determining the response to perturbed boundary conditions in the context of paleoclimate analysis. An initial investigation by Liao et al. (1994)[129] with the UKMO GCM investigated the influence of two different cloud parameterization schemes to simulate climate changes at 6 ka BP, which were then compared with paleoclimate reconstructions. This study found that a slightly better agreement with the proxy data was achieved with the cloud scheme based upon a cloud water parameterization as compared with that based upon relative humidity.

### **2.3.6. Intercomparisons with North American climate reconstructions**

Reconstructions of terrestrial climate inferred from palynological and geological data constitute a vital contribution to the validation of climate model predictions of past climate states. Within the Canadian CSHD (Climate System History and Dynamics) research network, reconstructions of past climate are being investigated with a number of methodologies. In particular, Gajewski et

al. (2000)[68] have provided an initial detailed inference of North American and adjacent ocean climate for the 6 ka BP time period. Terrestrial climate has been estimated using four independent approaches through the use of two pollen-based reconstruction methods, on the basis of inferences of the movement of ecozone boundaries, and, finally, through the method of modern analogues. The empirically based reconstruction of surface temperature, precipitation, and lake level status based on these methods may be employed for the purpose of comparison with the same surface climate variables produced in the simulation of Holocene climate using the CCCma AGCM, provided that the limitations of both reconstructions are kept in perspective. Here I will describe some aspects of the surface temperature comparison as well as discuss geological inferences of lake level status in comparison with predictions based upon variations in precipitation and evaporation (runoff) within the AGCM. Two of the different AGCM simulations discussed in this chapter will herein be employed for the purpose of comparison with inferences of Holocene climate, namely the reduced constant bucket simulation (FB  $F\beta$ ) and that delivered by the original variable bucket simulation (VB  $V\beta$ ).

Climate reconstructions based upon Sphagnum-dominated peatlands have been employed to determine the temperature and precipitation distributions during the Holocene Optimum. Gajewski et al. (2000)[68] developed a peatland model which is "tuned" using modern climate conditions, namely precipitation and surface temperature, to reproduce the modern peatland distributions over North America. The model manages to represent the northern limits of the high and low sub-arctic interface of the peatlands with minor discrepancies and, in general, a good agreement with present-day distributions. At 6 ka BP, proxy reconstructions indicate that the Sphagnum-dominated peatlands were farther north than at present, which implies a warmer or drier climate or both. The peatland model and peatland distributions therefore present a methodology with which to validate the AGCM output for 6 ka BP and vice-versa. By employing the CCCma variable bucket AGCM simulation of modern and 6 ka BP climate to reproduce peatland distributions, the results indicate that the AGCM does not reproduce 0 ka BP and 6 ka BP distributions that are consistent with peatland reconstructions (see Gajewski et al. 2000 for a discussion of the results)[68].

Further comparisons may be made with the CCC AGCM using results from Gajewski et al. (2000)[68] by comparing lake level anomalies derived from this study and P-E distributions produced by the AGCM. Changes in lake levels in the Sahara regions of the globe were compared with model results in V98. The main conclusion of that work was that even the strong monsoon signal inferred from both model and data sources revealed that the model fails to reproduce the significant northward extent of the higher lake levels that were then characteristic of this region. The

North American region proves to be an even more difficult region in so far as model data inter-comparisons are concerned since the signals are much weaker compared with the enhancement of the African monsoon circulation. Nevertheless, this region provides an additional opportunity for model validation. Lake level and P-E variations over Canada are plotted in Figs. 2.11a and 2.11b for the variable and fixed bucket model simulations, respectively. Lake level variations are generally predicted to be slightly lower than present to much lower than present in much of southern Canada, an indication of a more arid climate during Holocene Optimum conditions. The GCM, however, predicts changes between 6 ka BP and 0 ka BP climate that are not much greater than the natural variability of the modern simulated climate. However, a comparison of the P-E anomalies between the two different simulations does demonstrate some consistency in the results. In particular, the southwestern region of Canada is predicted to be characterized by slightly wetter conditions, while the Great Lakes-St.Lawrence region is characterized by drier conditions. Anomalies over the Hudson Bay region are also consistent between the two simulations. A comparison between the lake level data and modelled P-E demonstrates agreement in the Great Lakes-St.Lawrence region, with the variable bucket model producing a very strong reduced signal in P-E of up to 160 mm/yr. Lake level anomalies inferred to have been characteristic of the southwestern region of Canada suggest very dry conditions to have been characteristic of 6 ka BP compared to modern levels. Both model simulations, however, predicted slightly wetter conditions, with 6 ka BP anomalies of between 40 and 60 mm/yr in southern Alberta and southern B.C.

A comparison of 6 ka BP summer surface temperature anomalies can also be qualitatively performed using some of the results from Gajewski et al. (2000)[68]. Fig. 2.12 shows changes in surface temperature between 6 ka BP and present over North America in both the variable and fixed bucket model simulations. The fixed bucket model delivers an enhanced signal over the western part of North America of 1-2 °C compared with the 0.5-1.5° changes delivered by the original variable bucket simulation. Ecoclimate zones described in Gajewski et al. (2000)[68] indicate an increase in growing season temperatures of between 0.5 and 1.5°C throughout much of the southern regions of Canada. In particular, there is a much stronger signal observed in the fixed bucket simulation in the southwestern region of Canada where there was disagreement with the lake level data. Reconstructions of pollen assemblages from Gajewski et al. (2000)[68] also indicate that conditions were warmer and drier in much of Canada at 6 ka BP; however, quantitative assessments are difficult due to the uneven distribution of pollen sites.

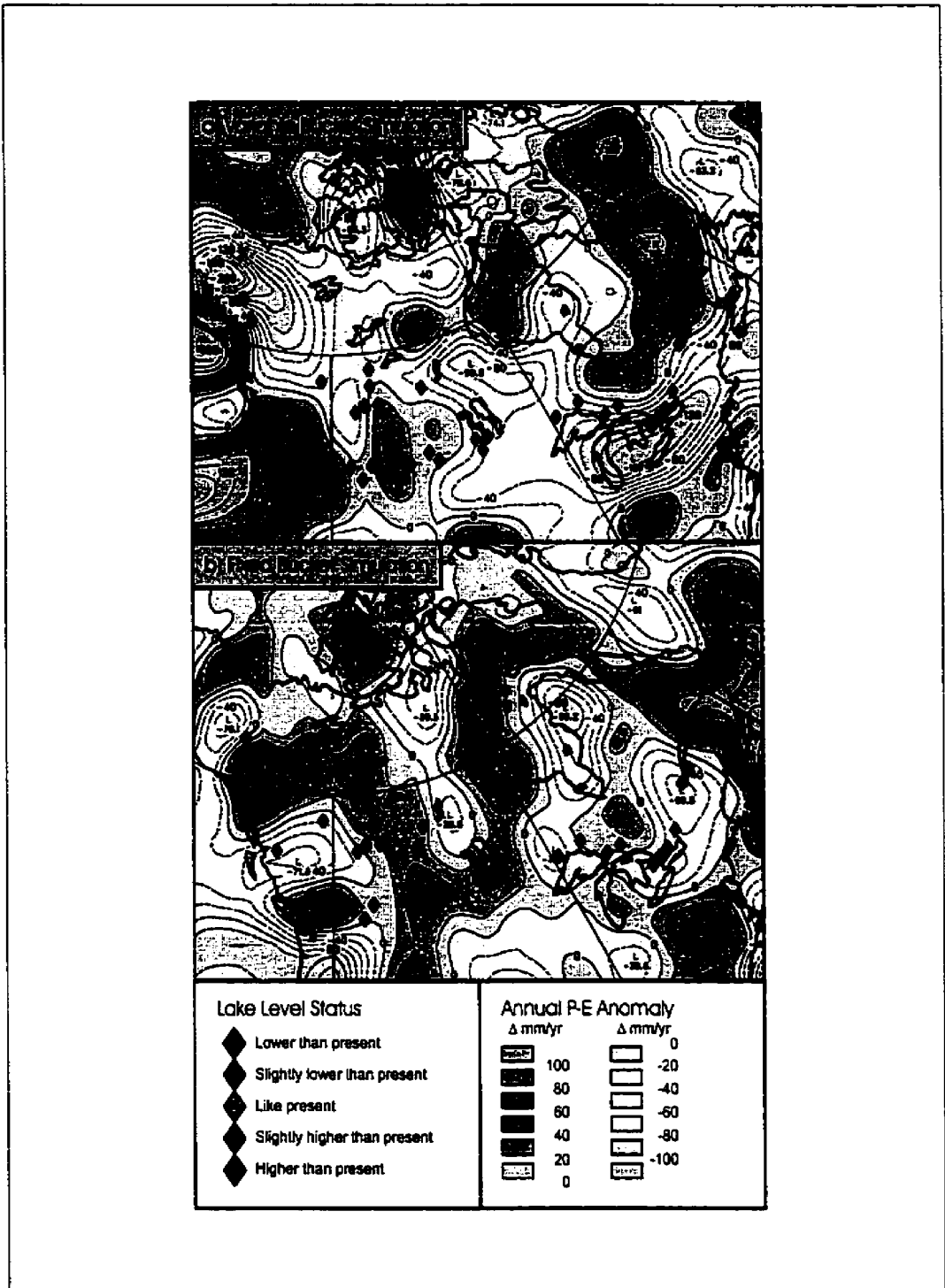


Figure 2.11: Lake level status and Precipitation minus Evaporation (P-E) anomalies at 6 KBP for the (a) variable bucket simulation (VB  $V\beta$ ) and (b) fixed bucket simulation (FB  $F\beta$ ). P-E is in  $\text{mm yr}^{-1}$  in contour intervals of  $20 \text{ mm yr}^{-1}$ .

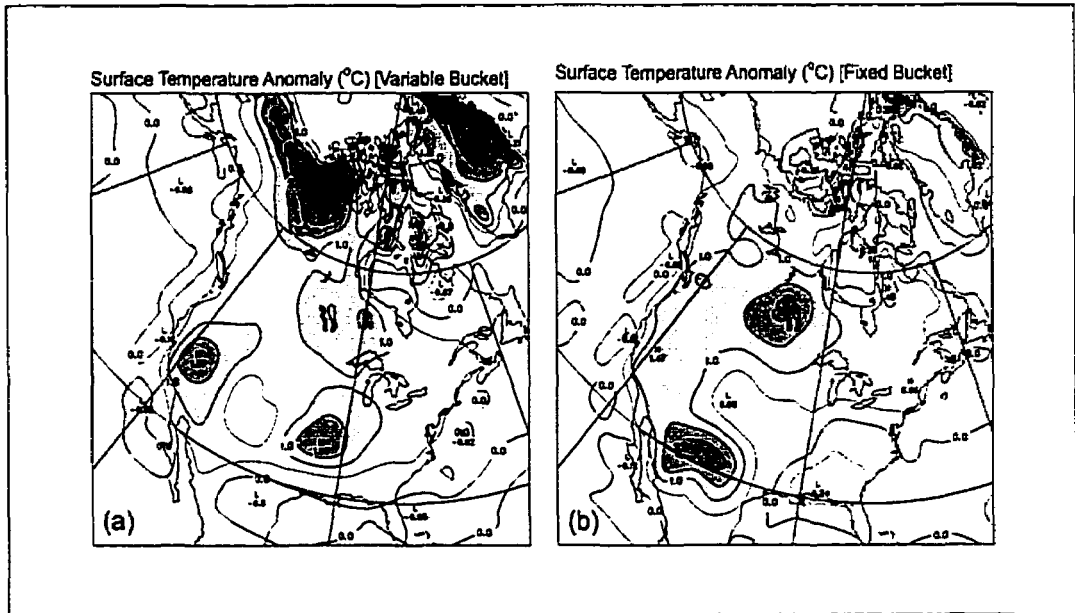


Figure 2.12: Changes in JJA surface temperature between 6 KBP and modern for (a) the variable bucket simulation (VB  $V\beta$ ) and (b) the fixed bucket simulation (FB  $F\beta$ ).

## 2.4. Discussion and Conclusions

The CCCma AGCM was modified in this investigation in order to document the changes in climate under mid-Holocene boundary conditions characteristic of those at 6 000 years before present with a modified land surface scheme. By conducting four experiments I assessed the impact on changes in both control climate and that of the orbitally forced 6 ka BP climate. The four experiments, consisting of four modern controls and four 6 ka BP simulations employed a combination of either the original variable bucket model or the modified constant 20 cm bucket and the variable evapotranspiration slope factor or the globally modified constant evapotranspiration slope factor of 0.5. The results from a pair of these simulations were then compared to results obtained from the set of models involved in the PMIP collaboration. This comparison was conducted in order to examine what differences, if any, might reduce the degree to which the CCCma GCMII is a significant outlier in the set and also to address the sensitivity of the CCCma GCMII to changes in the land surface parameterization scheme. Comparison with these other models has enabled us to investigate more thoroughly the physical mechanisms through which changes occur in reference to a spectrum of models. The PMIP collective model behaviour has also provided a framework in which to compare climate model responses in a new radiation regime, namely that characteristic of 6 ka BP.

The experiments have also provided a useful opportunity to demonstrate the ability of model-

model intercomparisons in helping to investigate the discrepancy in the mid-latitude behaviour that characterizes the CCCma GCMII model. The discrepancy was most clearly revealed in the JJA 6 ka BP zonally averaged surface temperature anomaly over land which is characterized by a cool temperature anomaly in the northern mid-latitudes at 6 ka BP whereas other models exhibit a warm anomalous behavior. This paleoclimate discrepancy would not have been nearly so apparent based solely on the simulated modern climate since the CCCma model performs very much like other models in these intercomparisons (Cess et al. 1990)[32]. The discrepancies in soil moisture in both the modern control and 6 ka BP experiment compared with the original variable bucket land surface scheme provided an indication of what I thought might explain the anomalous mid-latitude climate simulated by the CCCma model. This, however, turned out not to be so straightforward. The 4 sensitivity studies revealed that it is possible to obtain a great deal of variability in the paleoclimate response within these simulations by slightly modifying the land surface scheme. The detailed characteristics of the surface energy balance and related surface diagnostics revealed further information concerning changes in both the control climate and the simulated 6 ka BP climate under the modified land surface schemes.

In particular: 1) In the set of four modern control simulations, the reduction in moisture availability in the 20 cm bucket simulation increased the shortwave absorption and increased the net longwave at the surface in tropical and northern mid-latitudes over land. This was also complemented by a re-partitioning of the latent and sensible heat flux in the same regions of the globe. The reduction in soil moisture led to decreases in the upward latent heat flux and a compensatory increase of the energy into upward sensible heat flux. Changes in ground temperature revealed a northern mid-latitude surface that was approximately 2°C warmer. These changes in the fixed bucket modern control simulations can be attributed to cloud cover changes in mid-latitudes and in snow cover changes at polar latitudes, which in turn affect the albedo. The changes observed in the pair of fixed bucket control simulations demonstrate that it is the changes in cloud cover (i.e. the cloud effect) and surface characteristics which are the primary mediators of the surface absorbed solar radiation in the northern mid-latitudes.

2) In the set of 4 simulations of summer 6 ka BP climate, the variations of the land surface scheme through a reduction of bucket depth and a change in the evapotranspiration slope factor revealed an interesting zonally averaged behaviour over land. The surface air temperature response over land showed regions of low and high variability in the northern hemisphere. The 4 sensitivity experiments revealed 6 ka BP summer anomalies which were rather similar in the tropical and sub-tropical latitudes. At higher latitudes the variability in the response between the simulations

increased. In particular, the model paleoclimate response in the mid-latitudes and high polar arctic was investigated in detail. The observed 6 ka BP response of the zonally averaged surface temperature over land was a result of the changes in the surface energy balance components along with changes in cloud cover, albedo and snow cover at various latitudes. In particular, the climate variability in the mid-latitude 6 ka BP anomalies appeared as a result of changes in cloud cover and its influence on the radiative response at the surface. The variability in polar latitudes was apparently not influenced by cloud changes but more so by the state of the land surface in each of the 4 sensitivity experiments. The sensitivity of the land surface parameterization to changes under the 6 ka BP insolation regime becomes highly variable when the fractional snow cover and frozen soil moisture become significant north of the arctic circle.

3) The intercomparison between PMIP models demonstrated that the changes induced in the original version of the bucket model produced a CCCma mid-latitude model behaviour which was in closer agreement with the PMIP model mean, but more importantly demonstrated the large range of variability that can be obtained by modifying the land surface parameterizations. The intercomparison of the mid-latitude changes in modern ground temperature and the 6 ka BP ground temperature anomaly clearly demonstrated that the paleoclimate response is significantly determined by the temperature simulation in the modern control. The models appear to segregate evenly into two groups, one group which is warm biased and one which is cold biased in both the modern control and 6 ka BP simulations. The behaviour of the components that make up the surface energy balance over land in both the modern control and 6 ka BP climate in JJA were characterized once again by the balance and partitioning of the radiative and heat flux components as described above. The results still demonstrate, however, that while one might argue that an improvement was obtained with respect to the other models, the CCCma model still behaves anomalously. The intercomparisons indicate that the role of the total cloudiness over land is such that the PMIP 6 ka BP JJA temperature response is strongly connected to both the modern simulated, and the 6 ka BP simulated changes in cloud cover.

4) The intercomparison between the model results and paleoclimate reconstructions over Canadian regions revealed some degree of agreement in changes in surface temperature and changes in lake level status as inferred from P-E variations. However, climate reconstructions based upon lake level data indicate drier conditions in southwestern Canada, whereas model predictions are the opposite of this. In eastern Canada, there is some consistency between the lake level data and the results delivered by the model. Signals within the model are, however, rather small, making any definitive comparison difficult.

The variations in the land surface schemes do provide an indication of the significant influence that a change in boundary conditions can have on modelled climate. Thus, the need for more sophisticated land surface schemes has been made readily apparent by the analysis reported herein. The structure of the 6 ka BP JJA zonally averaged temperature anomalies seen in the 4 sensitivity studies behaved differently with respect to the PMIP averaged warming simulated at northern latitudes. The polar anomalies at the highest northern latitudes were more consistent in the reduced bucket depth simulations but remain peculiar. The intercomparison of the total cloudiness over land suggests that the next step in the sequence of analyses to which this chapter contributes must be to investigate changes in the cloud cover parameterizations within the models and the role that cloud feedbacks play in the determination of the equilibrium land surface temperature. The current investigation has therefore provided a natural basis on which to further investigate such behaviour, not only of the CCCma GCMII, but also of the entire suite of PMIP models.

---

## CHAPTER 3

---

# Climate Simulation of the Last Glacial Maximum: Global Water Balance and Atmospheric Water Vapour Transport

### 3.1. Introduction

As discussed in the introduction of this thesis, the origins of the 100 ka cycle of continental ice volume variability must be associated with non-linear processes that arise internally to the climate system itself. The earliest attempts to identify the precise nature of the required non-linear effects were based upon rather simple models (Hyde and Peltier 1985; Imbrie et al. 1993; Lindzen and Pan 1994)[95][100][130]. More recently, considerably more elaborate models consisting of global Energy Balance Models (EBMs) coupled to explicit ice-dynamics models, or ice-sheet models (ISMs), have been shown to be successful at reproducing the complete cycle of glaciation and deglaciation from inception through to maximum glaciation, glacial collapse, and continuing into the modern Holocene climate state. These climate models have employed the ICE-4G model of Peltier (1994)[170] as a target for the purpose of verifying their predictions (Tarasov and Peltier 1997a, and 1999)[216][218]. Problems with these reduced climate models continue to exist in fully explaining the fast terminations that mark the end of each glacial period which, although they do occur in the models, do not possess the detailed space-time characteristics that surface geomorphological constraints suggest. Extra processes, in addition to the main feedbacks such as ice-albedo feedback, vertical lapse rate effects, and isostatic rebound, must apparently be invoked to obtain more precise agreement with the observations. An overview and detailed discussion of plausible additional feedbacks is provided in Tarasov and Peltier (1997a, 1997b, and 1999)[216][217][218].

In the most recent models of the ice-age cycle, attempts have been made to parameterize the influence of changes in atmospheric state, including the (critical) supply of moisture for the ice-sheets by employing a global energy balance model to infer the nature of the time-dependant surface temperature perturbation to a modern observational climatology that is induced by ice-sheet growth (Tarasov and Peltier 1997b, 1999)[217][218]. There have also been efforts to incorporate AGCM derived climate "snap shots" of the modern and Last Glacial Maximum (LGM) time periods into

models of the ice-age cycle that include full representations of the accumulation and flow of glacial ice. In the latter work, the variation of climate state through the glacial cycle has been determined by interpolating between the LGM and Holocene time slices using the GRIP ice core record of  $\delta^{18}\text{O}$  variability to fix the characteristics of successive epochs (Marshall et al. 2000)[142]. The extent to which the major northern hemisphere ice-sheets were in equilibrium with LGM climate has also been investigated using a thermo-mechanical ice-sheet model forced with AGCM simulated climate using the LMD model (Ramstein and Joussaume 1995; Fabre et al. 1998)[185][57]. These studies demonstrate the mass balance of the LGM ice-sheets to be very sensitive to LGM simulated summer surface temperature and therefore highly model dependant. On the basis of analyses of this kind, it therefore seems clear that the state of the atmosphere plays a critical role throughout the glacial cycle, suggesting that much more detailed analyses of the time-dependant coupling between the atmosphere and the ice-sheets are required.

There have, of course, already been numerous analyses directed towards investigation of the role that atmospheric mechanisms play in the maintenance of the ice-sheets at LGM. Manabe and Broccoli (1985)[141], Kutzbach and Wright (1985)[117], and Kutzbach and Guetter (1986)[118], in the first series of papers directed towards understanding mid-latitude climate at LGM, demonstrated that the presence of CLMAP (CLIMAP project members 1981)[38] project inferred ice-sheets in the northern hemisphere acted so as to split the mid-latitude jet stream into two air streams that flowed to the north and south of the Laurentide ice complex. More recent analyses have tended to suggest that this phenomenon is not as pronounced in LGM simulations performed using the Peltier (1994)[170] ICE-4G LGM topography (Ramstein and Joussaume 1995)[185]. Rind (1986)[190] employed a relatively low resolution AGCM to perform a detailed investigation of the changes in the dynamical state of the atmosphere that occur between warm and cold climates. On the basis of these analyses, he suggested that the zonally averaged dynamics showed little change between climate extremes with the spatial arrangement and strength of the Hadley cell and atmospheric energy transports in particular remaining much the same. The sensitivity of the location of northern hemisphere storm tracks, in particular over the Atlantic Ocean, in response to changes in ice-sheet size and configuration, have been investigated by Shinn and Barron (1989)[207] and Felzer et al. (1996)[60].

Questions invariably exist, of course, as to how sensitive such results are to the horizontal resolution of the model employed to obtain them. Many analyses have in fact been performed to specifically investigate climate sensitivity to horizontal resolution, the main finding being that large-scale climate features remain relatively constant when a spectral AGCM is run at a horizontal resolution

beyond T42. Recently, Boer and Denis (1997)[22], for example, used the CCCma AGCM at resolutions ranging from T20 to T96 to examine the rate of dynamical convergence in the CCCma model and discovered that primary climatological characteristics remained the same beyond T32. Held and Phillips (1993)[83] also focused on the issue of the sensitivity to resolution, particularly concerning the impact of meridional resolution on eddy momentum fluxes. Their findings, as well as those of others (Boville 1991)[25] demonstrate that mid-latitude eddies are, in fact, sensitive to horizontal resolution even beyond T42. Hall et al. (1996)[77] recently conducted a simulation of LGM climate at T42 resolution specifically to improve upon the simulation of mid-latitude depressions and to more fully understand the role of the atmospheric circulation in the maintenance of the LGM ice-sheets. Their findings differ significantly from those obtained on the basis of lower resolution studies performed in the past and clearly demonstrate the importance of resolution in the accurate simulation of the planetary waves (both stationary and transient) and storm tracks in controlling the LGM hydrological cycle.

In this chapter I will describe results from two AGCM simulations of Last Glacial Maximum climate. One simulation which uses the CCCma GCMII model coupled to mixed-layer ocean and sea ice modules in order to compute SSTs and sea ice and one in which SSTs are prescribed using the CLIMAP SST data set (CLIMAP project members 1981)[38]. Comparisons between these two integrations will be made only when looking at particular regional differences in climate between the two experiments in order to resolve differences which result from changes in lower boundary forcing. When global characteristics are very much the same between the two simulations (e.g., mass balance and water vapour transport), the computed SST LGM experiment will be referred to.

To begin this discussion, I will briefly compare LGM climate predictions made with the CCCma AGCM in computed SST mode with various climate proxy data, work that has been conducted as part of a PMIP (Paleoclimate Model Intercomparison Project) intercomparison study (Joussaume and Taylor 1995)[107]. I will then go on to compare LGM surface climate state predictions based upon an ice-sheet coupled energy balance model simulation of the complete ice-age cycle (Tarasov and Peltier 1999)[218] and the simulation of LGM climate with computed SSTs. On the basis of ongoing efforts to simulate the glacial cycle using thermo-mechanical ice-sheet models, it is clear that a detailed simulation of mass balance is a crucial aspect of the coupled system (for example, in understanding the details of the dynamical processes which thereafter lead to total deglaciation of much of the surface following LGM at 21 000 years before present). This chapter will therefore focus upon the changes in the LGM hydrological cycle that are simulated with the version of the AGCM which computes SSTs, the results from which will allow us to provide an assessment of the LGM

mass balance over the Laurentide complex. Next, changes in the LGM SST and sea ice distribution and the effect that this has on atmospheric circulation will be investigated by comparing the results obtained from the two AGCM simulations of LGM. The vital role that the mid-latitude eddies play in the maintenance of the ice-sheet has been a subject of considerable previous analysis and will be discussed further herein. In the final part of the results section, I will discuss the modification to the behaviour of these mid-latitude depressions that occurs in response to the application of LGM boundary conditions based upon the version of the AGCM in which SSTs are computed.

In the following Section 3.2, I provide a description of the ISM/EBM model that is to be intercompared with the AGCM in this study. This is followed in Section 3.3 by a discussion of the design of the LGM numerical experiments that are to be performed. Results of these analyses are discussed in Section 3.4, following which, in Section 3.5, I offer a brief summary of the conclusions suggested on the basis of this work.

## 3.2. Model Descriptions

As previously mentioned, the intention in this chapter is to intercompare the results that have been obtained for LGM climate on the basis of analyses performed with two radically different models of the climate system. These models, one a fully articulated modern atmospheric general circulation model that is described in the introduction to this thesis (or see Appendix B and C) and the other a highly parameterized model that is designed to enable very long time scale integrations to be performed is described in the following subsection.

### 3.2.1. Energy Balance-ice-sheet model

A thermo-mechanical ice-sheet model, which is orbitally forced through an energy balance model of the atmosphere, has been extensively developed for use in the simulation of late Pleistocene glacial/inter-glacial ice volume fluctuations. This model, which is described in detail in Tarasov and Peltier (1997a, 1997b, 1999)[216][217][218] is a numerical outgrowth of early work by Deblonde and Peltier (1991, and 1993)[47][48] and is based upon now conventional thermo-mechanical treatments of the ice dynamics (Huybrechts 1990a, 1990b)[92][93]. The model solves mass, momentum, and energy balance equations in a spherical coordinate system to simulate the three-dimensional velocity components and the temperature profile within the ice-sheet (see also Janssen 1977 and Mahaffy 1976)[102][136]. The model employs a finite-difference approximation on a spherical grid with dimensions of  $1^\circ$  by  $0.5^\circ$  in longitude and latitude, respectively. Time steps of 3.125-25.0 years, and

12.5-50.0 years, are employed for the implicit ice dynamic and thermodynamic solutions, respectively.

The ice-sheet model ice thickness is determined by the time evolution of the balance between the vertically averaged divergence of the horizontal mass flux and the ice-sheet mass balance (accumulation minus ablation). The vertically integrated momentum equations are reduced using Glen's flow law (or an alternative rheology discussed in Peltier 1998a)[172] to express the Stokes flow equations as local functions of ice thickness and topography. The three-dimensional temperature field is derived from the balance of internal energy within the ice-sheet, taking into account vertical conduction of heat as well as the full three-dimensional advection of heat within the ice-sheet. The energy balance equation also contains a term describing the strain heating due to the internal deformation of ice as well as a source term representing heating due to basal sliding (see Marshall et al. 2000, for a detailed discussion)[142]. The treatment of ice sheet evolution also requires a computation of the ice-bed isostatic adjustment under transient loading of the crust. The isostatic adjustment process is parameterized so as to enable the model to accurately fit the variations of relative sea level which occurred following the last deglaciation event of the current ice age and is assumed to respond with a damping factor (e-folding time) of 4 ka. This is a timescale that is near the average of the isostatic adjustment times characteristic of the postglacial rebound of the crust in Hudson Bay and the Gulf of Bothnia (see Peltier 1998a for a detailed discussion of these isostatic adjustment constraints).

The ice-sheet model is asynchronously coupled to an EBM which estimates surface temperature fields based upon changes in orbital configuration, surface albedo, ice-sheet topography, surface heat capacity, CO<sub>2</sub> concentration, and a parameterization of the flux of heat from the surface of the North Atlantic ocean to the atmosphere. During a specific "time slice", the EBM-derived surface temperature field, expressed as a difference from modern climatology, together with the assumption of constant atmospheric lapse rate, is employed to drive the ice-sheet model. The EBM is solved every 500 years for a new (global) equilibrium annual cycle based upon the assumption that ice-sheet and orbital boundary conditions evolve much more slowly than does the atmosphere. The precipitation field is determined in this model by simply modulating the amplitude of the modern climatological field such that as temperature falls so does the water vapour content of the atmosphere. The reasonableness of this assumption is something that I will illustrate through the analyses discussed herein.

### 3.3. Experimental Design

We will present results derived from a paleoclimate AGCM experiment that calculates both SSTs and sea ice using the mixed-layer ocean and sea ice modules described in McFarlane et al. (1992)[146] and from a simulation in which SSTs are held fixed. The present day fixed SST simulation employs SSTs from Alexander and Mobley (1976)[3], while that for LGM, in which SSTs are fixed, imposes CLIMAP SSTs (CLIMAP, 1981)[38]. The AGCM experiments then consist of two modern controls and two paleoclimate simulations of LGM. LGM boundary conditions and an inferred LGM climatology from an ice age cycle, simulated with the ISM/EBM from Tarasov and Peltier (1997b)[217], will then be employed for comparison with the LGM "snap-shot" climate modelled with the AGCM in which SSTs are computed. The present day AGCM control simulation has the atmospheric CO<sub>2</sub> concentration set to a "pre-industrial" level of 280 ppmv, while the control simulation in which SSTs are fixed is set to 345 ppmv. The AGCM simulation of LGM conditions prescribes a CO<sub>2</sub> concentration that is fixed to that of the minimum glacial level of approximately 200 ppmv, while in the ISM/EBM the CO<sub>2</sub> history from the Eemian interglacial at 125 000 years BP to the present day is assumed to be known based on gas concentrations derived from the Vostok ice-core record (Barnola et al. 1987; Jouzel et al. 1987)[11][109]. At LGM the Vostok record is consistent with an atmospheric concentration of 200 ppmv.

According to ice-sheet thickness reconstructions based upon post-glacial relative sea level histories from regions that were ice-covered at LGM (vis. the ICE-4G model of Peltier 1994, and 1996)[170][171], the Laurentide ice-sheet was fully extended southward to North American mid-latitudes at that time while the Fennoscandian ice-sheet covered much of Northern Europe including the Barents and Kara Seas. These ice-sheets, the first centred over the Hudson Bay lowlands and the second centred over the Gulf of Bothnia, both reached maximum elevations above LGM sea level of approximately 2500m. At that time eustatic sea level was approximately 120 m lower than at present, implying that significantly less ice covered the continents at that time than had been inferred in the context of CLIMAP whose minimum and maximum reconstructions corresponded to sea level lowering of 127m and 163m, respectively. This large drop in sea level exposed large areas of continental shelf which, for the purpose of the LGM climate simulations to be described herein, had to be incorporated into a new AGCM land-sea mask (see Peltier 1998a for a discussion of the geophysical theory that has been developed to infer the glacial to interglacial variations of the land-sea distribution).

Vegetation patterns and soil types together with all other internal boundary conditions have

also been fixed to modern according to PMIP programme specifications (Joussaume and Taylor 1995)[107]. In the new areas of exposed continental shelf resulting from the lower sea level at LGM, a soil of medium type (Wilson and Henderson-Sellers 1985)[243] was specified. The drag coefficients over the newly imposed Laurentide and Fennoscandian ice-sheets were set to the same value as that which is employed over the Greenland and Antarctic ice-sheets in the simulation of present day climate. The envelope orography variance which is used in conjunction with the gravity wave drag parameterizations in the AGCM is set to zero over the LGM ice-sheets, for reasons of simplicity and on the basis of the fact that the surfaces of these ice-sheet are expected to have been rather smooth. The differences in the insolation received at the top of the atmosphere between 21 ka BP and present are rather minor and are therefore not expected to exert any significant influence on LGM climate (e.g., see Hewitt and Mitchell 1997, for a detailed discussion)[85]. The orbital variations are much the same as modern (Fig. 1.4) and result in a negative insolation anomaly of 1% in northern hemisphere summer and a positive anomaly of approximately 0.5% in northern hemisphere winter. For a review of issues surrounding changes in insolation see Vettoretti et al. (1998)[229] and references therein.

In the AGCM mixed-layer ocean experiment for LGM, the globally and annually averaged surface temperature was employed in these analyses to investigate the spin up to equilibrium. In the mixed-layer ocean analysis, the modern pre-industrial control experiment was initially spun up for 50 annual cycles with the last 10 annual cycles being averaged to produce the modern climatology (see Vettoretti et al. 1998)[229]. The LGM experiment, which was initiated with surface temperatures interpolated from CLIMAP SSTs, was also found to adjust to equilibrium within 50 annual cycles (Fig. 3.1). The e-folding time in the northern hemisphere was found to be approximately 5 years while that of the global spinup was approximately 11 years. The last 10 years of the LGM mixed-layer simulation was used to derive the 10 year averaged climatology for this time period. Both the modern day fixed SST control and the CLIMAP fixed SST LGM experiment were run for 12 years with the first two years being discarded as spinup and the last 10 years averaged to define the climatology.

In the ISM/EBM, the EBM is employed in a perturbative mode whereby the surface temperature perturbations are computed relative to a high resolution present day observational climatology (ds090.0 NMC/NCAR global reanalysis project dataset), the methodology of which is described in Tarasov and Peltier (1999)[218]. The temperature field produced by the EBM at the point of maximum ice volume in the ISM glacial cycle simulation, taken as LGM, is used as comparison with the results obtained from the AGCM. The ice-sheet topography and precipitation at LGM will also be compared with the AGCM topography and the AGCM precipitation field over the Laurentide

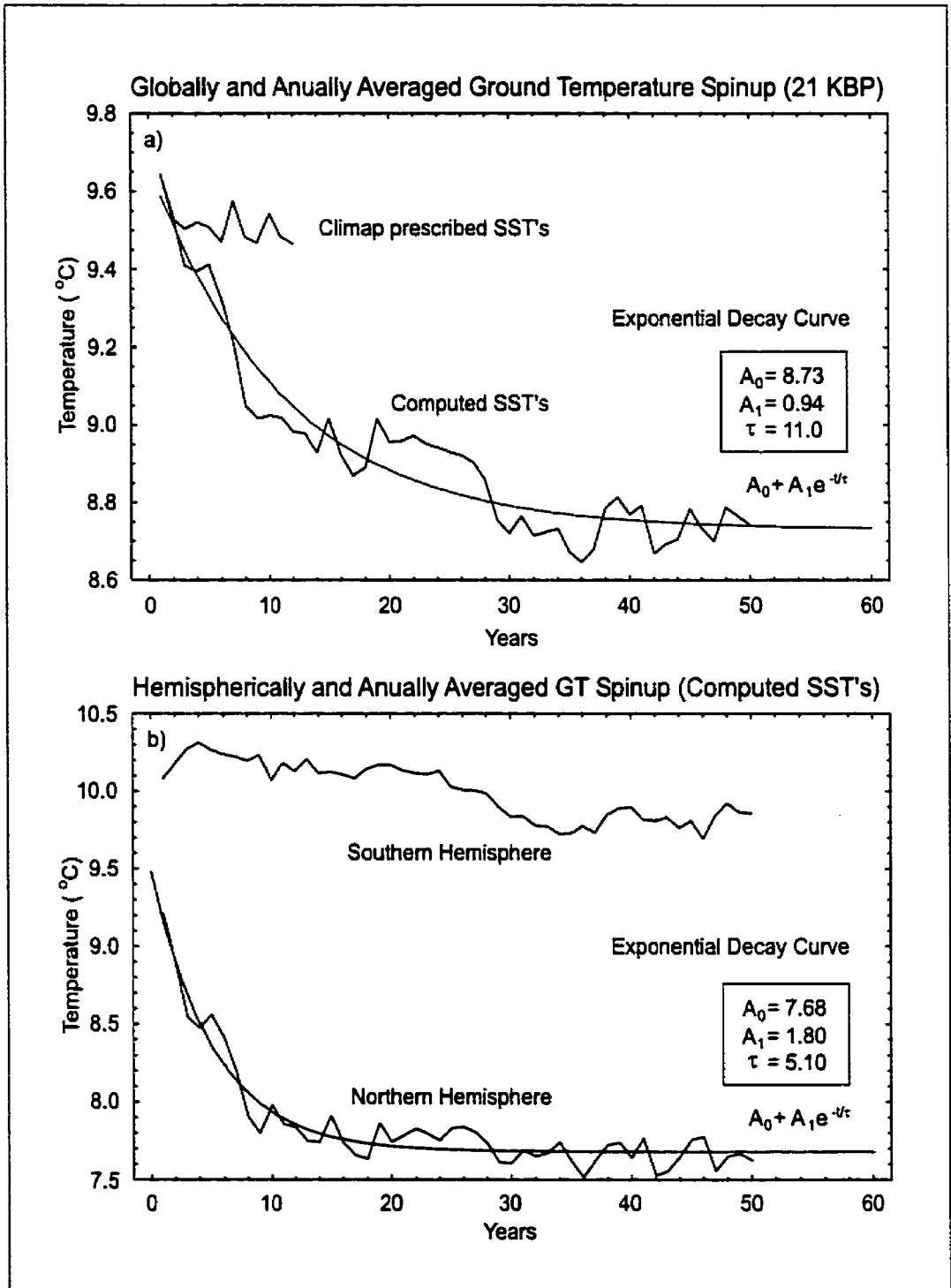


Figure 3.1: (a) Globally and annually averaged LGM ground temperature (°C) vs. model time (years) for the CLIMAP prescribed SST and computed SST simulations. (b) northern and southern hemisphere annually averaged ground temperature for the LGM computed SST simulation. An exponential fit to the decay curves for global and northern hemisphere temperatures are displayed for the computed SST experiments.

ice-sheet. The AGCM topography is the spectrally decomposed T32 topography diagnosed from the ICE-4G reconstruction. The ISM/EBM model computes the precipitation based on a similar perturbative method as for the temperature field. Precipitation is reduced by a factor of 1.03 for each degree by which the sea-level temperature at a grid point is decreased from its present day value. This provides reasonable correspondence with expectations based upon the exponential behaviour embodied in the Clausius-Clapyron equation used to model the dependence of atmospheric moisture content on temperature.

### 3.4. Results

In this section I will discuss the main results obtained in this initial analysis of LGM conditions in four parts. To begin, I will briefly discuss results obtained on the basis of proxy data reconstructions of both oceanic and terrestrial conditions at LGM and the extent to which these geological inferences compare with the AGCM simulation of LGM climate. In the second part I will focus the discussions upon some of the differences revealed between the ISM/EBM predicted climate and the climate delivered by the AGCM simulation. In the third part I will investigate certain characteristics of the global AGCM hydrological cycle at LGM and the corresponding changes simulated over the Laurentide ice-sheet. In the final results subsection the focus will be upon the dynamical aspects of the general circulation as simulated by the AGCM which are fundamental to the transport of water vapour in the atmosphere.

#### 3.4.1. Model-Model Model-Data comparison at LGM

Our current understanding of glacial paleoclimate suggest that tropical climate was cooler and more variable during LGM. The tropical ocean, especially in areas such as the Western Pacific, provide major sources of heat and water vapour to the atmosphere and are fundamental factors in dictating the global response to climate change. Various proxy reconstructions of SSTs at last glacial maximum have been used in an attempt to infer the state of this vital component of the climate system. The major sources of SST reconstructions are derived from oxygen isotope studies of planktonic and benthic foraminifera (CLIMAP 1981; Broecker 1986)[38][30], Sr/Ca ratios in porite corals (Guilderson et al. 1994; McCulloch et al. 1999)[76][144], and by analyzing alkenones preserved in high-resolution marine sediment cores (Ohkouchi et al. 1994; Bard et al. 1997)[164][10]. However, there still remain large discrepancies between these various types of reconstructions. The current consensus is that Sr/Ca ratios in porite corals, such as those extracted from Barbados (McCulloch

et al. 1999)[144], provide the best basis on which to infer tropical SSTs at LGM. Alkenone paleothermometry and planktonic microfossil assemblage methods may be affected by changes in the coupling between surface and thermocline temperatures (Fairbanks and Wiebe 1980)[58]; however, alkenone paleothermometry which is conducted on coccolithiphorid cultures is thought to be better constrained. The algae, used in alkenone studies, are constrained to the upper 100m of the surface ocean (Ohkouchi et al. 1994)[164] and the analysis of  $U_{37}$  in alkenones to infer SSTs are well constrained at temperatures above 24 °C (Bard et al. 1997)[10]. Coral records imply that tropical SSTs were up to 6 °C colder at LGM, which is consistent with those changes inferred from terrestrial records inferred from tropical snow line depressions (Webster and Stretten 1978)[240], and ice cores from tropical mountain ranges (Thompson et al. 1998)[222]. In Barbados, SST changes based on coral reconstructions (Guilderson et al. 1994)[76] are 3 to 4 °C colder than CLIMAP SSTs which show relatively little cooling across tropical oceans, and even indicate warmer conditions that present in the tropical pacific at LGM.

Modelling studies of LGM tropical climate (Pinot et al. 1999)[179] have recently been conducted in the context of the PMIP project (Joussaume and Taylor 1995)[107]. This study investigated 17 simulations of LGM climate, including the AGCM in this thesis, under the same prescribed LGM boundary forcing, using both prescribed (CLIMAP 1981)[38] and computed SSTs by coupling the AGCMs with a mixed layer thermodynamic slab ocean. Following Pinot et al. (1999)[179], Fig. 3.2 depicts the changes in tropical land and ocean temperatures between 30 °S and 30 °N for present and LGM climate. Simulations which compute SSTs show tropical terrestrial cooling which is about 1.3 times that of the tropical SST decrease (Fig 2a) as noted by Pinot et al. (1999)[179]. Simulations which compute SSTs consistently show decreases in tropical SSTs from those changes reconstructed from CLIMAP, with only 5 of the models (CCC2, UKMO, CCM1, MRI2, and CLIMBER2) showing reasonable agreement with cooling reconstructed from terrestrial proxy data. The CCCma model which is used in this study (CCC2), which is one of the 5 models which agrees with the proxy data, delivers one of the largest coolings over the tropical oceans (3.4 °C) which is in agreement with tropical SST reconstructions derived from corals (Guilderson et al. 1994)[76]. However, the model delivers a uniform cooling throughout the tropical oceans which is thought to be unrealistic based upon the larger spatial variability of the proxy reconstructed tropical data (Pinot et al. 1999)[179].

The anomalies displayed in Fig. 3.2a are slightly sensitive to model resolution as well as in the treatment of the land-sea mask. Some models use a land-sea mask which has fractional land cover at some grid cells (grid cells which have been omitted in this intercomparison) and may affect the anomalies displayed in Fig. 3.2 (GEN2, MRI2, and CLIMBER2). The lower resolution models are

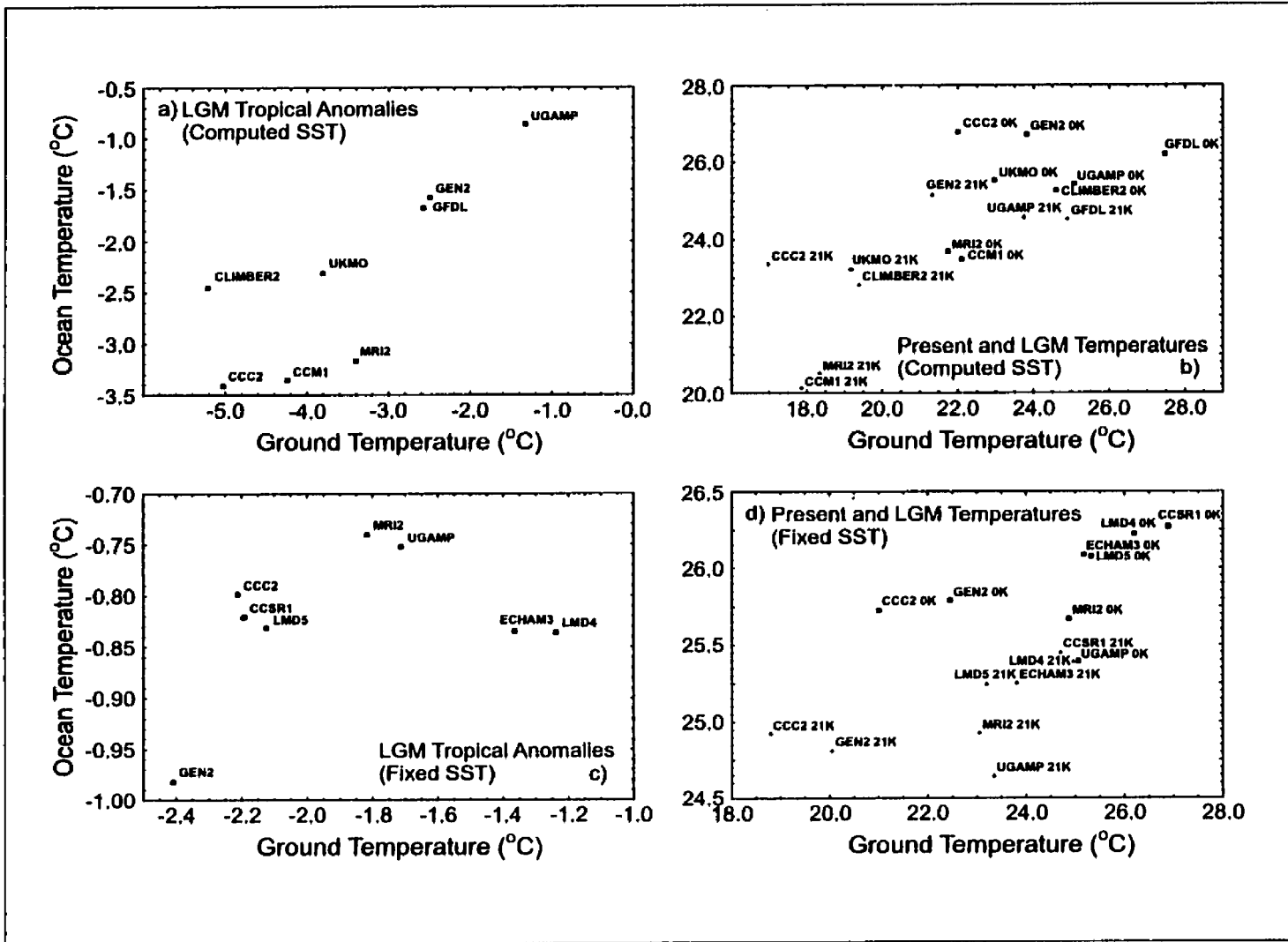


Figure 3.2: PMIP differences in tropical ground temperature vs. tropical ocean SSTs between 30°S and 30°N. (a) LGM - Modern tropical land and ocean differences in the computed SST PMIP experiments. (b) Present and LGM tropical temperatures for the computed SST experiments. (c) LGM - Modern tropical land and ocean differences in the CLIMAP fixed SST PMIP experiments. (d) Present and LGM tropical temperatures for the fixed SST experiments.

also very sensitive to area averaging; for example, the CLIMBER2 model has data displayed at a resolution of approximately  $10^\circ$  in latitude  $\times$   $50^\circ$  in longitude. It is also interesting to note that some of the models which have a cold modern tropical climate in the computed SST experiment (MRI2, and CCM1) as compared with the rest of the PMIP models display LGM anomalies which are also large (Fig. 3.2b). The model used in the present study (CCC2) and the UKMO model have tropical climates which are similar to those of the other models in the PMIP intercomparison and also display the large tropical coolings which are in agreement with the terrestrial and oceanic proxy data.

The LGM tropical ocean anomalies in the CLIMAP fixed SST experiments (Fig. 3.2c) are rather close as would be expected ( $-0.8^\circ\text{C}$ ). The differences are the result of a combination of the sea level lowering by 120 m at LGM, which influences the land sea mask at each epoch in each model, and the individual model resolution. The LGM anomalies of terrestrial temperature in the fixed SST experiments range from about  $-2.5$  to  $-1.0^\circ\text{C}$ , and are much less than the changes observed in the computed SST experiments which range from about  $-5.0$  to  $-1.0^\circ\text{C}$ . Of the models that have been run with both fixed and computed SSTs (CCC2, MRI2, GEN2, and UGAMP) the CCC2 model demonstrates the largest terrestrial cooling in both experiments. In the fixed SST experiments, two of the models which display the largest terrestrial tropical cooling, CCC2 and GEN2, have tropical control climates which are rather cool compared with the other models in the PMIP intercomparison (Fig. 3.2d). Nevertheless, these results obtained from this model-data intercomparison lend credence to the results which will be discussed in the following subsections.

### 3.4.2. Simulated AGCM and ISM/EBM climatology at LGM

In considering the minimum requirements for accurate long timescale climate simulation it is important to recognize the profound separation of the time scales on which atmospheric dynamics and ice-sheet dynamics evolve, atmospheric processes clearly being "faster" and glaciological processes "slower". An AGCM may therefore be employed to define "snap-shots" of climate state on the basis of approximately a decade of integration, a period during which the ice-sheets would evolve imperceptibly. The boundary conditions required as basis for such integrations may be obtained on the basis of inferences from the geological record. Climate predictions based upon such AGCM simulations are also compared with proxy climate data to determine whether the model is able to acceptably recreate such inferences of past climate state (e.g., Webb et al. 1997; Bush and Philander 1998; Weaver et al. 1998; Pinot et al. 1999)[239][31][238][179]. ISM based simulations, on the other

hand, are intended to describe the evolution of northern hemisphere ice-sheets on time scales of tens of thousands of years, scales that are much larger than those over which one is able to extend on AGCM simulation. The ISM simulations which include the complex web of feedbacks that act within the atmosphere/cryosphere/lithosphere system are themselves intended for comparison with histories of ice-sheet volume variations derived from long-time scale records such as those provided by ice cores and deep sea sedimentary cores from which total global ice volume may be inferred (e.g., Imbrie et al. 1984)[99] and relative sea-level histories that may be employed to constrain continental ice volume variations since the last glacial maximum (Peltier 1994, and 1996)[170][171]. One might eventually envision incorporating all of the slow time-scale ice-sheet dynamics into a state of the art atmosphere-ocean-cryosphere GCM. However, even given the extraordinary computational power available on modern supercomputers, integrations as comprehensive as this are as yet not possible.

Modern ice-sheet coupled climate models now incorporate more advanced parameterizations of the atmosphere than previously, a component of the climate system which is clearly vital to the accurate determination of the accumulation and ablation processes which drive the evolution of the ice-sheets on long time scales. The global Energy Balance Model (EBM) that is employed in the model of Tarasov and Peltier (1997a, 1997b, 1999)[216][217][218], which contains realistic geography, can be compared directly with fields obtained from an AGCM simulation of LGM climate in order to assess the quality of the parameterization schemes employed in the ISM/EBM.

The 2-D geographic distribution of ISM predicted ice-sheet topography is usefully validated against geophysical reconstructions of this field. A first step in the comparison of the model of LGM climate state to that predicted by the ISM/EBM will therefore involve investigation of differences in the T32 spectrally decomposed Laurentide ice-sheet topography derived from the raw ICE-4G data itself. This smoothing process reduces the original 1° by 1° ICE-4G resolution to the 3.5° by 3.5° resolution that is characteristic of the AGCM. Figs. 3.3a and 3.3b compare these two respective realizations of the ICE-4G topography and thereby illustrate the extent of the spectral smoothing that occurs when the original ICE-4G structure is inserted into the T32 CCCma spectral AGCM. The saddle feature centred over the Hudson Bay region is an artifact of the neglect of the influence of "implicit ice" (Peltier 1998b)[173] in the geophysical reconstruction of topography. The Cordilleran ice-sheet in Western Canada is also smoothed substantially and is lower than the ICE-4G height by 300 meters. The ice-sheet distribution and extent at LGM in the ISM integration is characterized by features which are significantly different from those characteristic of the ICE-4G model (Fig. 3.3c). Specifically, in the ISM simulation, the ice height maxima are located directly over the modern Hudson Bay region and the Western Cordillera. As already mentioned, when

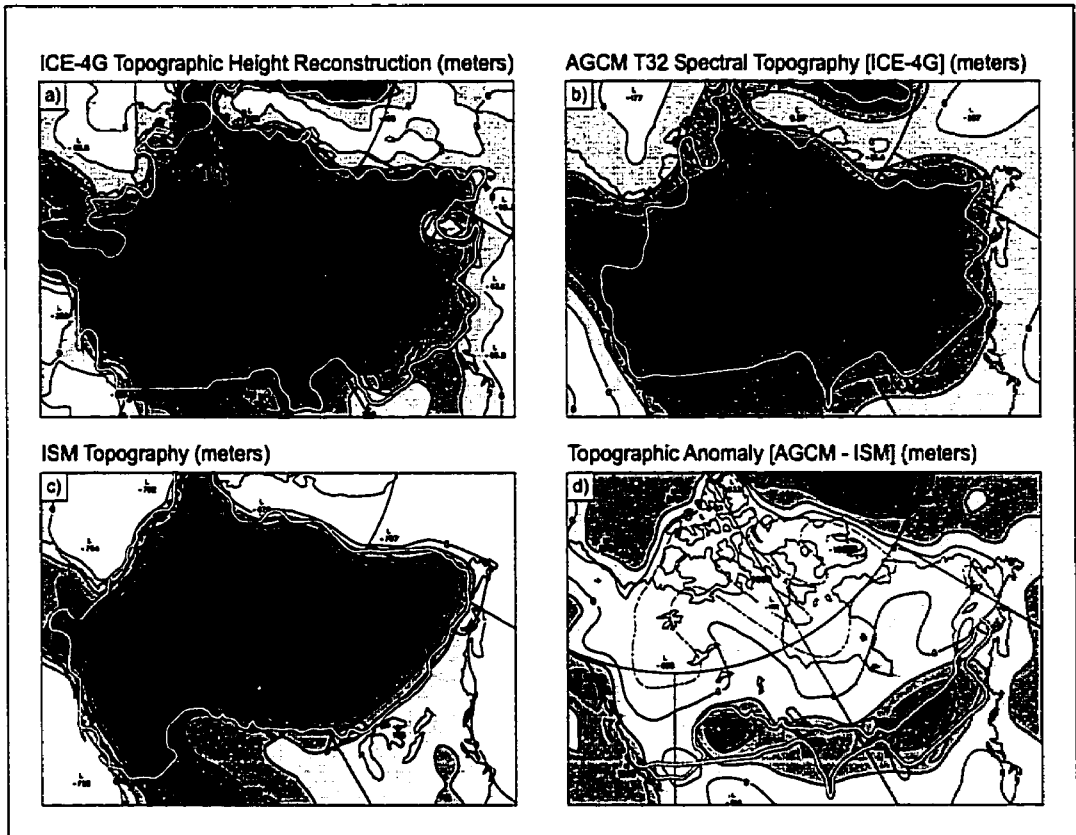


Figure 3.3: Last Glacial Maximum topography. (a) ICE-4G hi-resolution data set. (b) AGCM T32 spectrally smoothed ICE-4G LGM topography. (c) ISM topography at maximum ice volume. (d) AGCM minus ISM LGM topographic anomaly. The ice-sheet margin in Figs. (a),(b) and (c) is displayed by a white line along with the southern ice margin extent of Figs. (b) and (c) in (d).

the influence of "implicit ice" is included in the geophysical reconstruction of topography then the saddle in the inferred topography is in fact removed. A shortcoming of the ISM simulation, on the other hand, is the lack of the ice-sheet extension into South Eastern Canada and the United States which is known to have existed on the basis of geomorphological considerations (e.g., Vincent and Prest 1987; Clark 1996)[233][37]. Inspection of the difference between the AGCM (geophysically inferred) topography and the ISM predicted topography for LGM reveals a difference of up to 1500 meters over the Great Lakes region (Fig. 3.3d). In fact, there is a positive height anomaly along much of the southern portion of the geophysically inferred ICE-4G Laurentide ice-sheet, coupled with a negative anomaly over much of Northern Canada. The ICE-4G model, which fits the surface geomorphological inferences of Vincent and Prest (1987)[233] is both thinner in the north than the ISM/EBM prediction and extends to significantly lower latitudes as indicated by the extent of the ice margins plotted in Fig. 3.3d.

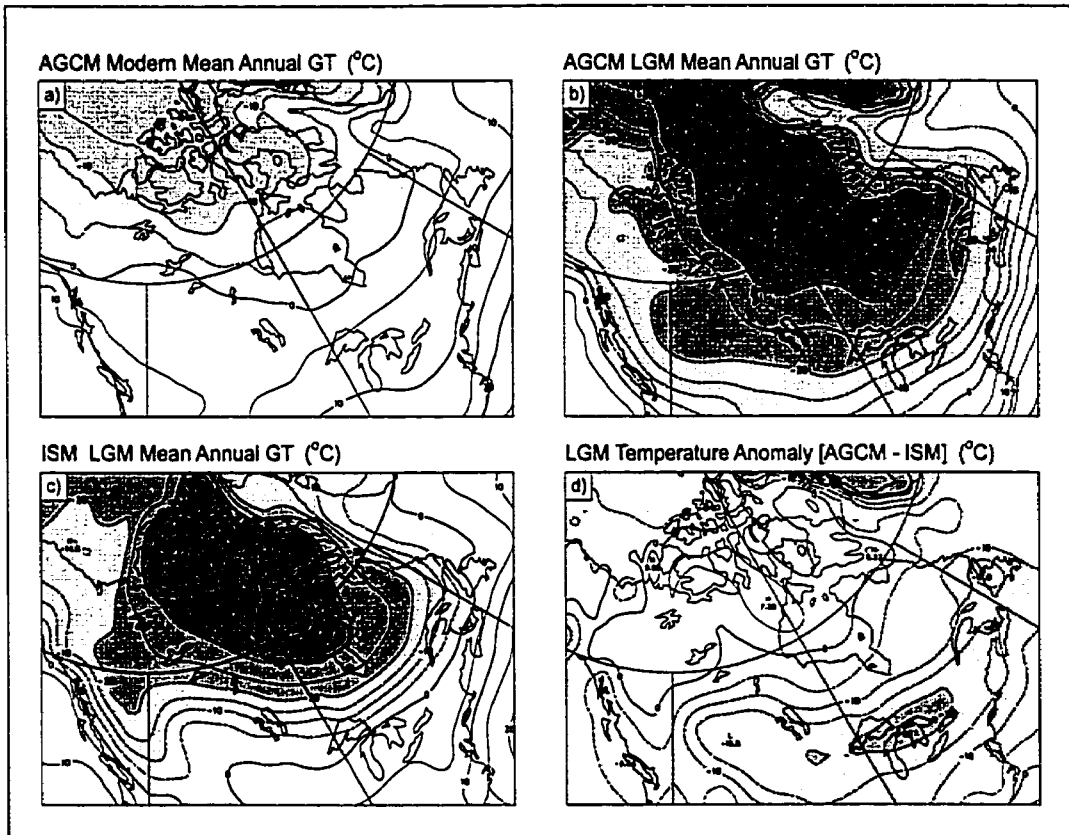


Figure 3.4: Annual mean ground temperature reconstructions ( $^{\circ}\text{C}$ ). Contour and shading intervals are 5 and  $10^{\circ}\text{C}$ , respectively. (a) Modern AGCM simulated climate with computed SSTs. (b) LGM AGCM simulated climate with computed SSTs. (c) ISM ground temperature at maximum ice extent. (d) AGCM minus ISM LGM ground temperature anomaly.

The surface temperature difference between the ISM/EBM prediction for LGM and that from the AGCM is illustrated in Fig. 3.4. The annual mean modern climatology produced by the AGCM is displayed in Fig. 3.4a. The presence of the Laurentide ice-sheet is clearly seen in Fig. 3.4b which displays the simulated AGCM ground temperatures over the ice-sheet at LGM. Temperatures are more than  $30^{\circ}\text{C}$  lower in the central portions of the ice-sheet than in the same geographical region at present. The LGM temperature distribution produced by the ISM/EBM is displayed in Fig. 3.4c along with the difference between the AGCM and ISM temperature in Fig. 3.4d. The anomaly pattern clearly includes very significant differences with a large minimum of more than  $20^{\circ}\text{C}$  existing over the Great Lakes area. Also of note is the maximum of about  $7^{\circ}\text{C}$  to the northwest of Hudson Bay. The temperature anomalies are for the most part dominated by elevation effects. If one assumes a lapse rate of  $7.5^{\circ}\text{C}/\text{km}$ , the 1500 meter elevation anomaly over the Great lakes region (Fig. 3.3d) should correspond to a reduction of approximately  $10^{\circ}\text{C}$ . This effect alone therefore fails

to account for the more than 20 degree depression of temperature observed in this region. Hewitt and Mitchell (1997)[85] conducted a sensitivity study using the UKMO AGCM to investigate the radiative forcing of climate at LGM. Changes to surface albedo, insolation and a lowering of CO<sub>2</sub> concentrations were used to isolate the effect of each of the ice age boundary conditions. This study concluded that the cooling over the ice-sheets is in large part due to the high albedo of the ice-sheets and not to the increased elevation of the topography. This is likely to account for the extra 10 °C lowering noted above as the ice-sheet in the EBM/ISM does not extend to the same southern latitude as it is assumed to do in the AGCM (one would expect large thermal effects given the larger insolation incident at lower latitudes). Hewitt and Mitchell also noted that cloud cover changes, which were found not to be independent of surface albedo, caused a further negative feedback on the climate so as to slightly reduce the cooling over the ice-sheets. Interestingly, the maximum elevation anomaly of 1100 meters over Northwestern Hudson Bay corresponds to a positive temperature anomaly of 7.3°C, in precise agreement with the typical atmospheric lapse rate which suggests that, in fact, changes in albedo are indeed very significant.

As with the temperature intercomparison, the precipitation distributions are illustrated in Fig. 3.5. The annual mean modern climatology simulated by the AGCM shown in Fig. 3.5a captures some of the main features of the present day observed precipitation pattern (not shown). Heavy precipitation over the west coastal areas of Canada and the corresponding rain shadow regions to the east are faithfully represented. At LGM the AGCM precipitation distribution is reduced over much of the northern regions of Canada (Fig. 3.5b). The ISM LGM simulated precipitation, which is a temperature-corrected modern observed distribution, is characterized by a much greater decrease of precipitation than that predicted by the AGCM at LGM (Fig. 3.5c) and may be taken to reveal deficiencies in this ISM parameterization as the AGCM precipitation is a much less constrained parameterization. The LGM precipitation anomaly (Fig. 3.5d) displays the major differences between the ISM and LGM distributions. In particular, there is again a maximum of 0.7 meters/year in the Great Lakes region, an area in which the ISM fails to produce a significant southward extension of the Laurentide ice-sheet. This anomaly may be associated with changes from present in the mid-latitude storm tracks which at LGM are expected to flank the southern regions of the Laurentide ice-sheet, variations which might well provide us with an explanation of the south eastern lobes of the Laurentide ice-sheet. Probably more significant, however, is the perturbation to the temperature field that I expect to arise in consequence of the enhanced stationary planetary wave response to the marked change in topography, a subject which is further investigated in the third part of the results section.

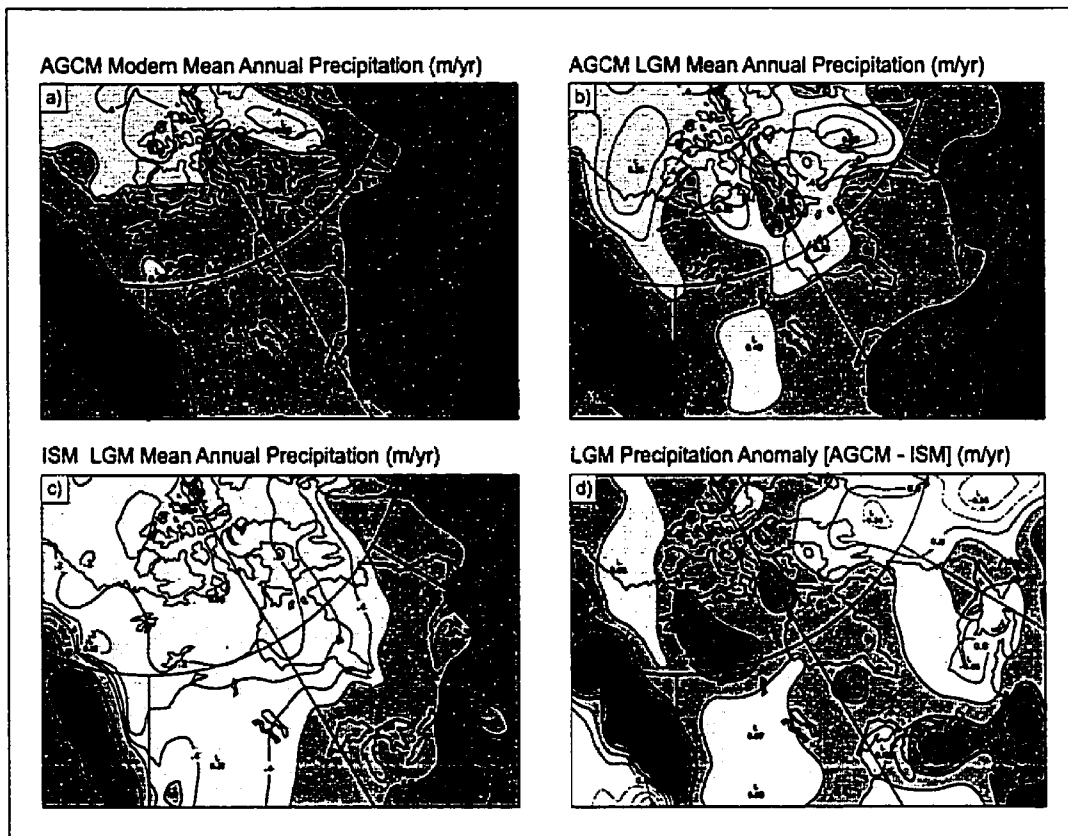


Figure 3.5: Annual mean precipitation distributions ( $\text{m a}^{-1}$ ). (a) Modern AGCM simulated climate with computed SSTs. (b) LGM AGCM simulated climate with computed SSTs. (c) ISM precipitation at maximum ice extent. (d) AGCM minus ISM LGM precipitation anomaly.

### 3.4.3. Mass Balance and the AGCM hydrological cycle at LGM

The detailed balance between the accumulation and ablation over the Laurentide ice-sheet is of central importance in ISM ice dynamics. It is the persistence of small differences between accumulation and ablation, and processes within the ice-sheet, that determines the long term growth or decay of the ice-sheet. The accumulation mainly results from the annual snow mass accumulation and refrozen snow melt minus changes due to evaporation and sublimation. Ablation occurs on a much smaller spatial scale than that of accumulation, being confined primarily to a thin ablation zone at the edge of the ice-sheet. Thus, ice-sheet models often employ a parameterization scheme for ice ablation based on the Positive Degree Day (PDD) formalism (e.g., see Braithwaite 1995; Huybrechts and T'siobbel 1995)[26][94]. An appropriate definition of a PDD is as the number of hours within the day in which the temperature is above  $0^{\circ}\text{C}$  divided by 24 hours. This is intended to represent the period during which there is energy available to melt the snow or ice. The annual melt rate

is then set proportional to the number of PDDs per year multiplied by some suitable rate of snow and ice melt, with a fraction of snowmelt assumed to refreeze. In the ISM/EBM of Tarasov and Peltier (1997b, and 1999)[217][218], the snow and ice melt rates are assumed to be 3.0 and 8.0 mm PDD<sup>-1</sup>, respectively. Other physics is also involved in the ablation of ice-sheets, including iceberg calving along ocean margins. No detailed attempt to represent this process is incorporated within the ISM/EBM or AGCM models discussed in this study, but it is nevertheless important. In the EBM/ISM, ice-sheets are allowed to expand onto the continental shelves to the 400 meter modern bathymetric contour, at which point calving is assumed complete.

The vigour of the atmospheric components of the hydrological cycle, namely precipitation and evaporation, during LGM conditions will clearly determine the accumulation of snow mass over the ice-sheets. The simulation of LGM climate in which SSTs are computed using a thermodynamic mixed-layer slab ocean produces a reduction of 4.8°C in the global average surface temperature. Since the atmospheric moisture content is nonlinearly related to changes in atmospheric temperature through the Clausius Clapyron equation, the amount of moisture in the atmosphere and the energy available for evaporation at the ocean surface should be significantly reduced. In fact, an investigation of the mean global quantities of precipitation and evaporation over land and ocean do very clearly reveal a reduction in the vigour of the hydrological cycle at LGM (Table 3.1). From the subtropical oceans, where evaporation exceeds precipitation, moisture is transported to regions over land where the precipitation is in excess of evaporation. The excess moisture is then either subsequently shed as run off to the oceans, or, in regions such as those over the Laurentide ice-sheet at LGM, contribute to the accumulation of snow mass. The AGCM simulated modern global hydrology appears somewhat more vigorous than that which is actually observed at present. Table 3.1 indicates that the observed values (Baumgartner and Reichel 1975)[12] are slightly smaller over the oceans and much more so over land. At LGM, the global precipitation and evaporation are both reduced compared to the simulated modern climatology, with evaporation being reduced less over the oceans than precipitation, and vice versa over land. It is notable that the strength of the predicted LGM hydrological cycle appears to be in better agreement with the strength of the modern observed cycle, clearly revealing a deficiency of the AGCM modern predicted circulation. The reduced strength of the hydrological cycle at LGM as compared with present is also in accord with studies of dust concentrations at LGM found in ice cores from Greenland and Antarctic. Yung et al. (1996)[244], for example, suggest on the basis of the magnitude of the enhancement of the dust concentrations observed in ice cores at LGM, that the strength of the hydrological cycle at that time must have been approximately half that of the observed modern circulation. The stronger

Table 3.1: The global hydrological cycle. Area averaged quantities for modern observed (from Baumgartner and Reichel 1975 ) [12], modern AGCM simulated and 21 kyr BP AGCM simulated hydrological components over land and ocean

	<i>Modern Observed</i>		<i>Modern Simulated</i>		<i>LGM Simulated</i>	
	Ocean	Land	Ocean	Land	Ocean	Land
Global area (%)	71	29	71	29	67	33
Precipitation (cm/yr)	107	75	111	92	102	83
Evaporation (cm/yr)	118	48	123	63	119	49
Transport/(Run off) (cm/yr)	11	(27)	12	(29)	17	(34)

reduction in evaporation than of precipitation, as a result of the reduced hydrological cycle over land at LGM, might be expected to provide a source of excess moisture (runoff or snow accumulation) in the northern regions of the globe especially since the majority of the land area is in the northern hemisphere.

Zonally averaged changes in precipitation minus evaporation (P-E), between LGM and modern, over a portion of the northern half of North America (Fig. 3.6a) are displayed in Fig. 3.6b. Both precipitation and evaporation anomalies are substantially reduced, especially over the latitudinal regions occupied by the Laurentide ice complex. Decreases in evaporation are larger than those in precipitation and result in positive zonal P-E anomalies of up to 30 cm/a centred at 50°N over the Laurentide ice-sheet. The spatial variation of this anomaly is clearly displayed in the P-E anomaly in Fig. 3.7a where three distinct maxima are observed. The largest anomalies are over the modern Great Lakes region and over the Western Cordillera with local maxima of 956 Kg m<sup>-2</sup> a<sup>-1</sup> (956 mm water equivalent) and 1262 Kg m<sup>-2</sup> a<sup>-1</sup>, respectively while the other somewhat weaker maximum is located over North Western Canada. A comparison of the snow mass accumulation rate over the Laurentide ice-sheet (Fig. 3.7b), for the LGM experiment in which SSTs were computed, reveals a strong correlation with the LGM P-E anomaly from Fig. 3.7a. The snow mass accumulation is defined as the annual average snow mass accumulation from the beginning to the end of the equilibrium 10 year simulation period. The snowfall term in the LGM mass budget would, however, be expected to follow that of the LGM precipitation while that of the snow accumulation must result from a combination of LGM P-E and LGM snow melt over the Laurentide ice-sheet since snow melt does not refreeze in the AGCM. This suggests that the modification of the modern hydrological cycle at LGM is largely responsible for the distribution of the snow mass accumulation zones over the Laurentide ice-sheet. The lack of interannual variability in snow mass accumulation in the model produces a nearly linear annual accumulation rate of 246 mm a<sup>-1</sup> over the region indicated

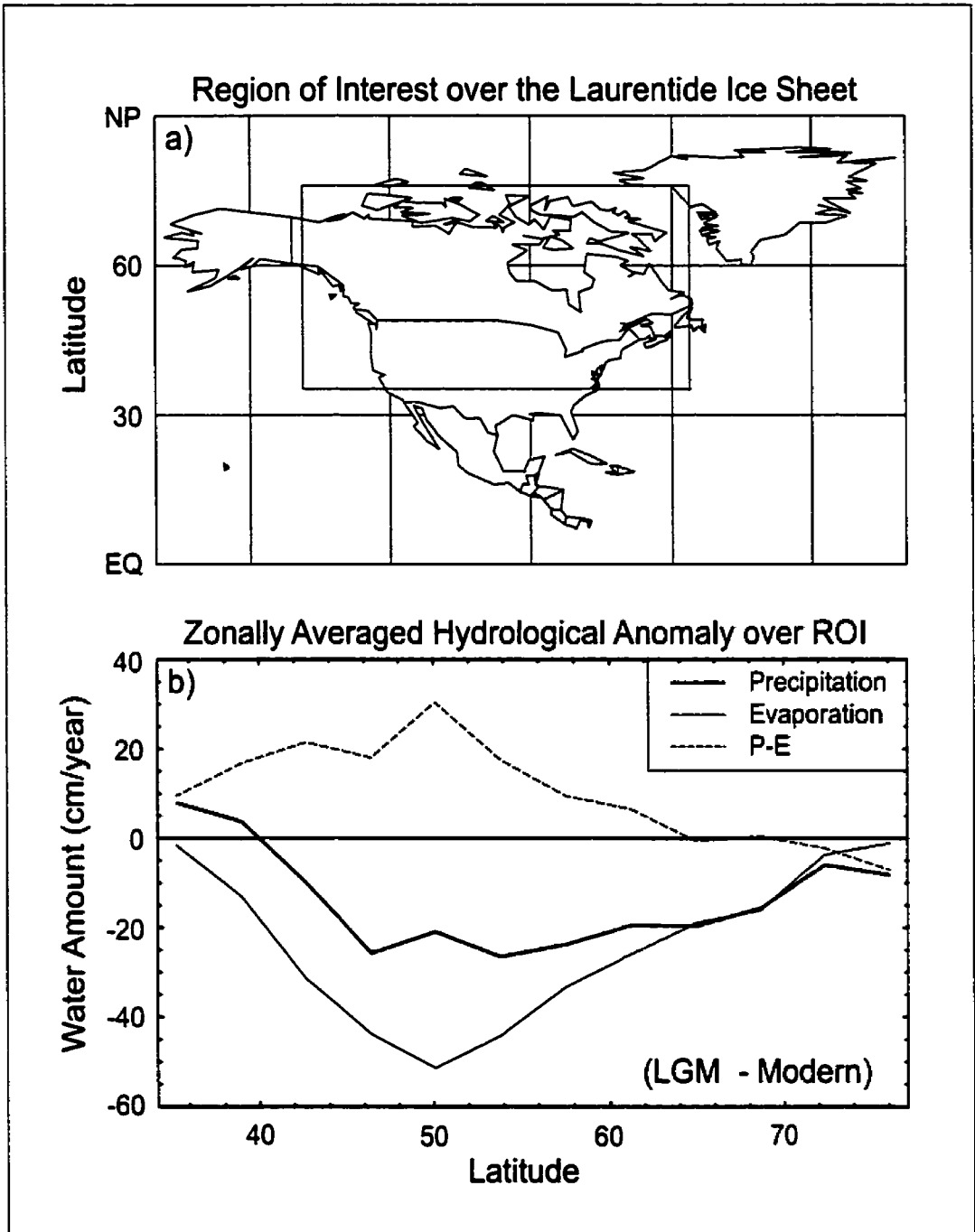


Figure 3.6: AGCM simulated zonally averaged P-E anomaly over the Laurentide ice-sheet ( $\text{cm a}^{-1}$ ). (a) The region of interest:  $35^{\circ}\text{N}$  to  $75^{\circ}\text{N}$  and  $138^{\circ}\text{W}$  to  $56^{\circ}\text{W}$ . (b) Changes in P-E between LGM and present zonally averaged over the region of interest.

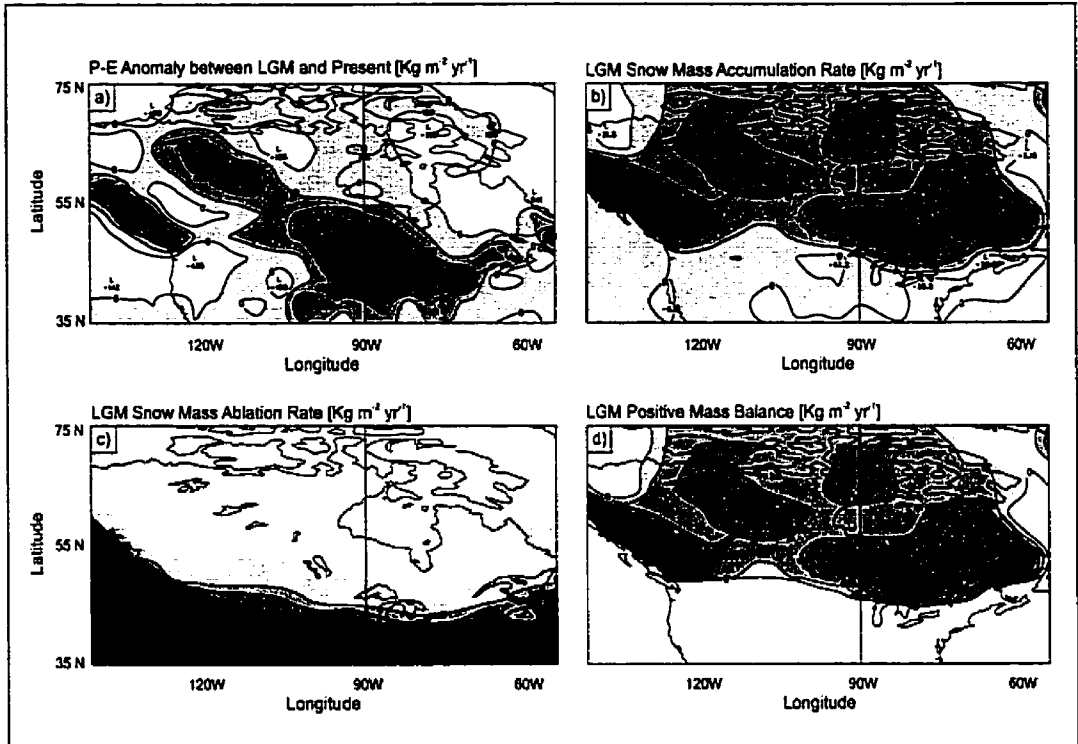


Figure 3.7: LGM ice-sheet mass balance simulated in the AGCM computed SST experiment over the region of interest (Fig. 5a). (a) Annual mean P-E anomaly between LGM and present ( $\text{Kg m}^{-2} \text{a}^{-1}$ ). (b) Snow mass accumulation rate at LGM ( $\text{Kg m}^{-2} \text{a}^{-1}$ ). (c) Snow mass ablation rate at LGM ( $\text{Kg m}^{-2} \text{a}^{-1}$ ) (d) Positive mass balance at LGM ( $\text{Kg m}^{-2} \text{a}^{-1}$ ).

in Fig. 3.6a. The LGM experiment in which SSTs were fixed to CLIMAP inferred values produces a P-E anomaly and snow mass accumulation which are nearly the same as the distributions in the computed SST experiment (not shown).

The ablation rates along the edges of the Laurentide ice-sheet can also be assessed at least qualitatively in the AGCM. ISM/EBM models such as that of Tarasov and Peltier (1997b, 1999)[217][218] employ mass balance parameterizations based upon the PDD formalism described above. The calculations are based upon the surface temperatures produced with the EBM component of the model, in which the ablation rates are set proportional to the annual number of PDDs. A similar calculation employing the AGCM ground temperatures to deduce the LGM annual ablation rates is calculated from the number of PDDs times the snow melt factor described above. The LGM snow melt rate is displayed in Fig. 3.7c over the same region as for the snow mass accumulation. Much of the area over the Laurentide ice-sheet has zero PDDs as is expected to be the case from the position of the mean annual zero degree isotherm (Fig. 3.4b). The ablation rates then quickly rise near the margins

of the Laurentide ice-sheet and along oceanic fronts. The steep gradients which occur along the edge of the ice-sheet are of course instrumental in determining the equilibrium line of the ice-sheet. The LGM positive mass balance (Fig. 3.7d) which is the combination of the accumulation minus the ablation terms of Figs. 3.6b and 3.6c indicates that the majority of the Laurentide ice-sheet has a positive mass balance in the AGCM simulation.

The equilibrium line, which is clearly observed in Fig. 3.7d, is more accurately resolved in Fig. 3.8, which displays the ablation zones along the edges of the Laurentide ice-sheet for both the ISM/EBM (Fig. 3.8a) and AGCM (Fig. 3.8b). The resolution of the ISM/EBM is much greater than that of the AGCM, and demonstrates the need to adequately resolve this sensitive region of the ice-sheet. The Laurentide ice-sheet ablation zone in the ISM/EBM is approximately 1 to 2 grid cells in most areas, where the grid cells are displayed at a  $1^\circ$  by  $1^\circ$  resolution. The corresponding Laurentide ice-sheet ablation zone in the AGCM is much less defined where the AGCM resolution is  $3.75^\circ$  by  $3.75^\circ$ . The ablation rates along the edges of the ice-sheet in the ISM/EBM quickly rise to more than  $6000 \text{ Kg m}^{-2} \text{ a}^{-1}$  (6 meters water equivalent) within one or two grid cells along the southern margins of the ice-sheet. The AGCM, however, has a more discontinuous ablation gradient as compared with the ISM/EBM. Also of note is the degree to which the AGCM Laurentide ice-sheet extends much further southward than the corresponding ice-sheet in the ISM/EBM.

The obvious differences between the ice-sheet mass balance in the two models and in particular the sharp ablation zone demonstrates the need for a high resolution land surface scheme if corrections for lapse rate effects and an improved radiation balance are to be achieved within an AGCM. Studies of this type using an AGCM (e.g., Glover 1999)[73] have demonstrated that by incorporating high resolution adjustments into the modern simulation of the Greenland ice-sheet, a more detailed and accurate mass balance can be obtained. This will, of course, also apply to the differences noted in the Laurentide ice-sheet mass balance and should be incorporated within AGCM paleoclimate simulations.

#### **3.4.4. The General Circulation and Eddy Moisture Transport at LGM**

Sea level pressure and surface wind anomalies give a good indication of changes in the surface circulation at LGM. The differences that occur in the low-level circulation at LGM have been well documented in the past and with increasing resolution over time (e.g., Manabe and Hahn 1977; Broccoli and Manabe 1987; Joussaume 1993; Lorenz et al. 1996; Hall et al. 1996)[140][28][106][131][77]. Nevertheless, it will prove instructive to investigate the nature of the changes delivered by the CC-

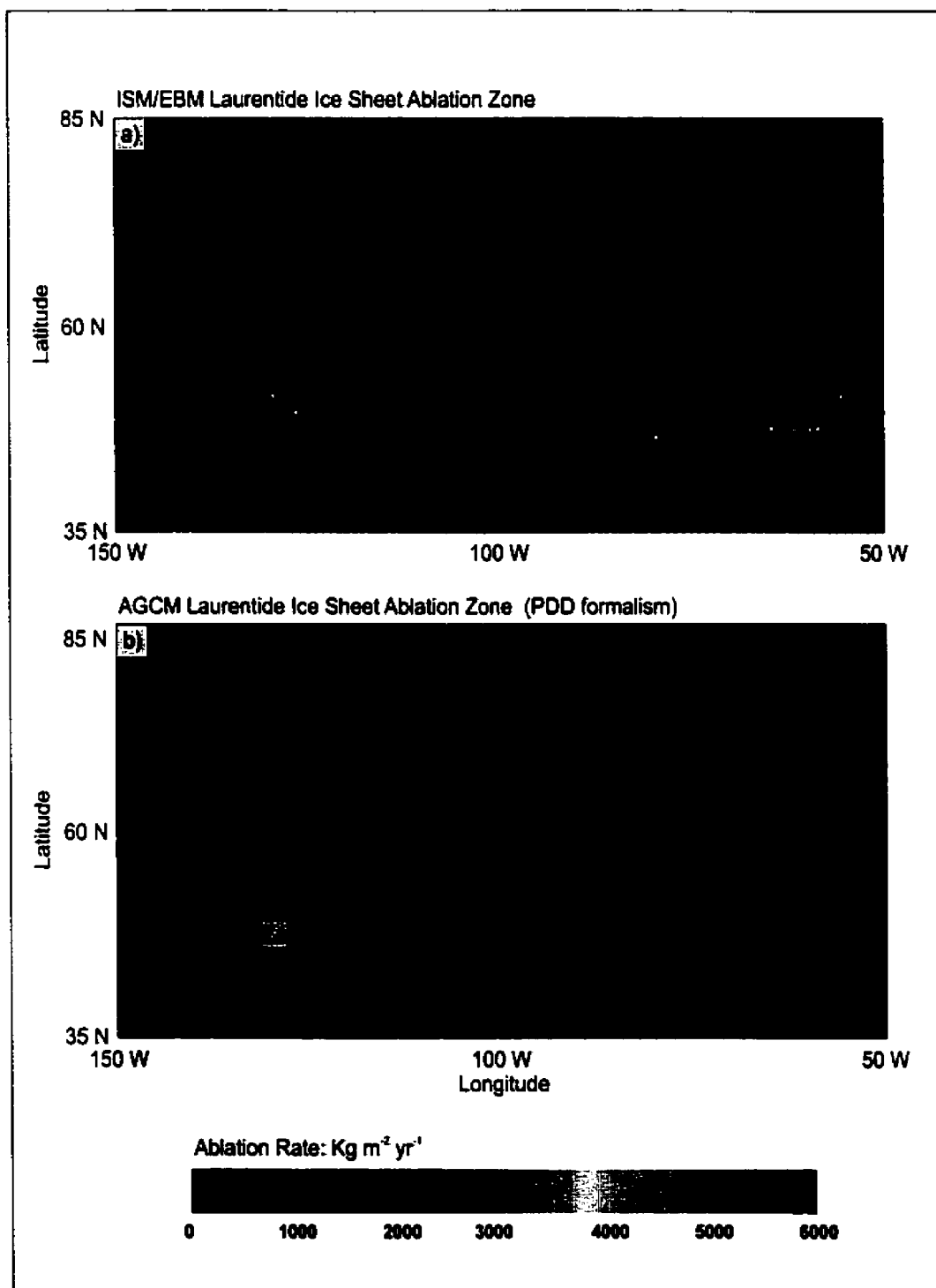


Figure 3.8: Laurentide ice-sheet ablation zones for the (a) ISM and (b) AGCM. Units are in  $\text{Kg m}^{-2} \text{a}^{-1}$ .

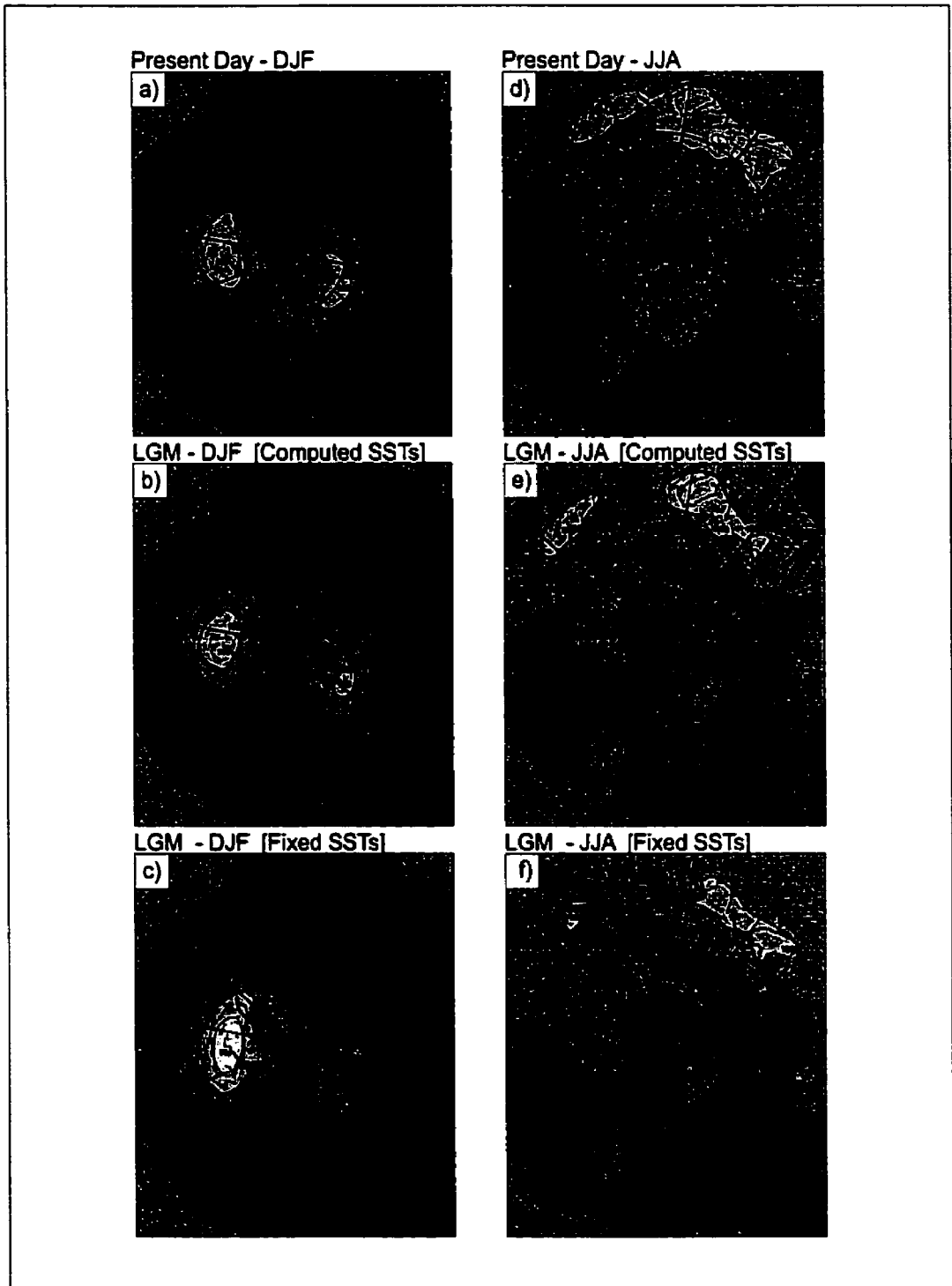


Figure 3.9: Northern hemisphere mean sea level pressure (hPa) and surface winds (meters/second) for (a) modern DJF, (b) computed SST LGM DJF, (c) fixed SST LGM DJF, (d) modern JJA, (e) computed SST LGM JJA, and (f) fixed SST LGM JJA. Contour interval is 10 hPa.

Cma AGCM and to note similarities and differences with those obtained in previous investigations. The mean sea level pressure and surface wind vectors for modern and both the computed and fixed SST LGM experiments are displayed in Fig. 3.9 with the corresponding LGM anomalies displayed in Fig. 3.10 for December-January-February (DJF) and June-July-August (JJA). The anticyclone positioned over the Laurentide ice-sheet in northern hemisphere winter and summer is readily apparent in both the computed and fixed SST LGM anomalies in Fig. 3.10. The surface wind on the southern flank of the Aleutian low, which flows onto the west coast of North America in the modern circulation, is almost arrested by the presence of the ice-sheet and is deflected mostly northward (see also Lorenz et al. 1996; Hall et al. 1996)[131][77]. The decrease in the intensity of the sub-tropical high in the Eastern Pacific basin along with the increased pressure over the Laurentide ice-sheet at LGM results in a weak southward surface flow of air which replaces the strong winter westerlies present over the United States in modern times. The modification of the Icelandic low in the north Atlantic along with an intensification and a more easterly repositioning of the Azores high during winter results in a more southward flow of air along the east coast of North America (Lorenz et al. 1996)[131] as is observed in the anomalies in Figs. 3.10a and 3.10c. Based upon the winter anomalies in both LGM experiments one would expect that the nature of the North Atlantic Oscillation (NAO) would have been much different at LGM (Appenzeller et al. 1998)[8]. Changes in northern hemisphere winter over the Fennoscandian ice-sheet, which is also overlain by an atmospheric anticyclone, are similar to the Laurentide ice-sheet but are of much reduced extent.

The summer circulation in Figs. 3.9 and 3.10 displays the same anticyclonic response over the Laurentide ice-sheet but is of a slightly lower magnitude. In this season it is a reduction in the intensity of the sub-tropical Pacific high and a slight easterly displacement of the Azores high that result in the anticyclonic flow over the Laurentide ice-sheet. A comparison of the summer surface wind vector anomalies over the North Pacific for the computed and fixed SST experiments (Figs. 3.10b and 3.10d) demonstrate that the nature of the boundary forcing in the North Pacific gyre strongly influences the westerly air flow over the North Pacific. The nature of this boundary forcing will be further illustrated in this section of the chapter. Another interesting feature of the summer circulation is the weakening of the Indian monsoon as depicted by the southward wind vector anomalies in Figs. 3.10b and 3.10d. The northward flow of air in the Bay of Bengal is reduced at LGM due to the decrease in the land-sea temperature contrast, which is indicated by the reduced monsoon low pressure system over India. The monsoon appears stronger in the fixed SST LGM experiment and is likely a result of a warmer land surface temperature of more than 10°C in this region relative to the computed SST LGM experiment (not shown). Likewise, the modification

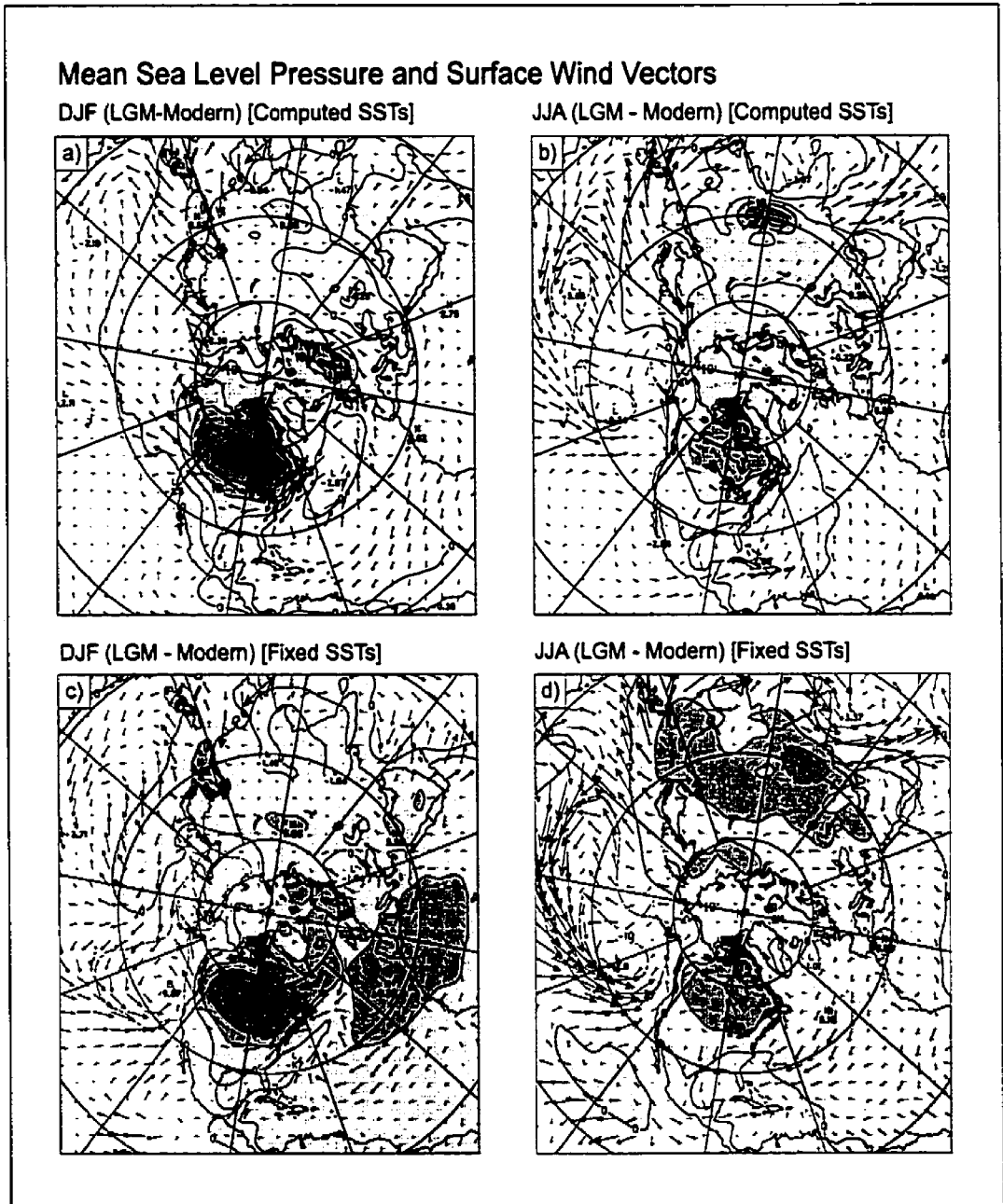


Figure 3.10: Northern hemisphere mean sea level pressure (hPa) and surface winds (meters/second) anomalies (LGM - Present) for (a) computed SST DJF, (b) computed SST JJA, (c) fixed SST DJF, and (d) fixed SST JJA. Contour interval is 5 hPa.

of the low pressure system over the southwestern U.S. gives rise to a weakening in the Mexican monsoon at LGM which reduces the transport of warm moist air into eastern North America.

The winter 500 hPa geopotential height, which is often used to illustrate the winter stationary wave pattern, is displayed along with the 500 hPa wind vectors in Fig. 3.11. Figs. 3.11a and 3.11b, for modern and LGM, display a wave number two pattern which is typically expected of the winter northern hemisphere circulation. In Figs. 3.11a and 3.11b the 500 hPa jet stream is indicated by the arrows which display wind strengths greater than 10 m/s. The vertical stretching of the air columns upstream of the west Laurentide ice-sheet causes the air parcels to flow more northward than at present (Fig. 3.11b). As the air columns cross the increased vertical barrier, the anticyclonic relative vorticity in the flow increases and drives the parcels southward relative to the background vorticity. The constraint of the conservation of potential vorticity results in the more diffuent air flow over western North America at LGM. Figs. 3.11c and 3.11d display the winter anomalies between LGM and present for both the computed SST experiment and the fixed SST experiment in which CLIMAP SSTs are used as lower boundary condition. The wave number two anomaly, which is apparent in both simulations, is characterized by a long wave pattern with a meridional structure which decreases towards equatorial latitudes. The two anomalies in Fig. 3.11c and 3.11d also illustrate the broad decreases in geopotential height which imply a cooler temperature (thickness) of the column of air in the LGM climate. In the computed SST anomaly (Fig. 3.11c), the spreading of the westerly jet upstream over the west Laurentide ice-sheet is clearly visible on the west coast of North America, which is characterized by a high thickness anomaly to the north and a low thickness anomaly to the south. It is interesting to note that this result is very similar to the result obtained in a R15 lower resolution study of LGM climate with a mixed-layer slab ocean (Broccoli and Manabe 1987)[28]. This sensitivity study concluded that most of the 500 hPa features were a result of the inclusion of the LGM topography and not due to CO<sub>2</sub> or albedo effects.

On the basis of both the computed and fixed SST LGM experiment anomalies, it will be observed that each local minimum (local maximum) in the longitudinal variability can be coupled with a local maximum (local minimum) of the more southerly longitudinal variability (see adjoining lines between highs and lows in Figs. 3.11c and 3.11d). This feature may be a result of an enhancement of the wave number 2 stationary Rossby wave at LGM as a result of the fluid parcels being deflected well beyond their position relative to the mean background vorticity. This enhancement of the stationary wave pattern, which may also partly be a consequence of the nature of the diabatic forcing in this region, also correlates with the difference in temperature between the AGCM and ISM/EBM, simulated in the south eastern lobes of the Laurentide ice-sheet at LGM (Fig. 3.4d). Over Eastern Canada, the

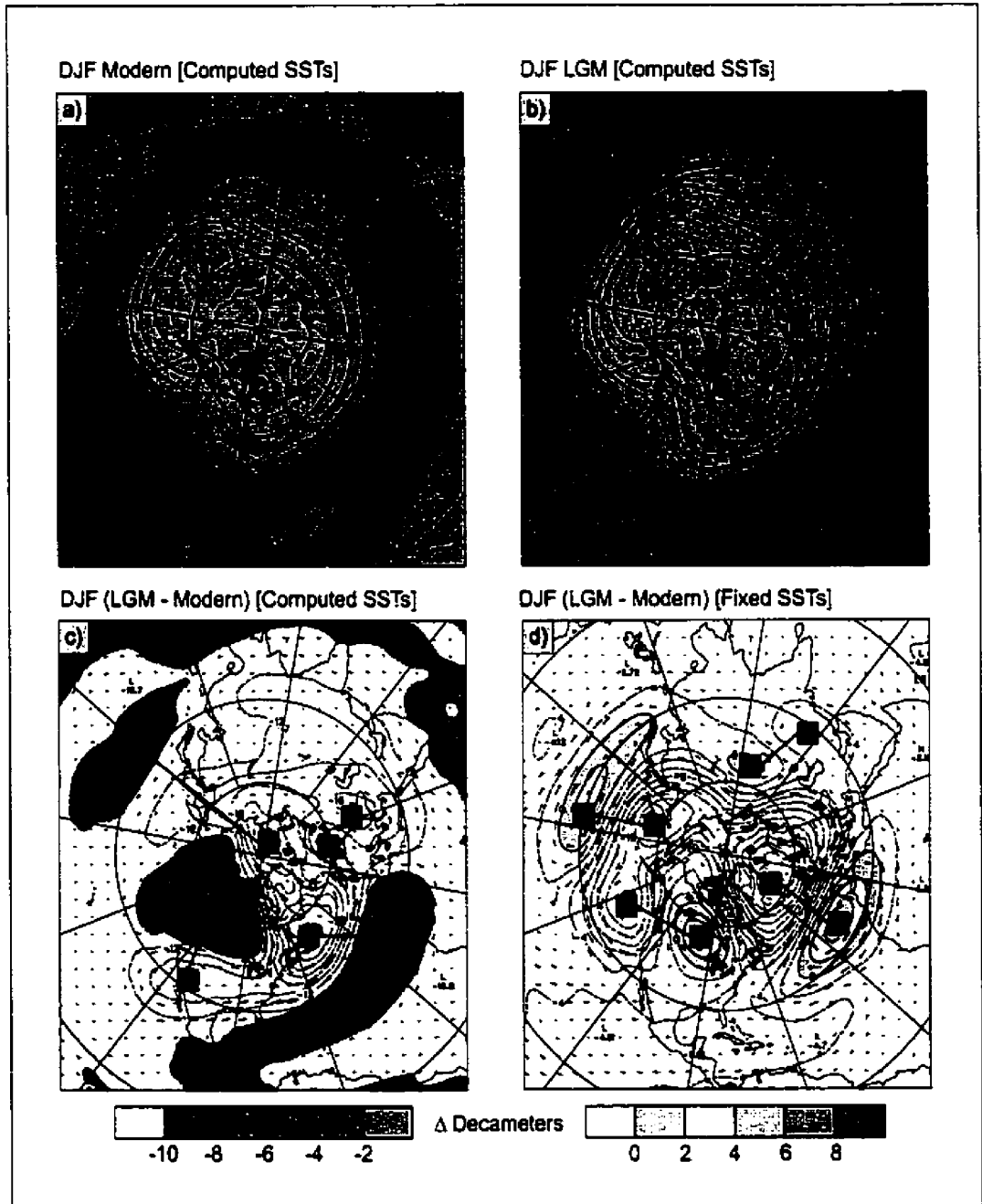


Figure 3.11: Northern hemisphere winter 500 hPa geopotential height (decameters) and wind vectors (meters/second) for (a) modern, (b) LGM, (c) computed SST LGM - modern, and (d) fixed SST LGM - modern. In (a) and (b) contours are at 10 decameter intervals with wind vectors greater than  $10 \text{ m s}^{-1}$  shown. In (c) and (d) contours are at 2 decameters with shaded regions greater than -10 and 0 decameters, respectively.

anomalies in the 500 hPa jet stream depicted in Figs. 3.11c and 3.11d for the two LGM experiments reveal a consistent increase of the geostrophic flow between the geopotential high over Canada and the geopotential low over the North Atlantic. This results in a southward flow of cold air being driven directly to these southern lobes of the Laurentide ice-sheet which extended into the New England region of the United States at LGM. Implications of this pattern in the maintenance of the southeastern margin of the North American ice-sheet as well as in the strengthening of the western portion of the North Atlantic storm track were first discussed in Broccoli and Manabe (1987)[28]. This study showed that an increase in winter precipitation associated with the increased intensity of the storm track might be essential to the mass budget of the ice-sheets and provide a self sustaining mechanism for ice-sheet growth.

Both 500 hPa anomalies for each LGM experiment have fairly consistent features. However, there are differences in the nature of the planetary wave structure which is certainly a result of the differences of the lower boundary forcing between the two experiments. An interesting feature involves the jet stream over the North Atlantic ocean. Both anomalies in Figs. 3.11c and 3.11d show a strengthening of the jet over the North Atlantic. The anomalies also indicate changes in the curvature of the jet in this region. The high-low meridional pattern extends in a northwest direction in the computed SST experiment and has an almost northward orientation in the fixed SST experiment over the North Atlantic. Thus, the jet is slanted more to the northeast in the computed SST experiment. Clearly, this is the influence of the repositioning of the Atlantic storm track to coincide with the region of steep horizontal temperature gradient along the edge of the sea ice distribution which is displayed in Fig. 3.12. This behaviour has also been noted in a study of 10 sets of simulations of present day and LGM climate in the context of the PMIP project (Kageyama et al. 1999)[110]. That study, which investigated the nature of the high frequency transients in the storm track zones, noted increased baroclinicity in the traditional baroclinic zones along the Atlantic ocean sea ice edge.

The sea ice used in the fixed SST experiment is based upon an interpolation of CLIMAP inferred distributions of sea ice for February and August (Fig. 3.12b). The sea ice thickness, which was not estimated by CLIMAP, was introduced into the model based upon observed gradients in modern sea ice thickness. The sea ice in the computed SST experiment (Fig. 3.12a) is calculated from a thermodynamic sea ice module which is linked with modern day ocean heat transports which were left almost unmodified in the LGM experiment. At LGM much of the continental shelves were exposed as a result of the lowering of the ocean surface by 120 meters on average. This therefore requires a modification of the implied oceanic heat transports which are necessary in these simplified

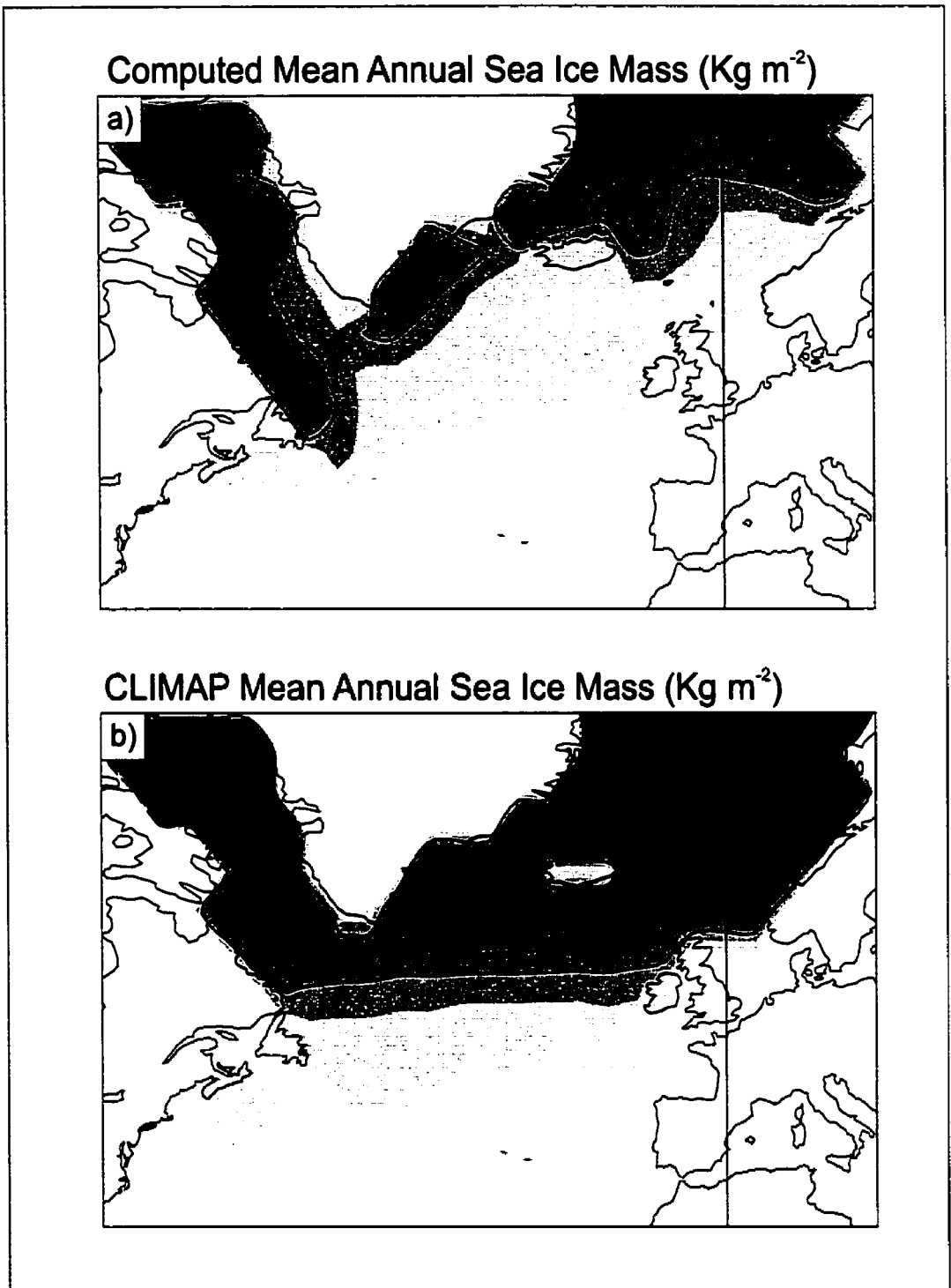


Figure 3.12: Annual mean sea ice mass distributions ( $\text{Kg m}^{-2}$ ). (a) Computed SSTs and sea ice distribution. (b) CLIMAP SSTs and sea ice distribution.

models to remove climate drift. Ocean points which became exposed as land at LGM have residuals which are combined into the average meridional oceanic heat transport on each latitudinal circle so as to maintain the globally averaged oceanic heat convergence. The logic here is based upon the assumption that the deep ocean circulation in this experiment would have a thermohaline component which is not significantly weaker at LGM but much the same as modern. This is however, a topic of current debate (e.g., Weaver et al. 1998)[238] and the currently emerging consensus seems to be that the LGM thermohaline circulation was shallower and of reduced northerly extent in the high Northern Atlantic region than at present. There remains, in fact, a great degree of uncertainty as to the state of the thermohaline circulation at LGM, but the sea ice distributions in the computed SST experiment nevertheless agree well with reconstructions of the sea ice distribution in the north Atlantic based upon dinoflagellate cysts (de Vernal et al. 1993, 2000)[50][51]. It may be argued, however, that the assumptions of modern day oceanic heat transports at LGM may be inhibiting the growth of sea ice in the computed SST LGM experiments and therefore biasing the North Atlantic climate.

Changes over the North Pacific at LGM are also apparent upon inspection of the differences in Figs. 3.11c and 3.11d. The intense high-low geopotential anomaly over the North Pacific in the fixed SST experiment indicates an increase in the anomalous mid-latitude westerlies in this region. This appears to be a result of the juxtaposition of the anomalously warm North Pacific subtropical gyre of the CLIMAP reconstruction of SSTs (Fig. 3.13a) with an increase in high latitude cooling relative to the computed SST experiment in winter (Fig. 3.13b). The sensitivity of the North Atlantic and Pacific jet streams to the sea ice distribution and SSTs in the two LGM experiments clearly demonstrates that an understanding of LGM atmosphere-ocean interactions, based upon the use of a fully coupled atmosphere-ocean GCM, will be crucial in the next generation of paleoclimate experiments.

Water vapour plays a critical role in climate processes, both by influencing the amount of radiative transfer within the atmosphere and as a carrier of latent heat energy. The annual mean movement of moist air masses is well characterized by the vertically integrated moisture transport which is displayed in Fig. 3.14. Regions of divergence of this moisture transport, indicated by lows in the sub-tropical Pacific and Atlantic oceans in Figs. 3.14 a,b and c, are associated with moisture sources and demonstrate that much of the moisture necessary for precipitation or snowfall over the continents is supplied by the oceans. Figs. 3.14a and 3.14b compare the modern observed moisture transport with that simulated from the modern computed SST experiment. The observed field was extracted from a five-year climatology which was prepared using the Canadian Meteorological Center's (CMC)

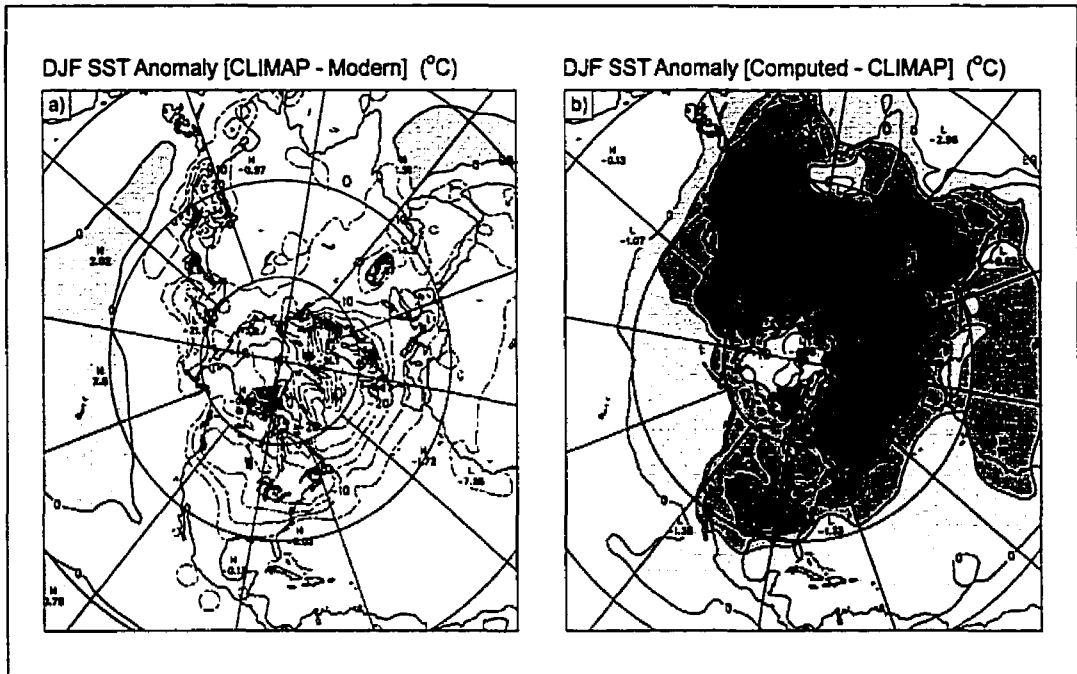


Figure 3.13: DJF ground temperatures and sea surface temperatures. (a) CLIMAP fixed SSTs - Modern (b) Computed SSTs - CLIMAP SSTs. Contour interval is 5 °C.

operational analyses for the period December 1990 to November 1995. The CMC data assimilation system is described in Mitchell et al. (1993)[152] and Mitchell et al. (1996)[153]. The total moisture transport in the model simulation agrees well with the observations but is more intense, indicating the increased vigour of the modern simulated hydrological cycle which was also noted in Table 3.1.

Since much of the water vapour lies in the lower troposphere, the earth's orography modifies the transport of water vapour from ocean to land. The influence of the Rocky mountains is clearly visible in Figs. 3.14a and 3.14b, which display a deceleration and a subsequent convergence of moisture upstream of the mountain range. This inhibits the penetration of water vapour into the interior of the continent. Much of the moisture received within the interior of the North American continent originates from the Gulf of Mexico in the observations. However, in the modern simulation the major source is from the Pacific which appears to be about 50% too strong. Changes in the supply of moisture to the Laurentide ice-sheet are clearly revealed in the LGM moisture transport shown in Fig. 3.14c and the LGM anomaly shown in Fig. 3.14d. The LGM moisture transport anomaly demonstrates that moisture flow along the mid-litudinal band is reduced over the North American and Asian continents at LGM. Fig. 3.14c also shows that the moisture received within the interior of North America at LGM originates from the Gulf of Mexico as in the modern observations. The

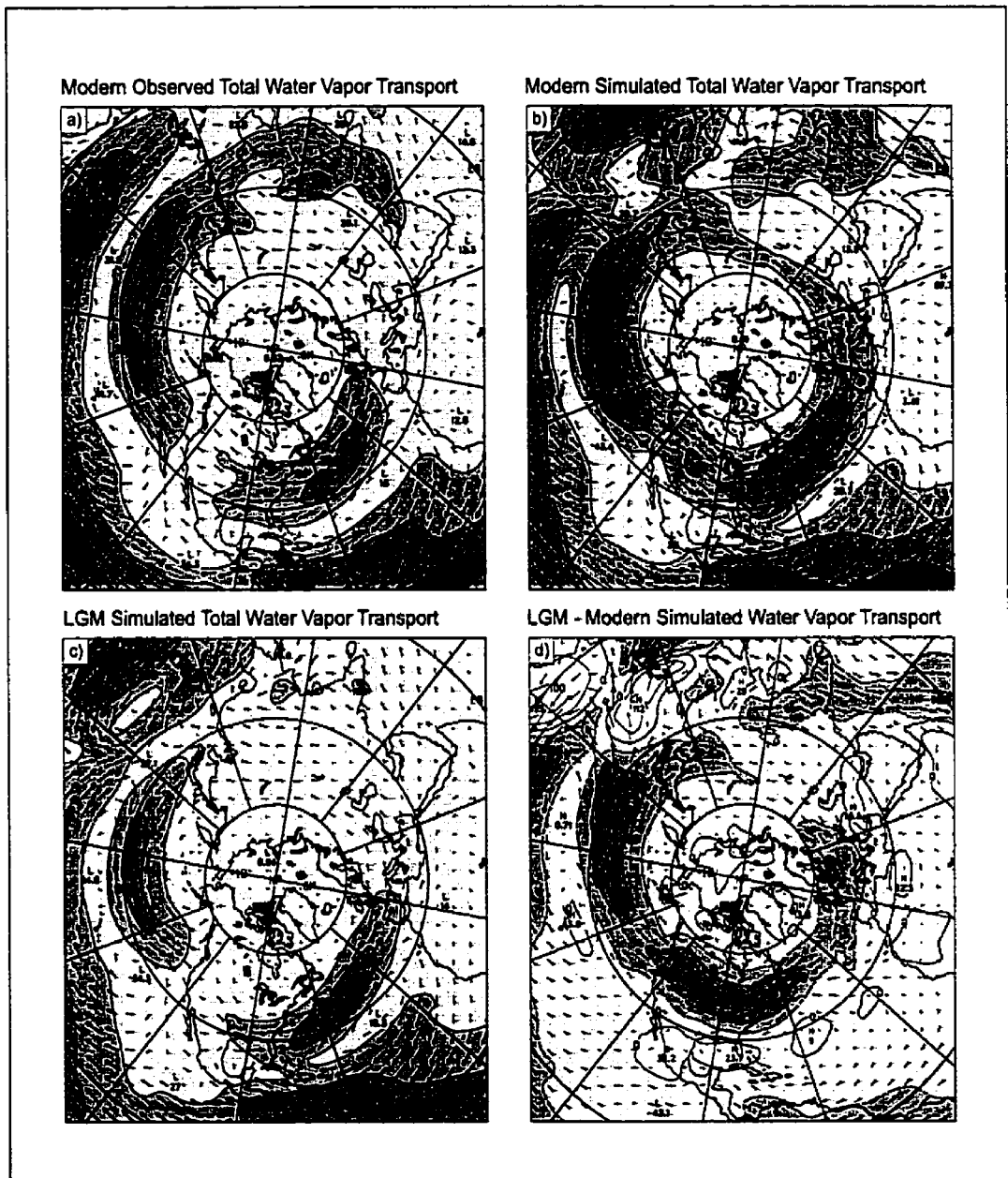


Figure 3.14: Annual mean total water vapour transport ( $\text{Kg m}^{-1} \text{s}^{-1}$ ). (a) Modern observed. (b) Modern computed SST simulation. (c) LGM computed SST simulation. (d) LGM - modern anomaly. Contour interval is 100  $\text{Kg m}^{-1} \text{s}^{-1}$  in (a), (b), and (c) and 50  $\text{Kg m}^{-1} \text{s}^{-1}$  in (d).

largest decreases in the moisture flow occur just to the south of the Laurentide and Fennoscandian ice-sheets. The LGM anomaly also indicates that there is a decrease in the supply of moisture from the Mexican monsoon into the North American interior and also a decreased supply in the Indian monsoon region of the globe. The decrease in precipitation simulated over the Laurentide ice-sheet (Fig. 3.6) indicates that this reduced precipitation results from the decrease of the intrusion of moist air into the North American interior.

The meridional flux of moisture varies considerably with the seasonal cycle but is predominantly poleward in the annual mean. This moisture transport is accomplished mainly by the transient eddies associated with the baroclinic lows along the polar front and the stationary eddies in the sub-tropical anticyclones. The transient eddies contribute a much greater fraction of the total transport of water vapour in the meridional than the zonal direction and are displayed in Fig. 3.15. The meridional transient eddy transport of water vapour is therefore very similar to the total meridional transport in the mid-latitude regions (not shown). Figs. 3.15a and 3.15b show the annual mean meridional transport of water vapour by transient eddies from both the modern CMC observed climatology and the AGCM modern simulated transport, respectively. The simulated transient activity is more enhanced and more variable than that in the observed climatology but both display a similar structure. The simulated transient activity is again much too strong (by about 50%) in northern latitudes as well being much too vigorous in the intertropical convergence zone over Africa, Asia and the Western Pacific. The strong modern poleward flux in the mid-latitudes in both hemispheres is shown in the zonally averaged meridional transient eddy moisture transport in Fig. 3.16a. This figure reveals poleward flow at all latitudes and at all levels with maxima in the mid-latitudes below 850 hPa. The LGM zonally averaged anomaly shown in Fig. 3.16b displays a poleward decrease in the meridional transport of water vapour by the transient eddies. In the northern hemisphere there is a slight increase in transport at 50° N latitude in the lowest model level indicating a possible convergence in moisture at this latitude. Fig. 3.17 shows the spatial distribution of the LGM meridional transient eddy anomaly over North America and Europe, where the Laurentide and Fennoscandian ice-sheets are located. Areas of moisture convergence are characterized by decreasing northward gradients such as those on the eastern and western parts of central North America (Fig. 3.17a). The two regions in Fig. 3.17a correspond well with the regions of snow accumulation in Fig. 3.7b. Fig. 3.17b displays a similar but much broader LGM anomaly over the Fennoscandian ice-sheet. The region of convergence is centred over the Scandinavian region and illustrates the nature of the moisture supply by the transient eddy activity.

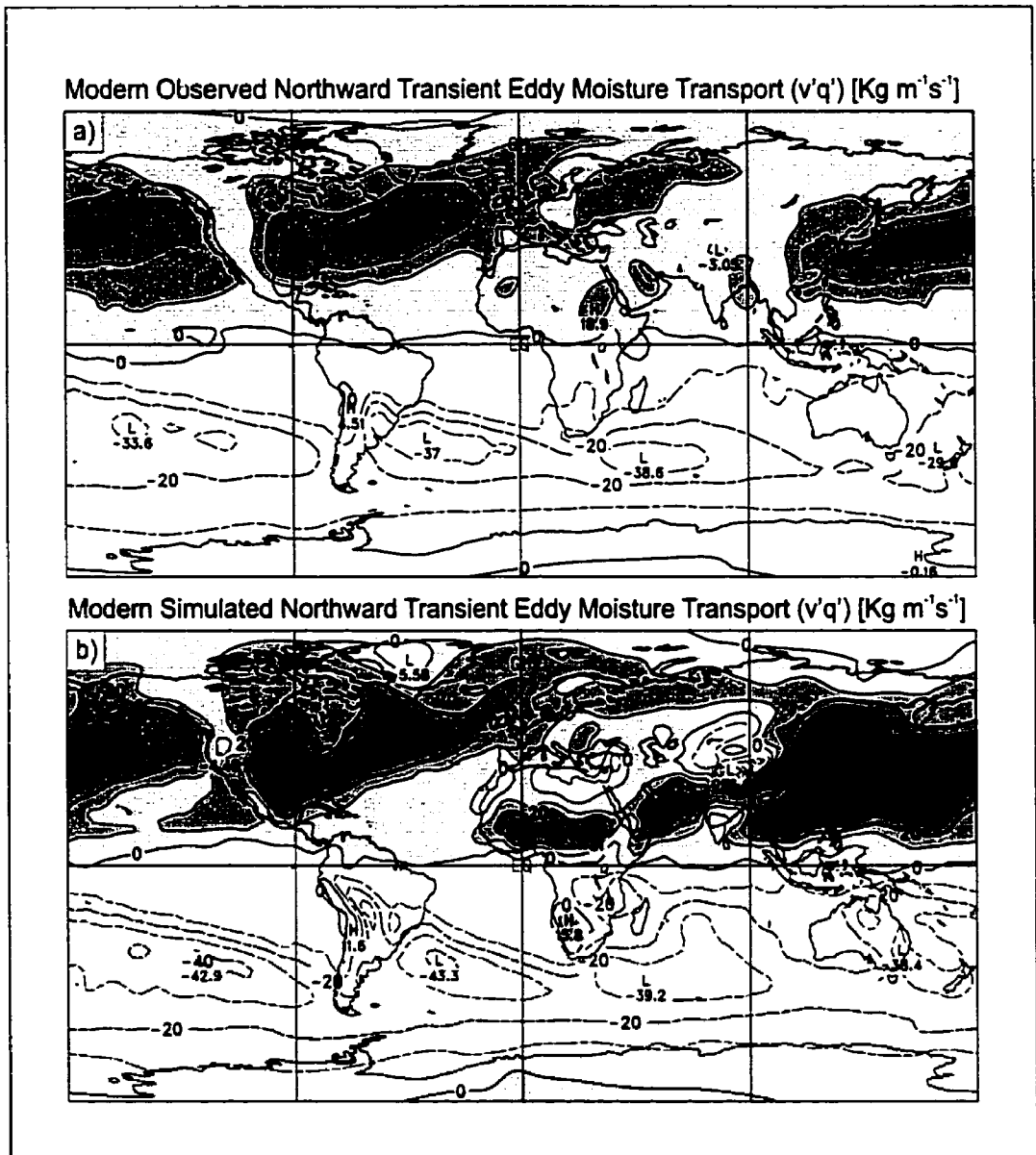


Figure 3.15: Annual mean northward meridional transient eddy moisture transport ( $\text{Kg m}^{-1} \text{s}^{-1}$ ). (a) Modern observed. (b) Modern computed SST simulation. Contour interval is  $10 \text{ Kg m}^{-1} \text{s}^{-1}$ .

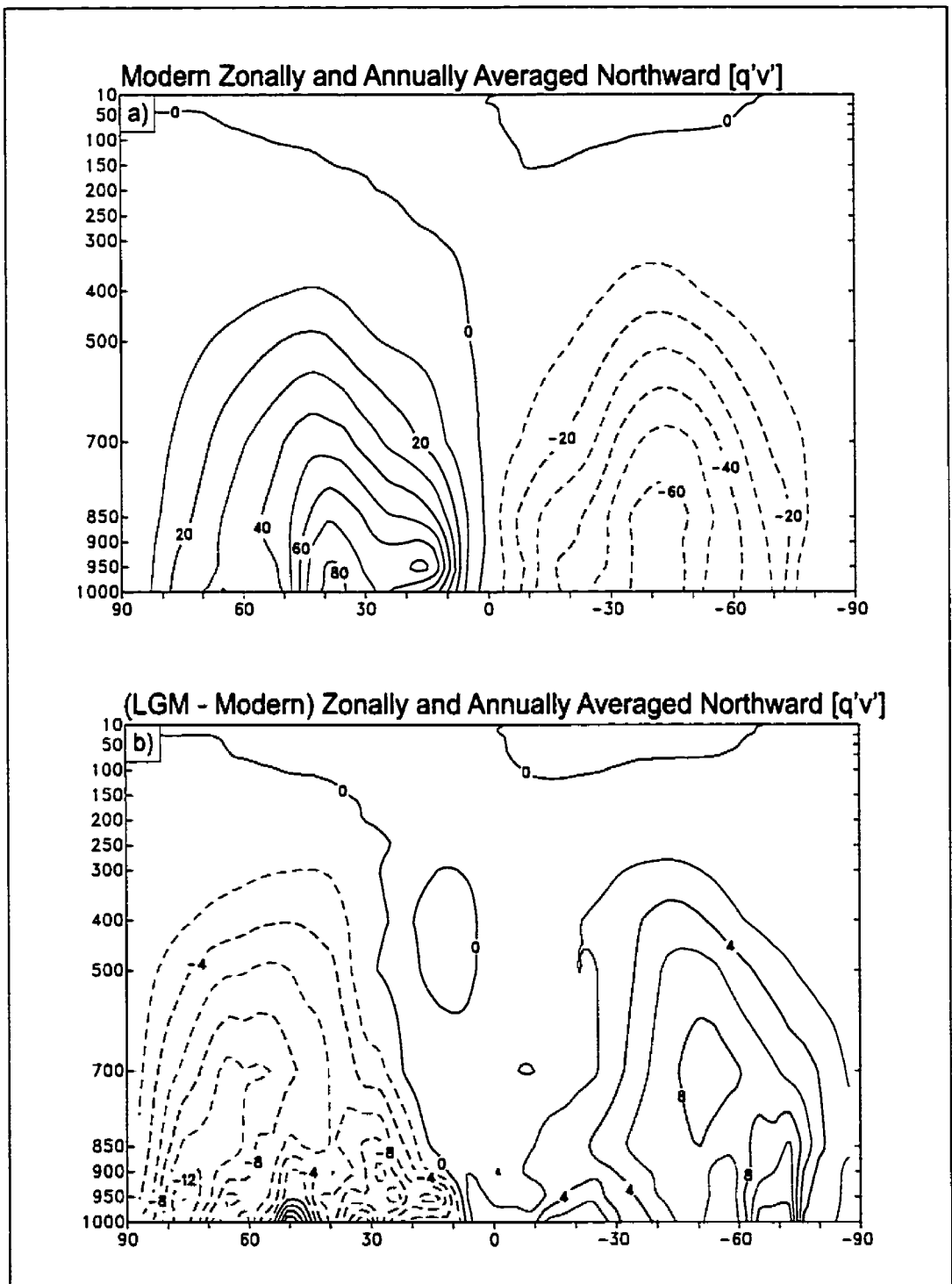


Figure 3.16: Annually and zonally averaged northward meridional transient eddy moisture transport ( $\text{Kg m}^{-1} \text{s}^{-1}$ ). (a) Modern with a contour interval of  $10 \text{ Kg m}^{-1} \text{s}^{-1}$  (b) LGM - modern anomaly with a contour interval of  $2 \text{ Kg m}^{-1} \text{s}^{-1}$ .

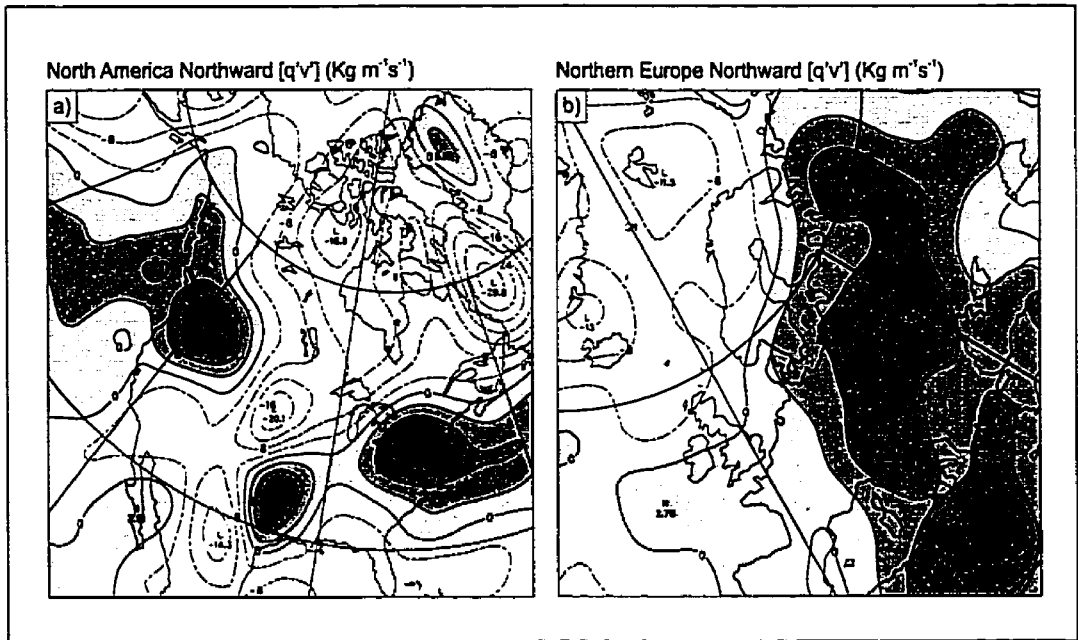


Figure 3.17: North American and (b) European annual mean northward meridional transient eddy moisture transport anomalies between LGM and modern ( $\text{Kg} \cdot \text{m}^{-1} \cdot \text{s}^{-1}$ ). The contour interval is  $4 \text{ Kg} \cdot \text{m}^{-1} \cdot \text{s}^{-1}$ .

### 3.5. Summary and Conclusions

This investigation, conducted using the CCCma AGCM under LGM paleoclimate boundary conditions, has revealed significant changes in the behaviour of the atmospheric general circulation which may have been characteristic of climate state at this time. These changes were compared with results from a reduced climate system model. The results have identified a number of atmospheric mechanisms which may be important in the determination of mass balance over the northern hemisphere ice-sheets at LGM. An understanding of this behaviour is clearly relevant in the context of the design of reduced climate system models which are obliged to employ parameterizations of the "fast physics" involved in determining atmospheric behaviour over time periods extending many millennia into the past. Thus, outputs from two distinctly different models, which operate on widely separated time scales and levels of spatial resolution, were compared to illustrate similarities and differences in the manner in which they simulate the climate of the LGM epoch. I focused especially on the investigation of specific atmospheric mechanisms which may be responsible for the differences identified in the course of these comparisons. In particular, the simulations described in this chapter have shed light on a number of issues. Specifically:

- 1) Comparison of changes of temperature and precipitation based upon the ISM/EBM model

and the AGCM at LGM have revealed a number of interesting differences. The lack of southward extension of the Laurentide ice-sheet in the ISM/EBM simulation resulted in differences in topographic heights over the North American region between the two models. The ISM/EBM calculates temperature and precipitation based on an EBM perturbation of modern climatology which takes into account changes in temperature, lapse rate effects and the non-linear dependence of precipitation on temperature. Some of the observed differences in surface temperature over the southern portion of the Laurentide ice-sheet were therefore a result of a lapse rate effect due to the difference in topography. The AGCM predicted LGM temperatures over the Great Lakes region were lower than those delivered by the ISM/EBM even taking lapse rate effects into consideration. The remaining portion of this temperature difference is most likely explained by the differences in albedo in this region in the ISM/EBM and AGCM where the albedo of the AGCM in this region is much greater due to the greater southward extent of the ice sheet. Precipitation in the AGCM simulation of LGM climate was also greater in this especially interesting region, contrary to what might be expected based upon the lower temperatures for this region predicted by the AGCM. These changes are plausibly the consequence of changes in the atmospheric general circulation, and in particular, those associated with the moisture transport by transient eddy activity. The most significant control may be exerted through the field of stationary planetary waves that is forced by the modified topography. These differences in precipitation anomalies between the ISM/EBM and AGCM imply that there are problems in using the types of perturbative methods which are employed in the ISM/EBM simulation of precipitation under significantly different climate regimes. The use of perturbative methods appears to be highly restricted to the largest spatial variations of climate change during transient ice age cycle simulations.

2) The LGM hydrological cycle simulated in the AGCM was significantly reduced in intensity from that in the modern control simulation. Changes over the Laurentide ice-sheet were especially significant as P-E was increased over that predicted by the simpler ISM/EBM. Changes in the evaporation component of the hydrological cycle were much more reduced from modern than those in precipitation, leading to a net excess of snow build up over the Laurentide ice-sheet at LGM. The accumulation of snow mass over the Laurentide ice-sheet was shown to be precisely correlated with the P-E anomaly between LGM and present, indicating that a major change in the structure of the hydrological cycle had in fact occurred at LGM. A calculation of the ablation using the PDD formalism over the Laurentide ice-sheet demonstrated that the ablation zone is very thin in the AGCM simulation. This raises the question as to the accuracy with which this important aspect of ice-sheet dynamics can be simulated with an AGCM.

3) The general circulation is modified in accordance with changes expected based upon the incorporation of the Laurentide and Fennoscandian ice-sheets in the LGM simulation. The anticyclonic flows over the Laurentide ice-sheet are in agreement with previous studies. Changes in the northern hemisphere winter planetary wave structure are very evident in both the fixed and computed SST LGM experiments. The major modification is an enhancement of the longitudinal planetary wave number two mode as a result of the vertical stretching and compression of the air parcels as they encounter the large northern hemisphere ice-sheets and thereby move under the constraint of potential vorticity conservation. The resulting 500 hPa geopotential height and wind anomaly between LGM and present demonstrated an increased southward flow of air which is likely responsible for the evolution and maintenance of the south eastern lobes of the Laurentide ice-sheet. The jet stream is also significantly enhanced over the North Atlantic at LGM and also over the North Pacific in the CLIMAP SST experiment. The specific behaviour of the intensification of the North Atlantic jet stream observed in both the fixed and computed SST experiments leads to the conclusion that changes in sea ice distribution significantly affect atmospheric flow in the northern hemisphere region. The reduced distribution of sea ice in the computed SST experiment produced a North Atlantic jet stream with a more northeasterly flow at LGM than that with CLIMAP imposed SSTs. The anomalously warm North Pacific gyre of the CLIMAP reconstruction along with increased high latitude winter cooling also gives rise to an increase in the intensity of the North Pacific jet stream in the fixed SST experiment but not in the computed SST experiment.

4) Changes in the total moisture transport at LGM were such that transport was much reduced from modern and naturally in agreement with the reduction in the overall intensity of the hydrological cycle noted previously. The total moisture transport anomalies, being directly influenced by LGM topography, revealed that the zonal flow was significantly impeded by the presence of the northern hemisphere ice-sheets. An investigation of the meridional transport of moisture by transient eddies demonstrated that an increase in northward transport to the south of both the Laurentide and Fennoscandian ice-sheets occurred along with a corresponding increase in the southward transport to the north resulting in regions of convergence directly over the northern hemisphere ice-sheets at LGM.

These changes in the atmospheric circulation and the hydrological cycle at LGM appear to explain much of the discrepancy between the predictions of the AGCM and ISM/EBM. AGCM's, however, still suffer from numerous shortcomings in the simulation of the modern climate. Processes which are fundamental in driving the mass balance at LGM, such as precipitation, are still poorly represented in modern AGCM's. The discrepancy between grid resolution in GCMs and ISMs indicate further

problems in using low resolution models to assess mass balance where changes within one GCM grid cell surely represent the difference between accumulation and ablation along the edge of an ice-sheet. This illustrates the need for higher resolution land surface schemes coupled within the low resolution AGCM if simulations of ice-sheet mass balance are to be incorporated successfully within the AGCM. The use of a high resolution land surface scheme would allow the incorporation of lapse rate corrections in regions of large orographic variance in the spectrally decomposed T32 AGCM.

The incorporation of this enhancement of capability will support the next step in detailed modelling of the 100 ka ice age cycle which will involve asynchronously coupling of ISM/EBMs and GCMs. This will require only moderate increases in computing power as a limited number of AGCM snapshot simulations would be required during a 120 000 year glacial cycle integration that was initiated in the Eemian interglacial. Equilibrium annual cycle AGCM simulations could be carried out every 5000 years, say, without aliasing the insolation cycle which has a highest frequency precessional harmonic at a period of approximately 11 to 12 ka. Between the AGCM simulations, the EBM would be used to perturb the AGCM state to deduce climate state at 500 year intervals. During periods of rapid transition such as at the last interglacial and following Last Glacial Maximum the AGCM simulations might be run at a higher frequency in the range of 2000 to 3000 year intervals. The role of the ocean would of necessity be crucial in the simulation of specific temporal and regional effects of the glacial transition in the eastern North Atlantic and would require the use of a fully coupled atmosphere-ocean GCM and very significant increases in computing power. The asynchronous coupling of the AGCM and ISM/EBM is, however, a much more realistic next step to take in the understanding of the detailed evolution of climate over a full transient ice age cycle simulation. Analyses of this kind will be described elsewhere.

# Climate Simulation of Post Eemian Glacial Inception

## 4.1. Introduction

The relatively benign and stable climate of the Holocene epoch, which one might imagine to characterize conditions during all interglacial periods, is expected to be similar to the climate state that occurred during marine isotopic stage (MIS) 5e. This period, known as the Eemian interglacial, began at approximately 130 ka BP and terminated at approximately 117 ka BP (Imbrie et al. 1984)[99]. These interglacial periods, which occur with the same frequency as the 100 ka eccentricity cycle, precede transitional periods of rapid accumulation of land ice that lead to the formation of continental ice-sheets as discussed in the introduction of this thesis. The most recent such occurrence during the MIS 5e/5d transition began at roughly 117 ka BP, was most intense at 111 ka BP, and continued until 106 ka BP (McManus 1994)[147].

There is in fact widespread evidence that post Eemian glacial inception began during the MIS 5e/5d transition. For example, significant accumulation of land ice was inferred to have occurred on the basis of a strong sea level drop at 115 ka by Shackleton (1987)[203] based upon oxygen isotope chronologies from deep sea cores. Regions in Northern Canada, particularly Baffin Island and the Queen Elizabeth Islands have often been suggested to have been the initiation points of the Laurentide ice sheet at 115 ka (e.g. Clark et al. 1993)[36]. Andrews et al. (1985, 1986)[6][7] also argued that a significant advance in glacial extent in the Canadian Arctic region occurred at this time. Lithological and biogeochemical records from Eastern Siberia have also been interpreted to suggest an abrupt and intense glacial advance beginning at 117 ka and lasting for approximately 12 000 years (Karabonov et al. 1998)[111].

Periods of glacial inception indicated by relative sea level chronologies throughout the Late Pleistocene (e.g. Chappell and Shackleton 1986; Rohling et al. 1998)[33][195] are extremely well correlated with large reductions in northern hemisphere high latitude summer insolation based upon calculations of incoming solar radiation at the top of the atmosphere for the Late Pleistocene epoch of Earth history (Berger 1978; Laskar et al. 1993)[14][124]. The numerous sea level chronologies and

oxygen isotopic signatures present in various proxy data indicate dominant modes of variability at the obliquity and eccentricity modulated precessional frequencies of the long term insolation signature. The theory that glacial cycles originated as a consequence of the cyclical evolution of the Earth's orbital configuration was first proposed by Milankovitch (1941)[148]. The Milankovitch theory of glaciation asserts that long term variations in the Earth's orbital parameters produce conditions in which there are significant reductions in the mean summer insolation at high northern latitudes. The most significant reductions in summer insolation arise during periods of high eccentricity and low obliquity and are characterized by a precession angle which aligns the summer solstice with aphelion. This unique configuration results in a seasonal cycle that is characterized by a strong reduction in northern hemisphere summer high latitude insolation as compared with modern. Milankovitch proposed that it is precisely the resulting reduction in summer temperatures that would allow for the previous winter snowfall to persist through the summer season at high latitudes. This would lead to a situation in which high latitude snowfields would be continuously augmented over periods of hundreds of years. This snow mass would then further increase in response to positive feedbacks in the Earth's climate system. The main snow-ice albedo feedback would lead to a further decrease in summer temperatures and thus to a further increase in continental ice sheet area and volume. Over many millennia the snow packs would combine into continental ice-sheets that eventually covered the high latitude continents.

Studies based upon the use of simple energy balance models (EBMs) have been directed towards the simulation of perennial snow cover under the influence of modified orbital parameters. Such inexpensive diffusive approximations to the heat transport in the climate system allow for a large number of sensitivity studies to be performed in which the full parameter space of model variables can be investigated. This allows for a more complete examination of the various equilibria that may exist. However, reduced models of this type fail to accurately include many of the more important feedback mechanisms present in the real Earth system, such as an explicit representation of the hydrologic cycle and storm track behaviour that may be crucial to the accurate simulation of glacial climates (Kageyama et al. 1999, Chapter 3). The latitudinal extent of northern hemisphere snow cover was first shown to be particularly sensitive to the seasonal variation of insolation by Suarez and Held (1979)[214]. Other energy balance studies have also examined the earth's climatic response to orbitally induced radiation changes (North et al. 1983; Hyde et al. 1985)[161][95]. More recently, the simulation and termination of the 100 ka glacial-interglacial cycle has been modelled through the synchronous coupling of an EBM to an isothermal dynamical Ice Sheet Model (ISM) (Tarasov and Peltier 1997a)[216] and to a full three dimensional thermomechanical model (Tarasov and Peltier

1999)[218]. Transient simulations of this nature demonstrate post Eemian glacial nucleation over Baffin and Ellesmere islands in accord with the stratigraphic record (e.g. see the discussion in Clark et al. 1993)[36]. However, the regions of Northern Labrador/Quebec fail to serve as sites of ice-sheet nucleation, which is discordant with other geological evidence (e.g. Vincent and Prest 1987)[233].

It would be of much greater interest to model changes in ice accumulation at high northern latitudes using fully coupled AGCM and ISM models that include the relevant hydrological feedbacks which couple the atmospheric/cryospheric system. The significant computational requirements of such fully coupled simulations are only now becoming feasible with the existing state of computational technology. Previous sensitivity studies of glacial inception in GCMs have required that these be run in "snap shot" mode in which the orbital parameters are set fixed to the post Eemian insolation minimum. These attempts to simulate glacial inception in modern general circulation models have delivered a wide variety of often conflicting results. Many of the AGCM simulations performed in the past have failed to initiate glaciation by solely modifying the geometry of the orbit to that which existed at 115 or 116 ka BP. One of the first low resolution GCM simulations of glacial inception (Royer et al. 1983)[198] did not explicitly investigate the net mass balance in high northern latitudes but did propose that increased precipitation and cooling due to changes in insolation at 115 ka BP would favour the accumulation of permanent snow cover. In a simulation that employed three different choices for a cold summer insolation regime (116 ka BP, 106 ka BP and more intense reductions in summer insolation), Rind et al. (1989)[191] demonstrated that the Goddard Institute for Space Studies (GISS) model failed to produce any perennial snow cover at high northern latitudes. In a similar study which employed the National Center for Atmospheric Research (NCAR) AGCM, Oglesby (1990)[163] and Verbitsky and Oglesby (1992)[227] investigated glaciation-sensitive regions in this model. By initially seeding a uniform mid-winter 1m snow cover and then modifying model boundary conditions such as CO<sub>2</sub> and snow albedo, perennially snow covered regions were suggested to exist. However, this study did not investigate the influence of changes in the orbital parameters. Phillipps and Held (1994)[178] performed a sensitivity study that investigated the impact of physically realizable maxima and minima in the precession and obliquity parameters which determine the Earth's orbital configuration. Investigations of both extreme warm and extreme cold summer conditions were employed to determine the paleoclimate response of the model climate system. Cold summer conditions, however, failed to produce any permanent snow cover in their low resolution R15 AGCM coupled to a mixed layer ocean. Mitchell (1993)[152] in an investigation of various paleoclimate epochs, also failed to produce glacial initiation in the United Kingdom Meteorological Office (UKMO) AGCM. Syktus et al. (1994)[215], however, using a GCM

coupled to a dynamical upper ocean model reported success in achieving perennial snow cover. To achieve permanent snow cover orbital insolation changes were combined with a reduction in CO<sub>2</sub>.

More recent studies have delved still deeper into the possible mechanisms within the climate system that might combine to sustain permanent snow cover. Dong and Valdes (1995)[54] investigated 115 ka BP climate using the high resolution T42 U. K. Universities Global Atmospheric Modelling Programme (UGAMP) model in both fixed, and mixed layer computed, sea surface temperature (SST) mode. The inclusion of a simple mixed layer model coupled to the GCM revealed that changes in SSTs and the extension of sea ice in the reduced insolation regime favoured the inception of the Fennoscandian, Laurentide and Cordilleran ice sheets. The ample production of snow cover in this model may be attributed in part to the higher resolution, but also to the fact that the model employed spectral corrections to the topography based on the orographic variance within the model. The addition of an envelope orography produces a one sided topographic correction and therefore favours glacial inception. Schlesinger and Verbitsky (1996)[201] also achieved widespread snow cover when reduced summer orbital forcing and reductions in greenhouse gas concentrations were introduced. Gallimore and Kutzbach (1996)[69] performed a set of 5 sensitivity experiments with orbital parameters set to those characteristic of 115 ka BP, as well as changes in CO<sub>2</sub> and surface albedo. The experiments involving changes in albedo were designed to represent the effects of a feedback through the replacement of tundra with boreal forests, the so-called "tundra-taiga" feedback. This study, which employed the low resolution R15 NCAR Community Climate Model version 1 (CCM1) coupled to mixed layer ocean and interactive sea ice models, delivered perennial snow cover in 2 of the experiments. The first simulation produced only slight perennial snow cover with decreased summer insolation and increased surface albedo inferred through the prescription of a biome model estimate of tundra expansion. The second and more successful experiment, with a 25% increase in areal expansion of tundra, through tundra-taiga feedback, produced widespread permanent snow cover over much of the region poleward of 60 °N. Given the coarse resolution of the model and the amount of areal snow cover it would likely be difficult to reconcile this result with the geological record. In a study of atmosphere-biosphere interaction, de Noblet et al. (1996)[49] found that 115 ka BP orbital forcing alone was insufficient to initiate glaciation in the Laboratoire de Meteorologie Dynamique (LMD 5.3) model. This study led to the conclusion that the summers were sufficiently cool to enhance the southward migration of the tundra-taiga limit and therefore helped to maintain the duration of snow cover in northern high latitude regions but failed to produce glacial initiation. The failure was attributed to the excessive warm bias in the model control simulation of more than 5 °C. Vavrus (1999)[226] in a study that employed the GENESIS2 atmosphere-mixed

layer ocean GCM, and which focused upon an investigation of sea ice dynamics at 115 ka BP, also failed to produce permanent snow cover in northern Canada.

In this chapter I will describe the results obtained from three AGCM sensitivity studies of Post Eemian climate state. All simulations use the CCCma GCMII model coupled to mixed-layer ocean and sea ice modules with prescribed oceanic heat transports in order to compute SSTs and sea ice. To begin this discussion, I will describe the GCMII model parameterizations and the relevant boundary conditions that will be employed to produce variations in the modern control climate. In particular, I discuss modifications to the implied oceanic heat transports and the shortwave radiation scheme which combine to produce warm or cold biases in the modern climate. A brief discussion leading to the section on experimental design will also discuss several features of the model which are relevant to the accurate simulation of post Eemian climate. In the results section, comparisons are conducted between three modern control integrations and three 116 ka BP experiments. The results will be presented in two subsections, the first of which describes the three base simulations of the modern control climate, where in each case the model boundary conditions are modified so as to deliver modern climate simulations which are either warm, cold or unbiased in temperature. Comparisons are then made between these predictions of modern climate and modern observed land and ocean data sets. The second subsection investigates whether the reduction in seasonal summer insolation that occurred at 116 ka BP is able to induce a state in which there is significant perennial snow cover at high northern latitudes. This question is investigated by perturbing each of the three control simulations. In the second subsection I also illustrate the action of several positive feedback mechanisms that may be instrumental in maintaining perennial snow cover conditions in this model. In the concluding section I will review the results presented in this chapter and discuss them in the context of ongoing work.

## **4.2. Model Constraints and Experimental Design**

Appendix D is devoted to a discussion of the model parameterizations that influence the process of glacial inception. Appendix E describes other critical issues that are central to the simulation of this process. In the next subsection I focus on the design of the experiments that have been performed in order to test the sensitivity of the model employed in this study to the changes in boundary conditions that determine the post Eemian climate state.

#### 4.2.1. Experimental Design

The glacial-interglacial cycles which have dominated climate system variability over the past 900 000 years are characterized by transitions into glacial climate from interstadial conditions that may occur fairly rapidly and which are accompanied by large drops in sea level. One study that investigated changes in sea level based on strontium/calcium ratios in Porites corals from uplifted coral terraces along the Huon Peninsula in Papua New Guinea (McCulloch et al. 1999)[144] suggested the occurrence of very rapid changes in sea level following the Eemian interglacial that was centred upon 125 ka BP. Corals which live in the first 5 meters of water in the tropical Western Pacific may provide useful chronologies of sea level history and suggest a rapid decrease in sea level of 20 to 40 meters within 5 to 10 thousand years of the isotopic stage 5e/5d transition. This rapid decrease in sea level corresponds to the rapid increases in land ice volume during the Post Eemian glacial inception event and are most probably triggered by decreases in insolation at the top of the atmosphere. This insolation decrease (Fig. 4.1) may then be amplified by the global climate system through additional positive feedbacks to produce the large decreases in global surface temperatures needed to initiate glaciation. Based upon the Milankovitch theory of glacial inception (Milankovitch 1941)[148], it is high latitude cold summers along with the ice-albedo positive feedback mechanism that sustains a perennial snowfield and allows for the growth and spatial expansion of continental ice sheets.

Using either one or the other of two distinct and highly accurate calculations of past variations in the Earth's orbital parameters, one using a highly accurate analytical perturbation expansion (Laskar 1988 and Laskar et al. 1993)[122][124] and the other using a highly accurate numerical n-body integration of the solar system (Quinn et al. 1991)[184], one may compute the time of occurrence of the minimum of Arctic polar summer insolation to have been at 116 ka BP. This is a consequence of an optimal configuration arising between the eccentricity, obliquity and longitude of perihelion. As indicated on Fig. 4.1, the total insolation received during the summer season north of the Arctic circle at 116 ka BP is  $-4 \times 10^{23} J$  less than at present. In this scenario the summer solstice occurs 2.7 degrees from aphelion on a strongly elliptic orbit characterized by an ellipticity of 4.4% and a small axial tilt of 22.5 degrees, optimal conditions for producing decreases in insolation during the summer season of more than  $40 W m^{-2}$  at high polar latitudes (Fig. 1.4d). Northern hemisphere winter then occurred at perihelion at 116 ka BP and results in a large increase in winter insolation that was upwards of  $25 W m^{-2}$  but mainly in equatorial latitudes. Milankovitch theory proposes that the winters need only remain cold enough to sustain an existing perennial snow field and considering

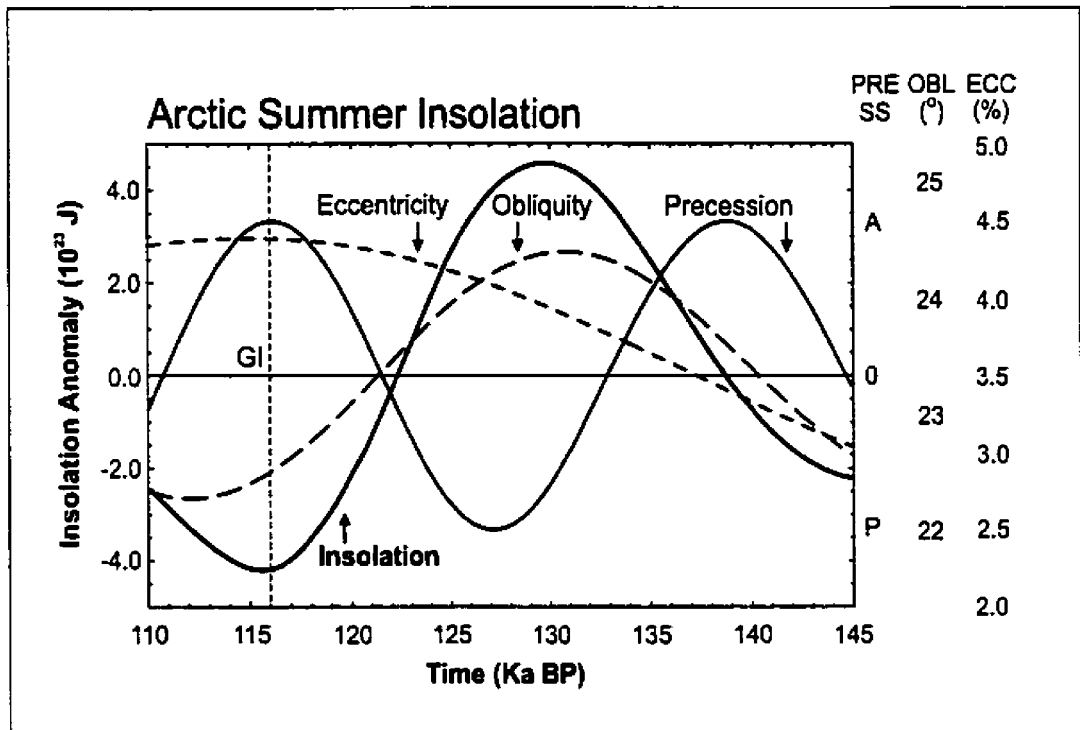


Figure 4.1: A timeseries of eccentricity, obliquity, precession and top of the atmosphere insolation anomaly from the penultimate deglaciation to post Eemian glacial inception spanning 35 ka. The point at which conditions would be most favourable for glacial inception is signified by the line labeled "GI". The insolation curve (left vertical axis) measures the total energy anomaly with respect to modern (in units of  $10^{23}$  Joules) received in the Arctic polar cap during summer. The orbital parameters for each of the three orbital elements are indicated on the right vertical axis.

the fact that much of the northern high latitudes are in 24 hour darkness during the winter season, this condition would hold true. However, the winter warming at equatorial latitudes could also be important in glacial inception as the subtropical oceanic sources of water vapor are required to be warm enough so as to allow for a sufficient amount of meridional water vapour transport to high latitudes to feed and maintain ice sheet growth (Ruddiman and McIntyre 1979)[199].

In comparing model climatologies for two different time periods, the date of the vernal equinox (March 21 at 12 noon in this case) along with the manner in which the seasons are defined for the two time periods must be consistent. The seasons can be defined either as they are at present, which is based on the astronomical calendar, or based on the angular position of the Earth in its orbit. The use of astronomical positions provides for a better phasing of the insolation patterns between the two time periods rather than defining the seasons as having the same angular duration as today. In Fig. 4.1, the calculated insolation anomalies follows the methodology proposed by Hall and Valdes (1997)[78] that minimizes the global and annual root mean square insolation anomaly by

adjusting the date at which the vernal equinox occurs during a specific paleoclimatic epoch. Through this minimization technique the 116 ka BP vernal equinox occurs 2.9 days before the present day vernal equinox. This provides an astronomical phasing of the seasonal lengths in the two different paleoclimate simulations, which vary in duration according to Kepler's second law, such that the seasonal lengths are centred upon one another in the winter and summer seasons (see Appendix A and Fig.1.4d).

In total, three control simulations and three 116 ka BP paleoclimate simulations were performed. The three experiments, each with thermodynamic mixed layer calculated SST's, involved adjusting radiation and implied oceanic heat transport parameters within the model so as to span the temperature parameter space at which glacial inception occurs within the model. This provides a method whereby the changes in the model dynamics and physics under a wide range of northern hemisphere temperature decreases may be used to illustrate some of the mechanisms and feedbacks involved in glacial inception. The first set of experiments to be termed "AMS1" involve adjusting a parameter such that the solar radiation calculation at each atmospheric level including the surface is carried out at every model timestep. By adjusting this parameter and using implied oceanic heat transports calculated using Alexander and Mobley (1976)[3] SSTs and determined under the full solar radiation calculation at every 9 model timesteps, a warm biased climate regime is obtained as described above. The second set of experiments with the original cold biased CCCma GCMII mixed layer atmospheric model with Alexander and Mobley SSTs and solar radiation calculations performed every 9 model timesteps is termed "AMS9". The final experiment involved calculating solar radiation at every timestep but adjusting the implied oceanic heat transports in the model according to newer SST estimates derived from the European Centre for Medium-Range Weather Forecasts and National Centres for Environmental Prediction (ECMWF and NCEP) observational reanalysis during the second phase of the Atmospheric Modelling Intercomparison Project (AMIP2). This simulation termed "AMIPS1" matches the observed AMIP2 SSTs and is considered unbiased. The accuracy of this simulation in reproducing modern climate will be demonstrated in the results section. Thus, the set of three experiments in this chapter that are warm biased, unbiased and cold biased with respect to AMIP2 SSTs are termed "AMS1", "AMIPS1" and "AMS9", respectively.

To provide a consistent set of simulations and to reduce the amount of simulation time required, the impact of changes in CO<sub>2</sub> were not addressed in this sensitivity study although the 116 ka BP paleoclimate simulations had reduced CO<sub>2</sub> levels. The 116 ka BP value was derived through gas concentration analysis from ice core data at Vostok, Antarctica (Barnola et al. 1987; Fischer et al. 1999)[11][62]. Each of the modern control simulations had CO<sub>2</sub> levels set to 345 ppmv and each

of the 116 ka BP glacial inception experiments have CO<sub>2</sub> values of 280 ppmv. The land surface characteristics and land surface scheme (see Chapter 2) were unchanged. During the peak of the Eemian interglacial at 125 ka BP, the land sea distribution was most certainly somewhat different as sea level was between 4 and 6 meters higher than at present. These relative sea level differences are based on dating of emergent coral reefs on tectonically stable coastlines distant from plate boundaries (Muhs et al. 1994)[158], a numerical modelling study based on a recalibration of ice core analyses from central Greenland (Cuffey and Marshall 2000)[44] and other analyses of Late Pleistocene sea level (e.g. see Rostami et al. 2000 and references therein)[196]. Considering that sea level would have dropped in the ensuing 10 ka after the Eemian optimum at 125 ka BP (McCulloch et al. 1999)[144] and the coarse nature of the model land-sea mask, the land-sea distribution in the model was fixed to that of the modern configuration.

All six simulations, three modern controls and three glacial inception experiments, were integrated to equilibrium based upon globally and monthly averaged SSTs. The simulations were then run for an additional 10 years of simulation to generate the climatology employed for the purpose of the analyses to follow. The time to reach equilibrium varied between 15 and 30 years depending upon the boundary conditions employed. For example the warmer control climate of AMS1 (See Appendix D) coupled with the cold climate induced by the 116 ka BP orbital configuration reduced the length of the spinup process. For the 3 modern control experiments, AMS9, AMIPS1, and AMS1 (See Appendix D), globally and annually averaged SSTs equilibrated to 16.50, 17.45 and 19.38 °C, respectively. The AMIPS1 simulation has implied oceanic heat transports which ensure a precise match with the observed globally and annually average AMIP2 SST. The large differences in global SSTs between the warm and cold biased experiments ensures a significant range of temperature so as to produce a range of simulated glacial inception conditions. The six simulations thus comprise 3 experiments designed to investigate the changes in the response of the climate system to changes in boundary conditions between 116 ka BP and present. The impact on simulated climate of a significant reduction in Northern Hemisphere summer insolation at mid to high latitudes will be central to the discussion that follows.

### 4.3. Results

I will discuss the main results obtained in this analysis of post Eemian glacial conditions in two subsections. To begin, I will discuss and intercompare the three modern simulated control climates in Appendix F. Next I will focus the discussion upon the main features of the simulated post Eemian

climate state. In particular, I will address the issue of glacial inception in the model used in this study and demonstrate no need for ad hoc assumptions or modification to the model boundary conditions as long as they are accurately constrained to the modern climate. In this second section I will also investigate a number of the dynamical feedback mechanisms that may be involved in the glacial inception process.

#### 4.3.1. Post Eemian Glacial Inception Climate

The change in forcing under the post Eemian orbital configuration at 116 ka BP is certain to influence much of the climatology at high polar latitudes in the model. According to the premise in the previous subsection, considerable understanding of the mechanisms involved in glacial inception can be garnered by investigating changes in climate north of the Arctic Circle. A logical starting point then is to investigate the extent of the perennial snow cover delivered by the model as a direct and/or non-direct response to the reduction in orbital summer insolation at the top of the atmosphere at 116 ka BP. Several of the mechanisms that influence the accumulation of snow cover at 116 ka BP will then be investigated in an attempt to address the complete climate system response to this decrease in orbital forcing.

Fig. 4.2 displays the accumulation of snowfall between August means separated by 10 years of simulation in the three glacial inception experiments. There is not a significant difference from using July, August or September in this analysis as they deliver essentially the same results. Changes in August snowfall are employed as the basis in which to determine perennial snowfall because this is the month in which snowfall reaches a minimum in the northern hemisphere. It may be safely concluded that the AMS1 warm biased experiment (Fig. 4.2a) does not deliver perennial snow cover except over central Greenland which has an accumulation maximum of  $6100 \text{ kg m}^{-2}$  over the 10 year period. The small patch of snow cover in Eastern Siberia in this simulation has a maximum value of  $83 \text{ kg m}^{-2}$  and is not likely significant considering that the model snow parameterization has a minimum threshold of  $10 \text{ kg m}^{-2}$  for a grid cell to be considered snow covered. If snow is present for all 10 annual cycles, values should be a minimum of  $100 \text{ kg m}^{-2}$  to be considered significant. It is also interesting to note the  $-700 \text{ kg m}^{-2}$  anomaly over southern Greenland in this experiment that indicates the presence of an ablation zone. The AMIPS1 experiment (Fig. 4.2b) has small patches of permanent snow cover over Eastern and Central Siberia with maxima of 433 and  $115 \text{ kg m}^{-2}$ . There is also a small area in the Canadian Arctic Archipelago that has extensive glaciation that exceeds  $1000 \text{ kg m}^{-2}$ , a number which agrees well with expectations for a location

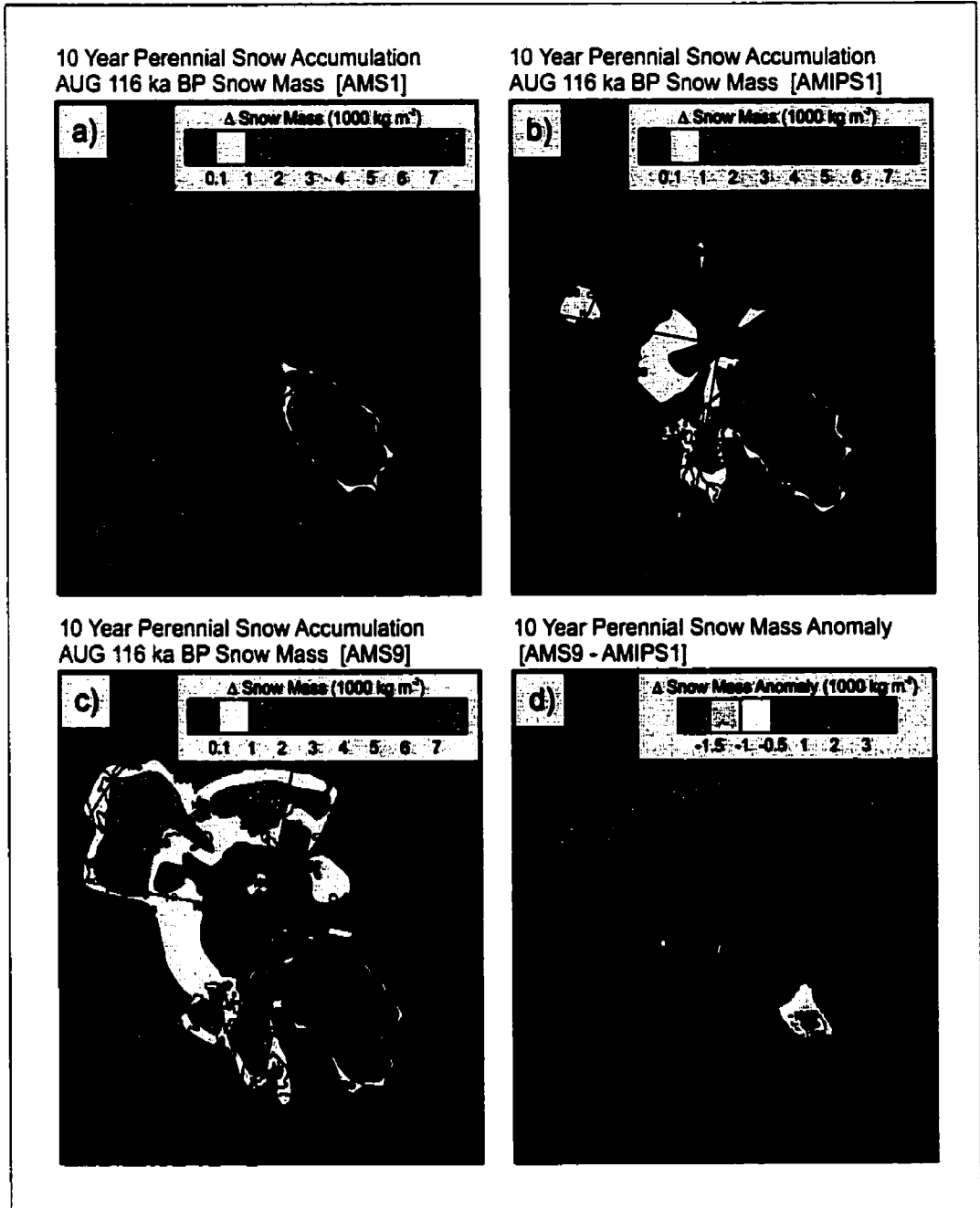


Figure 4.2: Northern hemisphere polar contour plots of August 10 year perennial snow accumulation for the (a) warm, (b) unbiased and (c) cold biased 116 ka BP experiments. Values above  $10 \text{ kg m}^{-2}$  are shaded. The contour interval is  $500 \text{ kg m}^{-2}$ . The difference between (c) and (b) is displayed in (d).

that is thought to have been one of the first nucleation sites of the Laurentide ice sheet (Andrews et al. 1985; Clark et al. 1993)[6][36]. Much of Greenland in this experiment also has perennial snow cover with an accumulation maximum at the centre of over  $7500 \text{ kg m}^{-2}$  over the 10 year period. The AMS9 experiment (Fig. 4.2c) has much larger regions of perennial snow cover. In particular, the glaciation in the Canadian Arctic Archipelago is now of slightly greater areal extent than in the AMIPS1 experiment. The eastern portion of Baffin Island, however, remains snow free in this simulation. This is a consequence of the topographic spectral anomaly in this region that was discussed previously in the present study. Other interesting regions in the AMS9 simulation include portions of Eastern and Central Siberia that have extensive amounts of snow accumulation with local maxima of more than  $2000$  to  $3000 \text{ kg m}^{-2}$  over the 10 year period.

There is much continuing debate as to whether Eastern Siberia ever entered a glacial state within the last ice age cycle. Lithological and biochemical evidence of glaciation from Lake Baikal in Eastern Siberia (Karabanov et al. 1998)[111] suggests abrupt and intense glaciation between 117 and 112 ka BP. AGCM (Dong and Valdes 1995)[54] and EBM/ISM (Tarasov and Peltier 1997a)[216] simulations indicate that this region is very susceptible to glacial initiation. However, given the fact that the two snow maxima in this region coincide precisely with regions of anomalous precipitation in the cold experiment, one is inclined to argue that this extensive glaciation is a model artifact. It is not unreasonable to expect this region to have been glaciated to some extent in the Post Eemian period, however the simulated snow accumulation over Eastern and Central Siberia may be too widespread given the amount of snowfall. In the Siberian region the maxima which exceed 2 meters ice equivalent in 10 years would result in very thick ice sheets. At this rate 200 meters of ice would collect in 1000 years, an amount which is excessive given that the most prominent ice sheets reached only 3 to 4 km thickness by Last Glacial Maximum (LGM) and that their growth required approximately 90 ka following glacial inception (Peltier 1994; Peltier 1998a)[170][172]. Of course, continental ice sheets evolve under a completely different regime of physics over these long time scales which involves ablation, ice calving and non-Newtonian flow processes. It is interesting to note that Alaska and Scandinavia are not expected to become glaciated on the basis of any of the three experiments, a point that will be a subject of investigation in what follows. If one considers the differences between the two experiments which do achieve perennial snow cover (Fig. 4.2d) we may note two features. Firstly, the Canadian Arctic Archipelago has about twice the accumulation in the AMS9 experiment as in the AMIPS1 experiment. Secondly, Central Greenland has greater accumulation (of more than  $1700 \text{ kg m}^{-2}$ ) in the AMIPS1 experiment while the AMS9 experiment has more accumulation in Southern Greenland. This may indicate a southward realignment of the

general circulation in this region and will be considered further in what follows.

In relation to future transient simulations of glacial inception that I intend to perform using an AGCM coupled to an Ice Sheet Model (AGCM/ISM) it is useful to consider the amount of land ice that would have been present after a period of 1000 years given the rate and area of snow accumulation as deduced using the three simulations of the glacial inception process. Neglecting positive feedbacks and glaciological processes such as ice calving that occur in regions where ice sheets extend onto the continental shelves, it is possible to infer the drop in sea level that would occur in each of the experiments. From warm to cold biased, the AMS1, AMIPS1 and AMS9 experiments imply sea level changes that would occur at a rate of 1.75, 2.72 and 4.94 m/ka given the permanent snowfall present in the northern hemisphere. It was also shown in Chapter 3 that the hydrological cycle in the CCCma AGCM is probably 20 to 25 % overly vigorous globally over land, but this is not likely to increase accumulation since evaporation is about 5 % more vigorous over land than precipitation in this AGCM. It is difficult to ascertain which simulation is most realistic for glacial accumulation rates given that an ISM would need to be coupled to the AGCM over time scales of more than a few thousand years. Also, Antarctic accumulation rates are not taken into consideration in this analysis. An estimate of the sea level change can be inferred from geologic data and data acquired from reduced model numerical simulations. Based upon the SPECMAP chronology and a coupled Energy Balance/Ice Sheet Model (EBM/ISM) simulation (Tarasov and Peltier 1997a)[216] one can estimate a change in sea level of approximately 10 meters during the climate minimum from approximately 117 ka BP to 112 ka BP. This value agrees well with the values obtained in the first two experiments, the second of which achieves glacial inception and appears to be the one that is most realistic.

In the remainder of this section I will investigate a number of mechanisms that may act in combination to control the Arctic perennial snow climatology simulated under 116 ka BP boundary conditions. Time series of the change in areal coverage by snow and sea ice in the Northern Hemisphere are presented in Fig. 4.3. The three simulations of snow coverage over land in Fig. 4.3a illustrate the degree of increase in snow coverage between the 116 ka BP simulations and the modern control simulations. The snow coverage in the observed data set (Foster and Davy 1988)[66] for each month of the year varies from a maximum of 40 million square kilometers in February to a minimum of about 2 million kilometers in August in the Northern Hemisphere (not shown). Each of the three control simulations has a temperature bias and therefore exhibits some degree of misfit to the observations. All three simulations tend to overestimate the snow cover from January to July with the warm biased AMS1 experiment being in best agreement during this time period. The

other two experiments, AMIPS1 and AMS9, match the observations well from August to December while the AMS1 experiment underestimates snow cover during this period (not shown). Dong and Valdes (1995)[54] found similar differences when comparing the predictions of the UGAMP (Universities Global Atmospheric Modelling Programme) AGCM with a NOAA (National Oceanic and Atmospheric Administration) observed snow climatology.

The 116 ka BP snow cover anomaly in the cold biased AMS9 experiment is quite different from that in the other two experiments (AMS1 and AMIPS1). The 116 ka BP snow cover anomaly simulated in the experiment with the cold control simulation has extensive snow cover over much of the year with a slightly smaller anomaly in winter. The largest anomaly is in late summer and early fall (Fig. 4.3a) with approximately 9 million km<sup>2</sup> more snow coverage than that observed in the control in August. The other two experiments that have unbiased (AMIPS1) and warm biased (AMS1) control temperatures in the summer northern hemisphere display similar anomalies except for the period from August through October where the AMIPS1 experiment has greater coverage as shown in Fig. 4.2. It has previously been argued that the spring snowfall anomaly and the corresponding temperatures at 116 ka BP during this season are crucial in maintaining the summer snow coverage in a glacial inception experiment (e.g. de Noblet 1996)[49]. The spring anomaly in the current experiment demonstrates that there is an increase of approximately half a million to one million km<sup>2</sup> in May and June areal snow coverage in the unbiased AMIPS1 experiment compared to that delivered by the warm biased AMS1 experiment. According to the present experiments, it is the late summer and early fall snow cover that seems to be most important in attaining perennial snow cover, a result that is in accord with the Milankovitch hypothesis that summer snowfall is crucial to the glacial inception process. This is an important result of the present analysis. The AMIPS1 experiment has a late summer-early fall snow cover anomaly that is greater than that delivered by the warm biased AMS1 experiment and decreases from three to one million km<sup>2</sup> from August to October. The AMIPS1 experiment has almost 5 million km<sup>2</sup> more snow coverage in fall than that observed in the corresponding control experiment and about 3 million km<sup>2</sup> more than is delivered by the warm biased (AMS1) experiment at 116 ka BP, a model that does not initiate perennial snow cover in the northern hemisphere.

The areal coverage and thickness of sea ice are variables which are difficult if not impossible to model properly using a thermodynamic sea ice model. Ice dynamics play a crucial role in determining the flow and thickness of sea ice at various times of the year (Pollard and Thompson 1994b)[182]. Compared with AMIP2 observed sea ice coverage all three modern control simulations tend to underestimate the modern annual cycle of sea ice cover (not shown). The anomalies in areal coverage

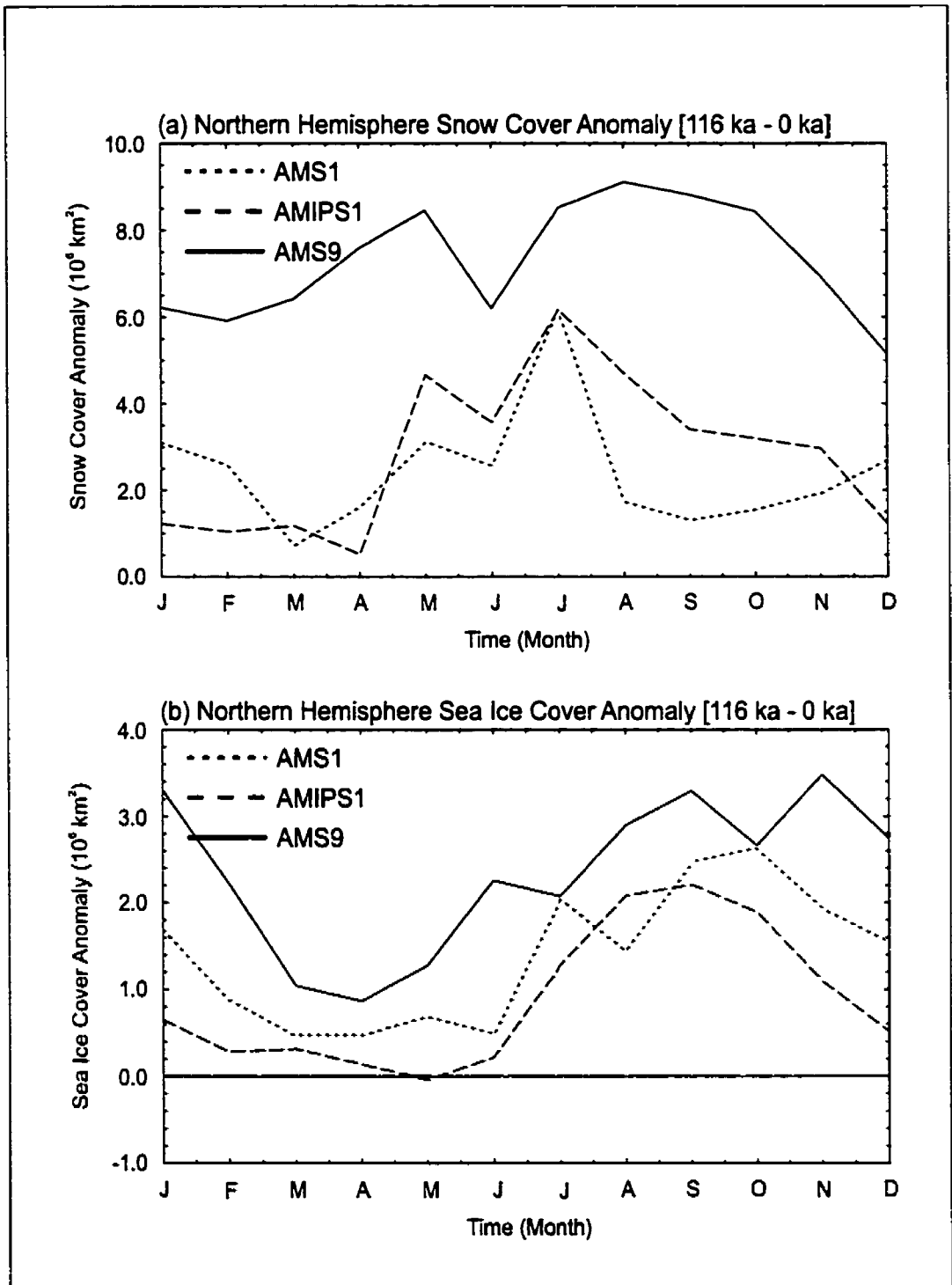


Figure 4.3: Time series of northern hemisphere (a) snow cover and (b) sea ice cover anomalies in millions of km<sup>2</sup> for the warm, cold and unbiased 116 ka BP experiments.

of sea ice at 116 ka BP (Fig. 4.3b) are characterized by similar time series in all three experiments. The extent of sea ice cover at 116 ka BP, at any particular time in the year, is likely to influence the amount of perennial snow cover at high latitudes. Extended sea ice distribution in spring, summer and fall are likely to moderate oceanic affects over land in these high latitude polar regions. Larger areas of sea ice cover at 116 ka BP would likely cool the surrounding land masses through albedo affects in the radiative balance at the surface and by restricting ocean-atmosphere heat and moisture exchange in the Arctic hemisphere. Dong and Valdes (1995)[54] investigated the sensitivity to sea ice extent in a glacial inception experiment at 115 ka BP and reported that only the simulations which employed a thermodynamic slab ocean would attain perennial snow cover under post Eemian boundary conditions. Vavrus (1999)[226] did an extensive study of the differences in climate state obtained by employing thermodynamic as opposed to dynamic sea ice models in an AGCM with solar input based upon 6 ka BP and 115 ka BP orbital insolation. The changes in the present study agree well with those obtained in the Vavrus (1999)[226] simulations that employed a thermodynamic sea ice model. The study by Vavrus (1999)[226] using the dynamical sea ice model found that ice motion more than doubles sea ice coverage under 115 ka BP orbital forcing. Vavrus' analyses suggest that the introduction of the dynamical sea ice model induces a positive feedback on the climate system under cold perturbations via an increase in sea ice thickness, expansion of sea ice margins and a narrowing of sea ice leads.

The 116 ka BP anomalies in August are characterized by increased sea ice distributions of two to three million km<sup>2</sup> in all three simulations. It is interesting to note that the sea ice anomalies in the warm and cold biased experiments display a similar behaviour to one another while that of the AMIPS1 unbiased experiment is characterized by a more uniform seasonal evolution. The behavioural differences likely arise due to the values that were prescribed for under ice upward heat fluxes in the sea ice model, where the AMS1 and AMS9 experiments have the same under ice heat flux. The spring season appears to be the season in which sea ice changes between 116 ka BP and modern are least significant. This is a period just after the time of maximum sea ice coverage and the slight difference between this result is most probably a consequence of the small insolation difference in winter between the 116 ka BP experiment and the modern control.

The 116 ka BP zonal land surface temperature anomalies in the Arctic circle (60 to 90 °N) for the entire year are displayed in Fig. 4.4a. All three experiments show that, on average, 116 ka BP temperatures are always below those simulated in the modern control simulations. The majority of the decreases in surface temperature in each of the experiments occurs from June through to December with the minimum in September. The magnitudes of the differences are very similar in

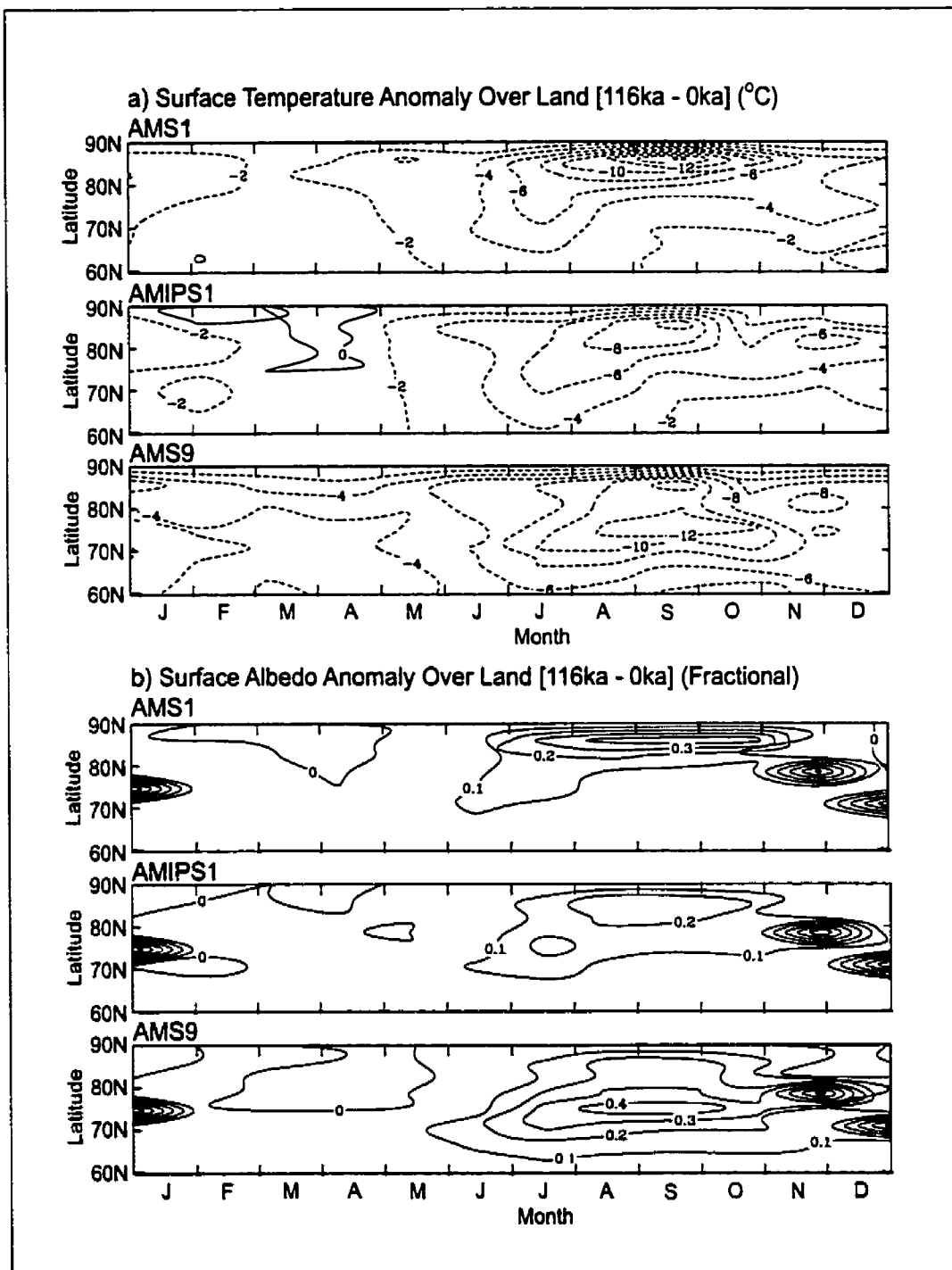


Figure 4.4: Arctic time series of (a) surface temperature and (b) surface albedo anomalies over land in the warm biased, unbiased, and cold biased experiments. The contour interval for the temperature is  $2^{\circ}\text{C}$  while that for the albedo is 0.1. Negative values are dashed.

each of the experiments with 116 ka BP zonal land anomalies displaying minima of -10 to -12 °C. The difference between each set of experiments, from warm to cold biased lies in the southward latitudinal position of the cold anomalies, with the cold biased AMS9 experiment displaying minima at 75 °N latitude while the other two experiments (AMS1 and AMIPS1) have minima at 85 °N. However, the isotherms in the AMIPS1 experiment are positioned further southward relative to the AMS1 experiment in summer. This southward movement of the region of strongest thermal gradient is likely to strengthen the baroclinicity along the polar front in each of the experiments. The spatial distribution of the summer polar temperature anomalies (not shown) are quite similar in each experiment and all three experiments produce Arctic land temperature anomalies at 116 ka BP that are significant at the 99% confidence level according to a univariate t-test. The maximum summer temperature decreases are in Eastern and Central Siberia and over the Canadian Arctic Archipelago and have local minima that drop more than -6 °C, -8 °C and -13 °C in the AMS1, AMIPS1 and AMS9 experiments, respectively. Scandinavia and Alaska also experience decreases in temperature but of approximately half the magnitude as the other glacially sensitive regions.

The decreases in surface temperature can also be directly correlated with changes in surface albedo. The changes in the annual cycle of Arctic zonally averaged surface albedo at 116 ka BP (Fig. 4.4b) display the same southward migration of the anomalies in summer as was observed in surface temperature. The increases in surface albedo progressively increase in southward areal extent from the warm biased AMS1 experiment to the cold biased AMS9 experiment. The changes in the AMS1 experiment are actually greater than those of the AMIPS1 experiment but only over Greenland. The AMS9 experiment has zonal average albedo changes of greater than 0.4 at 75 °N latitude. This distribution of temperature and surface albedo changes at 116 ka BP is a good example of the positive ice-snow-albedo temperature feedback which strengthens as glacial inception progresses and extends southward over the millennia. These changes in surface albedo are a major component influencing the radiative balance in the land surface scheme employed within this model. The changes in surface temperature and surface albedo have minima and maxima which lag the decreases in insolation at 116 ka BP by approximately two to three months (see Fig. 1.4d).

The energy balance in the land surface scheme in this model is governed by the balance of absorbed solar radiation at the surface, the subsequent emission of thermal radiation and the exchange of latent and sensible heat fluxes from the surface to the atmosphere (see Chapter 2 for a complete description). The change in soil moisture between liquid and solid phases along with the melting of snow cover also influence the surface energy balance in this model. The 116 ka BP anomalies in the absorbed shortwave radiation at the land surface in the model (Fig. 4.5a) for the annual cycle in

the Arctic circle reveals a pattern that is similar to the changes in temperature and albedo but with minima that lag the minima in the top of the atmosphere (TOA) insolation anomaly by one month. It is interesting to note that the decrease in absorbed shortwave at the surface is substantially greater than that which is seen in the 116 ka BP (TOA) insolation anomaly. The July anomalies display minima at 75 °N in the unbiased AMIPS1 and cold biased AMS9 experiments that are more than -50 and -80 W m<sup>-2</sup>, respectively. The changes in July albedo, which result from increases in snow cover, appear to explain much of the decrease observed in the absorbed shortwave radiation at 116 ka BP. The changes in total cloud cover in July over land range between -4 and -6 % in the three experiments (not shown) which implies that this component of the radiative balance allows for more shortwave absorption in summer at 116 ka BP. This decrease in cloud cover would allow for more shortwave radiation to reach the surface but also would allow for more longwave terrestrial emission to space. The decreases in the net terrestrial longwave radiation emitted from the land surface over the course of the Arctic annual cycle are illustrated in Fig. 4.5b for the three 116 ka BP experiments. The positive anomalies (maxima) in this figure indicate that there are decreases in the net upward emitted longwave radiation at 116 ka BP. The most interesting aspect of these figures is that the maxima in the anomaly occurs two months after the minima in absorbed shortwave radiation. The zero contour of the longwave anomaly also runs directly through the solar absorbed minimum in July in each of the three experiments. There is also a slight increase of approximately 5 W m<sup>-2</sup> in net longwave south of 70 °N in summer indicating that more longwave radiation may be emitted to space due to decreases in cloud cover and decreases in CO<sub>2</sub> concentration in the atmosphere at 116 ka BP. This change is more likely a result of a decrease in evaporative cooling and therefore a warmer surface and will be discussed in what follows. The two month delay in the decrease in net longwave from the surface as compared with the shortwave radiation may simply result from the fact that there is more snow cover in August, September and October in the glacial inception experiments and thus less terrestrial emission from the cooler surface at 116 ka BP. The increased amounts of soil moisture of 20 to 30 kg m<sup>-2</sup> that are present at 116 ka BP in August and September (not shown) are likely to influence the amount of emitted longwave radiation. Increased soil moisture would alter the energy balance at this period of the year by increasing the thermal heat capacity of the land at 116 ka BP. The changes in evaporation and precipitation that will be discussed in what follows may also explain this longwave radiative phase lag.

The changes in latent and sensible heat fluxes are displayed in Figs. 4.6a and 4.6b, respectively. Each of these components of the surface energy balance have maxima that occur in July and indicate a decrease in the upward latent and sensible heat fluxes from the surface. As with the solar radiation

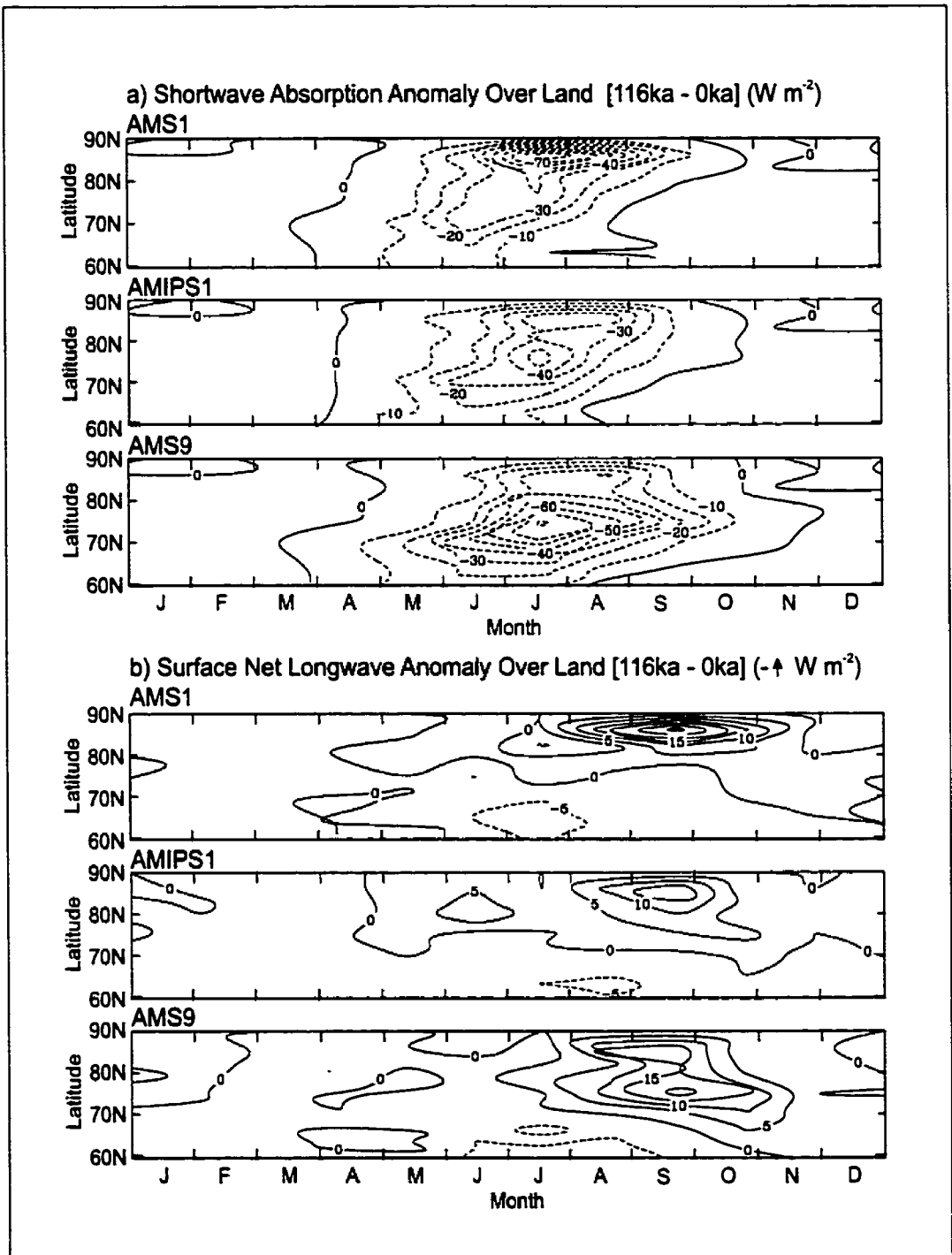


Figure 4.5: Arctic time series of (a) shortwave absorbed radiation and (b) surface net longwave radiation anomalies over land in the warm biased, unbiased, and cold biased experiments. The contour interval for the shortwave radiation is  $10 W m^{-2}$  while that for the longwave radiation is  $5 W m^{-2}$ . Negative values are dashed.

absorbed at the surface, the same characteristic patterns are observed in Fig. 4.6 for the surface fluxes. The decreases in latent surface heat fluxes from the Arctic land in summer range from 30 to 40  $\text{W m}^{-2}$  in the three glacial inception experiments, with the experiments with colder controls displaying the greatest changes (Fig. 4.6a). Likewise, the decreases in sensible heat flux from the surface at 116 ka BP are similar in character to the changes observed in latent heat flux but have summer decreases in the upward flux that range from 10 to 15  $\text{W m}^{-2}$  (Fig. 4.6b). At the lower boundary of the atmosphere, the transports of heat and water vapor across the earth's surface are proportional to the vertical gradient in temperature and specific humidity, respectively. These turbulent fluxes at or near the surface also depend on surface roughness, wind shear and thermal stratification (Peixoto and Oort 1992; Boer 1984)[168][20]. The evaporation at the surface in GCMII also depends upon the moisture availability and evapotranspiration slope factor which is a function of soil and vegetation type when the surface is snow free (see Chapter 2). Under snow covered conditions, the latent heat flux is solely determined by the potential evapotranspiration. Therefore, at 116 ka BP the summer evaporation changes observed in the Arctic circle are by and large determined by the vertical specific humidity gradient at the surface since the snow covered surface is considered saturated. In contrast to this, the modern evaporation during summer will also be a function of the moisture availability at the surface and the evapotranspiration slope factor. As was seen in Chapter 2, which investigated the influence of changes in soil moisture parameterization under mid-Holocene boundary conditions, the nature of the parameterizations must be considered when evaluating the behavior of the model under significantly different boundary conditions.

The July changes in surface heat fluxes do not come close to balancing the decreases in absorbed shortwave radiation. For example, the cold biased AMS9 experiment has a deficit of approximately 20 to 25  $\text{W m}^{-2}$  that is not accounted for in July at 75 °N. A decrease of 20  $\text{W m}^{-2}$  in the emitted thermal radiation is, however, observed two months later in the AMS9 annual cycle and may simply indicate that there is less energy available at the surface for snow melt during the summer season at 116 ka BP. A plot of the sum of the four surface flux anomalies (not shown) indicated that the time evolution of the surface temperature is changed at 116 ka BP and that energy is being employed for maintaining snow cover or melting snow cover. In this scenario the summer land is warming less quickly at 116 ka BP in summer and cooling less quickly in fall. This would in turn correspond to less snowmelt in summer and decreased snow formation in fall at 116 ka BP.

The vertical transport of heat and water vapour in the atmosphere by turbulent atmospheric boundary layer processes as well as horizontal transport by the atmospheric circulation primarily determines the behaviour of climate system. These atmospheric processes are of even greater impor-

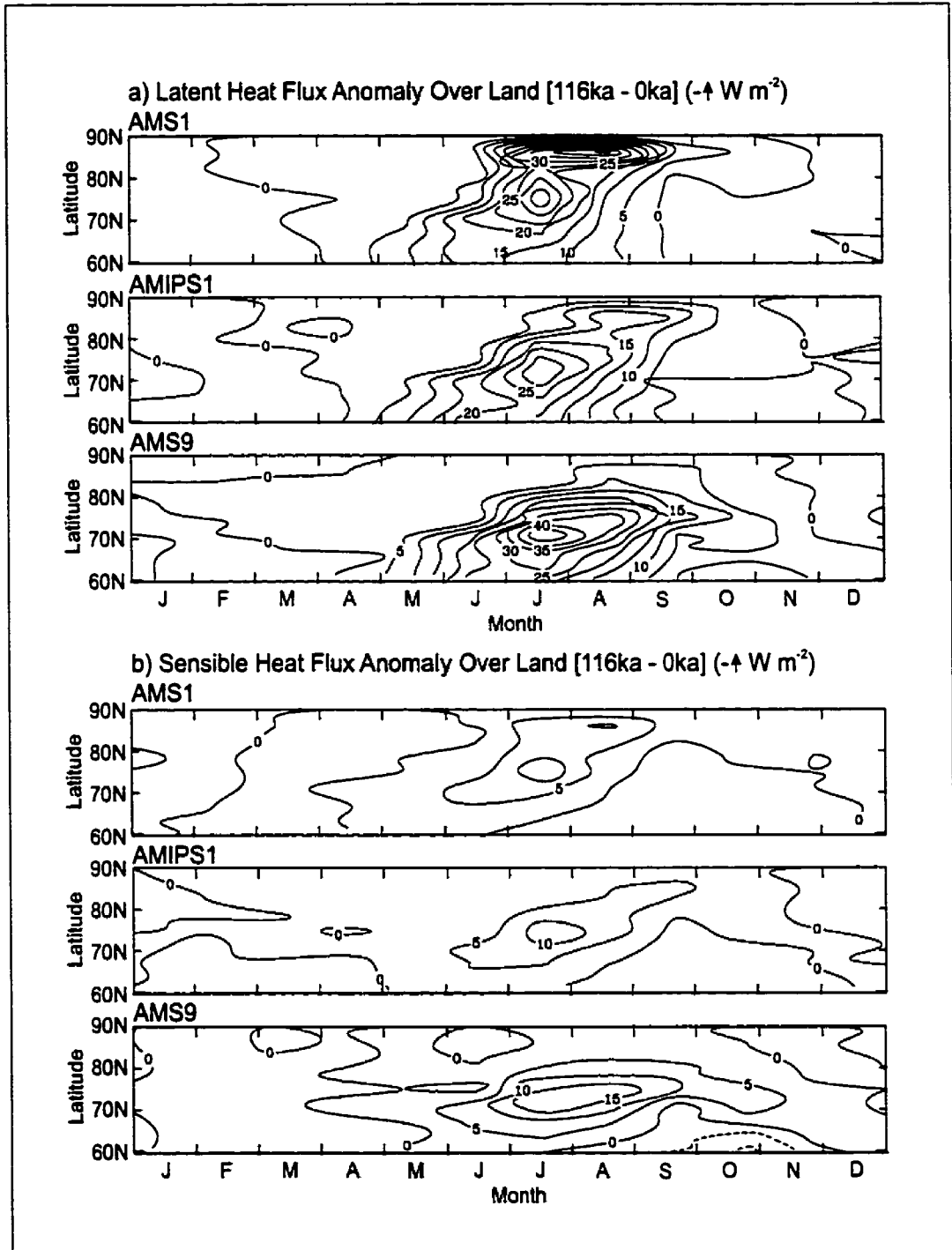


Figure 4.6: Arctic time series of (a) latent and (b) sensible heat flux anomalies over land in the warm biased, unbiased, and cold biased experiments. The contour interval is 10 W m<sup>-2</sup>. Negative values are dashed.

tance in considering how changes occur in climate state in response to changes in boundary forcing. Chapter 3, which investigated LGM climate using the GCMII model has demonstrated that the changes in the hydrological cycle under cold climate perturbations such as those observed at 21 ka BP, have a significant influence on snow accumulation. The enhanced reduction in evaporation over precipitation was found to lead to a net increase in the precipitation minus evaporation (P-E) anomaly over the Laurentide ice sheet at LGM. Thus, even though the vigour of the atmospheric components of the hydrological cycle are significantly decreased in cold climate scenarios, there can nevertheless be a positive impact on the terrestrial storage component of the hydrological cycle. This phenomenon is precisely what is occurring under the cold climate perturbation at 116 ka BP, except that the changes are confined to the North Polar region. A time series of the precipitation and evaporation north of the Arctic circle (Fig. 4.7) reveals the temporal evolution of this mechanism at 116 ka BP. The precipitation and evaporation are both dependant on the atmospheric moisture content which is non-linearly related to the changes in atmospheric temperature through the Clausius-Clapeyron relation. The 116 ka BP anomalies in precipitation (Fig. 4.7a) and evaporation (Fig. 4.7b) are negative in summer in all three glacial inception experiments. The changes in precipitation have minima that range between -0.4 and -0.6 mm/day in July and August. The evaporation anomalies at glacial inception range from -1.0 to -1.6 mm/day in July at 70 to 75 °N latitude, with the greatest changes occurring in the AMS9 cold biased experiment. The changes in evaporation are, of course, directly proportional to the decreases in latent heat flux from the surface (Fig. 4.6a) and are well correlated with the summer reduction of TOA solar insolation. The precipitation anomalies occur more evenly over summer and fall in each of the three experiments with the changes in summer being most intense. A time series of the P-E anomaly over the polar land regions shows a distinct maximum in July, August and September in all three experiments (not shown). In October and November the P-E anomaly over the polar land mass is negative which provides for anomalous addition of latent heat energy to the atmosphere at 116 ka BP and may contribute to the reduction in net upward longwave at the surface (Fig. 4.5 b) through increased downward emission from the atmosphere. The summer P-E anomaly plays a vital role in maintaining the summer snowfall during glacial inception. Increased summer P-E over polar land masses at 116 ka BP is a strong candidate for a positive hydrological cycle feedback mechanism on ice sheet expansion over millennial timescales.

The action of this feedback mechanism over land in summer is investigated in greater detail through examination of the atmospheric moisture balance equation:

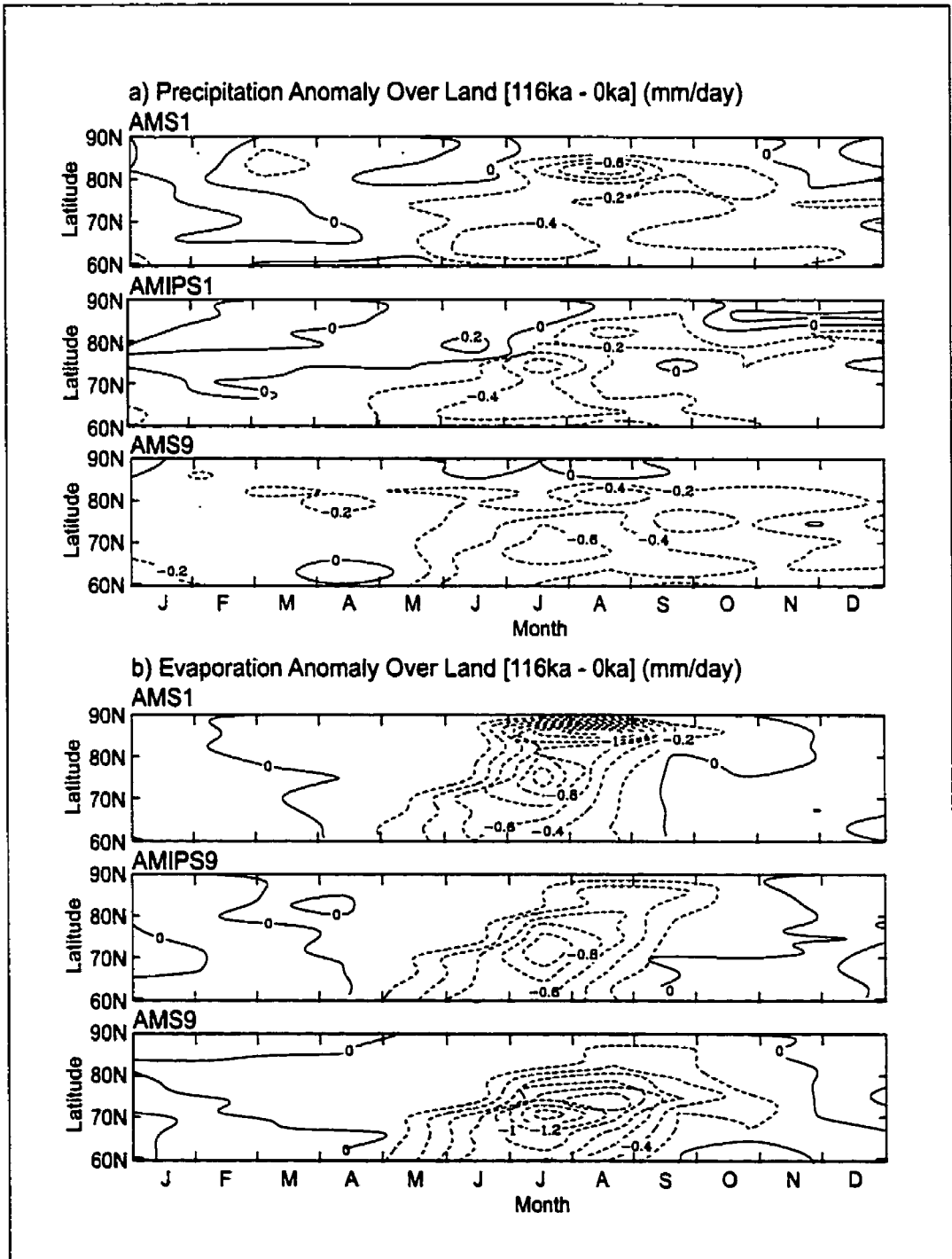


Figure 4.7: Arctic time series of (a) precipitation and (b) evaporation anomalies over land in the warm biased, unbiased, and cold biased experiments. The contour interval is 0.2 mm/day. Negative values are dashed.

$$\frac{\partial W}{\partial t} + \nabla \cdot \mathbf{q} = E - P. \quad (4.1)$$

In this equation the excess of evaporation over precipitation,  $(E(\theta, \phi, t) - P(\theta, \phi, t))$ , at the Earth's surface is balanced by the local time rate of change of vertically integrated specific humidity in pressure coordinates,  $W = g^{-1} \int_0^{p_0} q(\theta, \phi, p, t) dp$ , and by the divergence of the total atmospheric water vapor transport,  $\mathbf{q} = g^{-1} \int_0^{p_0} q(\theta, \phi, p, t) \mathbf{u}(\theta, \phi, p, t) dp$ . The vertical integrals are from the surface,  $p_0$ , to the top of the atmosphere, while  $\theta$  is the latitude coordinate and  $\phi$  is the longitude coordinate. In the atmospheric branch of the hydrological cycle, the time rate of change of precipitable water,  $\partial W / \partial t$ , is usually very small compared with the divergence and source terms over global scales and on annual average (Peixoto and Oort 1992)[168]. However, on a high latitude seasonal basis this is no longer the case. Following Peixoto and Oort, equation (4.3) can be reformulated in terms of the temporal and spatial average over a region bounded by a conceptual vertical wall at 60 °N latitude that results in a relation for the inflow and outflow of atmospheric water vapour contained within the Arctic region:

$$\left[ \frac{\partial W}{\partial t} \right] = F_v + [E - P]. \quad (4.2)$$

In this equation the local rate of change of total precipitable water  $[\partial W / \partial t]$  contained within the atmosphere north of the Arctic circle is balanced by the polar excess of evaporation over precipitation,  $[E - P]$ , and by  $F_v = g^{-1} \int_0^{p_0} \int_0^{2\pi} v(\frac{\pi}{3}, \phi, p, t) q(\frac{\pi}{3}, \phi, p, t) d\phi dp$ , the northward meridional flux of water vapour across the vertical wall at 60 °N.

By considering the atmospheric branch of the polar hydrological cycle as described by equation (4.4), we can investigate the nature of positive or negative feedbacks occurring as a result of the strong reduction in polar insolation at 116 ka BP. Fig. 4.8 displays the three quantities in equation (4.4) for the region north of 60 °N latitude for the three modern controls and three 116 ka BP experiments. The annual cycle of the area averaged rate of change in total precipitable water and total  $[E - P]$  are displayed in Figs. 4.8a and 4.8b, respectively, while the annual cycle of the total northward transport of water vapor into the Arctic circle is displayed in Fig. 4.8c. The rate of change in precipitable water has a maximum in late spring/early summer and a minimum in late summer/early fall. The maxima and minima in the modern controls range from  $\pm 65$  to  $\pm 95$   $\text{kg m}^{-2} \text{ yr}^{-1}$  ( $= \pm 65$  to  $\pm 95$   $\text{mm yr}^{-1}$ ) owing to the increased moisture content of the atmosphere in summer in the cold to warm biased experiments. The 116 ka BP experiments range from  $\pm 35$  to

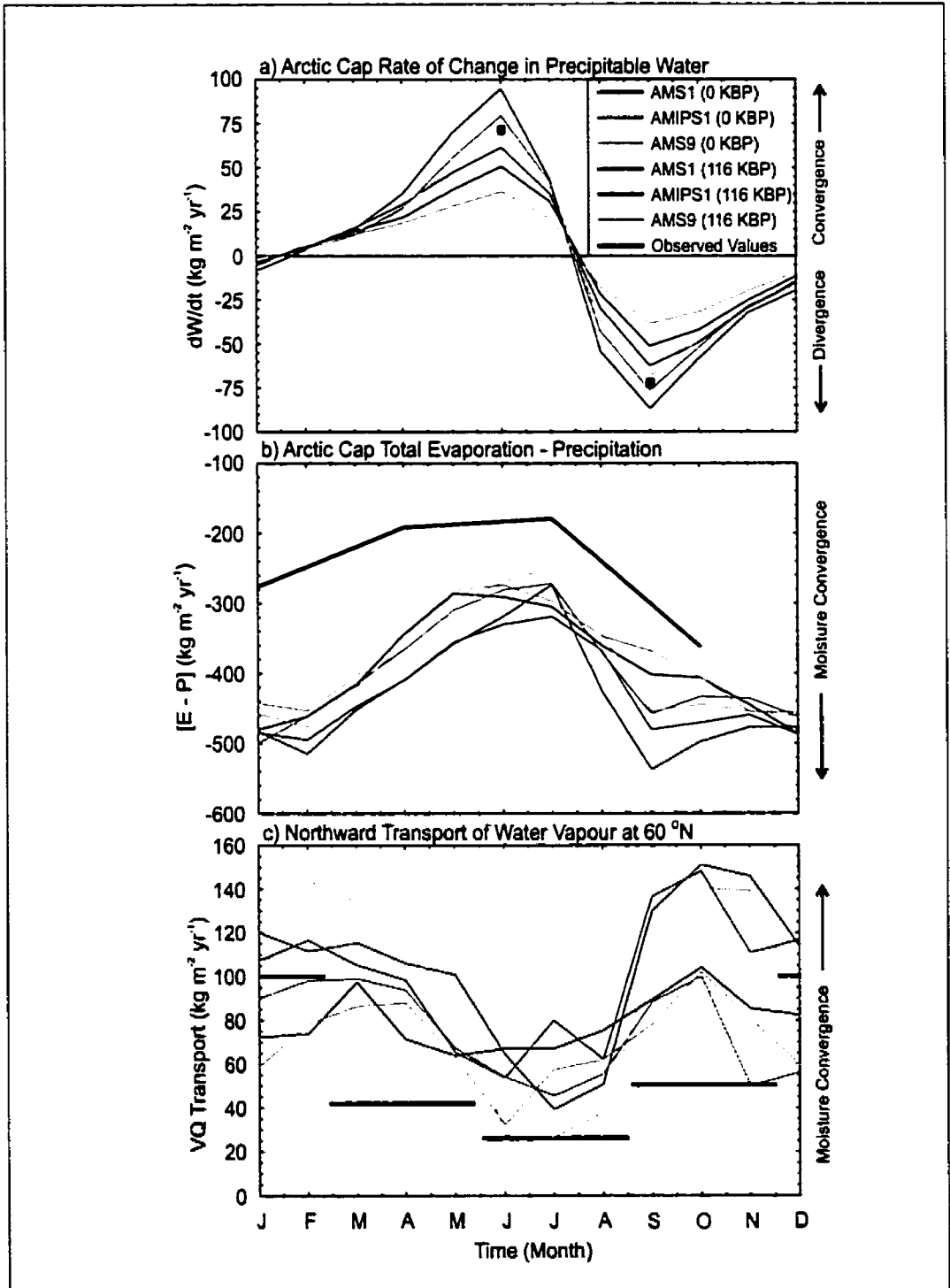


Figure 4.8: Time series of (a) the rate of change in total Arctic precipitable water, (b) Arctic E-P and (c) northward transport of water vapour into the Arctic circle for the three modern control and three 116 ka BP experiments. Observed values are indicated in black. Arrows indicate the direction of increasing divergence and convergence. Units are in  $\text{kg m}^{-2} \text{yr}^{-1}$ .

$\pm 60 \text{ mm yr}^{-1}$ . The observed maximum and minimum rates of change in precipitable water are slightly more than  $\pm 70 \text{ mm yr}^{-1}$  (Peixoto and Oort 1992)[168]. In each of the modern controls and 116 ka BP experiments there is also an excess of precipitation over evaporation all year round in the Arctic region with a maximum of  $500 \text{ mm yr}^{-1}$  in winter and  $300 \text{ mm yr}^{-1}$  in summer. The values from the modern control experiments are substantially more than the values obtained from observations (Legates and Willmot 1990)[126], which suggest the model polar  $P - E$  is excessive by approximately  $100$  to  $200 \text{ mm yr}^{-1}$  depending upon the time of year (Fig. 4.8b). The total meridional transport of moisture by all motions across the Arctic Circle not surprisingly has the same characteristic annual cycle as  $P - E$  with a winter maximum of between  $80$  and  $120 \text{ mm yr}^{-1}$  and a summer minimum of between  $40$  to  $80 \text{ mm yr}^{-1}$  in the modern controls and 116 ka BP experiments. Compared with the meridional transports derived from observed specific humidity and wind velocities (CMC: Mitchell et al. 1993 and Mitchell et al. 1996)[152][152], the model controls agree well with the general behaviour of the observed transport but again flow is too strong into the polar regions, most notably in the fall (Fig. 4.8c). It is not surprising that the model quantities do not balance, which likely results from a combination of the procedure used for eliminating negative specific humidities (spectral hole filling) that is employed in the model (McFarlane et al. 1992)[146] and the limited resolution of the model in the polar cap. The observed values do not balance either, suggesting a lack of spatial and temporal coverage at high polar latitudes. If we take into account the deficiencies present in the model and in the data, this comparison may nevertheless reveal a great deal of information about the dynamics of the climate change that is occurring in the polar region under the significantly modified solar forcing at 116 ka BP.

The differences between 116 ka BP and modern for the three quantities in equation (4.4) are displayed in Fig. 4.9. The 116 ka BP anomalies in the rate of change in total precipitable water in the polar cap display uniform changes between the warm biased AMS1, unbiased AMIPS1 and cold biased AMS9 experiments suggesting that the total amount of polar precipitable water is linearly correlated with the polar mean temperature in each of the simulations (Fig. 4.8a). The total polar precipitable water has a bell shaped annual cycle with a maximum value in summer and a minimum value in winter (time integral of Fig. 4.8a). The differences in the rate of change of precipitable water between the three modern and three 116 ka BP simulations are almost identical (Fig. 4.9a). This indicates a reduction in the rate of increasing polar precipitable water content in late spring of  $-30 \text{ mm yr}^{-1}$  and a mollified rate of decreasing polar precipitable water content in late summer of  $25 \text{ mm yr}^{-1}$  between 116 ka BP and modern. The similarities in the anomalies of the three experiments indicates that the 116 ka BP anomalies of the rate of change in polar precipitable

water is not dependant on the modern control simulation. Negative values of summer differences in  $E - P$  between 116 ka BP and modern (Fig. 4.9b) indicate increased anomalies of total polar  $P - E$  over land and ocean of approximately 25 to 40 mm yr<sup>-1</sup> in all three experiments. There is also a decrease in  $P - E$  over the same region in fall which indicates there is less precipitation over evaporation in this season at 116 ka BP. Thus, in summer there is more convergence from the  $P - E$  component in the polar cap at 116 ka BP considering  $dW/dt \simeq 0$ . The fall increase in evaporation over precipitation in all three simulations arises in part due to the weakening in the rate at which the content of polar precipitable water is decreasing from the atmosphere in fall. This may also explain the decrease in the surface net upward longwave (Fig. 4.5b) over land at this time of the year through the evaporative cooling mechanism. From equation (4.4), the decrease in summer evaporation over summer precipitation at 116 ka BP (Fig. 4.7) implies a local moisture convergence anomaly over land since  $dW/dt \simeq 0$  between July and August in all the simulations (Fig. 4.9a). The 116 ka BP anomaly in northward transport of moisture in summer of approximately 20 to 40 mm yr<sup>-1</sup> in all three experiments indicates convergence of moisture into the Arctic Polar Cap region at this time of the year (Fig. 4.9c). This suggests a balance with the increased summer  $P - E$  component as  $dW/dt \simeq 0$  in mid summer. The fact that each biased experiment displays the same behaviour in summer but not necessarily in winter implies that this climate mechanism is exerting a strong influence when a strong reduction in TOA insolation at 116 ka BP is implemented in the model. This cold perturbation positive feedback mechanism is a result of the increased northward moisture transport into the polar cap and compensating increased  $P - E$  while the temporal change in moisture content of the summer atmosphere remains nearly the same. Although the polar atmosphere is dryer at 116 ka BP, the increased moisture convergence over land that feeds summer snowfall may be considered as the end product of a stronger polar atmospheric "cryogenic moisture pump". This mechanism is ultimately a product of the large drop in the summer insolation at these high latitudes.

The modern simulated vertically integrated annual mean total water vapour transport reveals the circumpolar nature of the transport of moisture about the Arctic Circle. The modern simulated transport for the unbiased AMIPS1 experiment is displayed in Fig. 4.10a. The other AMS1 warm biased and AMS9 cold biased simulations have total water vapor transports that are very similar in structure to the AMIPS1 simulation (not shown). The general circulation of this quantity agrees fairly well with the observed circulation (e.g. see Chapter 3) but with an intensity that is increased by approximately 35 % in magnitude along the mid-latitude jet streams owing to the overly intense simulation of the hydrological cycle in this model. The differences between simulated

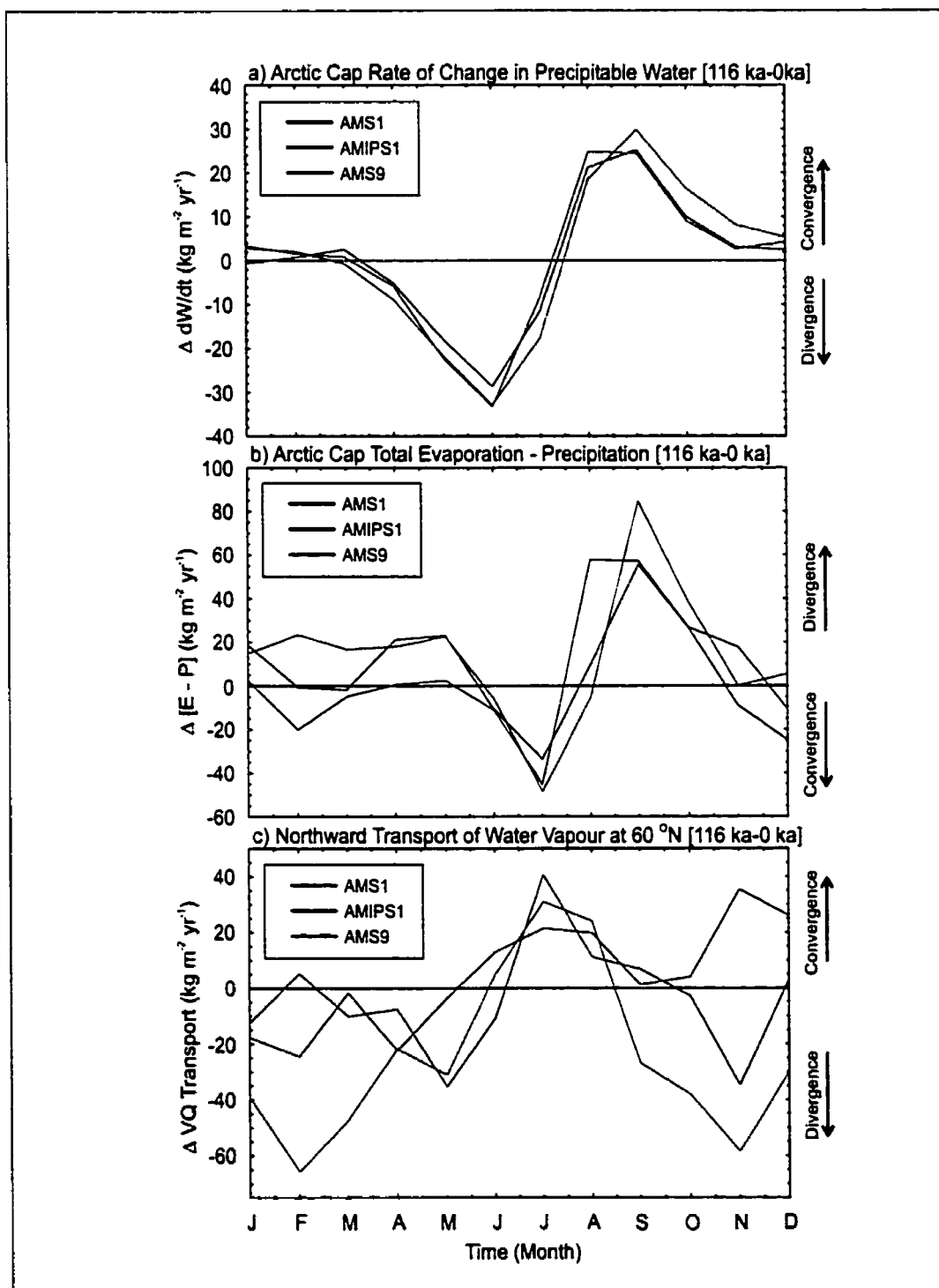


Figure 4.9: Time series of the 116 ka BP anomalies for (a) the rate of change in total Arctic precipitable water, (b) Arctic E-P and (c) northward transport of water vapour into the Arctic circle. Arrows indicate the direction of increasing divergence and convergence anomalies. Units are in  $\text{kg m}^{-2} \text{yr}^{-1}$ .

and observed transports are in much better agreement at high latitudes owing to the much drier conditions present in the atmosphere in this region. The atmospheric water vapor transport at high latitudes is influenced by the orography and the mid-latitude jet stream maximum over the Eastern Atlantic and Eastern Pacific Oceans. In the Western Pacific just south of the Arctic Circle moisture is advected northward over Alaska because of the planetary wave forcing in the atmosphere by the Western Cordillera. In the modern simulation some of the moisture transport over Alaska is split into two branches, one directed over Eastern Siberia and the other much stronger branch flowing over the Canadian Arctic Archipelago. A similar atmospheric flow pattern occurs over the Scandinavian region where moisture is again forced northward across the Arctic Circle and across Central Siberia through stationary wave forcing. Considering the circumpolar vortex structure of the total atmospheric water vapour transport within the Arctic Circle and the regions of perennial snow cover at 116 ka BP, we can see that the nucleation regions (Fig. 4.2) lie in the arid regions just to the north of the outflow branch of the total water vapour transport across the Arctic Circle. It is also interesting to note that the regions that did not nucleate, namely Alaska and Scandinavia, lie in the inflow branch of the atmospheric water vapour transport across the Arctic Circle. The fact that Alaska did not experience significant glaciation in the period subsequent to the 5e/5d transition is clearly in excellent record with this result. The fact that Fennoscandia did become glaciated, however, suggests that the glaciation of Canada may have been required before this could occur, the result of which could well have been a repositioning of the inflow branch of the atmospheric water vapour transport across the Arctic Circle away from the Scandinavian region.

The 116 ka BP total water vapour transport anomalies in the three glacial inception experiments, that range from warm to cold biased, are displayed in Figs. 4.10b through 4.10d. A common feature characteristic of all three flow anomalies is that the transport vectors are in a direction that is opposite to the circumpolar moisture current in the modern control simulation. Either the circumpolar current is reduced in magnitude in the cold post Eemian experiments or there is a southward migration of the main branches of the mid-latitude moisture transport or a combination of both. The warm biased AMS1 and unbiased AMIPS1 anomalies have features that are very similar to one another. One common feature is the decrease in outflow of moisture from the Canadian Arctic Archipelago as indicated by the tongue like anomaly in this region. This feature is also seen in the cold biased AMS9 experiment. This may be one of the reasons why there is an increase in moisture convergence over the Arctic land masses simulated during 116 ka BP summer conditions. The same phenomenon is occurring in the eastern-most portion of Siberia where the outflow is reduced in magnitude by approximately 20 % in all three glacial inception experiments. It is also interesting to

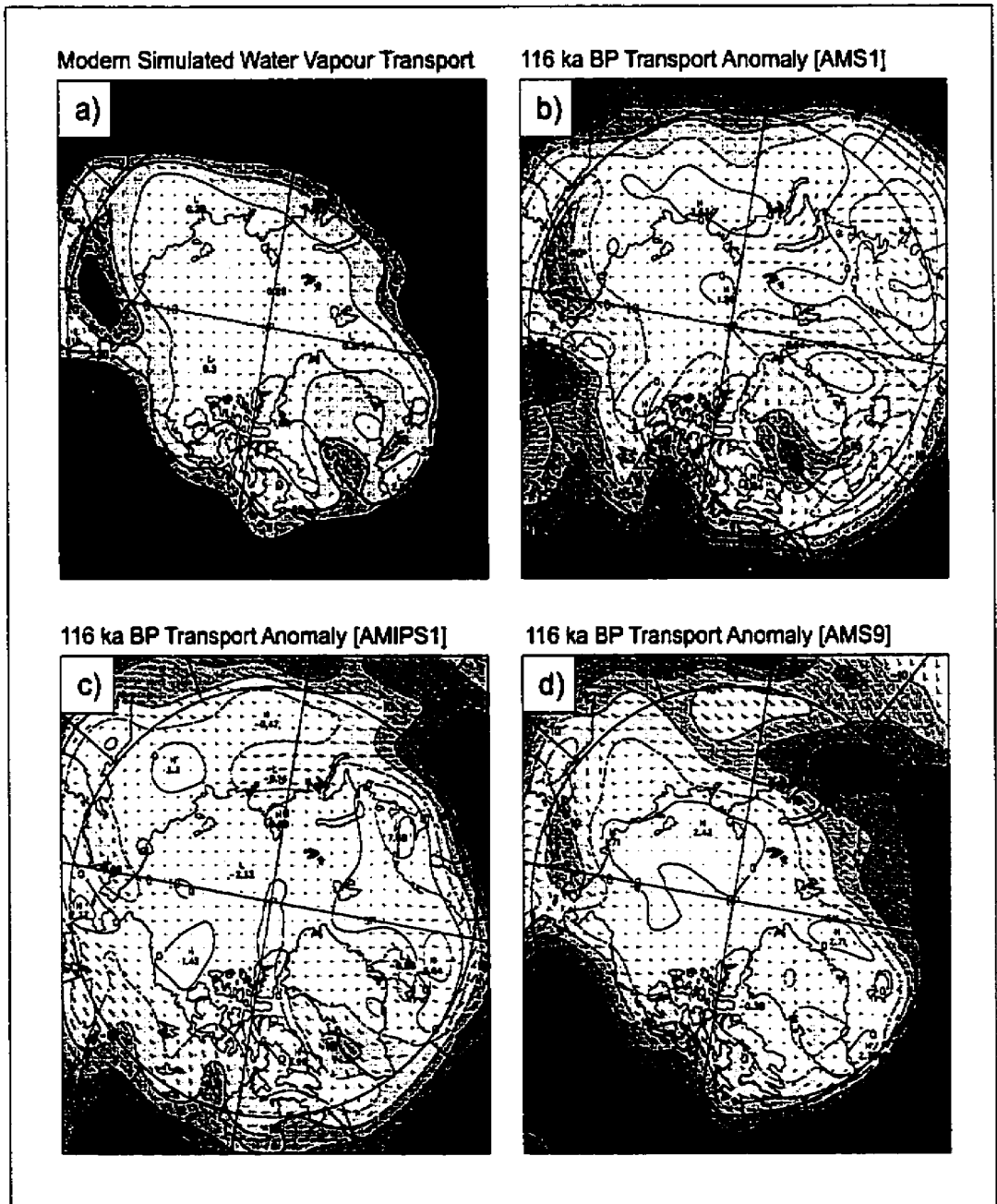


Figure 4.10: Contour plot of the modern simulated annual average total water vapour transport for the unbiased experiment. The 116 ka BP anomalies in total water vapour transport for the (b) warm biased, (c) unbiased, and (d) cold biased experiments. The contour interval is  $10 \text{ kg m}^{-1} \text{ s}^{-1}$  in (a) and  $5 \text{ kg m}^{-1} \text{ s}^{-1}$  in (b), (c), and (d).

note that there is an increase in the flow over Scandinavia in the warm AMS1 and unbiased AMIPS1 experiments but not in the cold biased AMS9 experiment. In fact, the changes in the cold biased experiment indicate a very strong decrease in the atmospheric transport over Alaska, Scandinavia and Western Europe due to the significant depression in summer temperatures. The significant glaciation seen in Central and Eastern Siberia in the cold biased AMS9 experiment may be a result of this significant re-alignment of the atmospheric inflow and outflow of water vapor into this region resulting in increased moisture convergence over land areas and areas of perennial snow cover.

The energetics of the atmosphere, as described by the main intrinsic forms of energy, namely the internal, gravitational-potential, kinetic and latent heat energy constitute essential components in the atmospheric heat engine. A complete analysis of the changes in energy balance in the 116 ka BP atmosphere is beyond the scope of this study and is part of an ongoing investigation. However, it is useful to briefly explore some changes in the transient eddy activity of the atmosphere in the north polar region to illustrate some differences in the high latitude atmospheric dynamics of the Post Eemian period. The meridional transport of latent and sensible heat by transient eddies is arguably the most important component of the energy exchange in the general circulation of the mid-latitude northern hemisphere atmosphere, especially in the vicinity of the highly baroclinic polar front. The moisture (latent heat) transport by transient eddies, predominantly in the mid-latitudes, is responsible for a much greater fraction of the total moisture transport in the meridional than in the zonal direction. The modern simulated annual mean northward transport by transient eddies is displayed in Fig. 4.11a for the unbiased AMIPS1 experiment. The modern simulated transport for the other two experiments is much the same as in Fig. 4.11a and agrees well with the magnitude and behaviour of the observed atmospheric eddy moisture transport (not shown) (CMC: Mitchell et al. 1993 and Mitchell et al. 1996; Peixoto and Oort 1992)[152][168]. Much of the northward moisture transport into the Arctic Circle by transient wave activity is dominated by maxima which lie just east of the two main continental land masses, namely North America and Asia. These maxima, which are associated with the Gulf Stream and Kuroshio western ocean boundary currents, are the source of a large portion of the northward transport of moisture in these strongly baroclinic regions. Although the maxima occur at approximately 35 °N latitude in the annual mean, the eddy activity is still significant even across the Arctic Circle in Eastern Canada and Eastern Siberia. Two other maxima in northward eddy moisture transport occur to the southwest of Alaska and to the southeast of Iceland. These maxima, which are of approximately half the magnitude, occur at the tail ends of the Gulf Stream and Kuroshio currents along the polar front where warm subtropical air interacts with cold polar air. Also of note are two weak minima of southward moisture transport by transient

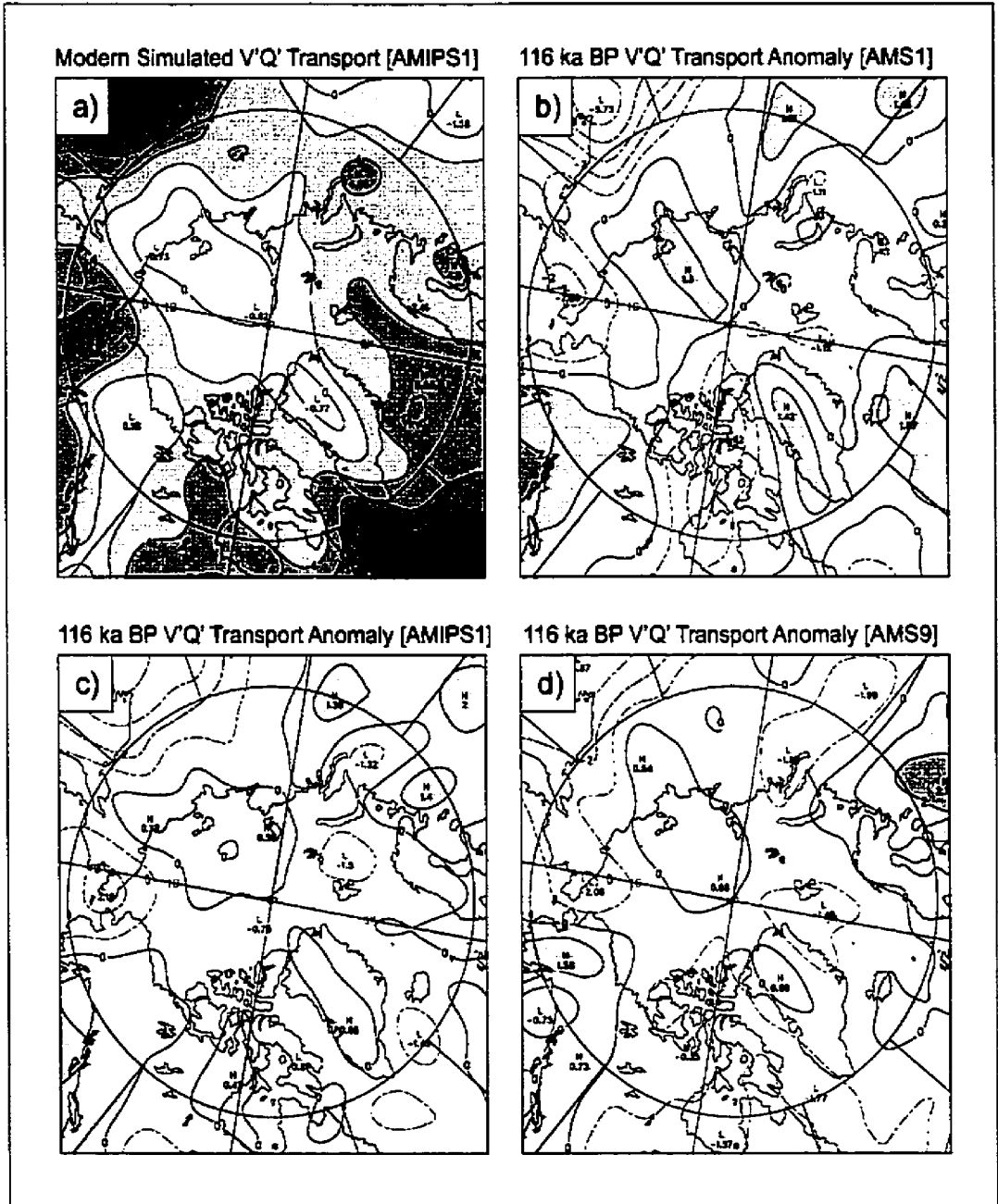


Figure 4.11: Contour plot of the annual mean northward transport of latent heat by transient eddies for the unbiased experiment. The 116 ka BP anomalies in northward transient eddy latent heat transport for the (b) warm biased, (c) unbiased, and (d) cold biased experiments. The contour interval is  $2 \times 10^7 \text{ W m}^{-1}$  in (a) and  $1 \times 10^7 \text{ W m}^{-1}$  in (b), (c), and (d). To convert to latent heat transport ( $\text{W m}^{-1}$ ), the moisture transport ( $\text{kg m}^{-1} \text{ s}^{-1}$ ) is multiplied by the latent heat of vaporization:  $L_e = 2.5 \times 10^6 \text{ J kg}^{-1}$ .

eddies that are situated symmetrically, 180° longitude apart, over Greenland and the Russian Arctic Ocean.

The 116 ka BP anomalies in the northward moisture (latent heat) transport by transient eddy activity for the three experiments are displayed in Figs. 4.11b to 4.11d. A fairly consistent pattern emerges in the 116 ka BP moisture transport anomalies with the reduction in summer insolation. The two regions of southward transport over Greenland and the Russian Arctic Ocean are significantly reduced while the transport over the Canadian West Coast and Alaska are significantly increased. Also of note is the decrease in northward transport over the Canadian Arctic Archipelago as well as over Eastern Siberia in all three experiments. Over Eastern Europe and Scandinavia the northward transport becomes successively stronger with increasing cold bias in each of the three experiments. The cold biased AMS9 experiment delivers a strong northward transport in Eastern Europe.

The modern annual mean northward sensible heat transport by transient eddies shown in Fig. 4.12a for the AMIPS1 experiment is very similar to the moisture or latent heat transport in Fig. 4.11a. The 116 ka BP anomalies for the annual mean meridional sensible heat transport by transient eddies for the three experiments (Figs. 4.12b to 4.12d) are also characteristically similar to the eddy moisture transport displayed in Figs. 4.11b to 4.11d, but are of approximately twice the magnitude. The 116 ka BP eddy heat transport anomalies are decreased substantially over Eastern Siberia and the Canadian Arctic Archipelago. The southward eddy heat transport over Greenland and the Russian Arctic Ocean are again significantly decreased. Likewise, the northward heat transport increases over Eastern Europe and Scandinavia as the experiments go from warm to cold biased, with the AMS9 experiment showing the greatest northward eddy transport of heat in this region.

The locations of perennial snow cover in the Arctic region (Fig. 4.2) and the location of the maxima and minima in the 116 ka BP anomalies of northward transport of latent and sensible heat (Figs. 4.11 and 4.12) by transient eddy activity are strongly correlated. The absence of perennial snow cover formation in Alaska and Scandinavia in any of these experiments is associated with the fact that increases of northward heat and moisture transport by transient eddies occurs in both these regions. The regions of nucleation over the Canadian Arctic Archipelago and over Central and Eastern Siberia, on the contrary, coincide with regions of decreased northward latent and sensible heat transport in the AMIPS1 and AMS9 experiments. It seems entirely plausible that the zonal spatial heterogeneity of the Arctic nucleation zones is in part a result of increases and decreases in the northward transient eddy transport of latent and sensible heat into the Arctic Circle at 116 ka BP. These relationships may actually be further amplified as the process of glacial inception proceeds and continental ice sheets grow and advance in this polar region (see the LGM eddy moisture transport

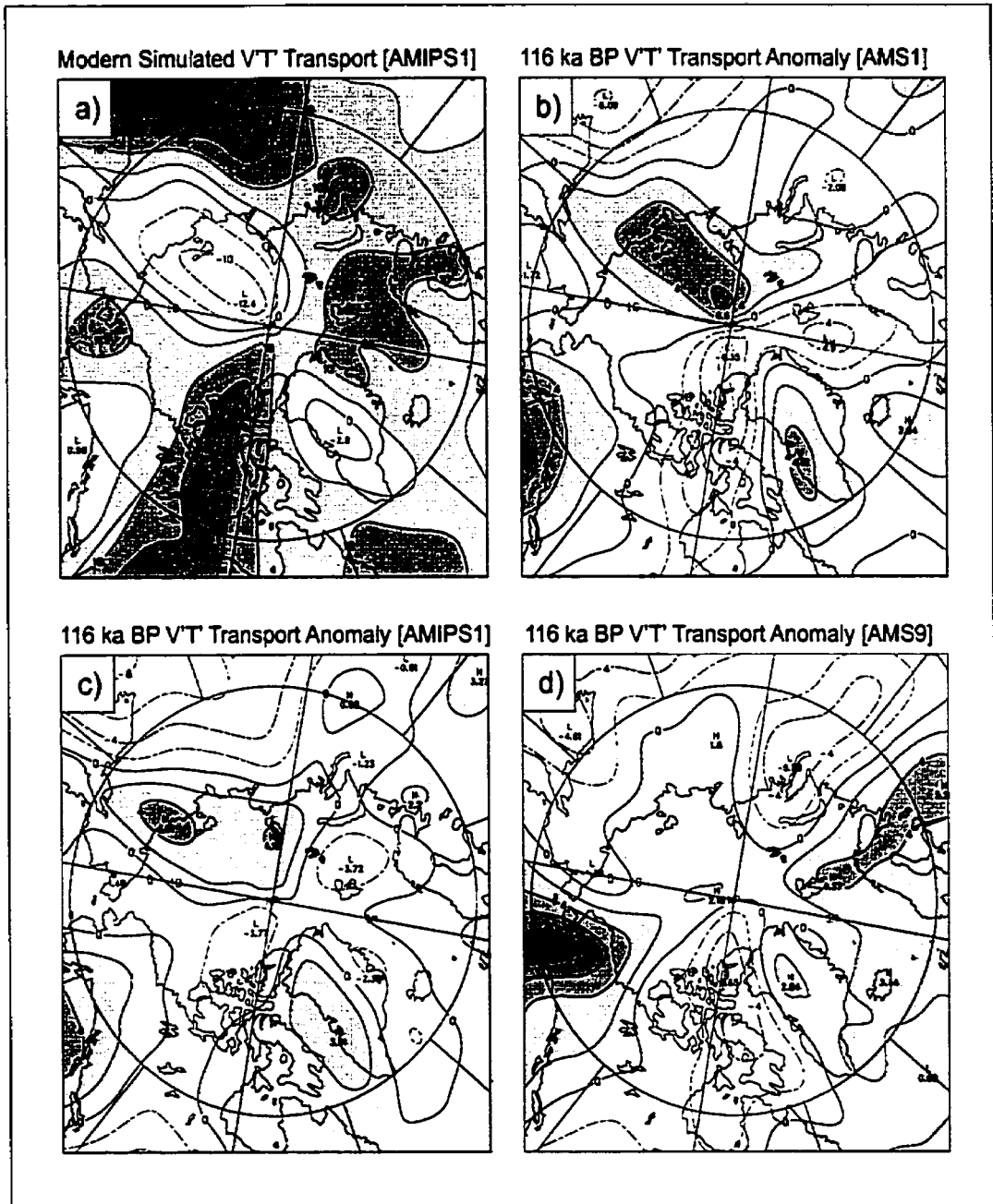


Figure 4.12: Contour plot of the annual mean northward transport of sensible heat by transient eddies for the unbiased experiment. The 116 ka BP anomalies in northward transient eddy sensible heat transport for the (b) warm biased, (c) unbiased, and (d) cold biased experiments. The contour interval is  $5 \times 10^7 \text{ W m}^{-1}$  in (a) and  $2 \times 10^7 \text{ W m}^{-1}$  in (b), (c), and (d). To convert to sensible heat transport ( $\text{W m}^{-1}$ ), the temperature flux ( $^\circ\text{C m s}^{-1}$ ) is multiplied by the specific heat capacity of air at constant pressure, the surface pressure and the inverse of gravity:  $c_p p_0 g^{-1} \approx 1 \times 10^7 \text{ J m}^{-2} \text{ }^\circ\text{C}^{-1}$ .

in Chapter 3; Fig. 4.8) and will be the focus of further study to be described elsewhere.

#### 4.4. Summary and Conclusions

An investigation of glacial inception conducted using the CCCma AGCM has demonstrated the operation of several climate feedbacks that may be instrumental in the determination of climate state in the Post Eemian period. Three experiments consisting of three modern controls and three 116 ka BP experiments were performed using mixed layer ocean and sea ice modules to assess the sensitivity of the model to the summertime insolation minimum that occurred at this time. In the three experiments, boundary conditions were modified such that a range of northern hemisphere land and sea surface temperatures were obtained. A pair of warm and cold biased experiments relative to an unbiased experiment form the set of three sensitivity experiments. In the unbiased experiment the modern SSTs and sea ice delivered by the mixed layer ocean and thermodynamic sea ice modules were constrained, through the use of implied oceanic heat transports, to those inferred from the AMIP2 SST and sea ice concentration data sets. In the cold biased experiment the SSTs and sea ice distribution were determined on the basis of the data sets of Alexander and Mobley (1976)[3]. In the CCCma GCMII model the rate at which the solar radiative transfer calculations are performed affects the temperature obtained at the surface of the model. In the cold biased simulation the full solar radiative transfer calculation, which is intermittently performed every 9 model timesteps and then interpolated to every model timestep, is demonstrated to induce a radiation deficit within the model. The correct implementation requires that a full solar radiative transfer calculation be carried out at every model timestep. In doing so, the implied oceanic heat transports inferred from the Alexander and Mobley data sets are no longer applicable when the full radiative transfer analysis is conducted at every timestep. The result, which constitutes the warm biased experiment, is a simulation with oceanic SSTs which are warmer when compared with the AMIP2 SST data set. Thus, the three control experiments provide a means of testing the sensitivity of the ability of the model to deliver perennial snow cover at high latitudes in response to a reduction in incoming summer solar radiation.

Modelling issues that are pertinent to the simulation of Post Eemian perennial snow cover in an AGCM were also discussed in this chapter. In particular, the inaccuracies that are present in the spectrally decomposed AGCM topography due to Gibbs oscillations in regions of rapidly varying elevation are central to determining the regions in which the model will attain perennial snow cover. In one instance, the large elevation changes that occur between the summit of Greenland and the

summit of Baffin island in the observed topography poses a series of problems in spectral models. In the CCCma GCMII (T32) spectral decomposition, the first spectral ripple to the southwest of Greenland induces more than a half kilometer error in the topographic elevation over Baffin Island which places the land mass below sea level in the model. This also has a direct affect on the perennial snow cover which is known to have existed in this region in Post Eemian times. Considering lapse rate adjustments to a corrected topography, the Baffin Island plateau would be about 4 °C colder in the model and would most certainly affect this glacially sensitive nucleation zone. The spectral ripples also have the additional effect of shifting the topographic maximum on Baffin Island horizontally away from areas of rapid elevation changes.

Taking into consideration the physical misrepresentations and inadequacies in the model that were discussed in Section 4.2 of this chapter, I then addressed the model's ability to adequately reproduce the modern observed climatology. Deviations in Arctic surface temperatures from observed were found to be fairly consistent in spatial distribution in the three modern simulations. The Canadian Arctic Archipelago and Scandinavia were found to be in good agreement with the observed surface temperature in the three experiments while temperatures over Eastern Siberia and Alaska were somewhat cold biased. The summer Arctic precipitation in the three sets of experiments is also similar, and in general wet biased when compared with the observed data. The CCCma GCMII is known to have a hydrological cycle which is overly vigorous compared with the modern observed cycle, and this leads to excessive precipitation in this polar region. The modern summer snow cover simulated in the model is a strong function of the temperature bias in the three sets of simulations. The unbiased simulation, in general, has the best agreement with the observed snowfall data. All three simulations tended to overestimate the summer snowfall in Eastern and Central Siberia.

The three 116 ka BP experiments demonstrated that glacial inception was successfully achieved in two of the three simulations performed with this model. The warm biased experiment delivered no perennial snow cover in the Arctic region except over Central Greenland. The cold biased 116 ka BP experiment had large portions of the Arctic north of 60 °N latitude covered in perennial snowfall. Strong regions of accumulation occurred over the Canadian Arctic Archipelago and Eastern and Central Siberia. The accumulation over Eastern Siberia appears to be excessive since there is little evidence that Eastern Siberia ever entered into a glacial state. The accumulation pattern in this region is likely a result of the excessive precipitation in the modern simulation. The unbiased experiment has the strongest nucleation zone centered over the Canadian Arctic Archipelago and slight perennial snow cover over Eastern and Central Siberia. The absence of nucleation over Alaska

and Scandinavia in these two experiments poses a number of interesting questions concerning the role of these regions in the evolution of the northern hemisphere into a glacial state. Alaska is thought to have been absent of continental ice cover throughout the last glacial cycle while Scandinavia is known to have been covered by the Fennoscandian ice complex. This raises the question as to the role that the Atlantic and Pacific oceans might play in the determination of ice advance in these regions. The absence of perennial snow cover in the Scandinavian region may be a result of inadequate resolution of the topography in this region. However, it is also possible that for Scandinavian glaciation to occur, the Northern American region needs to be in an advanced state of glaciation such as would have been characteristic of prevailing conditions at the time of the later insolation minimum that occurred at 70 ka BP. The strength of the thermohaline circulation would likely have been somewhat reduced at this time which would also have served to further cool the Scandinavian region as this lies downstream of the regions where deep water currently forms and the overlying atmosphere is thereby significantly warmed.

The three sets of sensitivity experiments, each with varying degrees of glacial inception at 116 ka BP, were also employed to investigate several climate feedback mechanisms that might be instrumental in further stimulating perennial snow cover.

In particular

(1) The seasonal evolution of snow cover is much different in each of the three experiments at 116 ka BP. The warm, unbiased and cold biased experiments all have extended northern hemisphere snow cover anomalies in late summer of 2, 5, and 9 million km<sup>2</sup>, respectively. The seasonal cycle of the land surface temperature and surface albedo anomalies grow successively colder and more reflective in each experiment with successively colder control temperatures. The extensive snow covered area in summer in the experiments would play the determining role in the transient evolution of land ice through the snow-ice-albedo feedback mechanism. The seasonal evolution of sea ice cover at 116 ka BP was characterized by extended sea ice distributions of 2 to 3 million km<sup>2</sup> in August in the three Post Eemian simulations. The differences between these simulations are somewhat dependent upon the under ice heat fluxes in the thermodynamic sea ice model. The lack of dynamical ice flow in this component of the model is certain to affect the 116 ka BP sea ice distributions. Nevertheless, sea ice expansion is known to influence perennial snow cover in glacial inception experiments. The expansion of sea ice to lower latitudes cools the surrounding land masses and restricts ocean-atmosphere heat and moisture exchange in the Arctic region.

(2) The Arctic anomalies in the land surface energy balance, dictated by the balance of absorbed shortwave radiation, emitted longwave radiation and the exchange of latent and sensible heat fluxes

from the surface to the atmosphere are very well correlated with the reductions in summer polar insolation at 116 ka BP. Reductions in the 116 ka BP net shortwave absorbed anomalies at the surface are well below the reduction in insolation with minima occurring in July in the three sets of experiments. The largest decreases in absorbed shortwave radiation reach  $80 \text{ W m}^{-2}$  in July in the cold biased experiment. Decreases in the net longwave radiation at the surface relative to the shortwave radiation minimum are delayed by approximately 2 months in each of the experiments, with the largest changes again occurring in the cold biased experiment in September. Decreases in net longwave are virtually non-existent during the July insolation minimum. Decreases in upward latent and sensible heat fluxes have maxima that also occur in July but with sensible heat flux anomalies of about half the magnitude of the decreases in latent heat flux. In mid summer the experiments have an imbalance between the decrease in the upward latent and sensible heat fluxes and the net solar radiation absorbed. Thus, at 116 ka BP there is excess heat flux being emitted from the surface and that may be an important mechanism for decreasing summer snow melt and maintaining perennial snowfall. In the fall, the 2 month delay in the net longwave radiation anomaly at the surface may simply indicate that the surface is cooling more slowly than it does under modern climate conditions. The combined effect is that the snow cover is maintained for much longer durations of time at these high polar latitudes at 116 ka BP.

(3) The enhanced reduction of summer evaporation over summer precipitation in the Arctic Circle over land results in a net increase in precipitation minus evaporation ( $P - E$ ) at 116 ka BP. This is the first indication that there may be a climate mechanism that is acting to create a convergence of moisture over Arctic land at 116 ka BP. A subsequent detailed analysis of the atmospheric moisture balance equation for the Arctic Polar Cap north of  $60^\circ$  latitude indicated a change in behavior of the polar climate at 116 ka BP. In the polar climate system the rate of change in precipitable water is balanced by the meridional flux of water vapour into the Arctic Circle and the total polar excess of evaporation over precipitation. The moisture being pumped into the polar region by the general circulation is much stronger in winter than in summer. With the reduction in insolation at 116 ka BP, this mechanism becomes more vigorous in summer. At 116 ka BP the decrease in evaporation over precipitation balances the increased influx of moisture transport into the polar region. With the rate of change in precipitable water being fairly constant in summer the change in the rate of change of precipitable water at 116 ka BP is negligible. Thus, I find a climate feedback mechanism which is pumping more moisture into the Arctic Circle along with enhanced convergence. This mechanism constitutes a positive feedback mechanism due to the reduction in insolation at 116 ka BP and would enhance ice sheet growth over the ensuing millennia.

(4) Changes in the northward transport of latent and sensible heat by transient eddy activity display similar behaviour in the Arctic Region in each of the three 116 ka BP experiments. The main features constitute a decrease in the northward heat transport into the Canadian Arctic Archipelago and over Eastern Siberia. Over Eastern Europe and Scandinavia the transport becomes successively stronger as the temperature of the modern control simulation decreases. Also of note is the consistent increase of latent and sensible heat transport over Alaska in all three 116 ka BP experiments. The eddy sensible heat transport anomalies are found to be approximately twice the magnitude of the eddy latent heat flux anomalies. In general it is found that the lack of formation of perennial snow cover in Alaska and Scandinavia in any of the experiments coincides with increases of northward heat transport by transient eddy activity. The zonal spatial heterogeneity of the Arctic nucleation zones appears to be in part a result of increases and decreases in the northward transient eddy transport of heat and moisture into the Arctic Circle at 116 ka BP. This effect is likely to increase with decreasing temperature and increased snow cover over time.

This investigation suggests that a number of climate mechanisms are acting to modify the 116 ka BP climate such as to make conditions for perennial snow cover more favorable. These mechanisms seem to constitute a set of positive feedback mechanisms which couple with the main Milankovitch ice-albedo positive feedback resulting from the decrease in summer insolation. A more detailed investigation of the energy balance in the polar atmosphere may provide greater insight into alterations in the atmospheric energy cycle that may have occurred at 116 ka BP. Downscaling the topographic representation in GCMII in order to achieve a more appropriate mass balance in simulating glacial inception conditions may also provide a new direction for research in glacial inception modelling. A transient simulation of Post Eemian glacial inception with a coupled AGCM/ISM spanning approximately 10 000 years may also reveal whether some of the candidates suggested to constitute positive feedback mechanisms in this study are actually further amplified. The use of a coupled AOGCM and ISM would ultimately allow a more detailed investigation of the transient evolution of continental ice sheet expansion in the northern hemisphere. As paleoclimate models become more sophisticated and paleoclimate data more abundant, a greater understanding of past climates will ensue, undoubtedly leading to a greater understanding of climate change processes in general, including those that will govern our future.

---

## CHAPTER 5

---

### Conclusion

#### 5.1. Model Development and Climate Prediction

In order to advance our understanding of the climate system, it is necessary to incorporate our collective understanding of the controlling physical mechanisms more accurately into present day Earth System Models. The model used in this study has evolved in a number of respects and has just been recently re-released as GCM3. Since the second release in 1992, the model has undergone major revisions to improve upon the deficiencies that are known to exist in GCM2, some of which have been revealed in this thesis and employed by the CCCma group to design improvements. In the course of this thesis I have investigated a number of issues and implemented a number of changes to the original CCCma GCM2 version of the model. 1) The original model calculated the solar forcing at the top of the model using only the declination of the Sun and thus a circular orbit. The model used in this thesis uses solar forcing resulting from both an elliptical orbit and the influence from the other orbital parameters as discussed in Appendix A. 2) The original model was initially unusable for paleoclimate studies due to an error that was discovered in the longwave radiation scheme. The longwave radiation parameterization employs transmissivities which vary as function of CO<sub>2</sub> concentration based upon a Padé approximation scheme which contained a hill condition at low CO<sub>2</sub> levels. This would subsequently cause the model to eventually fail in a cloud ice crystal parameterization. 3) The bucket depths in the original land surface scheme were found to be unreasonably high compared with global values. This led to the investigation of the influence of the land surface scheme on the mid-Holocene anomalous response simulated by the model (cf. Chapter 2). This revealed further problems with the high latitude 6 ka BP response in the model compared with other models in the PMIP set. This investigation illustrated the mechanism in the land surface parameterization which resulted in this high latitude behaviour. 4) Implementing the high LGM topography into the model can result in multivalued variables in the vertical coordinate which then causes the model to fail. 5) Considering the error of using partial instead of full solar radiation calculations at each timestep (cf. Chapter 4), and the issues cited above, required that

the mixed layer ocean component of the model be reformulated so as to reproduce an accurate representation of the modern climate through the reformulation of implied ocean heat transport. With these changes to the model, I have gained confidence in the ability of the model to accurately simulate the modern climate and therefore the simulation of paleoclimates.

In light of model progress, GCM3 replaces the land surface scheme in GCM2 with a more state of the art land surface scheme. This new land surface scheme which represents the biosphere and land-atmosphere interaction more accurately, is known as the Canadian Land Surface Scheme (CLASS). This new component of the model has many novel features such as an interactive vegetative canopy (Verseghy et al. 1993)[228]. Initial investigations with GCM3 and this new land surface scheme have delivered promising results. GCM3 results which have been obtained to follow on from the results obtained in Chapter 2 reveal significant differences compared with the GCM2 predictions (Fig. 5.1). The modern and 6 ka zonally averaged surface temperature response are both displayed in Figs. 5.1a and 5.1b, respectively. Two experiments were conducted with GCM3, one in which the CO<sub>2</sub> concentrations were varied together with the 6 ka BP orbital changes and one without. In the modern climate simulation, GCM3 has mid-latitude land surface temperatures which are warmer than GCM2 by approximately 2 °C and are in much better agreement with observed values. What is more striking is the very significant improvement in the 6 ka BP response relative to the PMIP model mean. GCM3 also resolves the pole problem that was revealed by the GCM2 land surface analysis in Chapter 2 of this thesis.

In the course of my research I have also attempted to implement new parameterizations into the model to resolve some of the issues regarding glacial nucleation sites described in Chapter 4. In other modelling groups, asynchronous off-line downscaling parameterizations have been developed to modify results obtained from their GCMs in order to further enhance the simulation of the modern climate (e.g. Glover 1999)[73]. Therefore, a new downscaling scheme was implemented into GCM2 to adjust the hydrological component of the model for differences in temperature between the resolved spectral topography in the model and the actual topography. This new scheme adjusts the form of the precipitation between solid or liquid as it reaches the model surface dependant upon the inferred temperature correction at different model resolutions. This lapse rate adjusted mass balance scheme proved very difficult to implement correctly due to model complexity, the nature of the synchronous downscaling and conservation of the precipitable quantities in transferring data between high and low resolutions. Still, preliminary results are encouraging as demonstrated in Fig. 5.2. The differences between the solid precipitation received at the surface for modern and 116 ka BP is displayed for two different resolutions. In Figs. 5.2a and 5.2b the solid precipitation for the

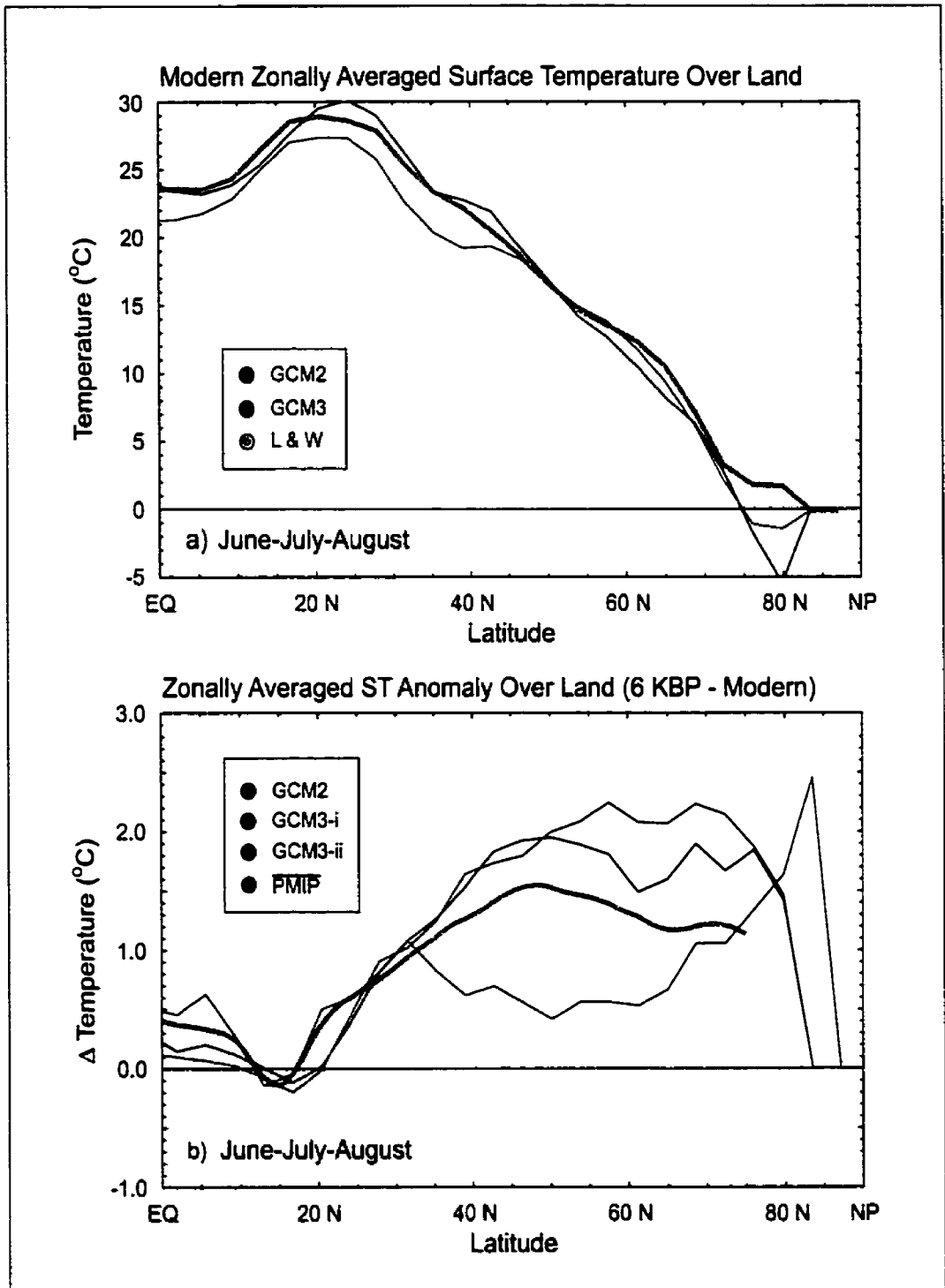


Figure 5.1: The same plot as in Fig. 2.5 but for the GCM2 version with the land surface which employs the variable buck and variable evapotranspiration slope factor and two GCM3 simulations of 6 ka BP climate which use modern (GCM3-i) and pre-industrial (GCM3-ii) CO<sub>2</sub> levels.

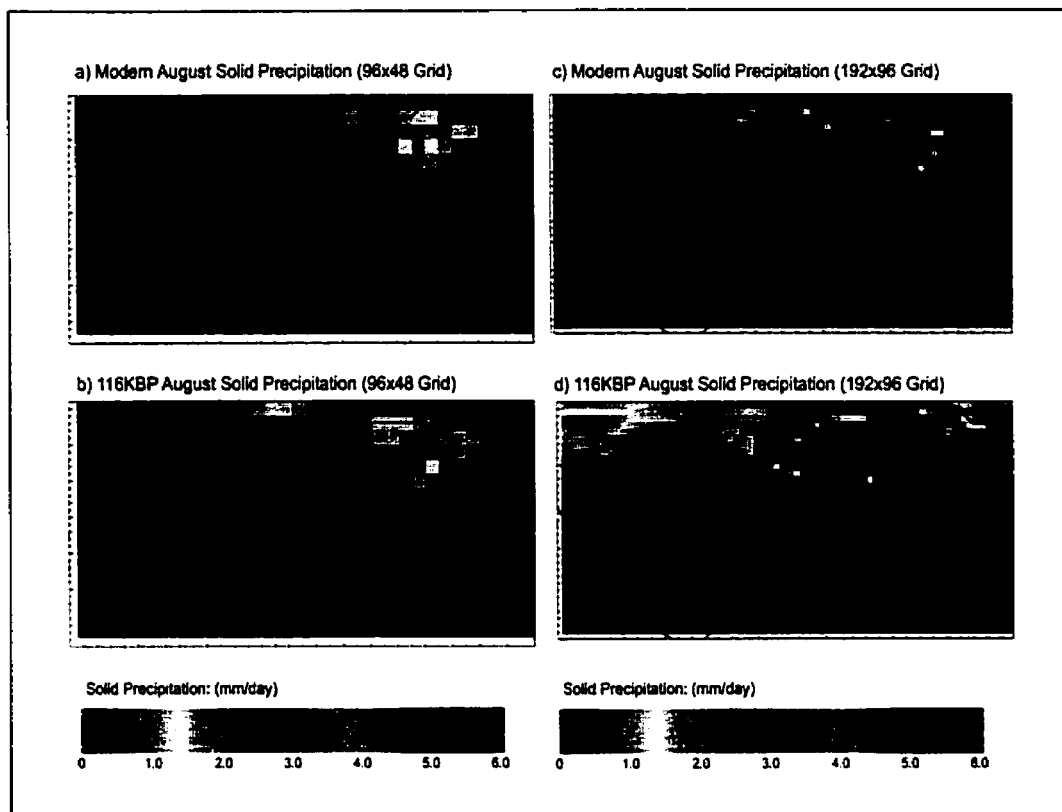


Figure 5.2: Differences in August solid precipitation between modern and 116 ka BP for the standard model resolution (a) and (b). Differences in August solid precipitation between modern and 116 ka BP for the lapse rate adjusted downscaling parameterization at double the model resolution (c) and (d).

standard model is displayed, while that for the differences in a doubled resolution model is displayed in Figs. 5.2c and 5.2d. The most interesting feature is that solid precipitation is occurring in August over Baffin Island at 116 ka BP in the high resolution scheme while in the low resolution scheme it is not.

Also of interest in future research concerns the main reason for conducting paleoclimate studies at all, which is to attempt to better assess future climate change. The work in this thesis has improved and corrected a number of aspects of the GCM2 representation of the modern climate (e.g. cf. Chapter 4). In particular, I modified the ocean heat transports in the mixed layer ocean model to correctly simulate the current best estimates of global SSTs and sea ice. It is interesting to investigate the differences between the CO<sub>2</sub> doubling results obtained on the basis of the model integrations initially performed in 1992 at the Canadian Climate Centre with the model that has evolved in my possession at present. The differences in the predicted temperature change between

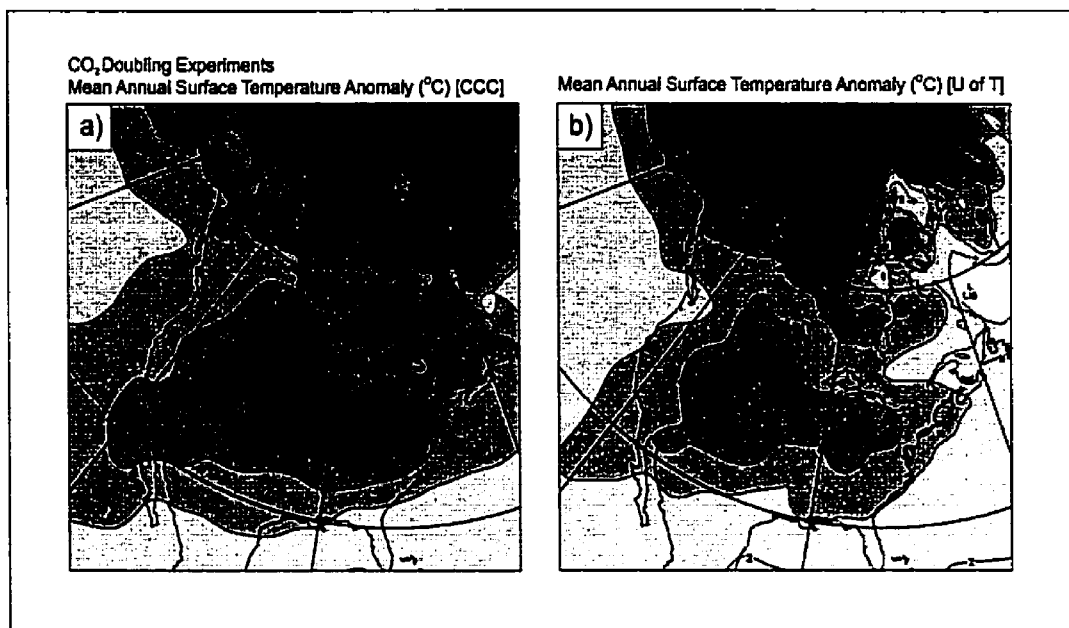


Figure 5.3: Annual mean surface temperature over North America in CO<sub>2</sub> doubling experiments with the original 1992 CCC version of GCM2 (a) and the current U of T 2000 version of the model (b). Contour interval is 1 °C.

the two versions of the model in each of the CO<sub>2</sub> doubling experiments over North America are displayed in Fig. 5.3. The main difference between the two simulations is that the version of the model which I have developed delivers a more muted temperature response to CO<sub>2</sub> doubling in the interior of the North American continent by about 1 °C. At polar latitudes, however, this model delivers a warmer response to CO<sub>2</sub> doubling. The difference between the globally averaged temperature change between the CCC and U of T experiments is 3.5 °C and 3.0 °C, respectively. This is encouraging since the mean temperature of a model's response to CO<sub>2</sub> doubling has decreased as models have improved (IPCC 2001)[101].

As a conclusion to this thesis it is interesting to speculate upon the meaning of the CO<sub>2</sub> doubling when taken together with the results obtained in Chapter 4 on glacial inception, along with aspects of the astronomical theory of the ice ages described in the introduction to this thesis. Based upon annual insolation calculations for the Arctic Circle that I have produced from 600 000 years in the past to 200 000 years in the future (Fig. 5.4) it is fairly apparent we are in or entering a period that we would expect to lead to a next episode of pronounced continental glaciation. The curves in Fig. 5.4 contrast the  $\delta^{18}\text{O}$  inferred changes in ice volume with changes in annual Arctic insolation. Each initiation and termination displayed in the last 600 ka of the proxy sample can be directly mapped

onto the insolation calculation which I have performed. The glacial-interglacial cycles appear to have one of two characteristic periods, 82 ka and 123 ka, which are each multiples of the 41 ka dominant obliquity cycles. It is not unreasonable therefore to extrapolate on the basis of these results to develop alternative hypotheses concerning the nature of possible future scenarios of the onset of the next glacial cycle.

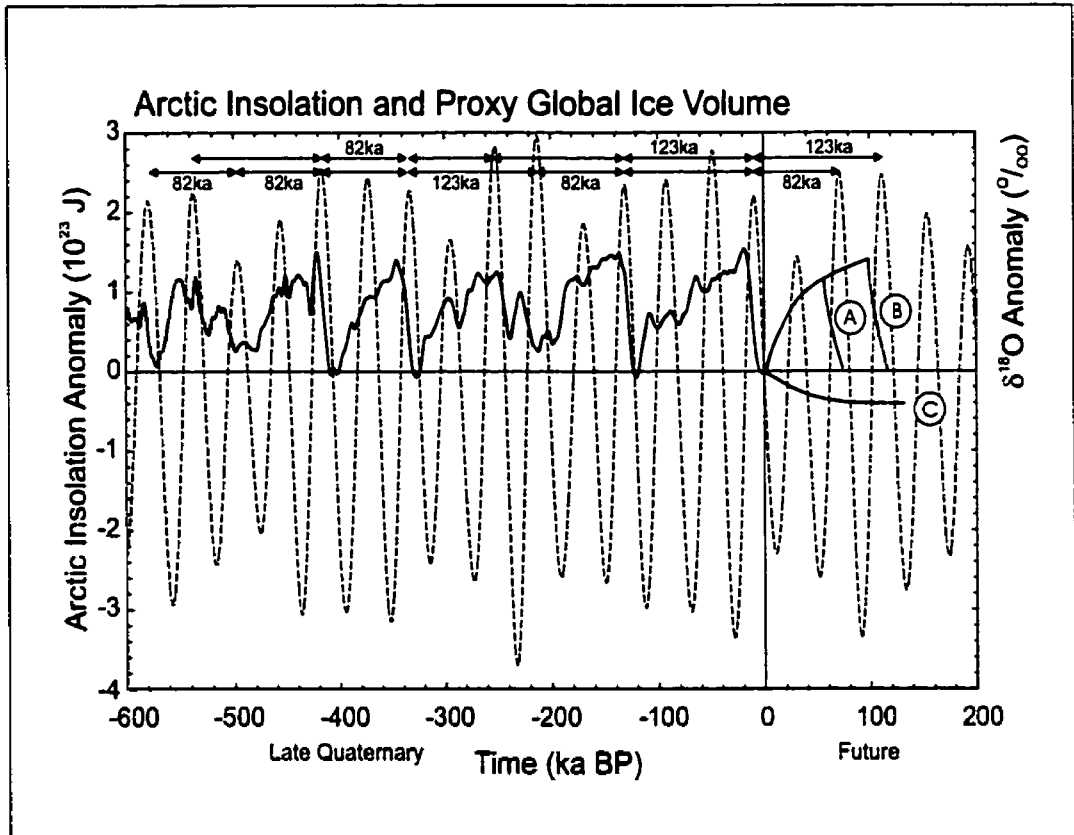


Figure 5.4: Annual Arctic insolation above  $60^\circ\text{N}$  latitude from 600 000 years before present to 200 000 years after present (dashed line) and the  $\delta^{18}\text{O}$  record from ODP-677 for the last 600 000 years (solid line). The measures at the top of the plot indicate the length of the dominant modes of the glacial-interglacial cycles. Three future climate scenarios are also presented. (A) A short 82 ka cycle. (B) A longer 123 ka cycle. (C) The collapse of the glacial-interglacial cycles due to the influence of future anthropogenic  $\text{CO}_2$  levels in the atmosphere.

Three future scenarios are displayed in Fig. 5.4. Both scenario A and scenario B begin with the nucleation of a continental ice sheet in the Arctic within the next 10 000 years but do not consider the anthropogenic influence of greenhouse gas forcing. The expansion of the continental ice sheets should continue for a cycle of approximately 82 000 years (scenario A) or 123 000 years (scenario B) depending upon some additional aspect of the Earth's orbital elements (possibly linked with

the 413 000 year eccentricity cycle). Also, the higher frequency influence of the Earth's precession on ice accumulation is not displayed in the hypothetical curves of these two scenarios. Scenario C demonstrates what may ultimately be the end of the late-Pleistocene glacial-interglacial cycles due to the influence of anthropogenic CO<sub>2</sub> emissions into the atmosphere. While trying to assess the importance of anthropogenic influence on the distant geological future is unrealistically ambitious, an attempt to assess the near term effects (the coming millennia) may be useful. Given the CO<sub>2</sub> warming results at high latitudes provided in Fig. 5.3 and the sensitivity of model predicted glacial initiation to the northern hemisphere high latitude radiation regime (Chapter 4), it is not unreasonable to expect a significant impact on the glacial inception process within the next thousand years. The exact length of the current interglacial may also extend longer than we expect as "super-interglacials" have occurred such as the one that has been suspected to have occurred during marine isotopic stage 11 (400 000 years ago), a period where the orbital configuration was very similar to that of today (Raymo et al. 1990; Hodell 1993; Oppo et al. 1998)[187][88][165].

This "super-interglacial" scenario or one in which the northern hemisphere ice sheets do grow but remain confined to the most northerly latitudes of the northern hemisphere is the most likely candidate based upon the projection of incoming TOA insolation for the next 8 000 years (Fig. 5.5). This figure, which displays the insolation anomalies at the TOA in 1 000 year intervals into the future, provides a fairly good indication of when an inception event over Northern Canada might occur, similar to that demonstrated in Chapter 4. The most apparent result that follows by inspection of Fig. 5.5 is that the near future insolation distribution is characteristically different from that which occurred at 116 ka BP. If one inspects the 8 ka insolation anomaly (Fig. 5.5h), we see that this is almost identical to the insolation anomaly for 116 ka BP (Fig. 1.4d) but that the seasonal contrast is reversed. The high latitude southern hemisphere summer insolation at 8 ka after present (8 ka AP) is identical to the 116 ka BP insolation in high latitude northern hemisphere summer reaching  $-40 \text{ W m}^{-2}$ . The most likely period in which continental ice might accumulate at high northern latitudes would likely occur 4 000 years from now. The reason for this is that from Fig. 5.5d we see that there is an Arctic minimum in July and August which reaches more than  $-24 \text{ W m}^{-2}$  in August. There is also an Arctic maximum of approximately  $10 \text{ W m}^{-2}$  in May. If we consider the hypothesis that Arctic summer deficits in insolation are required to initiate glaciation, which was also confirmed from the results in Chapter 4, we would expect the possibility of perennial snow cover to be highest around 4 ka AP. It would be of interest to see if the model developed in the present study could achieve perennial snow cover during this epoch. It would also be of interest to consider the influence of a CO<sub>2</sub> warmed world on the simulation of the same epoch. If, in fact, the

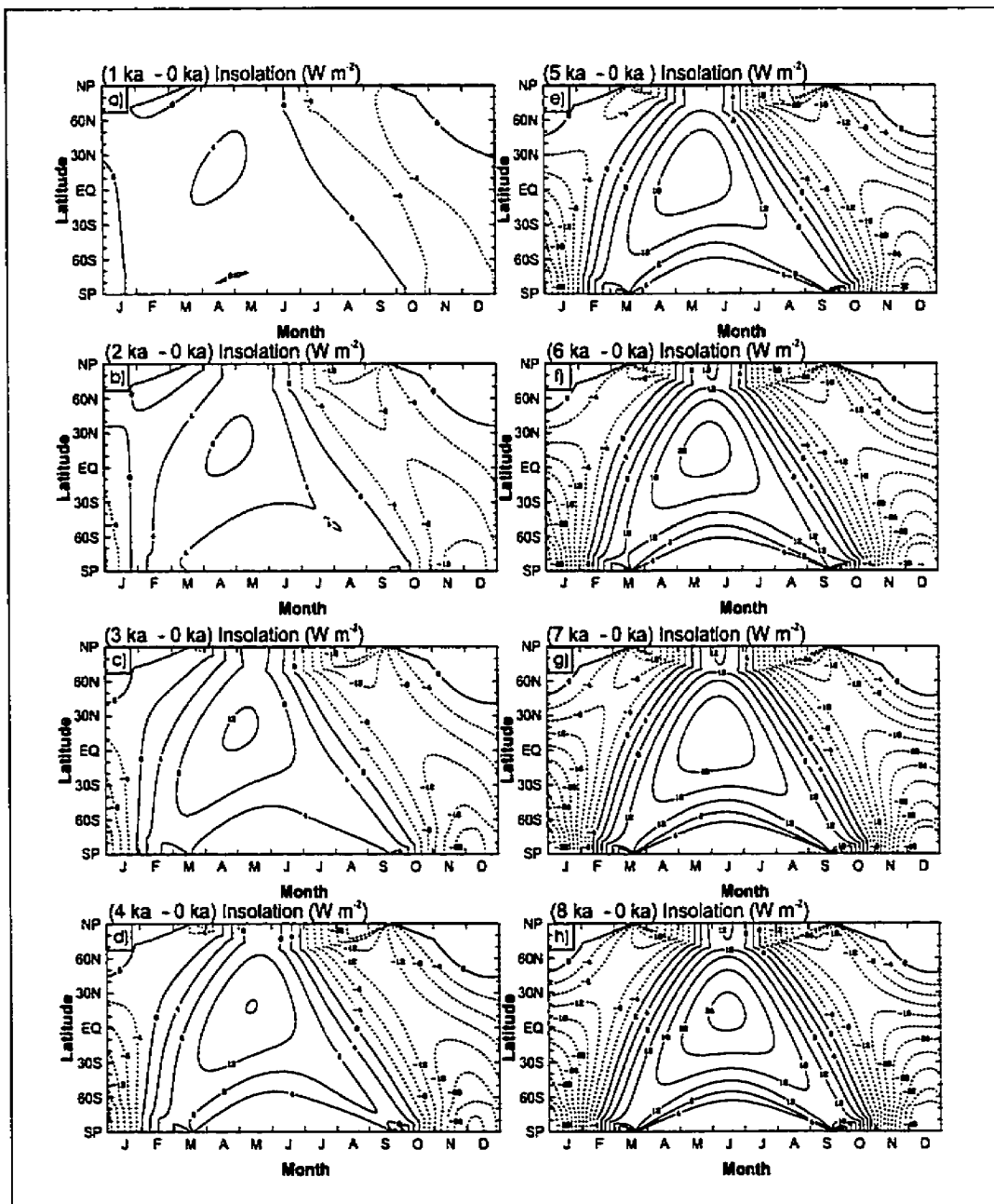


Figure 5.5: The difference from modern in insolation at the top of the atmosphere as a function of latitude and time of year for the next 8 000 years at 1000 year intervals are displayed in (a) to (h). Contour intervals  $4 W m^{-2}$ .

Arctic does not become glaciated within the next 4 000 years, colder high latitude summer conditions would not occur until at least 19 250 years from now when the summer solstice is at perihelion and a configuration similar to that observed at 116 ka BP would not occur again until at least 54 000 years from now.

## 5.2. General Conclusions

This thesis has focused upon a series of modelling experiments designed to probe the nature of the climate system response, including its internal variability, to changes in boundary conditions and forcing that are representative of the range of Late Quaternary conditions, a period characterized by the occurrence of intense glacial-interglacial cycles. A study of three unique time periods within the last glacial cycle has been undertaken to investigate various aspects of the ability of a modern atmospheric general circulation model to reproduce the properties of climate states that differ fundamentally from present. The results obtained on the basis of these three distinct analyses may be best summarized in terms of their connection to the three primary goals of the work as follows,

**1) To better understand climate mechanisms and feedback processes that may develop in response to changes in paleoclimate boundary conditions such as occur solely as a consequence of changes in the solar input at the top of the atmosphere.** Within these complex 3-D models, the exact nature of the response has been demonstrated to be highly dependant on the nature of the parameterizations in the model used to represent sub-gridscale physical phenomena (cf. Chapter 2). This has been demonstrated in the Holocene Optimum experiments where the alteration of the land surface scheme was used to test the sensitivity of the model to the 6 ka BP forcing. Since a global climate model contains a significant amount of complexity, especially in terms of the resolved atmospheric flows, it has been demonstrated that these models can be used to investigate massive changes in the general circulation of the atmosphere, such as those which occur near the mid-latitude edge of a full continental ice sheet or in high latitude regions where ice sheet nucleation begins (cf. Chapter 3 and Chapter 4). The role of the hydrological cycle and atmospheric water vapour transport have also been demonstrated in this thesis to be crucial to glacial climate modelling, as both have a strong impact on the evolution of the cryosphere. The roles of other climate mechanisms and feedbacks have also been described in this thesis and a summary of each is provided in the concluding discussion at the end of each of the individual chapters.

**2) To attempt to facilitate a means for assessing the validity of the response modelled in each of the various complex models developed by different groups in the global**

**climate modelling community.** The intercomparison of model results in the context of PMIP, many of which have been illustrated herein (cf. Chapter 2 and Chapter 3), provides a unique methodology for improving these models and for understanding their ability to produce rational predictions of previous climate states. While this thesis has demonstrated a great deal of variability between the models, which implies the need for more convergence in past climate prediction, it has also demonstrated that the specific response of a particular model is very dependant upon the ability of the model to faithfully represent the modern climate. This is especially apparent in Chapter 2 where the 6 ka BP solar forcing is weak compared with other changes that have occurred in the geologic past. Likewise, the initiation of glaciation in a GCM is strongly influenced by the quality of the simulation of present climate that the model delivers as global temperature biases in the model effect the high-latitude regions of nucleation (cf. Chapter 4).

**3) To further investigate model-data intercomparison using the climate states that are inferred to have existed based upon the available proxy data reconstructions of 6 ka and 21 ka BP.** This thesis has shown that direct comparison of proxy lake level data with the model results for 6 ka BP climate reveals significant problems with the "snapshot" mode of model-data intercomparison. This is especially apparent over regions such as North America, where the model response to paleoclimate forcing may be significant in one variable, but not in others (i.e. temperature vs. precipitation) and in Northern Africa where the model response is significantly discrepant from the implications of the proxy data. On a more positive note, the model employed in this thesis delivered the strongest depression in tropical SSTs at LGM among the entire suite of PMIP models. These predictions are in closest accord with the more reliable changes in SSTs that are inferred from certain proxy data such as those obtained from Sr/Ca ratios in corals. Other models fail to show the same sensitivity to the LGM climate in this region. It was also demonstrated in Chapter 3 that this sensitivity in reproducing the inferred changes is dependant on the model ability to reproduce the modern tropical climate.

These concluding remarks along with the more epoch specific conclusions presented in the discussions at the end of each chapter have demonstrated that the ability of a specific climate model to reproduce the climate of past epochs may be used to gauge how the model may be improved. Through additional careful modelling, we may hope to continue to improve our understanding of the internal climate mechanisms that operate on both the short timescales under radically different paleoclimate conditions such as those described in this thesis, and those processes which operate only over much longer geologic timescales.

## APPENDIX A

### The Earth's Insolation Distribution Over Time

#### A.1. Daily Insolation

At any latitude, the distribution of solar radiation at the top of the atmosphere will be a function of the zenith angle,  $Z$  (Fig A.1a). This is the angle that an incident ray from the Sun makes with the normal from a point on a surface. From Fig. A.1a. we see that the zenith angle,  $Z(t)$ , can be calculated from the vector,  $\mathbf{s}$ , pointing from the Earth's centre to the Sun and the vector,  $\mathbf{p}$ , pointing from the Earth's centre to the point in question on the surface:

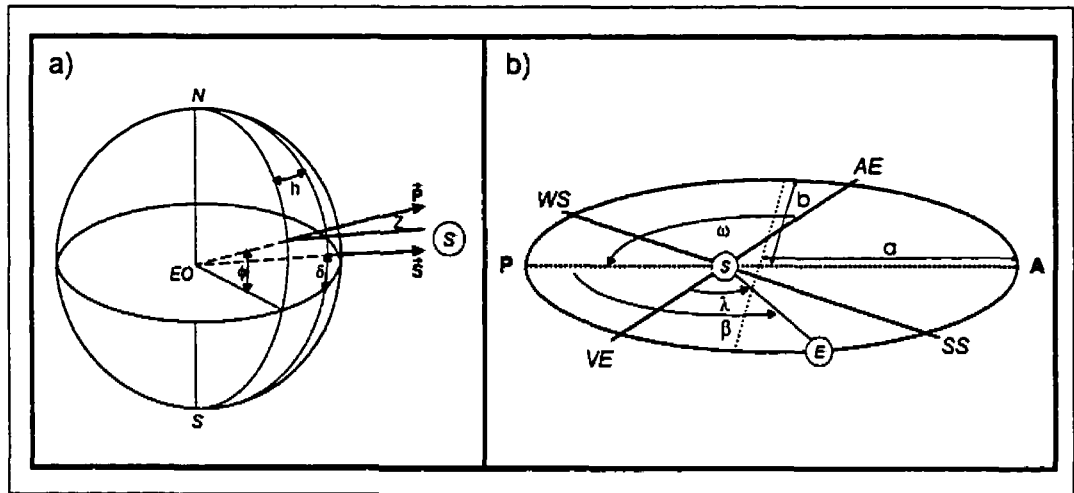


Figure A.1: (a) The definition of the Zenith angle  $Z$ , using the (zenith-pole-sun) spherical triangle. The vector  $\mathbf{p}$  denotes the vector from the center of the Earth to the point on the surface. The vector  $\mathbf{s}$ , is the vector from the centre of the Earth to the Sun;  $\phi$  is the latitude;  $\delta$  is the declination of the sun and  $h$  is the hour angle of the sun. (b) The elements of the elliptical geometry:  $\omega$  is the longitude of the perihelion with respect to the autumnal equinox;  $a$  and  $b$  are the lengths of the semi-major and semi-minor axes;  $e$  is the eccentricity;  $\beta$  is the true longitude of the Earth with respect to the perihelion;  $\lambda$  is the true longitude of the Earth measured from the vernal equinox.

$$(\mathbf{p}, \mathbf{s}) = (\cos(\phi) \cdot \mathbf{i} + \sin(\phi) \cdot \mathbf{k}, \cos(\delta) \cos(h) \cdot \mathbf{i} + \sin(h) \cos(\delta) \cdot \mathbf{j} + \sin(\delta) \cdot \mathbf{k}), \quad (\text{A.1})$$

Thus,

$$\cos Z(t) = \frac{\mathbf{p} \cdot \mathbf{s}}{|\mathbf{p}| |\mathbf{s}|} = \cos(\phi) \cos(\delta) \cos(h) + \sin(\phi) \sin(\delta). \quad (\text{A.2})$$

Here,  $h$  is the hour angle from the local meridian ( $h = 0$ ) of the sun;  $\phi$  is the latitude; and  $\delta$  is the declination angle of the Sun (Fig. A.1a). At sunrise and sunset  $z = \frac{\pi}{2}$  ( $h = \pm H$ ), so that we have

$$H = \cos^{-1}(-\tan \phi \tan \delta) \quad (\text{A.3})$$

in radians. The length of the day is  $24 \frac{H}{\pi}$  hours.

The incident solar radiation  $F(t)$  is also a function of the ratio of the squared normalized Earth-Sun distance with respect to the semi-major axis,  $a$ . We have:

$$F(t) = S \left(\frac{a}{r}\right)^2 \cos Z(t), \quad (\text{A.4})$$

where,  $S$  is the solar constant ( $1365 \text{ W m}^{-2}$ ) and  $(a/r)$  is the mean Earth-Sun distance ( $a$ ) divided by the actual distance ( $r$ ) at the specific time of the year. The total daily integrated insolation,  $Q_0$  ( $\text{W m}^{-2}$ ) at the top of the atmosphere (TOA) is computed as

$$Q_0(t) = S \left(\frac{a}{r}\right)^2 \frac{1}{\tau} \int_{\text{sunrise}}^{\text{sunset}} \cos Z(t) dt, \quad (\text{A.5})$$

where  $\tau$  is the length of the day (24 hours). Using (A.2) along with the angular velocity of the earth  $\Omega = \frac{dh}{dt}$  and  $\tau\Omega = 2\pi$ , (A.5) becomes

$$Q_0(\phi, \delta) = \frac{S}{\pi} \left(\frac{a}{r}\right)^2 \int_{-H}^H [\cos(\phi) \cos(\delta) \cos(h) + \sin(\phi) \sin(\delta)] dh \quad (\text{A.6})$$

which can then be reformulated using (A.2) at  $\pm H$  as,

$$Q_0(\phi, \delta) = \frac{S}{\pi} \left(\frac{a}{r}\right)^2 \sin(\phi) \sin(\delta) (H - \tan H). \quad (\text{A.7})$$

Careful consideration must be taken when  $H = \pi$  or  $H = 0$ . The 24 hour day and night values at high latitudes are  $Q_0(\phi, \delta) = S \left(\frac{a}{r}\right)^2 \sin(\phi) \sin(\delta)$  and  $Q_0(\phi, \delta) = 0$ , respectively.

## A.2. Radiative Forcing at the Top of the Model

In conducting paleoclimate modelling studies we must consider what the effect of changing orbital parameters will be on the insolation at the top of the atmosphere so that this may be incorporated into the atmospheric model. The insolation is a function of the declination,  $\delta$  and the ratio of the mean and actual Earth-Sun distance,  $a/r$ , which vary with the annual cycle and over geologic time scales. If we consider the orbit of the Earth around the Sun (Fig. A.1b) with respect to perihelion ( $\beta$ ), the precession of the autumnal equinox with respect to perihelion ( $\omega$ ), and the position of the Earth relative to the vernal equinox ( $\lambda$ ), we can connect the insolation at the top of the atmosphere throughout the year with the long term evolution of the Earth's orbital elements. The ratio of the mean and actual Earth-Sun distance can be expressed as,

$$r/a = (1 - e^2)/(1 + e \cos \beta) \quad (\text{A.8})$$

where,  $e$  is the eccentricity of the orbit and  $a$  is the semi-major axis. If we consider the geometric relation,  $\cos \beta = \cos(\lambda - \omega)$  along with the expression for the declination in terms of the obliquity,  $\epsilon$ , and the Earth's position in its orbit around the Sun,  $\lambda$ , we can express the instantaneous insolation (A.4) with  $\sin(\delta) = \sin(\epsilon) \sin(\lambda)$  as,

$$F(e, \epsilon, \omega, \phi, t) = S \frac{(1 + e \cos(\lambda - \omega))^2}{(1 - e^2)^2} [\cos(\phi) \cos(\Omega t) \sqrt{1 - \sin(\epsilon)^2 \sin(\lambda)^2} + \sin(\phi) \sin(\epsilon) \sin(\lambda)] \quad (\text{A.9})$$

The true longitude ( $\lambda$ ) of the Earth relative to the vernal equinox can be derived from Kepler's equation using a successive approximation technique (Berger 1978)[14] to obtain the relation

$$\lambda = \lambda_m(t) + (2e - \frac{1}{4}e^3) \sin(\lambda_m(t) - \omega) + \frac{5}{4}e^2 \sin 2(\lambda_m(t) - \omega) + \frac{13}{12}e^3 \sin 3(\lambda_m(t) - \omega) + O(e^4) \quad (\text{A.10})$$

where the mean longitude,  $\lambda_m(t_{day}) = t_{day} \cdot 2\pi/365$ . Thus the model TOA insolation at the latitude in question at each time of the day during the year can be expressed as a function of the 3 orbital parameters, the eccentricity, the obliquity and the precession of the Earth's rotation axis ( $e, \epsilon, \omega$ ).

### A.3. Defining the Seasons

There have been many attempts to formulate a methodology for comparing seasonal definitions in General Circulation Model paleoclimate simulations. The problem that arises when comparing seasons between different temporal epochs is that the eccentricity of the Earth's orbit changes and thus the length of the season (Kepler Second Law). The view taken in this thesis is to compare the seasonal simulation of each epoch (e.g. present and 116 ka BP) of equal time duration but to adjust the occurrence of the vernal equinox in the calendar year in each epoch so that the root mean square insolation difference between epochs over the entire annual cycle is minimized. Chapters 2 and 3 use a fixed Vernal Equinox that is assumed to occur 79.5 days after perihelion to conform with the simulations specified out by the international Paleoclimate Model Intercomparison Project (PMIP) collaboration. The more appropriate minimization technique described above is used for the forcing in Chapter 4 of this thesis. A calculation of the minimized annual insolation anomalies between paleoclimate epochs and modern produces a drift of a few days but does not have a significant impact on seasonal comparisons except at large eccentricity (Hall and Valdes 1997)[78]. The "drift" in the vernal equinox relative to January 1<sup>st</sup> which minimizes total annual insolation differences throughout geologic time is displayed in Fig. A.2. The drift is seen to be modulated by the 413 ka and 100 ka eccentricity cycles which are displayed with the shaded envelopes.

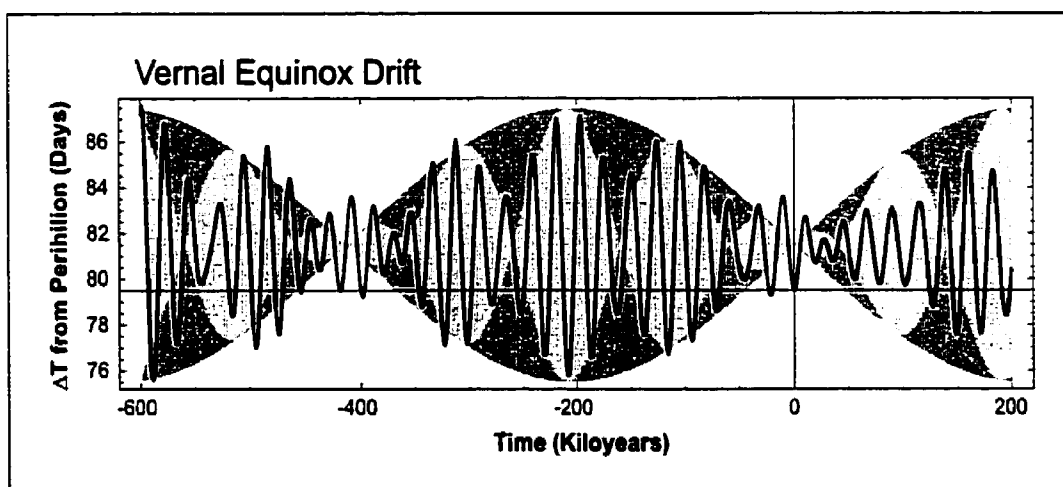


Figure A.2: The vernal equinox drift in days from January 1<sup>st</sup>. This drift is used to facilitate comparison of seasons with the same duration but in different paleoclimate epochs. The drift which varies with precession is modulated by the 413 ka and 100 ka components of the eccentricity.

---

## APPENDIX B

---

### The Dynamical Core of an AGCM

The governing equations of the atmospheric general circulation model are based upon the field equations of hydrodynamics which express the conservation of mass, momentum and energy. These are augmented by a balance equation for water vapor and an equation of state. The complete set of equations form a closed system subject to appropriately defined boundary conditions. The equations describe the motion of a compressible fluid in which a wide variety of wave types may propagate. In the case of the atmosphere, certain approximations may be applied to the full spherical coordinate forms of these equations in order to produce a more tractable set of equations that is usually referred to as the "primitive equations" (e.g. Undesirable high frequency sound waves are filtered by invoking the hydrostatic approximation). We then obtain

(a) the horizontal equations of motion (conservation of momentum),

$$\frac{du}{dt} = (f + u \frac{\tan \phi}{R})v - \frac{1}{\rho} \frac{\partial p}{R \cos \phi \partial \lambda} + F_{\lambda}, \quad (\text{B.1})$$

$$\frac{dv}{dt} = -(f + u \frac{\tan \phi}{R})u - \frac{1}{\rho} \frac{\partial p}{R \partial \phi} + F_{\phi}, \quad (\text{B.2})$$

where

$$\frac{d}{dt} = \frac{\partial}{\partial t} + u \frac{\partial}{R \cos \phi \partial \lambda} + v \frac{\partial}{R \partial \phi} + w \frac{\partial}{\partial z}; \quad (\text{B.3})$$

(b) the hydrostatic equation, an excellent approximation to the vertical component of the momentum conservation equation,

$$\frac{\partial p}{\partial z} = -\rho g; \quad (\text{B.4})$$

(c) the continuity equation (conservation of mass),

$$\frac{\partial \rho}{\partial t} = -\frac{1}{R \cos \phi} \left[ \frac{\partial}{\partial \lambda} (\rho u) + \frac{\partial}{\partial \phi} (\rho v \cos \phi) \right] - \frac{\partial}{\partial z} (\rho w); \quad (\text{B.5})$$

(d) the first law of thermodynamics (conservation of energy),

$$c_p \frac{d \ln T}{dt} - R_d \frac{d \ln p}{dt} = Q; \quad (\text{B.6})$$

where

$$Q = -\alpha \nabla \cdot \mathbf{F}_{rad} - L(e - c) - \alpha \nabla \cdot \mathbf{J}_H^D - \alpha \boldsymbol{\tau} \cdot \nabla \cdot \mathbf{c}; \quad (\text{B.7})$$

(e) the equation of state,

$$p = \rho R_d T (1 - 0.61q); \quad (\text{B.8})$$

and (f) the balance equation for water vapour,

$$\frac{\partial q}{\partial t} + \nabla \cdot \mathbf{q} = (e - c) + D. \quad (\text{B.9})$$

In these equations the predicted variables are the wind components,  $u$  and  $v$ , temperature  $T$ , specific humidity  $q$ , and, the surface pressure  $p_0$ ; which are a function of latitude,  $\phi$ , longitude,  $\lambda$ , and height,  $z$ . In these equations,  $R$  is the radius of the Earth;  $\rho$  is the density and  $\alpha$  is the specific volume of dry air;  $R_d$  is the dry air gas constant;  $c_p$  is the heat capacity of the air at constant pressure;  $g$  is the acceleration due to gravity. The horizontal frictional forces in the momentum equations,  $F_\lambda$  and  $F_\phi$  are mainly significant at the surface of the Earth or in regions of strong wind shear near the jet stream.  $Q$  represents the net radiative heating terms. The fluxes of solar (e.g. Appendix A) and terrestrial radiation are expressed as  $F_{rad}$  which is in turn represented in terms of the vertical distribution of temperature and details of the radiative transfer on radiatively active constituents in the atmosphere. The exchange of energy between various forms of water is expressed by the latent heat of the phase change,  $L$ , times the difference between condensation ( $c$ ) and evaporation ( $e$ ) in the atmosphere. The heat conduction due to molecular and turbulent eddy diffusion is expressed as  $\mathbf{J}_H^D$  and the heat generated by frictional dissipation is expressed as the product of the stress tensor,  $\boldsymbol{\tau}$ , and the divergence of the 3-D wind vector  $\mathbf{c}$ . The sources and sinks of water vapour is expressed in the balance equation for water vapour by  $D$ . (See Appendix C and Peixoto and Oort (1992)[168] for a more detailed description of the physics of the tendencies:  $F_{(\lambda,\phi)}$ ,  $Q$ , and  $D$ .)

One of the first considerations in developing an atmospheric model is the choice of vertical coordinate system. One of the landmark advances in numerical modelling came with the introduction

of a terrain-following coordinate system (Phillips 1957)[177]. The introduction of the "sigma" system allowed for a simple kinematic description of the lower boundary conditions. The conventional sigma system, with  $\sigma = p/p_0$  and the surface pressure  $p_0 = f(x, y, t)$ , suffers from the shortcoming that the slope of the coordinate surfaces does not decrease sufficiently rapidly at the top of the atmosphere an effect that produces truncation errors associated with the coordinate transformation. The sigma coordinate is furthermore not optimal for middle atmosphere dynamics so a hybrid coordinate was introduced in the 1980s to taper to zero the deflections of the coordinate surfaces at the top of the atmosphere. The so called "eta" coordinate system,  $\eta = \eta(p, p_0)$ , is implemented and described by the definition,

$$p(\eta) = p_0 \eta + (p_s - p_0) \left[ \frac{\eta - \eta_T}{1 - \eta_T} \right]^\tau. \quad (\text{B.10})$$

This equation relates the surface pressure,  $p_s$ , at  $\eta = 1$  and the top level pressure  $p_0 \eta_T = 5mb$  where  $\eta_T$  is the  $\eta$  coordinate at the model top. The slope adjustment parameter,  $\tau$ , is set equal to 2 and used to create a gradual rectification of the coordinate surface with height. The total derivative, equation (B.3), can be converted to the  $\eta$ -coordinate system as follows,

$$\frac{d}{dt}|_\eta = \frac{\partial}{\partial t}|_\eta + u \frac{\partial}{R \cos \phi \partial \lambda}|_\eta + v \frac{\partial}{R \partial \phi}|_\eta + \frac{d\eta}{dt} \frac{\partial}{\partial \eta}|_\eta; \quad (\text{B.11})$$

where the derivatives are evaluated along a surface of constant  $\eta$ . The conservation of mass and momentum in the  $\eta$  coordinate system then becomes,

(a) the horizontal vector equation of motion,

$$\frac{d\mathbf{V}}{dt} = -f\mathbf{k} \times \mathbf{V} + \nabla\Phi - RT\nabla \ln p + \mathbf{F}_{(\lambda, \phi)}, \quad (\text{B.12})$$

(b) the hydrostatic equation,

$$\frac{\partial p}{\partial \eta} = -\rho \frac{\partial \Phi}{\partial \eta}; \quad (\text{B.13})$$

(c) the continuity equation,

$$\frac{\partial}{\partial t} \left( \frac{\partial p}{\partial \eta} \right) = - \left[ \frac{1}{R \cos \phi} \left[ \frac{\partial}{\partial \lambda} \left( u \frac{\partial p}{\partial \eta} \right) + \frac{\partial}{\partial \phi} \left( v \cos \phi \frac{\partial p}{\partial \eta} \right) \right] + \frac{\partial}{\partial \eta} \left( \frac{d\eta}{dt} \frac{\partial p}{\partial \eta} \right) \right]; \quad (\text{B.14})$$

The other equations remain in the same form but are evaluated along constant  $\eta$  surfaces. To ensure total mass conservation the mixed Dirichlet and Neuman conditions are,

$$\frac{\partial \eta}{\partial t} = 0; \eta_0, \eta_T = \text{const.} \quad (\text{B.15})$$

When dealing with numerical integration of continuous equations it is desirable to preserve the invariants of the continuous equations. To conserve dynamical quantities in the model, manipulation of the governing equations and integration from the top to bottom and over the surface of the model can be carried out to obtain the integrals of the time rate of change of mass, momentum and energy (i.e. invariants). Details of the budget analysis are provided in Laprise and Girard (1990)[121].

The numerical method used for solving the set of primitive equations in the model involve a spectral decomposition of the equations to a spherical harmonic orthonormal basis. The Helmholtz theorem allows for the decomposition of the horizontal wind in terms of the solenoidal and irrotational scalar functions of the form:

$$\mathbf{V} = \mathbf{k} \times \nabla \psi + \nabla \chi. \quad (\text{B.16})$$

The set of primitive equations can be expressed in terms of the vorticity,  $\psi$ , and divergence,  $\chi$ , fields by performing the curl and divergence on the horizontal momentum equations. The spectral formulation of the primitive equations is written in terms of  $\psi$  and  $\chi$  and evolve according to the physical tendencies which contain non-linear terms of the form of the Jacobian of  $\psi$  and  $\chi$ . The spectral form of the non-linear tendencies are evaluated through the semi-spectral transform method where the non-linear quantities are transformed to and multiplied in grid-point space then transformed back to spectral space to evolve the spectral form of the dynamical equations (e.g. see Orszag 1970)[166]. For further details on the spectral form of the set of primitive equations used in the model see Boer et al. (1984)[20].

---

## APPENDIX C

---

### Model Documentation: CCCma Version 2 (T32 L10) 1992

#### **Model Lineage**

The model employed herein is the second-generation version of the CCCma model first developed in the early 1980s for climate applications. The model is similar in most respects to the original CCCma except for different initial conditions, some boundary conditions and the Earth's orbital configuration.

#### **References**

Main references: McFarlane et al. (1992)[146] ; Boer et al. (1984)[20].

#### **Numerical/Computational Properties**

##### Horizontal Representation

Spectral (spherical harmonic basis functions) with transformation to a Gaussian grid for calculation of nonlinear quantities and some physics.

##### Horizontal Resolution

Spectral triangular 32 (T32), roughly equivalent to 3.75 x 3.75 degrees latitude-longitude. longitude\*latitude dimension: 96\*48

##### Vertical Domain

Surface to 5 hPa. For a surface pressure of 1000 hPa, the lowest atmospheric level is at a pressure of about 980 hPa.

##### Vertical Representation

Piecewise finite-element formulation using hybrid coordinates (Laprise and Girard 1990)[121].

##### Vertical Resolution

There are 10 irregularly spaced hybrid levels. For a surface pressure of 1000 hPa, 3 levels are below 800 hPa and 4 levels are above 200 hPa. The model uses an eta-coordinate in the vertical with the following levels: 0.012, 0.038, 0.088, 0.160, 0.265, 0.430, 0.633, 0.803, 0.915, 0.980

##### Computer/Operating System

Simulations were run on Cray J916, NEC-SX3 and NEC-SX5 machines under various UNIX Operating Systems.

### Computational Performance

9 minutes Cray J916 computation time per simulation day (1 day = 72 timesteps). 30 seconds NEC-SX5 computation time per simulation day (1 day = 72 timesteps).

### Initialization

The model was started from initial conditions based on the present day climatology. The model atmosphere is initialized from FGGE III-B observational analyses for 1 January 1979. Soil moisture and snow cover/depth are initialized from January mean values obtained from an earlier multiyear model simulation.

### Time Integration Scheme(s)

A semi-implicit time integration scheme with an Asselin (1972)[9] frequency filter is used. The time step is 20 minutes for all dynamics and physics fields, except for full calculations of radiative fluxes and heating rates. Shortwave radiation is calculated every timestep, and longwave radiation every 3 hours, with interpolated values used at intermediate time steps (see McFarlane et al. 1992)[146]. Full Longwave Radiative heating calculation is carried out twice daily.

### Smoothing/Filling

Orography is truncated at spectral T32 (see Orography). Negative values of atmospheric specific humidity (which arise because of numerical truncation errors in the discretized moisture equation) are filled in a two stage process. First, all negative values of specific humidity are made slightly positive by borrowing moisture (where possible) from other layers in the same column. If column moisture is insufficient, a nominal minimum bound is imposed, the moisture deficit is accumulated over all atmospheric points, and the global specific humidity is reduced proportionally. This second stage is carried out in the spectral domain (see McFarlane et al. 1992)[146].

### Sampling Frequency

For the PMIP simulations, the model history is written every 12 hours. (However, some archived variables, including most of the surface quantities, are accumulated rather than sampled.)

## **Dynamical/Physical Properties**

### Atmospheric Dynamics

Primitive-equation dynamics are expressed in terms of vorticity, divergence, temperature, the logarithm of surface pressure, and specific humidity (see Appendix B).

### Diffusion

Horizontal diffusion follows the scale-dependent eddy viscosity formulation of Leith (1971)[128] as described by Boer et al. (1984)[20]. Diffusion is applied to spectral modes of divergence, vorticity, temperature, and moisture, with total wavenumbers  $>18$  on hybrid vertical surfaces.

Second-order vertical diffusion of momentum, moisture, and heat operates above the surface. The vertically varying diffusivity depends on stability (gradient Richardson number) and the vertical shear of the wind, following standard mixing-length theory. Diffusivity for moisture is taken to be the same as that for heat (see McFarlane et al. 1992)[146]. See also Surface Fluxes.

#### Gravity-wave Drag

Simulation of subgrid-scale gravity-wave drag follows the parameterization of McFarlane (1987)[145]. Deceleration of the resolved flow by dissipation of orographically excited gravity waves is a function of the rate at which the parameterized vertical component of the gravity-wave momentum flux decreases in magnitude with height. This momentum-flux term is the product of local air density, the component of the local wind in the direction of that at the near-surface reference level, and a displacement amplitude. At the surface, this amplitude is specified in terms of the mesoscale orographic variance, and in the free atmosphere by linear theory, but it is bounded everywhere by wave saturation values. See also Orography.

#### Solar Constant/Cycles

The solar constant is the prescribed value of  $1365 \text{ W m}^{-2}$ . The orbital parameters and seasonal insolation distribution are calculated after PMIP recommendations except in Chapter 4 and 5 of this thesis. Both seasonal and diurnal cycles in solar forcing are simulated.

#### Chemistry

The carbon dioxide concentration is the value of 345, 280 and 200 ppmv for 0 ka, 6 ka BP/116 ka BP and 21 ka BP, respectively. A monthly zonally averaged ozone distribution from data by Wilcox and Belmont (1977)[242] is specified. Radiative effects of water vapor also are treated (see Radiation).

#### Radiation

Shortwave radiation is modeled after an updated scheme of Fouquart and Bonnel (1980)[67]. Upward/downward shortwave irradiance profiles are evaluated in two stages. First, a mean photon optical path is calculated for a scattering atmosphere including clouds, aerosols, and gases. The reflectance and transmittance of these elements are calculated by, respectively, the delta-Eddington method (see Joseph et al. 1976)[105] and by a simplified two-stream approximation. The scheme evaluates upward/downward shortwave fluxes for two reference cases: a conservative atmosphere and a first-guess absorbing atmosphere; the mean optical path is then computed for each absorbing gas from the logarithm of the ratio of these reference fluxes. In the second stage, final upward/downward fluxes are computed for visible ( $0.30\text{-}0.68 \mu\text{m}$ ) and near-infrared ( $0.68\text{-}4.0 \mu\text{m}$ ) spectral intervals using more exact gas transmittances (see Rothman 1981)[197], and with adjustments made for the presence of clouds. The asymmetry factor is prescribed for clouds, and the optical depth and single-

scattering albedo are functions of cloud liquid water content (see Betts and Harshvardhan 1987)[105] and ice crystal content (see Heymsfield 1977)[87].

Longwave radiation is modeled in six spectral intervals between wavenumbers 0 to  $2.82 \times 10^5 \text{ m}^{-1}$  after the method of Morcrette(1984, 1990, 1991)[155][156][157], which corrects for the temperature/pressure dependence of longwave absorption by gases and aerosols. Longwave absorption in the water vapor continuum follows Clough et al. (1980)[39]. Clouds are treated as graybodies in the longwave, with emissivity depending on optical depth (see Platt and Harshvardhan 1988)[105], and with longwave scattering by cloud droplets neglected. The effects of cloud overlap in the longwave are treated following a modified scheme of Washington and Williamson (1977)[236] : upward/downward irradiances are computed for clear-sky and overcast conditions, and final irradiances are determined from a linear combination of these extreme cases weighted by the actual partial cloudiness in each vertical layer. For purposes of the radiation calculations, clouds occupying adjacent layers are assumed to be fully overlapped, but to be randomly overlapped otherwise. See McFarlane et al. (1992)[146] for further details.

#### Convection

A moist convective adjustment procedure is applied on pairs of vertical layers whenever the model atmosphere is conditionally unstable. Convective instability occurs when the local thermal lapse rate exceeds a critical value, which is determined from a weighted linear combination of dry and moist adiabatic lapse rates, where the weighting factor (with range 0 to 1) is a function of the local relative humidity. Convective instability may occur in association with condensation of moisture under supersaturated conditions, and the release of precipitation and associated latent heat (see Precipitation). See Boer et al. (1984)[20] for further details.

#### Cloud Formation

The fractional cloud cover in a vertical layer is computed from a linear function of the relative humidity excess above a threshold value. The threshold is a nonlinear function of height for local sigma levels  $>0.5$ , and is a constant 85 percent relative humidity at higher altitudes. (Note that the cloud scheme uses locally representative sigma coordinates, while other model variables use hybrid vertical coordinates—see Vertical Representation). To prevent development of excessive low cloudiness, no clouds are allowed in the lowest model layer. See McFarlane et al. (1992)[146] for further details. See also Radiation for treatment of cloud-radiative interactions.

#### Precipitation

Condensation and precipitation occur under conditions of local supersaturation, which are treated operationally as part of the model's convective adjustment scheme (see Convection). All the precip-

itation falls to the surface without subsequent evaporation to the surrounding atmosphere. See also Snow Cover.

#### Planetary Boundary Layer

The depth of the PBL is not explicitly determined, but in general is assumed to be greater than that of the surface layer (centered at the lowest prognostic vertical level—about 980 hPa for a surface pressure of 1000 hPa). The PBL depth is affected by dry convective adjustment (see Convection), which simulates boundary-layer mixing of heat and moisture, and by enhanced vertical diffusivities (see Diffusion), which may be invoked in the lowest few layers that are determined to be convectively unstable (Boer et al. (1984)[20]). Within the surface layer of the PBL, temperature and moisture required for calculation of surface fluxes are assigned the same values as those at the lowest level, but the wind is taken as one-half its value at this level (see Surface Fluxes).

#### Orography

Orographic heights with a resolution of 10 minutes arc on a latitude/longitude grid are smoothed by averaging over 1.8-degree grid squares, and the orographic variance about the mean for each grid box also is computed (see Gravity-wave Drag). These means and variances are interpolated to a slightly coarser Gaussian grid (64 longitudes x 32 latitudes), transformed to the spectral representation, and truncated at the model resolution (spectral T32) for control, 6fk and 21k run.

#### Ocean

The prescribed monthly climatological integrations were made by averaging Alexander and Mobley (1976)[3] monthly sea surface temperature fields, with daily values determined by linear interpolation. For the computed 21 ka BP simulation, the mixed layer model was started from a initial conditions based on CLIMAP 21ka BP reconstructed SST climatology and run for 50 years to equilibrium.

#### Sea Ice

For 0 ka, 6 ka BP, Alexander and Mobley (1976)[3] monthly sea ice extents are prescribed. Snow may accumulate on sea ice (see Snow Cover). The surface temperature of the ice (see McFarlane et al. 1992)[146] is a prognostic function of the surface heat balance (see Surface Fluxes) and of a heat flux from the ocean below. This ocean heat flux depends on the constant ice thickness and the temperature gradient between the ocean and the ice.

#### Snow Cover

If the near-surface air temperature is <0 degrees C, precipitation falls as snow. Prognostic snow mass is determined from a budget equation, with accumulation and melting treated over both land and sea ice. Snow cover affects the surface albedo of land and of sea ice, as well as the heat capacity

of the soil. Sublimation of snow is calculated as part of the surface evaporative flux. Melting of snow, as well as melting of ice interior to the soil, contributes to soil moisture. See McFarlane et al. (1992)[146] for further details. See also Surface Characteristics, Surface Fluxes, and Land Surface Processes.

#### Surface Characteristics

Local roughness lengths are derived (Boer et al. (1984)[20] from prescribed neutral surface drag coefficients (see Surface Fluxes). The 1 x 1-degree Wilson and Henderson-Sellers (1985)[243] data on 24 soil/vegetation types are used to determine the most frequently occurring primary and secondary types (weighted 2/3 vs 1/3) for each grid box. Averaged local soil/vegetation parameters include field capacity and slope factor for predicting soil moisture (see Land Surface Processes), and snow masking depth for the surface albedo (see below). These are obtained by table look-up based on primary/secondary vegetation types.

Over bare dry land, the surface background albedo is determined from a weighted average for each of 24 vegetation types in the visible (0.30-0.68 micron) and near-infrared (0.68-4.0 microns) spectral bands; for wet soil, albedos are reduced up to 0.07. For vegetated surfaces, albedos are determined from a 2/3 vs 1/3 weighting of albedos of the local primary/secondary vegetation types. The local land albedo also depends on the fractional snow cover and its age (fractional coverage of a grid box is given by the ratio of the snow depth to the specified local masking depth); the resulting albedo is a linear weighted combination of snow-covered and snow-free albedos. Over the oceans, latitude-dependent albedos which range between 0.06 and 0.17 are specified independent of spectral interval. The background albedos for sea ice are 0.55 in the near-infrared and 0.75 in the visible; these values are modified by snow cover, puddling effects of melting ice (a function of mean surface temperature), and by the fraction of ice leads (a specified function of ice mass).

The longwave emissivity is prescribed as unity (i.e., blackbody emission is assumed) for all surfaces. See McFarlane et al. (1992)[146] for further details.

#### Surface Fluxes

The surface solar absorption is determined from surface albedos, and the longwave emission from the Planck equation with prescribed emissivity of 1.0 (see Surface Characteristics). The surface turbulent eddy fluxes of momentum, heat, and moisture are expressed as bulk formulae following Monin-Obukhov similarity theory. The momentum flux is a product of a neutral drag coefficient, the surface wind speed and wind vector (see Planetary Boundary Layer), and a function of stability (bulk Richardson number). Drag coefficients over land and ice are prescribed after Cressman (1960)[41], but over the oceans they are a function of surface wind speed (see Smith 1980)[211]. The flux of

sensible heat is a product of a neutral transfer coefficient, the surface wind speed, the difference in temperatures between the surface and that of the lowest atmospheric level, and the same stability function as for the momentum flux. (The transfer coefficient has the same value as the drag coefficient over land and ice, but is not a function of surface wind over the oceans.)

The flux of surface moisture is a product of the same transfer coefficient and stability function as for sensible heat, an evapotranspiration efficiency (beta) factor, and the difference between the specific humidity at the lowest atmospheric level (see Planetary Boundary Layer) and the saturation specific humidity at the temperature/pressure of the surface. Over the oceans and sea ice, beta is prescribed as 1; over snow, it is the lesser of 1 or a function of the ratio of the snow mass to a critical value ( $10 \text{ kg m}^{-2}$ ). Over land, beta depends on spatially varying soil moisture and field capacities (see Land Surface Processes), and on slope factors for primary/secondary vegetation and soil types (see Surface Characteristics). For grid boxes with fractional snow coverage, a composite beta is obtained from a weighted linear combination of snow-free and snow-covered values. See Boer et al. (1984)[20] and details.

#### Land Surface Processes

Soil heat storage is determined as a residual of the surface heat fluxes and of the heat source/sink of freezing/melting snow cover and soil ice (see below). Soil temperature is computed from this heat storage in a single layer, following the method of Deardorff (1978)[46] which accounts for both diurnal and longer-period forcing. The composite conductivity/heat capacity of the soil in each grid box is computed as a function of soil type, soil moisture, and snow cover. Soil moisture is predicted by a single-layer "bucket" model with field capacity and slope factors varying by primary/secondary soil and vegetation types for each grid box (see Surface Characteristics). Soil moisture budgets include both liquid and frozen water. The effective local moisture capacity is given by the product of field capacity and slope factor, with evapotranspiration efficiency beta a function of the ratio of soil moisture to the local effective moisture capacity (see Surface Fluxes). Runoff occurs implicitly if this ratio exceeds 1 (which is more likely the higher the local slope factor and the lower the local field capacity). See McFarlane et al. (1992)[146] and Boer et al. (1984)[20] for further details.

---

## APPENDIX D

---

### Constraining the Model so as to Reproduce Modern Climate

The ability of an AGCM to accurately reproduce modern climate is dependant on model "parameterizations" which embody an attempt to represent subgrid scale physical phenomena that are not explicitly captured in the model dynamics. Typical AGCMs, such as the one employed in this study, require that the parameters which govern subgrid scale physical processes be "tuned" such that the large scale modern climatology, as represented by globally observed data sets, be faithfully reproduced. There are numerous issues involved in simulating modern climate with an AGCM (e.g. see McFarlane et al. 1992)[146] many of which are well beyond the scope of the present study. In the following subsections I will therefore focus upon the subset of such parameterizations that it will be crucial to understand in the context of the present work.

#### D.1. Oceanic Heat Flux Correction

One modelling issue which requires a concerted effort to resolve and which nevertheless still poses a problem in the most recent models concerns the way in which the atmosphere is coupled to the ocean. Many of the modern Atmosphere-Ocean General Circulation Models (AOGCMs) that are currently under development still suffer from the problems that arise in representing the exchange of moisture, heat and momentum between the atmosphere and ocean (see e.g. Lambert and Boer 2001)[120]. In an AGCM in which SSTs are prescribed, the atmosphere is forced by a boundary condition representative of the seasonally varying surface temperature of the modern oceans. The atmospheric model is then tuned with these and other fixed boundary conditions so as to reproduce the modern climate. When thermodynamic mixed layer slab ocean and sea ice modules are coupled to an AGCM there is also a need to impose "flux corrections" within the simple ocean model. Without some representation of the oceanic heat fluxes within a simple mixed layer ocean model of this kind the AGCM would be of limited utility.

The flux correction method that is employed for this purpose was first proposed by Hansen et al. (1984)[79] to adjust the GISS AGCM modern climatology when this model was coupled to a mixed layer slab ocean. The internal heat flux terms employed within the slab ocean embody an attempt

to model the effects of horizontal heat transport and exchange of heat with the underlying water during periods of shallowing or deepening of the mixed layer. These processes are modelled through a simple combination of the horizontal and vertical internal fluxes into a single term. This residual term ensures a realistic simulation of the observed modern climatology when forced with the net heat flux entering the thermodynamic mixed layer from above. The residual term also has the effect of correcting for misrepresentations of these net surface fluxes from the atmospheric component of the model. The residual term is specified on a monthly averaged basis and is obtained from the difference between the monthly mean net surface flux and the implied change in heat storage of the slab based on the mean monthly climatological SST field in the following form:

$$R(t_m) = [F_a]_m - \rho_w C_w \Delta T_w / \Delta t_m. \quad (\text{D.1})$$

In this equation, the term  $[F_a]_m$  denotes monthly mean values of the net surface flux from the atmospheric model, whereas the second term represents the local heat storage of the slab obtained from changes in the climatological SST field. The heat storage term is the product of the density times the heat capacity of the sea water and the change in SST over the period of month  $m$ . To produce an acceptably accurate estimate of the residual field which takes into account the natural variability of the atmospheric component of the model requires that the mean of the net heat fluxes,  $F_a$ , received at the surface of the ocean over many annual cycles, be assessed from a model simulation. It becomes quickly apparent that the ocean residual term can be stably determined within approximately 5 annual cycles of simulation. The residual term is only implemented in ice-free areas of the slab ocean model while a similar term is applied to regions underneath places where there is sea-ice coverage. The computation of the under ice heat flux requires much more careful consideration of the energy budget of the sea-ice layer.

The fluxes of heat from the slab ocean to the thermodynamic sea ice module must be specified because the oceanic mixed layer is not used when sea ice is present. The seasonally varying values of the under ice heat flux are determined so as to produce a realistic representation of the seasonal sea ice coverage, most importantly in spatial extent. This sea ice model does not include a representation of sea ice dynamics and therefore has limitations in determining the proper thickness of the ice covered regions near the pole. The under ice heat flux must also satisfy the additional physical constraint that there be a net upward heat flux from the sea water to sea ice. Changes in the ice mass due to melting and freezing at the bottom of the sea ice layer are determined from the difference between the upward flux of heat from the sea water and the downward fluxes of heat

from the overlying snow pack or in the case of thin ice the net downward atmospheric fluxes. The representation of a snowpack which evolves based on the amount of energy going into or leaving the snow within the sea ice model adds another degree of complexity to this simple model. Therefore it is not trivial to determine the residual field which controls the seasonal evolution of the sea ice pack. The procedure requires a climate simulation of several annual cycles. During the course of the simulation the evolution of both snow and sea ice are monitored so that the under ice residual term can be adjusted where there is excessive amounts of sea ice present. The procedure is then repeated in an adaptive manner for several annual cycles until a realistic representation of the sea ice annual cycle is achieved.

The mixed layer thermodynamic slab ocean residual field may be used to calculate the implied total northward oceanic heat transport as a function of latitude by zonally averaging the residual field and then carrying out an area weighted integral of the residual field northward from the south pole to that latitude (Fig. D.1). The observed northward oceanic heat transport (Trenberth and Solomon 1994)[225] is then found to be much different from that suggested by the model. Implied oceanic heat transports of this nature are not uncommon to mixed layer ocean models of this generation (Weaver and Hughes 1996)[237]. This misfit to the observations is a consequence of the inability of a simple thermodynamic slab ocean model to represent the heat transports associated with deep ocean overturning as well as from errors in the atmospheric component of the model associated with cloud parameterizations (Gleckler et al. 1995)[72]. The model implies a large northward transport in both the southern and northern hemisphere which is incorrect based upon the observed oceanic heat transport derived from the atmospheric residual method (Trenberth and Solomon 1994)[225]. As the observations suggest, the southern hemisphere annual northward transport should be negative as warm equatorial waters flow southward towards Antarctica. This problem is effectively resolved in the fully coupled version of the CCCma Atmosphere-Ocean Global Climate Model (AOGCM) which includes a full three dimensional ocean model coupled to the GCMII model to be employed in the present study (Flato et al. 2000)[63].

## **D.2. Solar Radiation Parameterizations**

In order to accurately simulate the diurnal cycle of radiation within this model, the solar radiation calculations must be reevaluated frequently during the course of a climate integration. This is the most computationally demanding of all the physical processes that are explicitly described. In order to carefully investigate how frequently it was necessary to update the radiative transfer calculation,

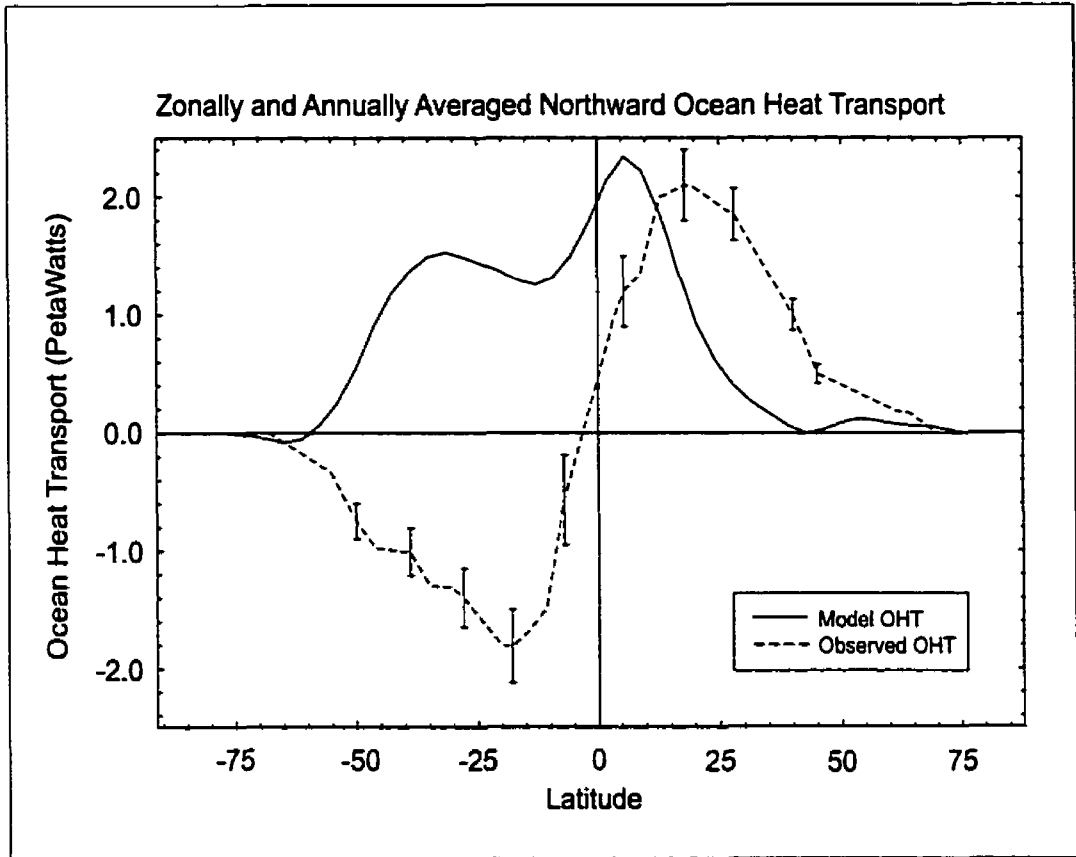


Figure D.1: The zonally and annually averaged all basin northward oceanic heat transport for the observed and the modern AGCM climate with computed SSTs. The observed values (Trenberth and Solomon 1994)[225] are derived indirectly by analyzing atmospheric measurements and heat fluxes from satellite data. The scale is in units of  $10^{15}$  Watts = 1 PetaWatt.

a scheme was devised in the context of the present work so that the rate of recomputation could be varied so as to repeat the analysis at an arbitrary multiple of the model timestep by adjusting a control parameter. In the original version of the model the solar radiation routine was called every three hours and the model timestep was fixed to twenty minutes. Thus, a smooth extrapolation of the solar radiative forcing was required at 8 timesteps in the interval between full radiation calculations. This was accomplished by calculating the absorbed solar irradiance at each level in the model, including the surface, and then normalizing by the cosine of the incident solar zenith angle. At each model timestep the instantaneous absorbed solar irradiances were then computed based on the previous save of the results of the full calculation in the following manner:

$$S_i(t) = (S_i(t_0) / \cos[\theta(t_0)]) * \cos[\theta(t)]. \quad (\text{D.2})$$

In this equation the instantaneous absorbed solar irradiance at each vertical level  $S_i$  is comprised of the product of the normalized absorbed solar irradiance at time  $t_0$  and the cosine of the instantaneous solar zenith angle  $\theta(t)$ . The solar zenith angle is measured from the normal to the Earth's surface. At each model timestep, the interpolation increases the heating rates in each atmospheric layer as the sun rises and likewise decreases the heating rates as the sun sets.

The use of a parameterization of this nature to decrease the computational load has merit, but it is not without a number of serious flaws. By employing a sparse set of times at which the full solar radiation calculations are performed, a bias in the radiative input is introduced into the model depending on the time of the day at which the full radiation calculations are performed. In particular, just after sun rise the model radiation input will be based upon the cosine of a zenith angle which is negative because the sun is below the horizon. This produces the aberrant effect of having no solar radiation absorbed in the model immediately following sunrise when clearly there is a finite, albeit small, forcing. Likewise, after sunset the model is still being fed by incoming solar radiation based upon the full calculation that was performed just before sunset. This effect is significantly enhanced in high latitude winter and summer hemisphere regions where the sun lies above or below the horizon for much of the day. The net effect of this inaccuracy is that the sunrise and sunset components of the excess radiation do not balance and there is a decrease in the globally and annually averaged solar radiation absorbed at the surface of approximately  $3 \text{ W m}^{-2}$ . This defect will be corrected in the analyses to be presented herein by computing full solar radiation calculations at every model timestep. This approach does not create any significant problem given the computational power now available.

The solar radiation anomalies between the correct (synchronous) and incorrect (intermittent) solar radiation schemes for the energy absorbed at the surface are very significant. Fig. D.2 demonstrates that the model parameterization which interpolates between timesteps lacks a significant amount of radiation at high latitudes and would therefore create a fictitiously cold climatology at mid to high latitudes. The model climatology based upon a sparse set of radiative transfer calculations has an excess of radiation of a few  $\text{W m}^{-2}$  at equatorial latitudes throughout most of the year. In the mid and high latitudes there is a deficit of 10 to 20  $\text{W m}^{-2}$  in mid-latitude spring and high latitude summer. The lack of symmetry in the anomaly suggests that the atmosphere, ocean and sea-ice modules play a nonlinear role in the magnitude and timing of the surface anomaly delivered by the computation. This poses a serious problem with the implementation of the full radiation calculation at every timestep based on the fact that the model oceanic heat transport was "tuned" based upon the interpolated calculations where a full radiation calculation was performed only every nine model

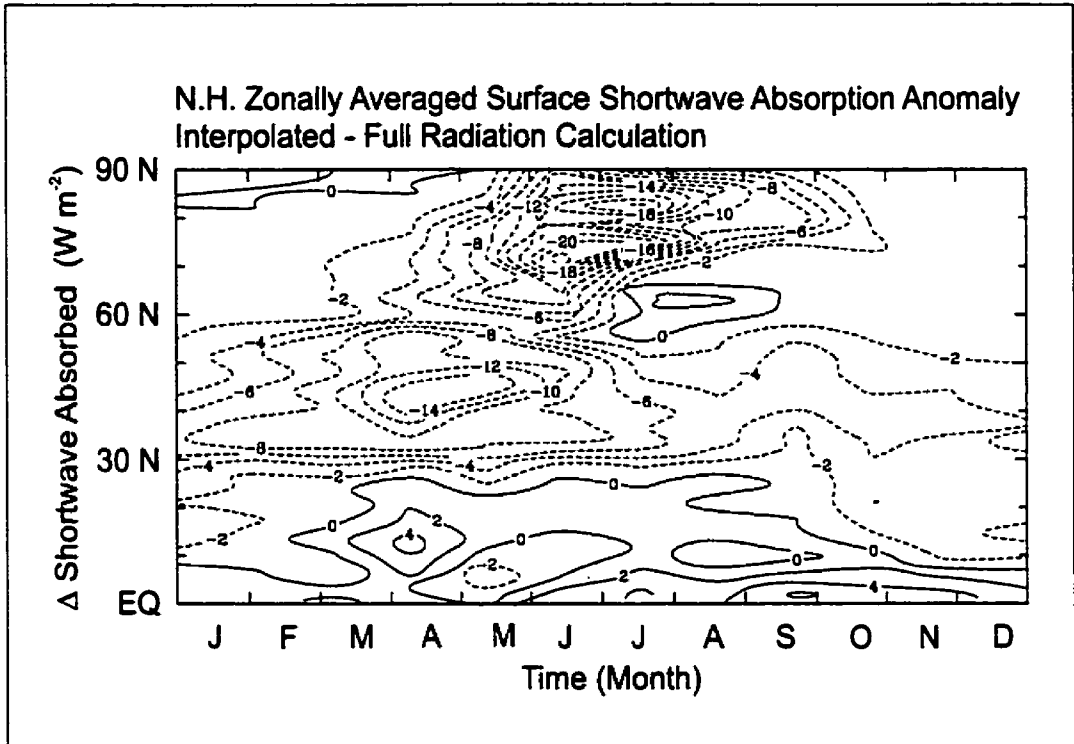


Figure D.2: A Hovmuller diagram of the northern hemisphere zonally averaged solar radiation anomaly absorbed at the surface in  $W m^{-2}$  between two AGCM simulations of modern climate. Each simulation employs ocean heat transports derived with full solar radiation calculations every 9 model timesteps but with one simulation subsequently run with full solar radiation calculations at every model timestep. High latitude negative anomalies reflect the deficit in solar radiation received at the surface when the model does not compute full solar radiation calculations at every timestep.

timesteps. Since the mixed layer slab ocean implied oceanic heat transports and under sea ice residuals were configured based upon the interpolated radiation scheme, the residual terms will no longer apply. There is therefore a significant warming in the land and ocean temperatures with the solar radiation scheme computed at every model timestep when the ocean heat transports based upon the model that employed sparse computations are used. Nevertheless, a stable equilibrium model climatology that is of use for the purpose of sensitivity analysis may be obtained with approximately 20 annual cycles of integration. Two differently biased simulations of modern climate are therefore available from the original model and from the original model with the full synchronous computation of radiative transfer. One of these models is warm biased and the other is cold biased, as we will see. Taken together with a new model with synchronously computed radiative transfer and retuned ocean heat fluxes so as to accurately fit observed SSTs, this suite of models will provide us a means of directly investigating the impact of model bias in the simulation of modern climate upon the

ability of the model to achieve glacial inception.

---

## APPENDIX E

---

### Glacial Inception Modelling Issues within Spectral AGCMs.

A number of reasons have been suggested to explain why the majority of AGCMs fail to produce glacial inception when the model insolation parameters are adjusted to those of the post Eemian epoch (see next section for a discussion of orbital insolation). The consensus view is apparently that these models either have inaccurate modern climatologies or lack critical features of the real climate system that are crucial in simulating the physical factors that contribute to producing perennial snow fields at high northern latitudes. Some of the components which AGCMs either account for only crudely or fail to represent altogether include the land surface and/or biosphere processes, ocean dynamics or cryospheric processes. Others argue that model deficiencies simply derive from the use of overly low AGCM horizontal and vertical resolutions of the dynamics, physics and boundary conditions. Based upon oxygen isotopic chronologies from deep sea sedimentary cores (Imbrie et al. 1984)[99] and atmospheric gas chronologies from deep ice cores (Barnola et al. 1987)[11], it is readily apparent that the global climate system exhibits a great deal of variability over millennial timescales. This climate system variability demonstrates that atmospheric behavior is significantly influenced by surface biomass variability, ocean dynamics and ice sheet growth/decay. In the context of one study of glacial inception (Dong and Valdes 1995)[54], it has been suggested that the surface thermal response of the ocean together with the representation of high elevation continental orography may be the most important requirements for a successful simulation of perennial snowfall. Others have suggested that migration of the distribution of vegetation may have lead to a positive (tundra-taiga) feedback in the climate system which was responsible for initiating the perennial snowfields required for ice sheet growth (Gallimore and Kutzbach 1996; de Noblet et al. 1996)[69][49]. Each of these analyses, however, has raised as many issues as they have resolved. The inclusion of an envelope orography is a one-sided non-symmetric addition to the resolved spectral topography and is biased towards higher elevation. This also affects surface temperatures as a whole and may lead to significant cold bias on average over a large scale high elevation area. Using an interactive biome model to generate what are thought to be possible distributions for the boreal forest and tundra transition zone may be useful. However, it is not readily apparent that the biosphere would respond

in the assumed linear fashion to the reduced insolation forcing since multiple equilibria may exist in coupled biosphere model - AGCM simulations (e.g. Foley 1994a; Foley et al. 1994b)[64][65]

The deep oceans and biosphere along with continental ice sheets would presumably require hundreds to thousands of years to adjust and evolve after the last Eemian interglacial. Each component of the climate system would likely play a role in the transient evolution of the cryosphere. However, the determining factors in generating the required initial perennial snowfields could conceivably be accounted for by the use of a mixed layer ocean model to compute SSTs and by the proper representation of high latitude high elevation plateaus as previously suggested (Dong and Valdes 1995)[54]. The dynamics and topographic boundary condition are represented using spherical harmonic expansions that are truncated at degree and order in the range from 15 to 42 in most spectral AGCMs employed in paleoclimate studies. There are therefore inadequacies in properly representing the elevation in mountainous regions where high elevation regions tend to exhibit a great deal of orographic variance. Spectral models provide a least squares approach to representing the rough terrain of high elevation regions and therefore cannot capture sub-gridscale orographic variance. Along with this small scale topographic misrepresentation, spectral models are plagued with Gibbs oscillations surrounding areas of rapid increase in large scale continental topography. These regions include, for example, areas around Greenland, the Rocky Mountains, the Andes, the Himalayas and Antarctica. These spectral ripples, which are readily apparent over ocean regions adjacent to steep coastal mountain ranges, result in modelling problems involving almost every major aspect of an AGCM, including radiation balance, the hydrological cycle and basic dynamical processes. Many parameterizations have been developed to smooth these spectral ripples such as employing spectral filters to "enhance" the spectrally decomposed topography within an AGCM (see e.g. Holzer 1996; Glover 1999)[89][73]. The spectral enhancements employed in AGCMs still do not resolve many of the issues surrounding glacial inception.

Modelling glacial inception accurately over land involves two issues that are not unrelated to one another, namely the horizontal and vertical displacement of the actual surface as this is represented in the spectral AGCM. The first involves the spectral elevation anomalies at high latitudes and the effect that these have on surface temperature when the atmospheric lapse rate is taken into account (Fig. E.1a). The second, which is more subtle, involves the land/ocean mask used in the AGCM. There are large displacements of high northern latitude high elevation land features that are in close proximity to large land masses with higher elevation such as is the case around the Greenland ice sheet (Fig. E.1b). When Greenland is spectrally decomposed to wavenumber 32 in the model, the steep slopes and high plateau are not adequately represented. Coastal elevations are too high while

the central regions of the ice sheet tends to be too low (Fig. E.1b). Since the spectral decomposition gives more weight to the 3 km high Greenland Ice Sheet, the 500 meter average elevation of Baffin Island which lies directly to the west of Greenland is subjected to large spectral ripples. The first Gibbs oscillation has the effect of placing the central portion of Baffin Island almost 600 meters below its true elevation which is below sea level (Fig. E.1a). When considering an average atmospheric lapse rate of about 7 °C it becomes apparent that regions such as Baffin Island are on average 4 °C warmer than would be expected if the true elevation were included within the model. Another feature seen in Figs. E.1a and E.1b is the positive height anomaly further to the west of Baffin Island that is 350 meters in elevation. This feature represents the spatial location of Baffin Island in the model and is likely to include ocean grid cells because of the nature of the overlap between the land-sea mask and the spectral representation of the topography. Baffin Island, which has mountain peaks that reach 2000 meters in elevation, is expected to have been a nucleation centre for the North American ice sheet during Post Eemian glacial inception (Clark et al. 1993, and references therein)[36] and is therefore not likely to have its role in glacial inception properly captured in a model of this nature. The Western Cordillera by and large are resolved much more accurately than the elevated regions to the east (Fig. E.1b). This mountain range, which lacks small scale features, would still significantly influence the North American general circulation and large scale snow accumulation. Bearing in mind these model limitations and the glacial inception modelling issues described above, I will present an experimental design that will allow for the investigation of the physical processes which are determinant of the ability of the model to achieve perennial snowfall in these high latitude regions.

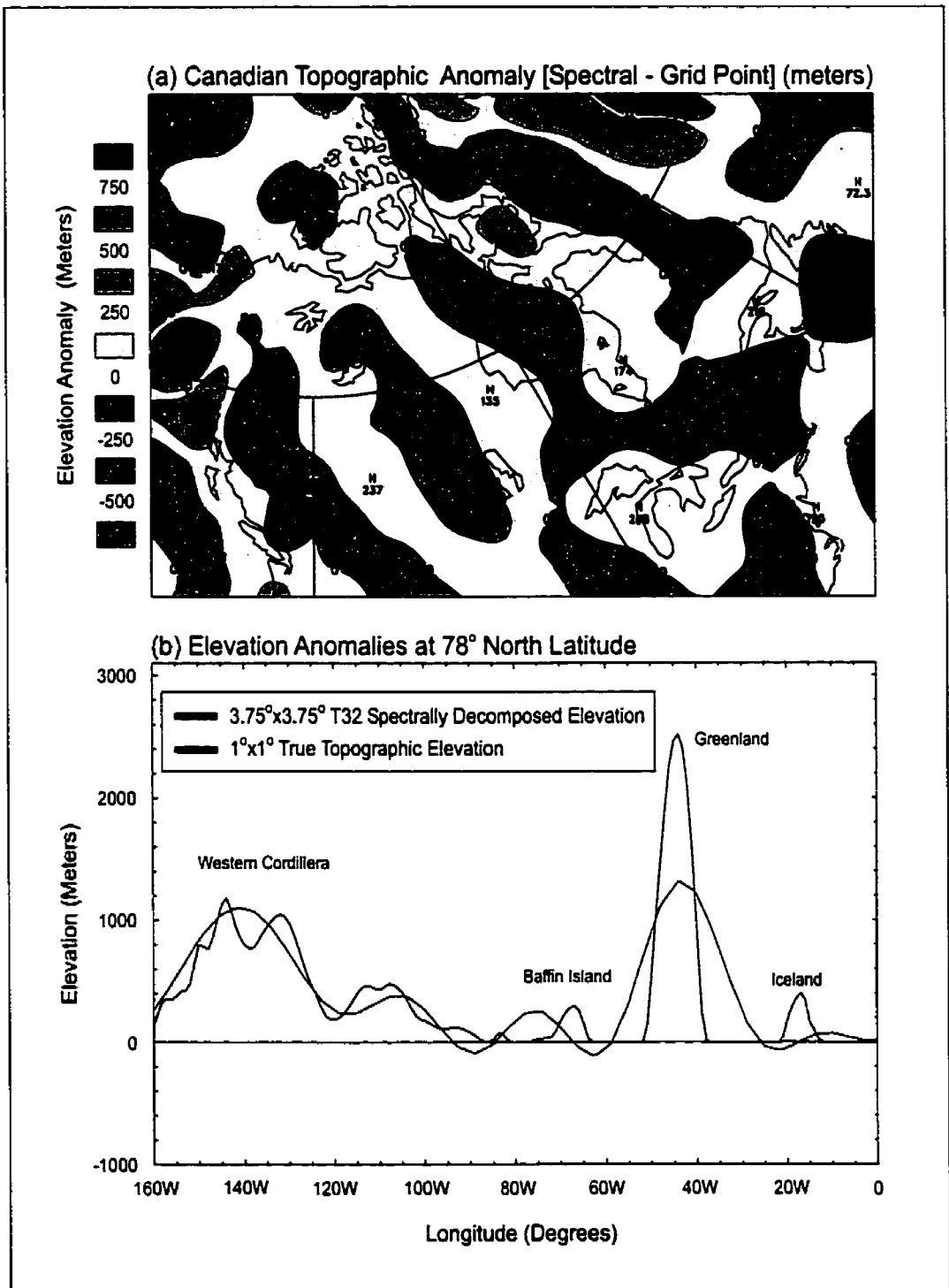


Figure E.1: Topographic anomalies over Canada (in meters) between T32 spectral and  $1^\circ$  grid point representation of the land-ocean surface in the model. (b) A cross-section at  $78^\circ$  N latitude demonstrating the elevation difference and spatial misrepresentation between spectral and grid point inferences of major continental features in the northern polar hemisphere.

---

## APPENDIX F

---

### The Modern Simulated Polar Climate

Through the simulation of specific paleoclimate epochs using modern AGCMs, the scientific community is gradually acquiring information concerning the nature of the response of AGCMs under significantly different conditions of forcing than those that have occurred over the last two hundred years. The role that the modern simulated climatology plays in determining the model response to paleoclimatic perturbations is being revealed both through model-data and model-model inter-comparisons. Model-model intercomparisons of the monsoon climates during the Holocene optimum at 6 ka BP have revealed that the model response to changes in boundary conditions has a strong dependance on the characteristics of the modern simulated climate. For example, the Paleoclimate Model Intercomparison Project (PMIP) has demonstrated that the northward shift in the Africa-Asia intertropical convergence zone (ITCZ) in response to the increased summer insolation at 6 ka BP is strongly dependant on the AGCM modern simulated northward position of the ITCZ (Joussaume et al. 1999)[108]. Other studies have also revealed that the biases in the modern climate amplify warm (cold) perturbations if the simulated modern climate is originally warm (cold) biased (see Chapter 2 and Chapter 3). Joussaume et al. (1999)[108] have also suggested that most of the AGCMs employed in these studies must lack some additional feedback mechanisms that do operate within the actual climate system and which are needed to bring these models into agreement with proxy data from the Sahara region. It is certainly apparent that paleoclimate simulation is not a linear problem where inaccuracies or errors in control climates can be neglected or removed by investigating paleoclimate anomalies that result from changes in boundary conditions. Thus, it is important to recognize precisely what the model does and does not faithfully represent in the modern climate.

Based upon the fact that a model's sensitivity to paleoclimate forcing depends on the accuracy of the control climate, it may be that the mechanisms influencing the climate of a certain epoch could be enhanced or inhibited depending upon the biases present in the control climate. This hypothesis is tested in the present study by investigating the way in which the high latitude temperature bias in the control simulation influences the process of glacial inception. It is argued that the feedback

mechanisms that are involved in glacial inception may be amplified as the inception process proceeds thereby more clearly revealing the underlying structure of the feedback mechanisms themselves.

The three control simulations described in the experimental design section have globally and annually average SSTs that lie within 3 °C of one another. A global plot of the annually averaged SST differences between the AMIP2 (Fiorino 1996)[61] and Alexander and Mobley (1976)[3] observed data sets is displayed in Fig. F.1a. The implied ocean heat transports in the AMIPS1 and AMS9 experiments described in the experimental design section are configured using the AMIP2 and Alexander and Mobley SST data sets, respectively. The resulting SST anomalies between the AMIPS1 and AMS9 modern control simulations at equilibrium are displayed in Fig. F.1b. The anomalies displaying the differences between the two computed slab ocean temperature fields are greater than the anomalies that are displayed in the difference between the two observed SSTs data sets (Figs. F.1a and F.1b). The spatial differences between the simulated and observed fields, are,

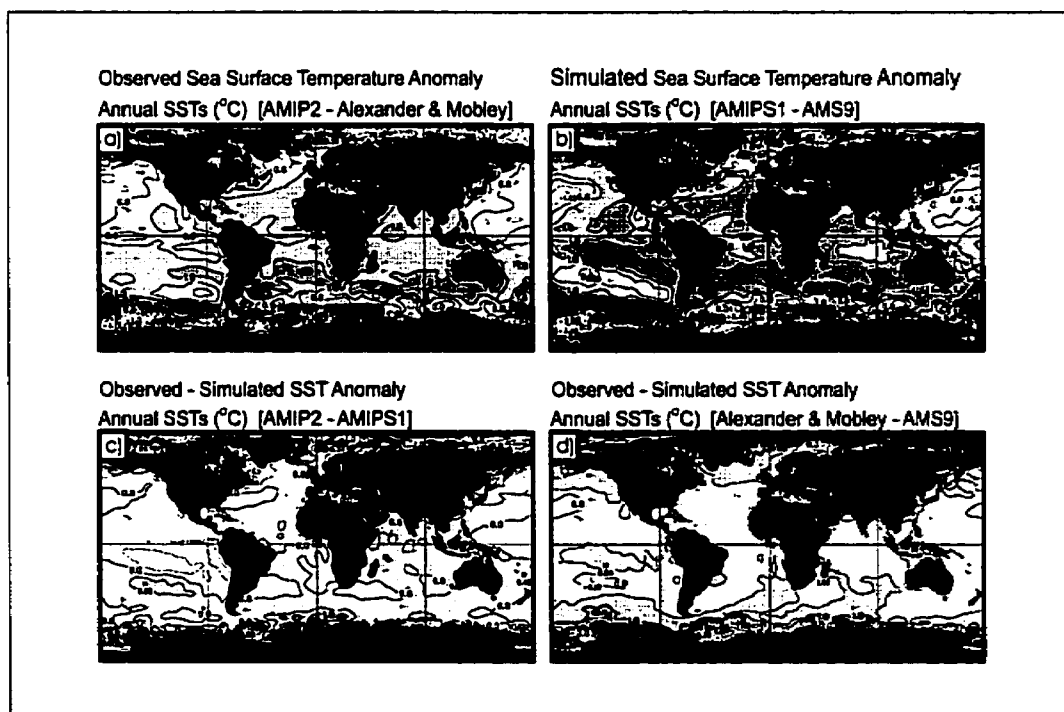


Figure F.1: A global plot of the annually averaged differences between two modern observed SST data sets (AMIP2 (Fiorino 1996) and Alexander and Mobley (1976))[61][3]. (b) A global plot of the annually averaged differences between two sets of simulated modern SSTs (the unbiased (AMIPS1) and cold biased (AMS9) experiments). (c) The differences between observed AMIP2 SSTs and the corresponding simulated SSTs (AMIPS1) and (d) the differences between observed Alexander and Mobley SSTs and the corresponding simulated SSTs (AMS9). Contours above 0 °C are shaded and the contour interval is 0.5 °C.

however, quite similar. The AMIP2 observed SSTs are generally warmer than the Alexander and Mobley observed SSTs by 0.5 to 1.0 °C in much of the northern hemisphere. The differences in the computed SSTs are slightly larger and range from approximately 1.0 to 2.0 °C in the northern hemisphere. The more accurate simulation of the observed SSTs between the two experiments can be ascertained from a direct comparison of the differences between the observed and simulated SSTs in each of the two experiments. The AMIPS1 simulated SSTs are in very good agreement with the AMIP2 observed values (Fig. F.1c), while the AMS9 simulated SSTs are colder by approximately 0.5 °C than those from the corresponding Alexander and Mobley observed SSTs (Fig. F.1d). The disagreement in the second simulation is likely a result of the changes that have occurred to this community version of the model (AMS9), which has been modified in a number of minor respects after the slab ocean model implied ocean heat transport was configured to reproduce the Alexander and Mobley SSTs. The simulated SSTs at high latitudes in both experiments display some considerable discrepancy with the observed SSTs (Figs. F.1c and F.1d) because of the difficulty in obtaining correct sea ice distributions with these limited thermodynamic models, along with the fact that there is more variability at high polar latitudes.

A scatter plot of the mean northern hemisphere winter and summer temperatures over land and sea (Fig. F.2) reveals the extent of the differences between control climates. Each of the simulations was extended ten model years after statistical equilibrium was achieved and each of the ten individual seasonal averages is plotted in Fig. F.2 to reveal the natural variability present in the simulations. This variability can be used as a qualitative indicator of the importance of the paleoclimate temperature perturbations which are revealed in the next section of the results. Figs. F.2a and F.2b illustrate the northern hemisphere July-August-September (JAS) and January-February-March (JFM) land versus ocean modern simulated surface temperatures, respectively. Also displayed are related results for two observed land surface temperature data sets (NCAR; Legates and Willmot 1990)[126] and three observed SST data sets (Shea et al. 1992; Alexander and Mobley 1976; AMIP2: Fiorino 1996)[206][3][61]. The intersection of the data sets that are displayed by the shaded regions give an estimate of where the position of the modern control climates should lie with respect to the northern hemisphere land and ocean observed means for JFM and JAS. Fig. F.2a reveals an approximately 3 °C spread in both ocean and land temperatures in the 3 control simulations with the AMIPS1 control simulation being in best agreement with the observed summer means. This is crucial to verifying the Milankovitch hypothesis of glacial inception which maintains that summer conditions should be crucial to achieving perennial snow cover. The other two simulations, AMS1 and AMS9, are respectively warm and cold biased as compared with the summer observed climate.

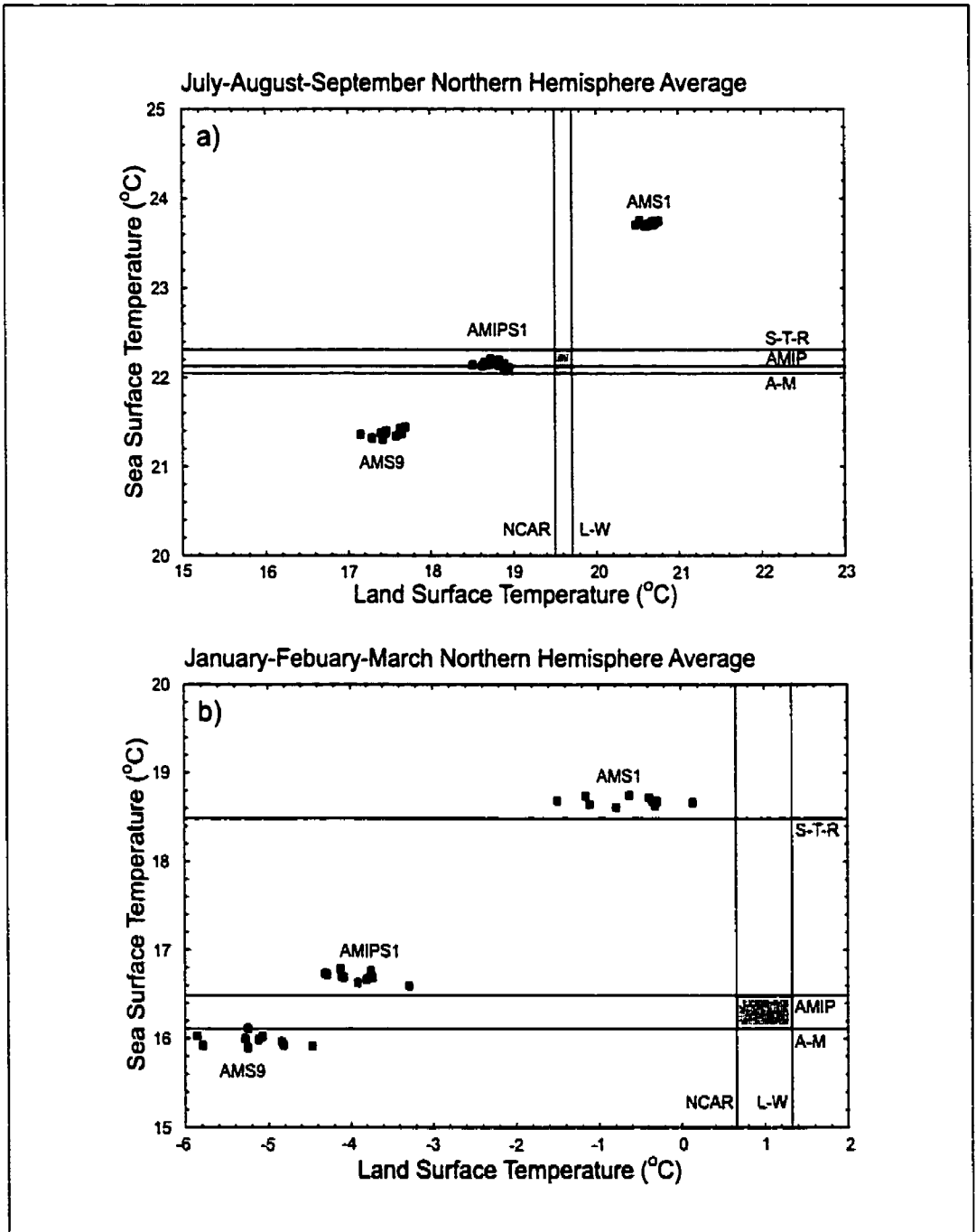


Figure F.2: A scatter plot of modern northern hemisphere land vs. ocean surface temperatures in the warm (AMS1), cold (AMS9) and unbiased (AMIPS1) experiments for (a) summer and (b) winter. Each point in the cluster of ten points in each simulation represents the average from each of the ten equilibrium years obtained for each simulation. The vertical and horizontal lines represent land and ocean temperature from observed data sets. The grey areas of intersection represent the best observed estimates.

AMS1 has northern hemisphere land temperatures which are within approximately 1 °C of the observed land temperatures and 2 °C of observed ocean temperatures. AMS9 has northern hemisphere land temperatures which are within approximately 2 °C of the observed land temperatures and 1 °C of the observed ocean temperatures. In winter (Fig. F.2b), there is a much greater spread between the models, more interannual variability and less agreement with observed values. AMIPS1 has northern hemisphere winter SSTs that are constrained to fit the best observed winter SSTs but land surface temperatures that depart more than 4 °C from the observed values. Incidentally, the Shea et al. (1992)[206] data set appears to be in considerable disagreement with the other more recent and reliable data sets and therefore is not accepted as valid for the purpose of winter analyses. The cold biased AMS9 model is close to the observed SSTs but is more than 5 °C colder than the land surface temperatures in winter. The warm biased AMS1 simulation is close to the observed land surface temperatures in winter but is approximately 3 degrees warmer than the winter observed SSTs. The winter simulated temperatures are not as crucial to achieving glacial inception as long as they are below freezing, but are nevertheless likely to impact upon the location and amount of perennial snowfall if they are warm biased as is the case with the SSTs characteristic of the AMS1 simulation.

It is expected that the modern simulated surface temperatures within the Arctic circle will significantly impact the response of the simulations to the 116 ka BP anomaly in insolation forcing. Fig. F.3 illustrates the differences between observed June-July-August (JJA) temperatures (Legates and Willmot 1990)[126] and summer temperatures in the three control simulations. The modern observed data set (Fig. F.3a) demonstrates the existence of regions within which the land temperatures are just above 0 °C and these locations are likely to nucleate first at 116 ka BP. These regions include the Queen Elizabeth Islands and Baffin Island of Canada as well as Central Siberia. Central Greenland has cold summer temperatures well below 0 °C but is of course covered at present by a continental ice sheet. Eastern Siberia, Alaska and Scandinavia all have mean temperatures of more than 8 °C in summer and are therefore likely to require a larger response to the 116 ka BP orbital configuration than is required to induce perennial snow cover in more critical regions if glacial inception is to occur in these areas. The modern simulated summer temperatures in the three experiments (Figs. F.3b, F.3c and F.3d), which range from warm to cold biased, are all characterized by differences which are much the same when compared with observed summer temperatures. The temperature anomalies over Greenland in all three experiments are similar and are likely the result of inaccuracies in both the observed data set and inaccuracies in the spectral topography in that region. The Hudson Bay and Baffin Island region also have spurious anomalies that are likely

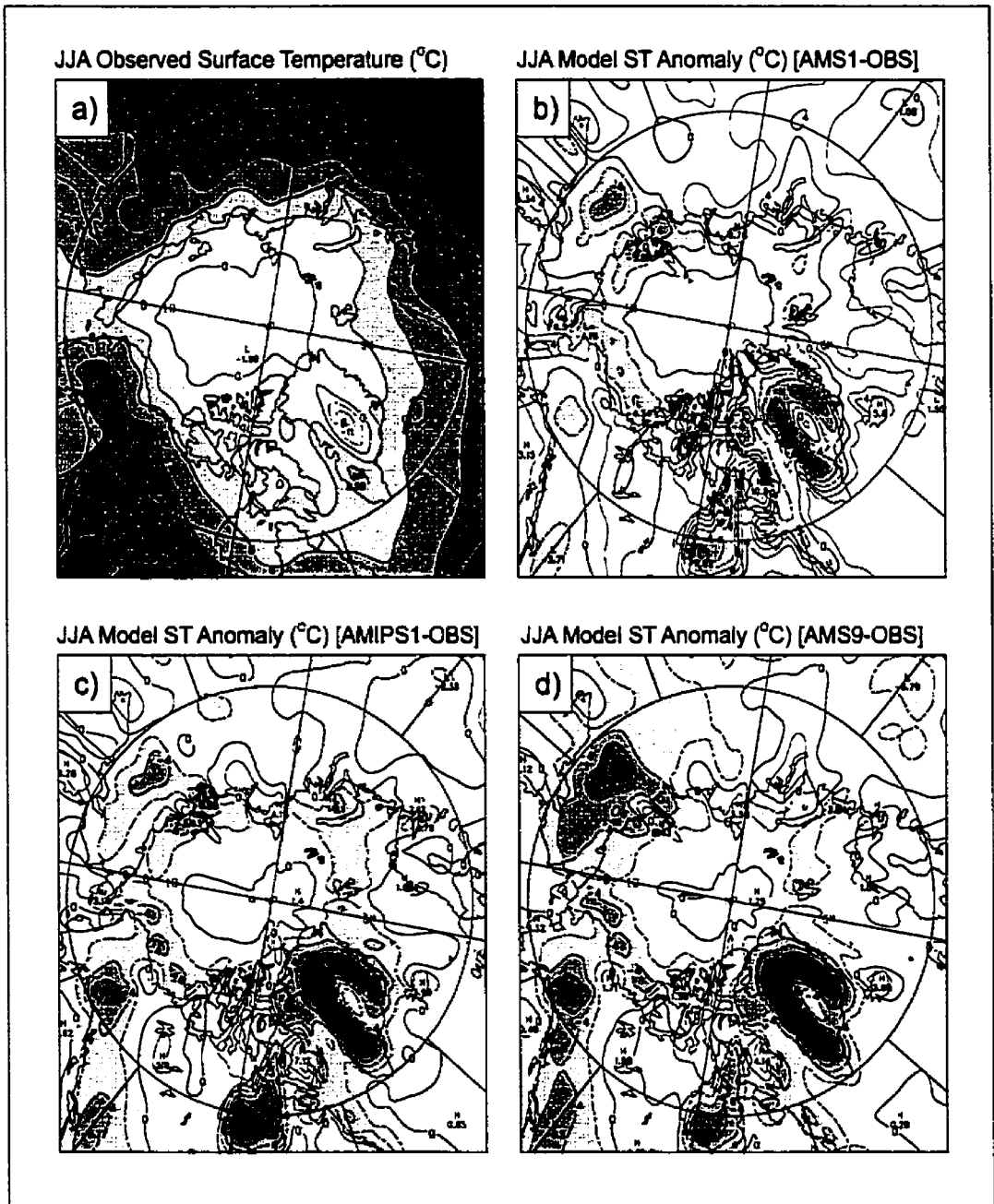


Figure F.3: (a) Northern hemisphere polar contour plots of summer surface temperature for modern observed values in °C. The contour interval is 4 °C. The modern control temperature anomalies with respect to observed are displayed for the (b) warm, (c) unbiased and (d) cold biased simulations. The anomaly contour interval is 2 °C. Positive values are shaded in the observed data, while negative anomalies in the modern simulated are shaded (i.e. simulated - observed).

the result of spectral topographic deviations and incomplete observed data in this region. In all three experiments the Queen Elizabeth Islands and Baffin Island regions of Canada are in good agreement with the observed data. Similarly the Scandinavian region is also in good agreement with observations except for the warm bias in the AMS1 experiment (Fig. F.3b). Other notable features include the cold modern temperature anomaly maxima of between  $-4$  and  $-8$  °C in Eastern Siberia, Western Canada and Alaska. The AMS1 and AMIPS1 simulations (Figs. F.3b and F.3c) have similar temperature anomalies over Central and Eastern Siberia of  $-4$  °C. The AMIPS1 and AMS9 simulations (Figs. F.3c and F.3d) have similar temperature anomalies over Alaska of approximately  $-8$  °C. These anomalies, which represent significant disagreement with observations are likely to impact strongly upon snow accumulation in these regions when boundary conditions are changed to those characteristic of conditions at 116 ka BP.

The simulated winter temperatures in the Arctic region (Fig. F.4) are also likely to have an effect on snow accumulation. The regions that exhibit the coldest depressions of more than  $-30$  to  $-40$  °C are located in the Canadian Arctic Archipelago and in Central and Eastern Siberia (Fig. F.4a). Scandinavia and Alaska are moderated by ocean SSTs and ocean circulation and thus are considerably warmer. Alaska, however, has much stronger inland temperature gradients than those over Scandinavia since the Atlantic Gulf Stream exports large amounts of heat to Western Europe. The three modern control simulations have winter anomalies that are similar in spatial extent but vary in magnitude from warm to cold biased as in summer. In the AMS1 warm biased control (Fig. F.4b), much of the land areas are above observed temperature values in the Arctic region except in Central and Eastern Siberia. In the other two simulations, AMIPS1 and AMS9 (Figs. F.4c and F.4d), there are large cold biases over much of the land area enclosed by the Arctic circle. There are also very large cold biased anomalies over Greenland of  $-20$  to  $-30$  °C that are likely a result of a combination of the topographic anomalies and missing observed data as previously mentioned. There are also large cold biases of between  $-6$  and  $-15$  °C in Central and Eastern Siberia and in the Canadian Arctic Archipelago. The cold biases over land are consistent with those changes that were described in the plots of Northern Hemisphere land and ocean temperature averages (Figs. F.1 and F.2).

Another crucial variable that will certainly influence perennial snow cover is the polar summer precipitation (Fig. F.5). Precipitation is one of the most difficult variables to model in AGCMs for a number of reasons. One significant factor lies in the coarse GCM resolutions that result in simulated precipitation patterns which suffer from a lack of mesoscale details (Goyette and Laprise 1996)[74]. Precipitation, along with other variables in the model, also suffers the same physical

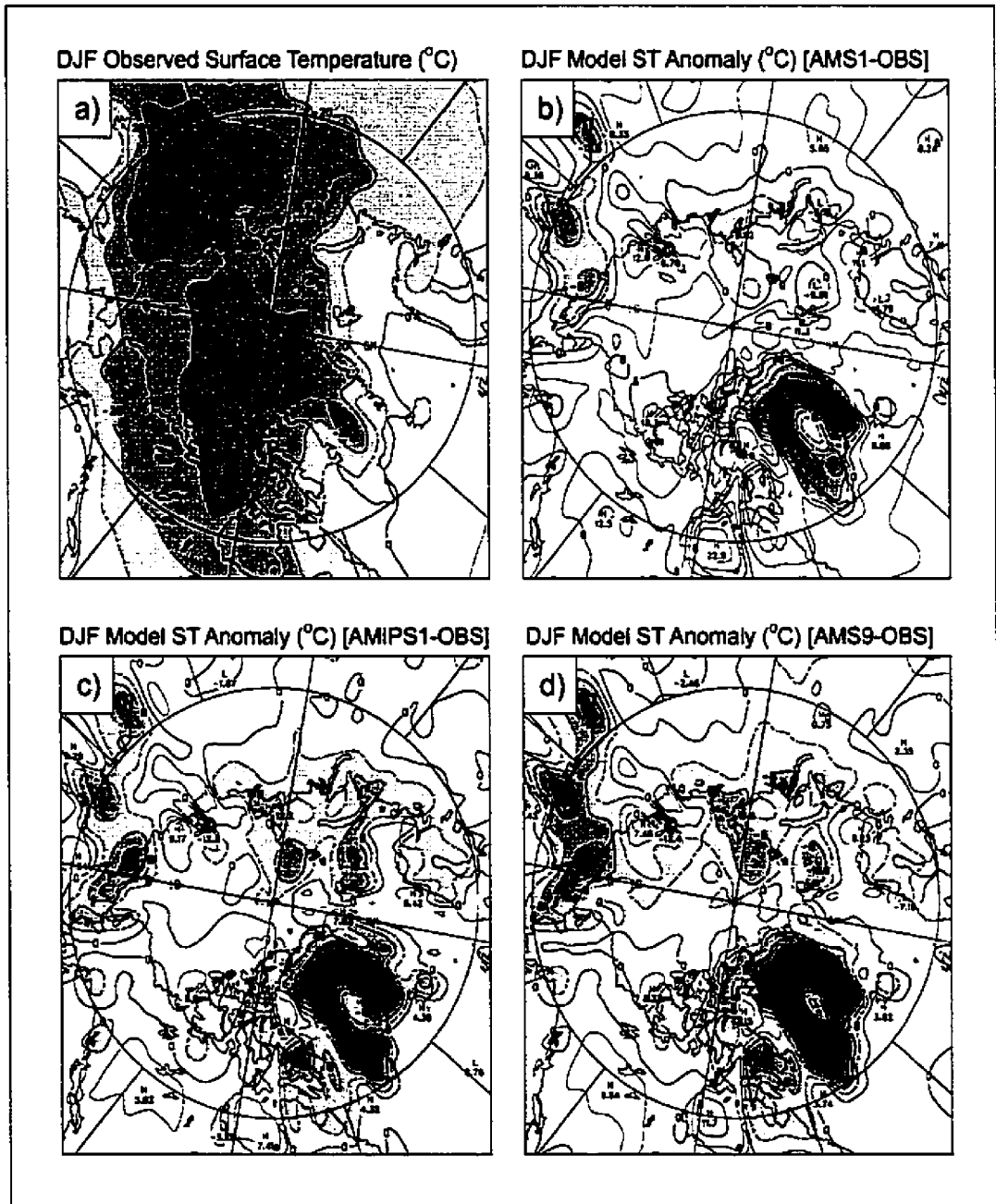


Figure F.4: Northern hemisphere polar contour plots of winter surface temperature for modern observed values in °C. The contour interval is 10 °C. The modern control temperature anomalies with respect to observed are displayed for the (b) warm, (c) unbiased and (d) cold biased simulations. The anomaly contour interval is 4 °C. Negative values and negative anomalies are shaded.

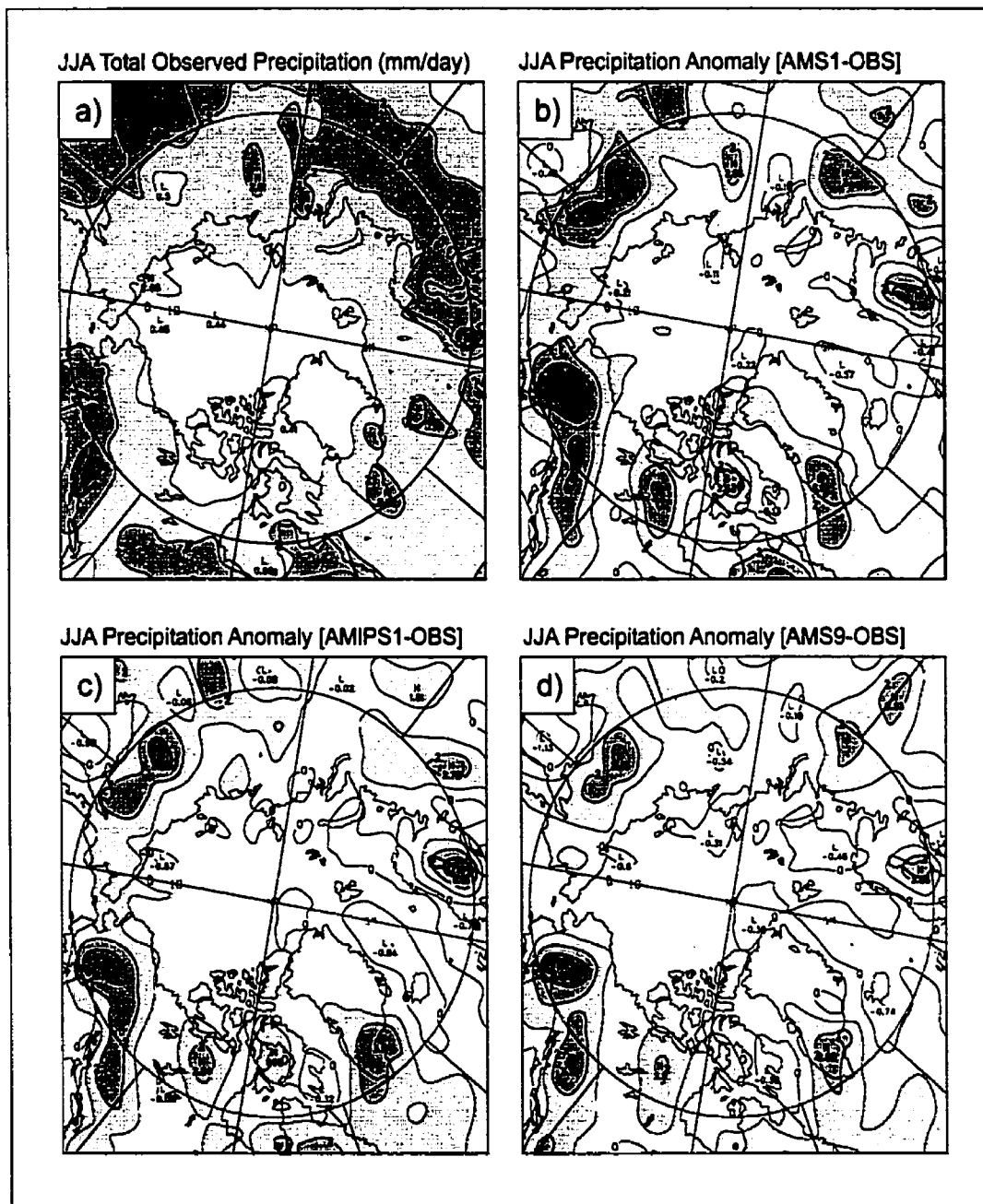


Figure F.5: Northern hemisphere polar contour plots of summer precipitation for the modern observed climate. The modern control precipitation anomaly (simulated - observed) for the (b) warm, (c) unbiased and (d) cold biased simulations. Positive values are shaded. The contour interval is 1 mm/day.

misrepresentation as temperature along rapidly varying orography due to Gibbs phenomena. In summer, the observed data (Legates and Willmot 1990)[126] reveals that much of the land north of the Arctic Circle experiences summer precipitation of 1 to 2 mm/day (Fig. F.5a). Scandinavia and Alaska receive about 2 to 3 mm/day due to oceanic effects. The colder more arid Canadian Arctic Archipelago receives amounts of between 0.4 to 1 mm/day. Upon examination of the modern simulated precipitation in the three control simulations (Figs. F.5b, F.5c, and F.5d), it becomes apparent that there are striking similarities between the anomalies in all three simulations. All three simulation possess excessive summer precipitation over the majority of the polar land areas. Likewise, a plot of the annual mean precipitation in this region of the globe (not shown) indicates that the CCCma model is in general wet biased in the Arctic Region. It has previously been demonstrated that the CCCma GCMII model also has a hydrological cycle which is more vigorous than that which is observed (see Chapter 3). The similar spatial patterns between the anomalies in the annual and summer means indicate that the maxima that exist over Scandinavia, Central Siberia, Eastern Siberia, Alaska, Northern Canada and Southern Greenland are a consequence of the effect of the spectrally truncated topography in the model (e.g. see Fig. E.1a). The Canadian Arctic Archipelago and the most northerly regions of Central Siberia are regions that are in fairly good agreement with observations. These spurious precipitation maxima are often of the same order as the observed precipitation and this must be taken into account when investigating the spatial distribution of perennial snow cover under 116 ka BP boundary conditions.

The modern simulated summer snow cover and snow depth reveal information that is also certain to influence the response of the model in regards to its ability to deliver perennial snow cover at 116 ka BP (Fig. F.6). The JJA observed snow climatology by USAF/ETAC (Foster and Davy 1988)[66] indicates that there are only a few land areas that have summer snow cover north of the Arctic Circle (Fig. F.6a). In particular, Central Siberia and the Canadian Arctic north of 60 °N latitude have only a few centimeters of summer snow cover. More advanced observed data sets from the Nimbus-7 Scanning Multichannel Microwave Radiometer (SMMR) are usually about ten percent less than those measured by earlier data such as the USAF/ETAC data set based on the fact that passive microwave sensors often can't detect shallow dry snow that is less than about 5 cm deep. This poses a problem in utilizing such satellite data in the present study as the summer snow depth is usually less than this threshold amount in many of the critical regions which are of interest with respect to glacial inception. In comparing the observed climatology with model simulated snow cover there is also likely to be some disagreement because of the modelling inaccuracies involved in the land surface parameterization (McFarlane et al. 1992; Chapter 2) and due to the sparseness

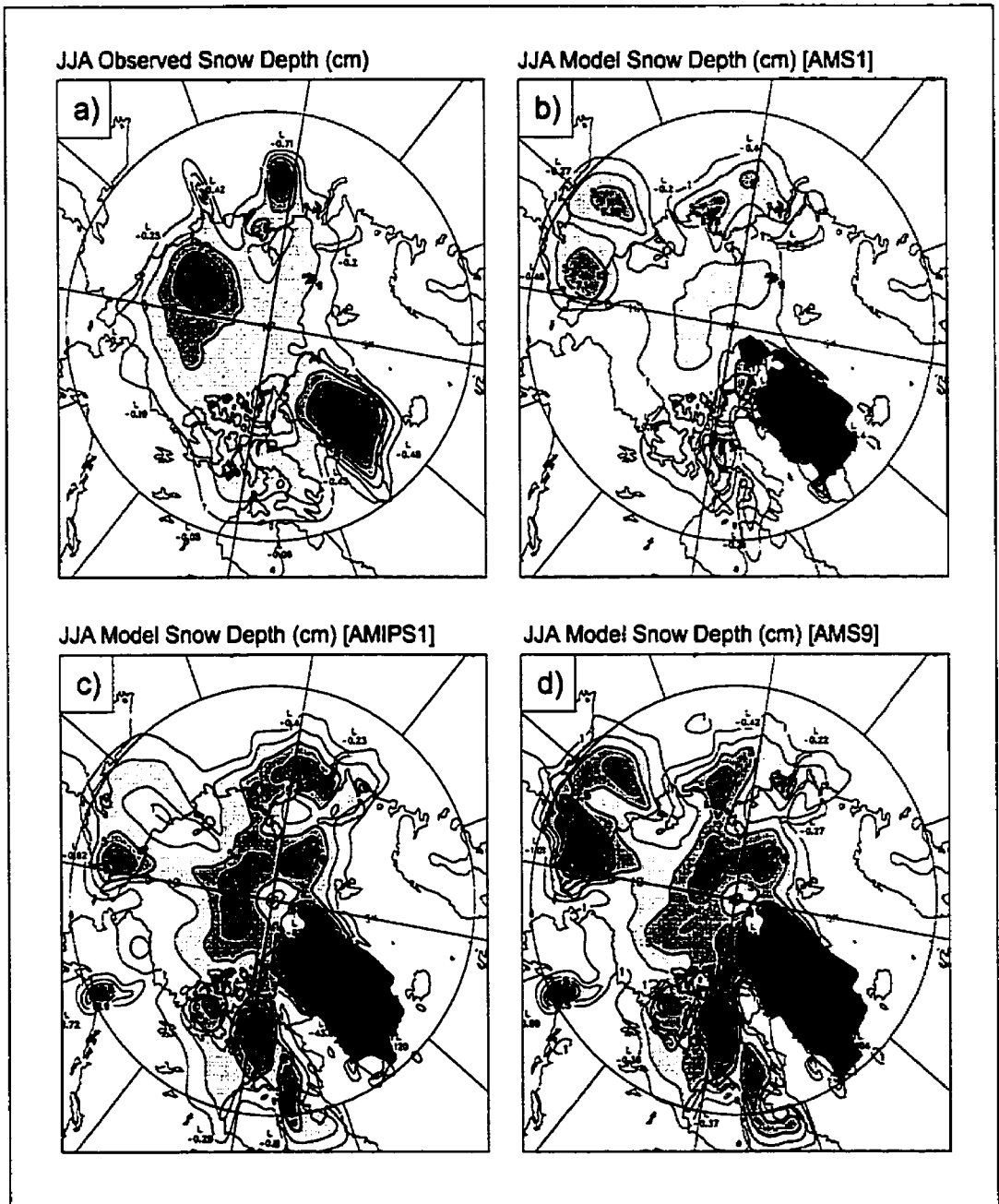


Figure F.6: Northern hemisphere polar contour plots of summer snow depth for the modern observed climate. The modern control snow depth for the (b) warm, (c) unbiased and (d) cold biased simulations. Values above 1 cm depth are shaded. The contour interval is 2 cm.

of the observed data in this polar region. The simulated snow cover in each of the three control simulations (Figs. F.6b, F.6c and F.6d) is similar since the solid precipitation is directly dependent on the spatial distribution of the modelled precipitation, which was shown to be quite similar for all these models in the previous figure.

The extent of the summer snow cover is also influenced by the mean temperatures determined by the radiative balance at the surface in each of the control simulations. This is readily apparent in the warm biased (AMS1) control simulation (Fig. F.6b), which has much less areal snow extent than the cold biased (AMS9) control (Fig. F.6d). The unbiased simulation (AMIPS1) has the best agreement with the observed data in terms of snow depth and is in better agreement with the observed areal extent especially in the Canadian Arctic Archipelago region (Fig. F.6c). All three simulations have two large maxima of summer snowfall in Eastern Siberia which are inconsistent with observed summer snowfall. This anomaly is precisely correlated with the precipitation maxima over this region and it is not clear why this distribution results but it may be associated with the spectral inaccuracies described previously. The simulated Central Siberian summer snowfall also covers a much larger areal extent than the observed. The unbiased and cold biased experiments (AMIPS1 and AMS9) in Figs. F.6c and F.6d have much more similar snow distributions than those of the warm biased experiment (AMS1; Fig. F.6b). In particular, in each of these two modern simulations, the Canadian Arctic Archipelago has snow depth on the order of 5 to 10 cm over Northern Labrador, Baffin Island and Queen Elizabeth Islands. The southern tip of Greenland is in negative mass balance in the warmer AMS1 experiment but not in the colder AMS9 experiment. Although there is significant snow present in summer in the control simulations, there is no land area except for Greenland in the Arctic which preserves snow cover through the month of August (not shown). In the following subsection of this results section the influence of 116 ka BP orbital parameters on the accumulation of permanent August snow cover for each of the three experiments will be described.

For a more complete description of the model behaviour on a global scale and its ability in reproducing the modern climate the reader is advised to review McFarlane et al. (1992)[146], Vettoretti et al. (1998)[229] and also Chapter 2 and Chapter 3.

## BIBLIOGRAPHY

### BIBLIOGRAPHY

- [1] Abramopoulos, F., C. Rosenzweig, and B. Choudhury, 1988: Improved ground hydrology calculations for global climate models (GCMs): Soil water movement and evapotranspiration. *J. Climate*, **1**, 921-941.
- [2] Agassiz, L., 1838: Upon glaciers, moraines, and erratic blocks. *New Philos. J. Edinburgh*, **24**, 864-883.
- [3] Alexander, R. C., and R. L. Mobley, 1976: Monthly average sea surface temperatures and ice pack limits on a 1° global grid. *Mon. Wea. Rev.*, **104**, 143-148.
- [4] Alley, R. B., D. A. Meese, A. J. Shuman, A. J. Gow, K. C. Taylor, P. M. Grootes, J. W. C. White, M. Ram, E. D. Waddington, P. A. Mayewski, and G. A. Zielinski, 1993: Abrupt accumulation increase at the Younger Dryas termination in the GISP2 ice core, *Nature*, **362**, 527-529.
- [5] Alley, R.B., A. J. Gow, S.J. Johnsen, J. Kipfstuhl, D.A. Meese, and Th. Thorsteinsson, 1995: Comparison of deep ice cores. *Nature*, **373**, 393-394
- [6] Andrews, J. T., A. Aksu, M. Kelly, R. G. H. Miller, W. N. Mode, and P. Mudie, 1985: Land/ocean correlations during the last interglacial/glacial transition, Baffin Bay, northwest North Atlantic: A review. *Quat. Sci. Rev.*, **4**, 333-355.
- [7] Andrews, J. T., G. H. Miller, J.-S. Vincent, and W. W. Shiels, 1986: Quaternary correlations in Arctic Canada. *Quat. Sci. Rev.*, **5**, 243-250.
- [8] Appenzeller, C., T. F. Stocker, and M. Anklin, 1998: North Atlantic Oscillation dynamics recorded in Greenland ice cores. *Science*, **282**, 446-449.
- [9] Asselin, R., 1972: Frequency filter for time integrators. *Mon. Wea. Rev.*, **100**, 487-490.
- [10] Bard, E., F. Rostek, and C. Sonzogni, C. 1997: Interhemispheric synchrony of the last deglaciation inferred from alkenone palaeothermometry. *Nature*, **385**, 707-710.
- [11] Barnola, J. M., D. Raynaud, Y. S. Korotkevich, and C. Lorius, 1987: Vostok ice core provides 160,000-year record of atmospheric CO<sub>2</sub>. *Nature*, **329**, 408-418.
- [12] Baumgartner, A., and E. Reichel, 1975: *The world water balance: Mean annual global, continental and maritime precipitation and run-off*. Elsevier Scientific Publishers, Amsterdam.
- [13] Beck, J. W., J. Recy, F. Taylor, R. L. Edwards, and G. Cabioch, 1997: Abrupt changes in Early Holocene sea surface temperature derived from coral records. *Nature*, **385**, 705-707.
- [14] Berger, A., 1978: Long-term variations of daily insolation and Quaternary climatic changes. *J. Atmos. Sci.*, **35**, 2362-2367
- [15] Berger, A., 1988: Milankovitch theory and climate. *Rev. Geophys.*, **4**, 623-658.
- [16] Berner, R.A., 1994: GEOCARB II: A revised model of atmospheric CO<sub>2</sub> over Phanerozoic time". *Am. J. Sci.*, **294**, 56-91.
- [17] Betts, A.K., and Harshvardhan, 1987: Thermodynamic constraint on the cloud liquid water feedback in climate models. *J. Geophys. Res.*, **92**, 8483-8485.
- [18] Bhumralkar, C.M., 1975: Numerical experiments on the computation of ground surface temperature in an atmospheric general circulation model. *J. App. Meteor.*, **14**, 1246-1258.
- [19] Blackman, R. B., and J. W. Tukey, 1959: *The measurement of power spectra*. Wiley, 191 pp.

- [20] Boer, G. J., N. A. McFarlane, R. Laprise, J.D. Henderson, and J.-P. Blanchet, 1984: The Canadian Climate Centre spectral atmospheric general circulation model. *Atmosphere-Ocean*, **22**, 397-429.
- [21] Boer, G. J. 1993: Climate change and the regulation of the surface moisture and energy budgets. *Climate Dyn.*, **8**, 225-239.
- [22] Boer, G. J., and B. Denis, 1997: Numerical convergence of the dynamics of a GCM. *Climate Dyn.*, **13**, 359-374.
- [23] Bonfils, C., D. Lewden, and K. E. Taylor, 1999: Summary Documentation of the PMIP Models. Web address: <http://www-pcmdi.llnl.gov/pmip/>
- [24] Bonan, G. B., 1996: A land surface model (LSM version 1.0) for ecological, hydrological, and atmospheric studies: technical description and user's guide, NCAR Tech. Note NCAR/TN-417+STR, Boulder, CO.
- [25] Boville, B. A., 1991: Sensitivity of simulated climate to model resolution. *J. Climate*, **4**, 469-485.
- [26] Braithwaite, R. J., 1995: Positive-degree-day factors for ablation on the Greenland ice-sheet studied by energy-balance modeling. *J. Glaciol.*, **41**, 153-160.
- [27] Braconnot, P., S. Joussaume, O. Marti, and N. de Noblet, 1999: Synergistic feedbacks from ocean and vegetation on the African monsoon response to mid-Holocene insolation. *Geophys. Res. Lett.*, **26**, 2481-2484.
- [28] Broccoli, A. J., and S. Manabe, 1987: The influence of continental ice, atmospheric CO<sub>2</sub> and land albedo on the climate of the last glacial maximum. *Climate Dyn.*, **1**, 87-99.
- [29] Broecker, W. S., and J. Van Donk, 1970: Insolation changes, ice volumes, and the <sup>18</sup>O record in deep-sea cores. *Rev. Geophys.*, **8**, 169-198.
- [30] Broecker, W. S., 1986: Oxygen isotope constraints on surface ocean temperatures. *Quat. Res.*, **26**, 121-134.
- [31] Bush B., and S. Philander, 1998: The role of ocean-atmosphere interactions in tropical cooling during the Last Glacial Maximum. *Science*, **279**, 1341-1344.
- [32] Cess, R. D., G. L. Potter, J. P. Blanchet, et al., 1990: Intercomparison and interpretation of climate feedback processes in 19 atmospheric general circulation models. *J. Geophys. Res.*, **95**, 16601-16615.
- [33] Chappell, J., and N. J. Shackleton, 1986: Oxygen isotopes and sea level. *Nature*, **324**, 137-140
- [34] Cheddadi, R., G. Yu, J. Guiot, S. P. Harrison, and I. C. Prentice, 1997: The climate 6000 years ago in Europe. *Climate Dyn.*, **13**, 1-9.
- [35] Chen, T. H., and Coauthors, 1997: Cabauw experimental results from the Project for Intercomparison of Land-surface Parameterization Schemes (PILPS). *J. Climate.*, **10**, 1194-1215.
- [36] Clark, P.U., J. J. Clague, B. B. Curry, A. Dreimanis, S. R. Hicock, G. H. Miller, G. W. Berger, N. Eyles, M. Lamothe, B. B. Miller, R. J. Mott, R. N. Oldale, R. R. Stea, J. P. Szabo, L. H. Thorleifson, and J. S. Vincent, 1993: Initiation and development of the Laurentide and Cordilleran ice sheets following the last interglaciation. *Quat. Sci. Rev.*, **12**, 79-114.
- [37] Clark, P. U., J. M. Licciardi, D. R. MacAyeal, and J. W. Jenson, 1996: Numerical reconstruction of a soft-bedded Laurentide ice-sheet during the Last Glacial Maximum. *Geology*, **24**, 679-682.
- [38] CLIMAP Project Members, 1981: Seasonal reconstructions of the earth's surface at the last glacial maximum, Geological Society American Map Chart Service. MC-36.

- [39] Clough, S. A., F. X. Kneizys, R. Davies, R. Gemache, and R. Tipping, 1980: Theoretical line shape for H<sub>2</sub>O vapor: Application to continuum. *In Atmospheric Water Vapor*, T.D. Wilkerson and L.H. Ruhnke (eds.), Academic Press, New York, 695 pp.
- [40] Corby, C. A., A. Gilchrist, P. R. Rowntree, 1976: The U.K. Meteorological Office 5-level general circulation model. *In Methods in Computational Physics*. Edited by J. Chang. Academic Press, New York.
- [41] Cressman, G. P., 1960: Improved terrain effects in barotropic forecasts. *Mon. Wea. Rev.*, **88**, 327-342.
- [42] Crowley, T. J., 1983: The geologic record of climate change. *Rev. Geophys.*, **21**, 828-877.
- [43] Crowley, T.C., 2000: CLIMAP SSTs revisited. *Climate Dyn.*, **16**, 241-255.
- [44] Cuffey, K.M., and S. J. Marshall, 2000: Substantial contribution to sea-level rise during the last interglacial from the Greenland ice sheet. *Nature*, **404**, 591-594.
- [45] Deardorff, J.W., 1977: A parameterization of ground-surface moisture content for use in atmospheric prediction models. *J. App. Meteorol.*, **16**, 1182-1185.
- [46] Deardorff, J.W., 1978: Efficient prediction of ground surface temperature and moisture, with inclusion of a layer of vegetation. *J. Geophys. Res.*, **83**, 1889-1903.
- [47] Deblonde, G., and W. R. Peltier, 1991: Simulations of continental ice sheet growth over the last glacial-interglacial cycle: Experiments with a one-level seasonal energy balance model including realistic geography. *J. Geophys. Res.*, **96**, 9189-9215.
- [48] Deblonde, G., and W. R. Peltier, 1993: Late Pleistocene ice-age scenarios based on observational evidence. *J. Climate*, **6**, 709-727.
- [49] de Noblet, N. I., I. C. Prentice, S. Joussaume, D. Texier, A. Botta., and A. Haxeltine, 1996: Possible role of atmosphere-biosphere interaction in triggering the last glaciation. *Geophys. Res. Lett.*, **23**, 3191-3194.
- [50] de Vernal, A., A. Rochon, C. Hillaire-Marcel, J.-L. Turon, and J. Guiot, 1993: Quantitative reconstruction of sea-surface conditions, seasonal extent of sea-ice cover and meltwater discharges in high latitude marine environments. *In Ice in the Climate System*. Edited by W.R. Peltier, Proceedings of NATO Advanced Research Workshop., Pergamon, pp. 611-621
- [51] de Vernal, A., C. Hillaire-Marcel, J.-L. Turon, and J. Mathiesson, 2000: Sea surface conditions in middle to high latitudes of the North Atlantic during the Last Glacial Maximum (LGM): the cold paradigm revisited. *Can. J. Earth Sci.*, **37**, 725-750.
- [52] Dickenson, R. E., and A. Henderson-Sellers, 1988: Modelling tropical deforestation: A study of GCM land-surface parameterizations. *Quart. J. Royal Meteorol. Soc.*, **114**, 439-462.
- [53] Ducoudre, N., K. Laval, and A. Perrier, 1993: SECHIBA, a new set of parameterizations of the hydrologic exchanges at the land/atmosphere interface within the LMD atmospheric general circulation model. *J. Climate*, **6**, 248-273.
- [54] Dong, B., and P. J. Valdes, 1995: Sensitivity studies of Northern Hemisphere glaciation using an atmospheric general circulation model. *J. Climate*, **8**, 2471-2496.
- [55] Dyke, A. S., and V. K. Prest, 1987: Paleogeography of Northern North America 11 000 - 8 400 Years Ago. Scale 1:12,500,000, Sheet 2 of 3. Geological Survey of Canada, Ottawa, Ontario, Map 1703A.
- [56] Emiliani, C., 1955: Pliocene temperatures. *J. Geol.*, **63**, 538.
- [57] Fabre A., Ramstein, G., Ritz, C., Pinot, S., and Fournier, N., 1998: Coupling an AGCM with an ISM to investigate the ice-sheet mass balance at the Last Glacial Maximum. *Geophys. Res. Lett.*, **25**, 531-534.

- [58] Fairbanks, R. G., and P. H. Wiebe, 1980: Foraminifera and chlorophyll maximum: Vertical distribution, seasonal succession and paleoceanographic significance. *Science*, **209**, 1524-1526.
- [59] Falkowski, P., R. J. Scholes, E. Boyle, J. Canadell, D. Canfield, J. Elser, N. Gruber, K. Hibbard, P. Höglberg, S. Linder, F. T. Mackenzie, B. Moore III, T. Pedersen, Y. Rosenthal, S. Seitzinger, V. Smetacek, and W. Steffen, 2000: The global carbon cycle: A test of our knowledge of Earth as a system. *Science*, **290**, 291-296.
- [60] Felzer, B., J. R. J. Oglesby, T. Webb, and D. E. Hyman, 1996: Sensitivity of a general circulation model to changes in northern hemisphere ice-sheets. *J. Geophys. Res.*, **101**, 19077-19092.
- [61] Fiorino, M., 1996: SST and Sea Ice Concentration Observations for the AMIP II Boundary Conditions: <http://www-pcmdi.llnl.gov/amip/AMIP2EXPDSN/BCS.OBS/amip2.bcs.htm>
- [62] Fischer, H., M. Wahlen, J. Smith, D. Mastroianni, and B. Deck, 1999: Ice core records of Atmospheric CO<sub>2</sub> around the last three glacial terminations. *Science*, **283**, 1712-1714.
- [63] Flato, G. M., G. J. Boer, W. G. Lee, N. A. McFarlane, D. Ramsden, M. C. Reader, and A. J. Weaver, 2000: The Canadian Centre for Climate Modelling and Analysis global coupled model and its climate. *Climate Dyn.*, **16**, 451-467.
- [64] Foley, J., 1994a: The sensitivity of the terrestrial biosphere to climate change: A simulation of the middle Holocene. *Global Biogeochem. Cycles*, **8**, 505-525.
- [65] Foley, J. E. Kutzbach, M. T. Coe, and S. Levis, 1994b: Feedbacks between climate and boreal forests during the Holocene epoch. *Nature*, **371**, 52-54.
- [66] Foster, D. J. and R. D. Davy, 1988: Global snow depth climatology, USAF Environmental Technical Application Center, USAFETAC/TN-88/006, Scott Air Force Base, Illinois, pp. 48.
- [67] Fouquart, Y., and B. Bonnel, 1980: Computation of solar heating of the Earth's atmosphere: A new parameterization. *Beitr. Phys. Atmos.*, **53**, 35-62.
- [68] Gajewski, K., R. Vance, M. Sawada, I. Fung, L. D. Gignac, J. J. Halsey, P. Maisongrande, P. Mandell, P. J. Mudie, P. J. H. Richard, A. G. Sherin, J. Soroko, and D. Vitt, D. H. 2000. The climate of North America and adjacent ocean waters ca. 6 ka., *Can. J. Earth Sci.*, **37**, 661-681.
- [69] Gallimore, R. G., and J. E. Kutzbach, 1996: Role of orbitally induced changes in tundra area in the onset of glaciation. *Nature*, **381**, 503-505.
- [70] Ganapolski, A., C. Kubatzki, M. Claussen, V. Brovkin, and V. Petoukhov, 1998: The influence of vegetation-atmosphere-ocean interaction on climate during the Mid-Holocene. *Science*, **280**, 1916-1919.
- [71] Gates, W. L., J. Boyle, C. Covey, C. Dease, C. Doutriaux, R. Drach, M. Fiorino, P. Gleckler, J. Hnilo, S. Marlais, T. Phillips, G. Potter, B. Santer, K. Sperber, K. Taylor and D. Williams, 1998: An overview of the results of the Atmospheric Model Intercomparison Project (AMIP), PCMDI Report 45, Program for Climate Model Diagnosis and Intercomparison, Lawrence Livermore National Laboratory, 47 pp.
- [72] Gleckler, P. J., D. A. Randall, G. Boer, R. Colman, M. Dix, V. Galin, M. Helfand, J. Kiehl, A. Kitoh, W. Lau, X.-Z. Liang, V. Lykossov, B. McAvaney, K. Miyakoda, S. Planton, and W. Stern, 1995: Interpretation of ocean energy transports implied by atmospheric general circulation models. *Geophys. Res. Lett.*, **22**, 791-794.
- [73] Glover, R. W., 1999: Influence of spatial resolution and treatment of orography on GCM estimates of the surface mass balance of the Greenland ice-sheet. *J. Climate*, **12**, 551-563.
- [74] Goyette, S., and J.-P. R. Laprise, 1996: Numerical investigation with a physically based regional interpolator for off-line downscaling of GCMs: FIZR. *J. Climate*, **9**, 3464-3495.
- [75] GRIP Project Members, 1993: Climate instability during the last interglacial period recorded in the GRIP ice core. *Nature*, **364**, 203-207.

- [76] Guilderson, T.P., R. G. Fairbanks, and J. L. Rubenstone, 1994: Tropical temperature variations since 20,000 years ago: Modulating interhemispheric climate change. *Science*, **263**, 663-665.
- [77] Hall, N. M. J., P. J. Valdes, and B. Dong, 1996: The maintenance of the last great ice-sheets: A UGAMP GCM study. *J. Climate*, **9**, 1004-1019.
- [78] Hall, N. M. J., and P. J. Valdes, 1997: A GCM simulation of the climate 6000 years ago. *J. Climate*, **10**, 3-17.
- [79] Hansen, J., A. Lacis, D. Rind, and G. Russell, 1984: Climate sensitivity: Analysis of feedback mechanisms. Climate Processes and climate sensitivity, *Geophys. Monogr.*, No. **29**, AGU, 130-163.
- [80] Harrison S. P., 2000: Palaeoenvironmental data sets and model evaluation in PMIP. In Paleoclimate Modelling Intercomparison Project (PMIP): Proceedings of the third PMIP workshop. WCRP-111 WMO/TD-No. 1007 ICPO Publication No. 34. 271 pp.
- [81] Hasselmann, K., 1976: Stochastic climate models. Part I. Theory. *Tellus*, **28**, 473-485.
- [82] Hays, J. D., J. Imbrie, and N. J. Shackleton, 1976: Variations in the Earth's orbit: Pacemaker of the ice ages. *Science*, **194**, 1121-1132.
- [83] Held, I. M., and Phillips, P. J., 1993. Sensitivity of the eddy momentum flux to meridional resolution in atmospheric GCMs. *J. Climate*, **6**: 499-507.
- [84] Hendricks, M. B., D. J. DePaolo, and R. C. Cohen, 2000: Space and time variation of  $\delta^{18}\text{O}$  and  $\delta^{18}\text{O}$  in precipitation: Can paleotemperature be estimated from ice cores? *Global Biogeochem. Cycles*, **14**, 851-862.
- [85] Hewitt, C. D., and J. F. B. Mitchell, 1997: Radiative forcing and response of a GCM to ice age boundary conditions: cloud feedback and climate sensitivity. *Climate Dyn.*, **13**, 821-834.
- [86] Hewitt, C.D. and J.F.B. Mitchell, 1998: A fully coupled GCM simulation of the climate of the mid-Holocene. *Geophys. Res. Lett.*, **25**, 361-364.
- [87] Heymsfield, A. J., 1977: Precipitation development in stratiform ice clouds: A microphysical and dynamical study. *J. Atmos. Sci.*, **34**, 367-381.
- [88] Hodell, D.A., 1993: Late Pleistocene paleoceanography of the south Atlantic sector of the Southern ocean: Ocean Drilling Program hole 704A. *Paleoceanography*, **8**, 47-67.
- [89] Holzer, M., 1996: Optimal spectral topography and its effect on model climate. *J. Climate*, **9**, 2443-2463.
- [90] Hostetler, S. W., and Mix, A. C., 1999: Reassessment of ice-age cooling of the tropical ocean and atmosphere. *Nature*, **399**, 673-676.
- [91] Houghton, J. T., 1997: *Global Warming - The complete briefing*. 2nd Edition. Cambridge University Press. 251 pp.
- [92] Huybrechts, P., 1990a: A 3-D model for the Antarctic ice-sheet: A sensitivity study on the glacial-interglacial contrast. *Climate Dyn.*, **5**, 79-92.
- [93] Huybrechts, P., 1990b: The Antarctic ice-sheet during the last glacial-interglacial cycle: A three-dimensional experiment. *Ann. Glaciol.*, **14**, 115-119.
- [94] Huybrechts, P., and S. T'Siobbel, 1995: Thermomechanical modelling of northern hemisphere ice-sheets with a two-level mass balance parameterization. *Ann. Glaciol.*, **21**, 111-117.
- [95] Hyde, W. T., and W. R. Peltier, 1985: Sensitivity experiments with a model of the ice-age cycle: The response to harmonic forcing. *J. Atmos. Sci.*, **44**, 1351-1374.
- [96] Hyde, W. T., T. J. Crowley, S. K. Baum, and W. R. Peltier, 2000: Neoproterozoic 'snowball Earth' simulations with a coupled climate/ice-sheet model. *Nature*, **405**, 425-429.

- [97] Imbrie, J. and N. Kipp, 1971: A new micropaleontological method for quantitative paleoclimatology: Application to a late Pleistocene Caribbean core. *In* The late Cenozoic glacial ages. K. K. Turekian, Yale Univ. Press, New Haven, pp. 71-181.
- [98] Imbrie, J. and K. P. Imbrie, 1979: *Ice ages: Solving the mystery*. Enslow Publishers, Short Hills, N. J., 224 pp.
- [99] Imbrie, J., J. D. Hays, D. G. Martinson, A. McIntyre, A. C. Mix, J. J. Morely, N. G. Pisias, W. L. Prell, and N. J. Shackleton, 1984: The orbital theory of Pleistocene climate: Support from a revised chronology of the marine  $\delta^{18}\text{O}$  record. *Milankovitch and Climate*. Edited by A. Berger et al., D. Reidel Publishing Company, Boston, 269-305.
- [100] Imbrie, J., and 17 others, 1993: On the structure and origin of major glaciation cycle, 2, The 100,000-year cycle, *Paleoceanography*, **8**, 699-735.
- [101] Intergovernmental Panel on Climate Change, Third Assessment Report, 2001: *Summary for Policymakers*. <http://www.ipcc.ch>. 17 pp.
- [102] Janssen, D., 1977: A three-dimensional polar ice-sheet model. *J. Glaciol.*, **18**, 373-389.
- [103] Jolly, D., C. I. Prentice, R. Bonnefille, A. Ballouche, M. Bengo, P. Brenac, G. Buchet, D. Burney, J-P. Cazet, R. Cheddadi, T. Ector, H. Elenga, S. Elmoutaki, J. Guiot, F. Laarif, H. Lamb, A-M. Lezine, J. Maley, M. Mbenza, O. Peryon, M. Reille, L. Reynaud-Farrera, G. Riollet, J. C. Ritchie, E. Roche, L. Scott, I. Ssemmanda, H. Straka, M. Umer, E. Van Campo, S. Vilimumbalo, A. Vincens, and M. Waller, 1998: Biome reconstruction from pollen and plant macrofossil data for Africa and the Arabian peninsula at 0 and 6000 years. *J. Biogeog.*, **25**, 1007-1027.
- [104] Jones, M. T., A. R. Tabor, and P. Weatherall, 1994: GEBCO Digital Atlas: CD-ROM and Supporting Volume. British Oceanographic Data Centre, Birkenhead UK.
- [105] Joseph, J. H., W. J. Wiscombe, and J. A. Weinman, 1976: The delta-Eddington approximation for radiative flux transfer. *J. Atmos. Sci.*, **33**, 2452-2459.
- [106] Joussaume, S., 1993: Paleoclimate Tracers: An investigation using and atmospheric general circulation model under ice age conditions: Desert Dust. *J. Geophys. Res.*, **98**, 2767-2805.
- [107] Joussaume S., and K. E. Taylor, 1995: Status of the Paleoclimate Modelling intercomparison project (PMIP). Proceedings of the first international AMIP scientific conference, WCRP Report 92, pp. 425-430.
- [108] Joussaume, S., and 35 co-authors including G. Vettoretti and W. R. Peltier, 1999: Monsoon changes for 6000 years ago: results of 18 simulations from the Paleoclimate Modelling Intercomparison Project (PMIP), *Geophys. Res. Lett.*, **26**, 859-862.
- [109] Jouzel, J., C. Lorius, J. R. Petit, C. Genthon, N. I. Barkov, V. M. Kotlyakov, and V. M. Petrov, 1987: Vostok ice core: A continuous isotope temperature record over the last climatic cycle (160,000 years). *Nature*, **329**, 403-408.
- [110] Kageyama, M., P. J. Valdes, G. Ramstein, C. Hewitt, and U. Wyputta, 1999: Northern Hemisphere storm tracks in present day and last glacial maximum climate simulations: A comparison of the European PMIP models. *J. Climate*, **12**, 742-760.
- [111] Karabanov, E. B., A. A. Prokopenko, D. F. Williams, S. M. Colman, 1998: Evidence from Lake Baikal for Siberian Glaciation during Oxygen-Isotope Substage 5d. *Quat. Res.*, **50**, 46-55.
- [112] Katayama, A., 1978: Parameterization of the planetary boundary layer in atmospheric general circulation models. Kisyo Kenkyu Note No. 134, Meteorological Society of Japan, 153-200. (in Japanese).
- [113] Kislov, A. V., 1991: Three-dimensional model of atmospheric circulation with complete description of physical processes and simplified dynamics. *Izvestiya, Atmos. Ocean. Phys.*, **27**(4), 241-246 (English Translation).

- [114] Kitoh, A., K. Kamazaki, and T. Tokioka, 1988: Influence of soil moisture and surface albedo changes over the African tropical rainforest on summer climate investigated with the MRI GCM-I. *J. Meteorol. Soc. Jap.*, **66**, 65-86.
- [115] Koster, R. D., and P. C. D. Milly, 1997: The interplay between transpiration and runoff formulations in land surface schemes used with atmospheric models. *J. Climate*, **10**, 1578-1591.
- [116] Kutzbach, J. E., 1981: Monsoon climate of the early Holocene: Climate experiment with the earths orbital parameters from 9000 years ago. *Science*, **214**, 59-61.
- [117] Kutzbach, J. E., and H. E. Wright, H. E., 1985: Simulation of the climate at 18,000 years BP: Results for the North American/North Atlantic/European sector and comparison with the geologic record of North America. *Quat. Sci. Rev.*, **4**, 147-187.
- [118] Kutzbach, J. E., and P. J. Guetter, 1986: The influence of changing orbital parameters and surface boundary conditions on climate simulations for the past 18 000 years. *J. Atmos. Sci.*, **43**, 1726-1759.
- [119] Lagrange, J. L., 1781-1784: Memoirs on problems in astronomy: Determination of the secular and periodic variations of the elements of the planets.
- [120] Lambert, S. J. and G. J. Boer, 2001: CMIP1: Evaluation and intercomparison of coupled climate models, *Climate Dyn.*, **17**, 83-106.
- [121] Laprise, R., and C. Girard, 1990: A spectral general circulation model using a piecewise-constant finite-element representation on a hybrid vertical coordinate system. *J. Climate*, **3**, 32-52.
- [122] Laskar, J., 1988: Secular evolution of the solar system over 10 million years. *Astron. Astrophys.*, **198**, 341-362.
- [123] Laskar, J., 1990: The chaotic motion of the Solar System: A numerical estimate of the size of the chaotic zones. *Icarus*, **88**, 266-291.
- [124] Laskar, J., F. Joutel, and F. Boudin, 1993: Orbital, precessional, and insolation quantities for the Earth from -20 Myr to +10 Myr, *Astron. Astrophys.*, **270**, 522-533.
- [125] Lea, D. W., D. K. Pak, and H. J. Spero, 2000: Climate impact of late Quaternary Equatorial Pacific sea surface temperature variations. *Science*, **289**, 1719-1724.
- [126] Legates, D. R., and C. G. Willmott, 1990: Mean seasonal and spatial variability in gauge-corrected, global precipitation. *Int. J. Clim.*, **10**, 111-127.
- [127] Legates, D. R., and C. J. Willmott, 1992: Monthly average surface air temperature and precipitations. Digital data on a 30 minute geographic (lat/long) 360x270 grid. In: Global ecosystems database version 1.0: disc A. 48 independant and 4 derived single attribute spatial layers on CD-ROM, 47.2MB, NOAA National Geophysical Data Center, Boulder, CO, U.S.A.
- [128] Leith, C. E., 1971: Atmospheric predictability and two-dimensional turbulence. *J. Atmos. Sci.*, **28**, 145-161.
- [129] Liao, X., A. Street-Perrott, and J. F. B. Mitchell, 1994: GCM experiments with different cloud parameterization: Comparisons with paleoclimate reconstructions for 6000 years B.P., *Paleoclimates*, **1**, 99-123.
- [130] Lindzen R. S., and W. Pan, 1994: A note on orbital control of equator-pole heat fluxes. *Climate Dyn.*, **10**, 49-57.
- [131] Lorenz, S., B. Grieger, Ph. Helbig, and K. Herterich, 1996: Investigating the sensitivity of the Atmospheric General Circulation Model ECHAM 3 to paleoclimate boundary conditions. *Geol Rundsch*, **85**, 513-524.
- [132] Lorius, C., J. Jouzel, C. Ritz, L. Merlivat, N. I. Barkov, Y. S. Korotkevich and V. M. Kotlyakov, 1985: A 150,000 year climatic record from Antarctica. *Nature*, **316**, 591-596.

- [133] Loughridge, M.S, 1986: Relief map of the earth's surface: *EOS (Transactions, American Geophysical Union)*, **67**, pg. 121.
- [134] Lyle, M. W., F. G. Prahl, and M. A. Sparrow, 1992: Upwelling and productivity changes inferred from a temperature record in the equatorial Pacific. *Nature*, **355**, 812-815.
- [135] Maasch, K. and B. Saltzman, 1990: A low-order dynamical model of global climatic variability over the full Pleistocene. *J. Geophys. Res.*, **95**, 1955-1963.
- [136] Mahaffy, M. W., 1976: A three-dimensional numerical model of ice-sheets: Tests on the Barnes ice cap, Northwest Territories. *J. Geophys. Res.*, **81**, 1059-1066.
- [137] Manabe, S., J. Smagorinsky, and R. F. Strickler, 1965: Simulated climatology of a general circulation model with a hydrologic cycle. *Mon. Wea. Rev.*, **93**, 769-798.
- [138] Manabe, S., 1969: Climate and ocean circulation. 1: The atmospheric circulation and the hydrology of the Earth's surface. *Mon. Wea. Rev.*, **97**, 739-774.
- [139] Manabe, S., and J. L. Holloway, 1975: The seasonal variation of the hydrologic cycle as simulated by a global model of the atmosphere. *J. Geophys. Res.*, **80**, 1617-1649.
- [140] Manabe, S., and D. G. Hann, 1977: Simulation of the tropical climate of an ice age. *J. Geophys. Res.*, **82**, 3889-3911.
- [141] Manabe, S., and A. J. Broccoli, 1985: The influence of continental ice-sheets on the climate of an ice age. *J. Geophys. Res.*, **90**, 2167-2190.
- [142] Marshall S. J., L. Tarasov, G. K. C. Clarke, and W. R. Peltier, 1999: Glaciology of Ice Age Cycles: Physical Processes and modelling challenges. *Can. J. Earth Sci.*, **37**, 769-793.
- [143] Mason, V., S. Joussaume, S. Pinot, and G. Ramstein, 1998: Impact of parameterizations on simulated winter mid-Holocene and Last Glacial Maximum climatic changes in the northern hemisphere. *J. Geophys. Res.*, **103**, 8935-8946.
- [144] McCulloch, M. T., A. W. Tudhope, T. M. Esat, G. E. Mortimer, J. Chappell, B. Pillans, A. R. Chivas, and A. Omura, 1999: Coral record of equatorial sea-surface temperatures during the penultimate deglaciation at Huon Peninsula. *Science*, **283**, 202-204.
- [145] McFarlane, N. A. , 1987: The effect of orographically excited gravity-wave drag on the circulation of the lower stratosphere and troposphere. *J. Atmos. Sci.*, **44**, 1775-1800.
- [146] McFarlane, N. A., G. J. Boer, J.-P. Blanchet, and M. Lazare, 1992: The Canadian Climate Centre second-generation general circulation model and its equilibrium climate. *J. Climate*, **5**, 1013-1044.
- [147] McManus, J.F., G. C. Bond, W. S. Broecker, S. Johnsen, L. Labeyrie, and S. Higgins, 1994: High-resolution climate records from the North Atlantic during the last interglacial. *Nature*, **371**, 326-329.
- [148] Milankovitch, M., 1941: Canon of insolation and the ice-age problem, K. Serb. Akad. Geogr., Spec. Publ., **132**, pp. 484 (English translation by Israel program for scientific translations Jerusalem, 1969).
- [149] Milly, P. C. D., and K. A. Dunne, 1994: Sensitivity of the global water cycle to the water-holding capacity of land., *J. Climate*, **7**, 506-526.
- [150] Milly, P. C. D., 1997: Sensitivity of greenhouse summer dryness to changes in plant rooting characteristics. *Geophys. Res. Lett.*, **24**, 269-271.
- [151] Mintz, Y., and Y. Serafini, 1981: Global fields of soil moisture and land-surface evapotranspiration. NASA Tech. Memo. 83907, Research Review-1980/81, NASA Goddard Space Flight Center, Greenbelt, MD, pp.178-180.
- [152] Mitchell, H. L., C. Charette, S. J. Lambert, J. Halle, and C. Chouinard, 1993: The Canadian global data assimilation system: Description and evaluation. *Mon. Wea. Rev.*, **121**, 1467-1492.

- [153] Mitchell, H. L., C. Chouinard, C. Charette, R. Hogue, and S. Lambert, 1996: Impact of a revised analysis algorithm on an operational data assimilation system. *Mon. Wea. Rev.*, **124**, 1243-1255.
- [154] Mitchell, J. F. B., 1993: Modelling of paleoclimates: examples from the recent past. *Phil. Trans. R. Soc. Lond. B*, **341**, 267-275.
- [155] Morcrette, J.-J., 1984: Sur la parameterisation du rayonnement dans les modeles de la circulation generale atmospherique. Ph.D. Thesis, l'Universite des Sciences et Techniques de Lille, 373 pp.
- [156] Morcrette, J.-J., 1990: Impact of changes to the radiation transfer parameterizations plus cloud optical properties in the ECMWF model. *Mon. Wea. Rev.*, **118**, 847-873.
- [157] Morcrette, J.-J., 1991: Radiation and cloud radiative properties in the ECMWF operational weather forecast model. *J. Geophys. Res.*, **96**, 9121-9132.
- [158] Muhs, D. R., G. L. Kennedy, and T. K. Rockwell, 1994: Uranium-series ages of marine terrace corals from the Pacific coast of North America and implications for last-interglacial sea level history. *Quat. Res.*, **42**, 72-87.
- [159] Muller, R. A., and G. J. MacDonald, 1997: Glacial cycles and astronomical forcing. *Science*, **277**, 215-218.
- [160] Noilhan, J., and S. Planton, 1989: A simple parameterization of land surface processes for meteorological models. *Mon. Wea. Rev.*, **117**, 536-549.
- [161] North, G. R., J. G. Mengel, and D. A. Short, 1983: Simple Energy Balance Model Resolving the Seasons and Continents: Application to the Astronomical Theory of the Ice Ages. *J. Geophys. Res.*, **88**, 6576-6586.
- [162] Nurnberg, D., 2000: Taking the temperature of past ocean surfaces. *Science*, **289**, pg. 1698.
- [163] Oglesby, R. J., and B. Saltzman, 1990: Sensitivity of the equilibrium surface temperature of a GCM to systematic changes in atmospheric carbon dioxide. *Geophys. Res. Lett.*, **17**, 1089-1092.
- [164] Ohkouchi, N., K. Kawamura, T. Nakamura, and A. Taira, 1994: Small changes in the sea surface temperature during the last 20 000 years: Molecular evidence from the western tropical Pacific. *Geophys. Res. Lett.*, **21**, 2207-2210.
- [165] Oppo, D. W., J. F. McManus, and J. L. Cullen, J. L., 1998: Abrupt climate events 500,000 to 340,000 years ago: Evidence from subpolar North Atlantic sediments. *Science*, **279**, 1335-1338.
- [166] Orszag, S. A., 1970: Transform method for the calculation of vector-coupled sum: Application to the spectral form of the vorticity equation. *J. Atmosp. Sci.*, **27**, 890-895.
- [167] Paillard, D., 1998: The timing of Pleistocene glaciations from a simple multiple-state climate model. *Nature*, **291**, 378-381.
- [168] Peixoto, J. P., and A. H. Oort, 1992: *Physics of Climate*. American Institute of Physics, p. 520.
- [169] Pelejero, C., J. O. Grimalt, S. Heilig, M. Kienast, and L. Wang, 1999: High resolution Uk37-temperature reconstructions in the South China Sea over the past 220 kyr. *Paleoceanography*, **14**, 224-231.
- [170] Peltier, W. R., 1994: Ice age paleotopography. *Science*, **265**, 195-201.
- [171] Peltier, W. R., 1996: Mantle viscosity and ice-age ice-sheet topography. *Science*, **273**, 1359-1364.
- [172] Peltier, W. R., 1998a: Postglacial variations in the level of the sea: Implications for climate dynamics and solid earth geophysics. *Rev. Geophys.*, **36**, 603-690.

- [173] Peltier, W. R., 1998b: "Implicit Ice" in the global theory of glacial isostatic adjustment, *Geophys. Res. Lett.*, **25**, 3955-3958.
- [174] Penck, A., and E. Bruckner, 1909: Die Alpen im Eiszeitalter, Tauchnitz, Leipzig.
- [175] Percival, D. B., and A. T. Walden, 1993: Spectral analysis for physical applications: Multitaper and conventional univariate techniques. Cambridge University. 580 pp.
- [176] Petit, J. R., J. Jouzel, D. Raynaud, N. I. Barkov, J. M. Barnola, I. Basile, M. Bender, J. Chappellaz, M. Davis, G. Delaygue, M. Delmotte, V. M. Kotlyakov, M. Legrand, V. Y. Lipenkov, C. Lorius, L. Pepin, C. Ritz, E. Saltzman, M. Stievenard, 1999: Climate and atmospheric history of the past 420,000 years from the Vostok ice core, Antarctica. *Nature*, **399**, 429-436.
- [177] Phillips, N. A., 1957: A coordinate system having some special advantages for numerical forecasting.. *J. Meteor.*, **14**, 184-185.
- [178] Phillipps, P. J., and I. M. Held, 1994: The response to orbital perturbations in an atmospheric model coupled to a slab ocean. *J. Climate*, **7**, 767-782.
- [179] Pinot, S., G. Ramstein , S. P. Harrison , I. C. Prentice , J. Guiot , M. Stute , S. Joussaume, 1999: Tropical paleoclimates at the Last Glacial Maximum: Comparison of Paleoclimate Modeling Intercomparison Project (PMIP) simulations and paleodata. *Climate Dyn.*, **15**, 857-874.
- [180] Platt, C. M. R., and Harshvardhan, 1988: Temperature dependence of cirrus extinction: Implications for climate feedback. *J. Geophys. Res.*, **93**, 11051-11058.
- [181] Pollard, D., and S. L. Thompson, 1994a: Use of a land-surface-transfer scheme (LSX) in a global climate model: The response to doubling stomatal resistance. *Global and Planetary Change*, **10**, 129-161.
- [182] Pollard, D. and S. L. Thompson, 1994b: Sea-ice dynamics and CO<sub>2</sub> sensitivity in a global climate model. *Atmos.-Ocean.*, **32**, 449-467.
- [183] Prentice, I. C., J. Guiot, B. Huntley, D. Jolly, and R. Cheddadi, 1996: Reconstructing biomes from palaeoecological data: a general method and its application to European pollen data at 0 and 6 ka. *Climate Dyn.*, **12**, 185-194.
- [184] Quinn, T. R., S. Tremaine, and M. Duncan, 1991: A three million year integration of the Earth's orbit. *Astro. J.*, **101**, 2287-2305.
- [185] Ramstein, G., and S. Joussaume, 1995: Sensitivity experiments to sea surface temperatures, sea-ice extent and ice-sheet reconstructions, for the Last Glacial Maximum. *Ann. Glaciol.*, **21**, 343-347.
- [186] Ramstein, G., Y. Serafini-Le Treut, H. Le Treut, M. Forichon, and S. Joussaume, S., 1998: Cloud processes associated with past and future climate change. *Climate Dyn.*, **14**, 233-247.
- [187] Raymo, M. E., W. F. Rudimann, N. J. Shackleton, and D. Oppo, 1990: Evolution of global ice volume and Atlantic-Pacific d13C gradients over the last 2.5 M.Y. *Earth Planetary Science Letters*, **97**, p. 353-368.
- [188] Rial, J. A., 1999: Pacemaking the ice ages by frequency modulation of Earth's orbital eccentricity. *Science*, **285**, 564-568.
- [189] Rind, D., and D. Peteet, 1985: Terrestrial conditions at the last glacial maximum and CLIMAP sea-surface temperature estimates: Are they consistent? *Quat. Res.*, **24**, 1-22.
- [190] Rind, D., 1986: The dynamics of warm and cold climates. *J. Atmos. Sci.*, **43**, 3-24.
- [191] Rind, D., D. Peteet, and G. Kukla, 1989: Can Milankovitch orbital variations initiate the growth of ice sheets in a general circulation model? *J. Geophys. Res.*, **94**, 12851-12871.

- [192] Robock, A., K. Y. Vinnikov, N. A. Speranskaya, and Y. Xue, 1995: Use of midlatitude soil moisture and meteorological observations to validate soil moisture simulations with biosphere and bucket models. *J. Climate*, **10**, 377-379.
- [193] Robock, A., K. Y. Vinnikov, and C. A. Schlosser, 1997: Reply (Evaluation of land-surface parameterization schemes using observations). *J. Climate*, **8**, 15-35.
- [194] Robock, A., C. A. Schlosser, K. Y. Vinnikov, N. A. Speranskaya, J. K. Entin, and S. Qui, 1998: Evaluation of the AMIP soil moisture simulations. *Global and Planetary Change*, **19**, 181-208.
- [195] Rohling, E. J., M. Fenton, F. J. Jorissen, P. Bertrand, G. Ganssen, and J. P. Caulet, 1998: Magnitudes of sea-level lowstands of the past 500, 000 years. *Nature*, **394**, 162-165.
- [196] Rostami, K., W. R. Peltier, and A. Mangini, 2000: Quaternary marine terraces, sea-level changes and uplift history of Patagonia, Argentina: comparisons with predictions of the ICE-4G (VM2) model of the global process of glacial isostatic adjustment. *Quat. Sci. Rev.*, **19**, 1495-1525.
- [197] Rothman, L. S., 1981: AFGL atmospheric absorption line parameters compilation: 1980 version. *Appl. Optics*, **20**, 791-795.
- [198] Royer, J. F., M. Deque, and P. Pestiaux, 1983: Orbital forcing of the inception of the Laurentide ice sheet. *Nature*, **304**, 43-46.
- [199] Ruddiman, W. F. and A. McIntyre, 1979: Warmth of the sub-polar North Atlantic Ocean during northern hemisphere ice sheet growth. *Science*, **204**, 173-175.
- [200] Saltzman, B., and M. Verbitsky, 1994: Late Pleistocene climatic trajectory in the phase space of global ice, ocean state, and CO<sub>2</sub>: Observations and theory. *Paleoceanography*, **9**, 767-779
- [201] Schlesinger, M. E., and M. Y. Verbitsky, 1996: Simulation of glacial onset with a coupled Atmospheric General Circulation/Mixed-Layer Ocean-Ice-Sheet/Asthenosphere Model. *Paleoclimate-Data and Modelling*, **2**, 179-201.
- [202] Shackleton, N. J. and N. D. Opdyke, 1973: Oxygen isotope and paleomagnetic stratigraphy of Equatorial Pacific core V28-238: Oxygen isotope temperatures and ice volumes on a 10<sup>5</sup> and 10<sup>6</sup> year scale, *Quat. Res.*, **3**, 39-55.
- [203] Shackleton, N. J., 1987: Oxygen isotopes, ice volume and sea level. *Quat. Sci. Rev.*, **6**, 183-190.
- [204] Shackleton, N. J., A. Berger, and W. R. Peltier, 1990: An alternative astronomical calibration of the lower Pleistocene timescale based on ODP site 677, *Trans. R. Soc. Edinburgh Earth Sci.*, **81**, 251-261.
- [205] Shackleton, N. J., 2000: The 100,000-year ice-age cycle identified and found to lag temperature, carbon dioxide and orbital eccentricity. *Science*, **289**, 1897-1902.
- [206] Shea, D. J., K. E. Trenberth, and R. W. Reynolds, 1992: A global monthly sea surface temperature climatology. *J. Climate*, **5**, 987-1001.
- [207] Shinn, R. A., and E. J. Barron, 1989: Climate sensitivity to continental ice-sheet size and configuration. *J. Climate*, **2**, 1517-1537.
- [208] Shukla, J., and Y. Mintz, 1982: Influence of land-surface evapotranspiration on the earth's climate. *Science*, **215**, 1498-1500.
- [209] Shukla, J., C. Nobre, and P. Sellers, P. 1990: Amazonia deforestation and climate change. *Science*, **247**, 1322-1325.
- [210] Shuttleworth, W. J., 1988: Macrohydrology: The new challenge for process hydrology. *J. Hydrol.*, **100**, 31-56.
- [211] Smith, S. D., 1980: Wind stress and heat flux over the ocean in gale force winds. *J. Phys. Oceanog.*, **10**, 709

- [212] Street, F. A. and A. T. Grove, 1979: Global maps of lake-level fluctuations since 30,000 yr BP. *Quat. Res.*, **12**, 83-118.
- [213] Stute, M., M. Foster, H. Frischkorn, A. Serejo, J. F. Clark, P. Schlosser, W. S. Broecker, and G. Bonani, 1995: Cooling of tropical Brazil (5°C) during the last glacial maximum. *Science*, **269**, 379-383.
- [214] Suarez, M. J., and I. M. Held, 1979: The sensitivity of an energy balance model to variations in the orbital parameters. *J. Geophys. Res.*, **84**, 4825-4836.
- [215] Syktus, J., H. Gordon, and J. Chappell, 1994: Sensitivity of a coupled atmosphere-dynamic upper ocean GCM to variations of CO<sub>2</sub>, solar constant, and orbital forcing. *Geophys. Res. Lett.*, **21**, 1599-1602.
- [216] Tarasov, L., and W. R. Peltier, 1997a: Termination of the 100 ka ice age cycle. *J. Geophys. Res.*, **102**, 21665-21693.
- [217] Tarasov, L., and W. R. Peltier, 1997b: A high resolution model of the 100 ka ice age cycle. *Ann. Glaciol.*, **25**, 58-65.
- [218] Tarasov, L., and W. R. Peltier, 1999: The impact of thermomechanical ice-sheet coupling on a model of the 100 kyr ice-age cycle. *J. Geophys. Res.*, **104**, 9517-9545.
- [219] Taylor, K. E., C. D. Hewitt, P. Braconnot, A. J. Broccoli, C. Doutriaux, J. F. B. Mitchell, and PMIP Participating Groups, 2000: Analysis of forcing, response, and Feedbacks in a paleoclimate modelling experiment. In Paleoclimate Modelling Intercomparison Project (PMIP): Proceedings of the third PMIP workshop. WCRP-111 WMO/TD-No. 1007 ICPO Publication No. 34. 271 pp.
- [220] Texier, D., N. de Noblet, S. P. Harrison, A. Hexeltine, D. Jolly, S. Joausaume, F. Laarif, I. C. Prentice, P. Tarasov, 1997: Quantifying the role of biosphere-atmosphere feedbacks in climate change: Coupled model simulations for 6000 years BP and comparison with palaeodata for Northern Eurasia and Northern Africa. *Climate Dyn.*, **13**, 865-882.
- [221] Thompson, L.G., E. Mosley-Thompson, M. E. Davis, P.-N. Lin, K. A. Henderson, J. Cole-Dai, J. F. Bolzan, and K.-b. Liu, 1995: Late glacial stage and Holocene tropical ice core records from Huascan, Peru. *Science*, **269**, 46-50.
- [222] Thompson, L. G., M. E. Davis, E. Mosley-Thompson, T. A. Sowers, K. A., Henderson, V. S. Zagorodnov, P.-N. Lin, V. N. Mikhailenko, R. K. Campen, J. F. Bolzan, J. Cole-Dai, and B. Francou, 1998: *Science*, **282**, 1858-1864.
- [223] Thompson, S.L., and Pollard, D. 1995: A global climate model (GENESIS) with a land-surface-transfer scheme (LSX). Part 1: Present climate simulation. *J. Climate*, **8**: 732-761.
- [224] Thomson, D. J., 1982: Spectrum estimation and harmonic analysis, *Proc. IEEE*, **70**, 1055-1096.
- [225] Trenberth, K. E., and A. Solomon, 1994: The Global Heat Balance: Heat transports in the atmosphere and ocean. *Climate Dyn.*, **10**, 107-134.
- [226] Vavrus, S. J., 1999: The role of the coupled arctic sea ice-atmosphere system to orbital forcing and ice motion at 6 kyr and 115 kyr BP. *J. Climate*, **12**, 873-896.
- [227] Verbitsky, M. Y., and R. J. Oglesby, 1992: The effect of atmospheric carbon dioxide concentration on the continental glaciation of the Northern Hemisphere. *J. Geophys. Res.*, **97**, 5895-5909.
- [228] Verseghy, D. L., N. A. McFarlane, and M. Lazare, 1993: CLASS-A Canadian land surface scheme for GCMs. Part II: Vegetation model and coupled runs. *Int. J. Climatol.*, **13**, 347-370.
- [229] Vettoretti G., W. R. Peltier, and N. A. McFarlane, 1998: Simulations of Mid-Holocene climate using an atmospheric general circulation model. *J. Climate*, **11**, 2607-2627.

- [230] Vettoretti G., W. R. Peltier, and N. A. McFarlane, 2000a: The simulated response of the climate system to soil moisture perturbations under paleoclimatic boundary conditions at 6000 years before present. *Can. J. Earth Sci.*, **37**, 635-660.
- [231] Vettoretti G., W. R. Peltier, and N. A. McFarlane, 2000b: Global water balance and atmospheric water vapour transport at Last Glacial Maximum: Climate simulations with the CCCma atmospheric general circulation model. *Can. J. Earth Sci.*, **37**, 695-723.
- [232] Vettoretti G., Peltier, W. R., 2001: On Post Eemian Glacial Inception. *J. Climate*, (submitted).
- [233] Vincent, J.-S., and V. K. Prest, 1987: The early Wisconsin history of the Laurentide ice-sheet, *Phys. Geog. Quat.*, **XLI(2)**: 199-213.
- [234] Vinnikov, K.Ya, and I. B. Yeserkepova, 1991: Soil moisture: Empirical data and model results. *J. Climate*, **4**: 66-79.
- [235] Warrilow, D.A., A. B. Sangster, and A. Slingo, 1986: Modelling of land surface processes and their influence on European climate. DCTN 38, Dynamical Climatology Branch, United Kingdom Meteorological Office, Bracknell, Berkshire RG12 2SZ, UK.
- [236] Washington, W. M., and D. L. Williamson, 1977: A description of the NCAR GCM. In *Methods in Computational Physics*, 17, J. Chang (ed.), Academic Press, New York, 111-172.
- [237] Weaver, A. J., and T. M. C. Hughes, 1996: On the incompatibility of ocean and atmosphere models and the need for flux adjustments. *Climate Dyn.*, **12**, 141-170.
- [238] Weaver, A. J., M. Eby, A. F. Fanning, and E. C. Wiebe, 1998: Simulated influence of carbon dioxide, orbital forcing and ice-sheets on the climate of the Last Glacial Maximum. *Nature*, **394**, 847-853.
- [239] Webb, R. S., D. H. Rind, S. J. Lehman, R. J. Healy, and D. Sigman, 1997: Influence of ocean heat transport on climate of the Last Glacial Maximum. *Nature*, **385**, 695-699.
- [240] Webster, P., and A. Streten, 1978: Late quaternary ice age climates of tropical Australasia: Interpretations and reconstructions. *Quat. Res.*, **10**, 279-309.
- [241] Wigley, T. M. L., 1976: Spectral Analysis: Astronomical theory of climate change, *Nature*, **264**, 629-631.
- [242] Wilcox, R. W., and A. D. Belmont, 1977: Ozone concentration by latitude, altitude, and month near 80 degrees West. Report No. FAA-AEQ-77-13, FAA Office of Environmental Quality, High Altitude Pollution Program, U.S. Department of Transportation, Washington, D.C., 41 pp.
- [243] Wilson, M. F., and A. Henderson-Sellers, 1985: A global archive of land cover and soils data sets for use in general circulation models. *Int. J. Climatology*, **5**, 119-143.
- [244] Yung, Y. L., T. Lee, C.-H. Wang, Y.-T. Shieh, 1996: Dust: A diagnostic of the hydrological cycle during the Last Glacial Maximum. *Science*, **271**, 962-963.